POLITECNICO
MILANO 1863

SCUOLA DI INGEGNERIA INDUSTRIALE
E DELL'INFORMAZIONE

The integration of wind and solar renewable energy sources into 3 kV DC railway systems.

TESI DI LAUREA MAGISTRALE IN
ELECTRICAL ENGINEERING
INGEGNERIA ELETTRICA

Author: **Marco Alessandro Cervi**

Student ID: 10690308
Advisor: Morris Brenna
Co-advisor: Hamed Jafari Kaleybar
Academic Year: 2021-22

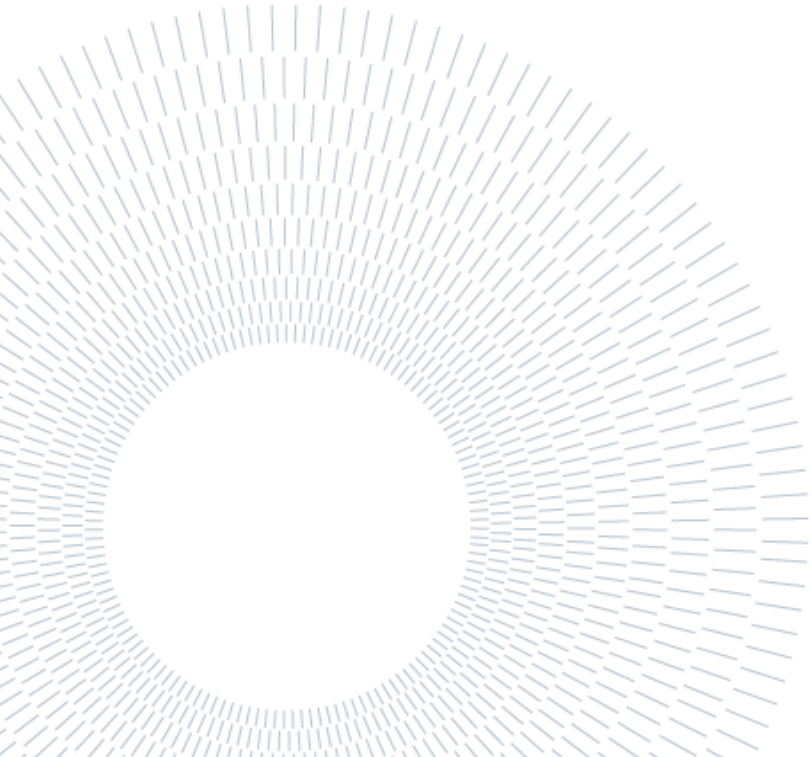

Abstract

This thesis focuses on the integration of photovoltaic and wind energy sources into 3 kV DC railway systems to aid in the power supply of the traction loads in conjunction with the traction substations. This solution is regarded with particular interest in research due to the possibility to exploit the DC section of the PV and wind generators for direct connection to the railway system, without the need for an AC conversion stage, while also preserving the inherent advantages that characterize DC railway traction. The thesis includes a theoretical overview of photovoltaic systems, wind systems, and DC railway traction systems and their relevant components, followed by the modeling of and simulation of a traction load based on the ETR 1000 high-speed train operating within the 3 kV DC railway system. The simulations are conducted considering different scenarios with and without the renewable generators in parallel to the traction substations, in order to investigate their contribution in terms of power and energy supplied to the traction loads.

Key words: Electric railway, renewable energy, PV system, wind energy, traction substation, catenary, voltage drop, bilateral power supply, high-speed train.

Abstract in Italiano

Questa tesi si focalizza sull'integrazione delle risorse di energia fotovoltaica ed eolica nei sistemi ferroviari a 3 kV in corrente continua per contribuire, congiuntamente alle sottostazioni di trazione, all'alimentazione dei carichi di trazione. Tale soluzione è considerata con particolare interesse a livello di ricerca grazie alla possibilità di sfruttare la sezione DC dei generatori fotovoltaici ed eolici per il collegamento diretto al sistema ferroviario in corrente continua, eliminando la necessità di un successivo stadio di conversione AC, e preservando i vantaggi intrinseci che caratterizzano i sistemi ferroviari in corrente continua. La tesi comprende una panoramica teorica dei sistemi fotovoltaici, eolici e dei sistemi di trazione ferroviaria in corrente continua e dei relativi componenti, seguita dalla modellazione e simulazione di un carico di trazione basato sul treno ad alta velocità ETR 1000 operante all'interno del sistema ferroviario a 3 kV DC. Gli scenari considerati nelle simulazioni comprendono casistiche con e senza i generatori rinnovabili in parallelo alle sottostazioni di trazione, al fine di indagare gli scambi di potenza con i carichi di trazione.

Parole chiave: trazione elettrica, energie rinnovabili sistemi fotovoltaici, energia eolica, sottostazione di trazione, catenaria, caduta di tensione, alimentazione bilaterale, alta velocità.

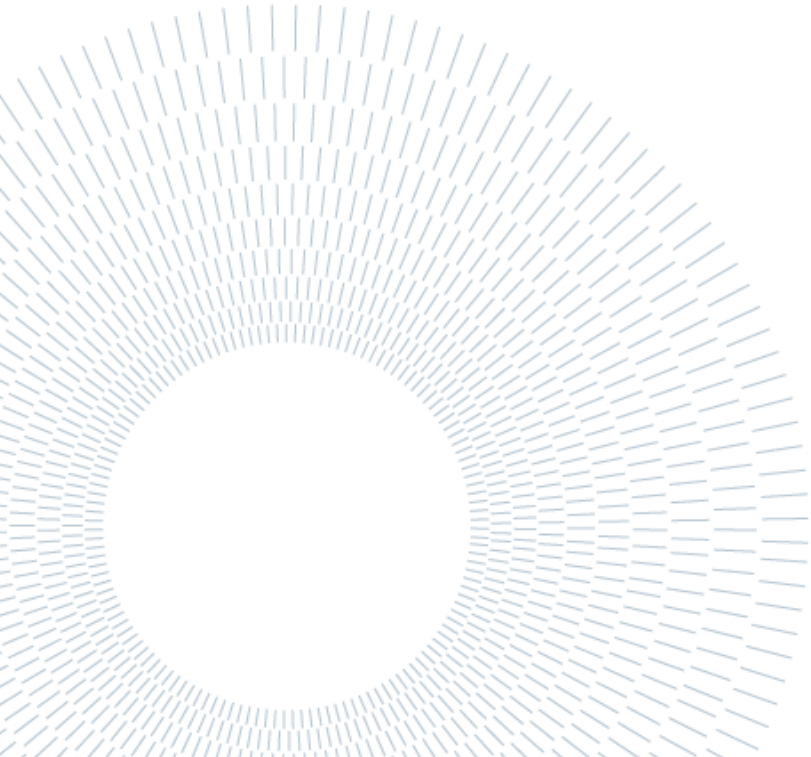

Contents

Introduction

The undisputed advantages of electric traction in terms of performance, specific power consumption, safety, sustainability, and economy of service, coupled with increasing demand for mobility of people and goods, have led to electric railway systems becoming one of the largest and highest-consumption end users of the utility grid [1]. It therefore stands to reason that the development of smart grid features and sustainable technologies aimed at reducing energy consumption and emissions, such as distributed renewable energy sources, that have made tremendous strides in several industrial power generation applications, should also be applied to the electric railway network. In fact, the integration of smart grid features such as distributed photovoltaic and wind energy sources (together with energy storage systems and charging infrastructures for electric vehicles and the associated energy management system) into electric railway systems is deemed to be highly suitable due the dedicated switchgear, transmission and distribution lines, and other essential infrastructure already in place along the traction lines. In this regard, the 3 kV DC railway, which accounts for 11921 km of the Italian railway line (followed by the 2x25 kV AC with 1296 km), has garnered considerable interest from researchers, due to the possibility to be directly fed by the DC section of photovoltaic and wind generators in parallel to the traction substations and without section breaks. Despite these outstanding potentialities and advantages, however, smart grid-based progress in electric railway systems is delayed, as further research and investigation into the most suitable connection points and technical solutions is required [1]. In regard to DC railway, on a research and development level, two main solutions are investigated. The first involves the adaptation of the conventional 3 kV DC railway to accommodate distributed renewable generators and other smart grid features such as energy storage systems and charging infrastructure for electric vehicles, which would preserve the existing railway power supply infrastructure. The second considers the revamping of DC railway power supply infrastructure (namely, traction substations and contact lines) to higher power ratings and to a novel medium-voltage in the range of 7.5-24 kV [2], in anticipation of future trends towards higher traffic intensity, higher operating speed (which entail higher power demands), and high-capacity energy storage units and charging facilities.

In light of the aforementioned considerations, this thesis focuses on the integration of a photovoltaic system and a wind farm into a section of the conventional Italian 3 kV DC railway network in order to increase network capacity, peak shaving, and energy savings associated with the power supplied to the traction loads. The considered section consists of a double track under bilateral power supply from two adjacent traction power substations, and is modeled based on the characteristics of the 3 kV DC high-speed line connecting Florence and Rome. The renewable generators, each having a power rating of 1.5 MW, are considered for the parallel connection to the traction substations to supply the traction loads. The traction load is modeled based on the characteristics of the ETR1000 high-speed train, which constitutes a good example of high-speed, high-power traction load. To this end, the thesis includes five chapters that are dedicated to the theoretical overview of photovoltaic systems, wind power generation, the Italian 3 kV DC electric railway system, and the DC railway microgrid concept, followed by a chapter dedicated to the modeling of the 3 kV DC traction circuit and the ETR1000 train. Finally, the development and simulation of the model within MATLAB® and Simulink-SIMSCAPE™, inclusive of the renewable generators, is illustrated to envision and compare the electrical quantities at play in the system (most importantly, the electrical power exchange) for different train mission profiles and availability of the photovoltaic and wind energy sources.

1 Solar photovoltaic power

1.1. Energy from the Sun

Every second, the Sun releases $3.846 \cdot 10^{26}$ J of energy. Every year, the fraction of energy emitted from the Sun that intercepts Planet Earth amounts to $5.456 \cdot 10^{24}$ J, almost ten thousand times the total primary energy consumed globally in 2019 [3]. For the coming eras, the Sun can be considered as a virtually unlimited source of energy, and for ages it has irradiated the Earth with electromagnetic energy sustaining all lifeforms, regulating climate and most meteorological phenomena. For centuries, mankind utilized the Sun's radiant light and heat in several rudimentary yet ingenious applications, including the illumination and heating of living spaces, fire ignition, and in the first greenhouses. Today, solar energy is harnessed extensively using a range of technologies, playing a role of fundamental importance in the generation of renewable electrical and thermal energy.

The3haptey produced from hydrogen fusion reactions In the Sun's core propagates through the Sun itself and the surrounding space in the form of heat, sound, and electromagnetic radiation characterized by different wavelengths and energetic properties:

- Gamma rays and X rays (wavelengths ranging from less than 1 pm to 100 nm)
- Ultraviolet rays (100÷400 nm)
- Visible light (400÷700 nm)
- Infrared rays (700 nm to 1 mm)
- Microwaves (1 mm to 10 cm)
- Radio waves (wavelengths greater than 10 cm)

The energy associated with each wavelength is represented in the solar irradiance spectrum shown in Figure 1.1 (relative to an Air Mass (AM) ratio[1] of 1.5), which also shows the energy losses in the electromagnetic radiation as it passes through Earth's atmosphere, due to absorption and diffusion phenomena [5]. In fact, the total power

[1] The AM ratio defines the distance traveled by the incoming solar radiation through the atmosphere relative to the shortest distance (Sun directly overhead, i.e., AM1) [4]. The notation AM1.5 stands for AM value of 1.5.

per unit surface, given by the area under the curves, decreases from 1366 W/m^2 outside the atmosphere to 1000 W/m^2 at sea level [5].

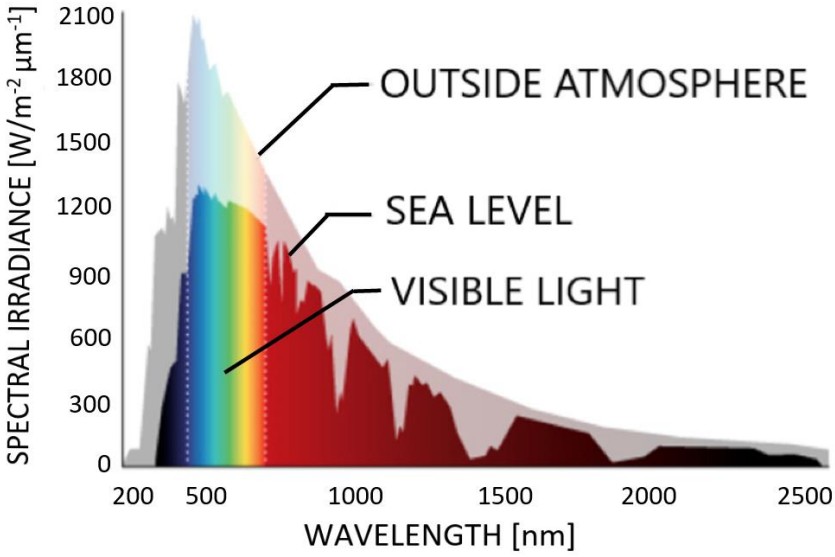

Figure 1.1: Solar spectral irradiance [6].

The passage of the solar flux through the Earth's atmosphere causes the incoming electromagnetic radiation to be split in a direct component (also called beam radiation), which is maximum for surface orientations normal to the solar flux, and a diffuse component, that does not possess any preferential angle of trajectory. The total global solar radiation is defined as the sum of the direct and diffuse components, as measured on a fixed flat plate on the Earth's surface [4]. Beam energy is measured by means of a pyrheliometer, while total global solar radiation is measured with a pyranometer. Solar irradiance, as well as the amounts of direct and diffuse components on the Earth's surface, vary widely according to several factors:

- The Earth's revolution around the sun, in conjunction with the Earth's rotational axial tilt (which varies yearly from +23.5° to -23.5°), causes locations at different latitudes to receive different irradiances throughout the year due the varying angle between the incoming solar flux and the Earth's surface, different daylight times, and different air mass ratios.
- The Earth's rotation that changes the relative position between a particular surface on Earth and the Sun, and thus the angle of incidence of the direct radiation component, as well as the air mass to be crossed by the solar flux.
- Atmospheric and meteorological conditions, landscape, and surrounding environment. On very cloudy days, a higher proportion of radiation is reflected, and the total global solar radiation is practically all diffuse [4].

Conversely, dry days with a clear sky are characterized by higher solar irradiance, which is predominantly direct. Other factors include the presence of large bodies of water, reflective surfaces (such as snow or lightly colored artificial surfaces), different types of terrain, prevailing winds [4], etc.

The reference value of solar irradiance used for the evaluation of performance parameters of solar power devices is 1000 W/m² (also known as *one Sun*). However, because solar irradiance is highly variable, the design of photovoltaic generators also relies on historical data and statistical models of the solar irradiance conditions (as well as other factors affecting solar power generation, such as temperature) of a preselected site.

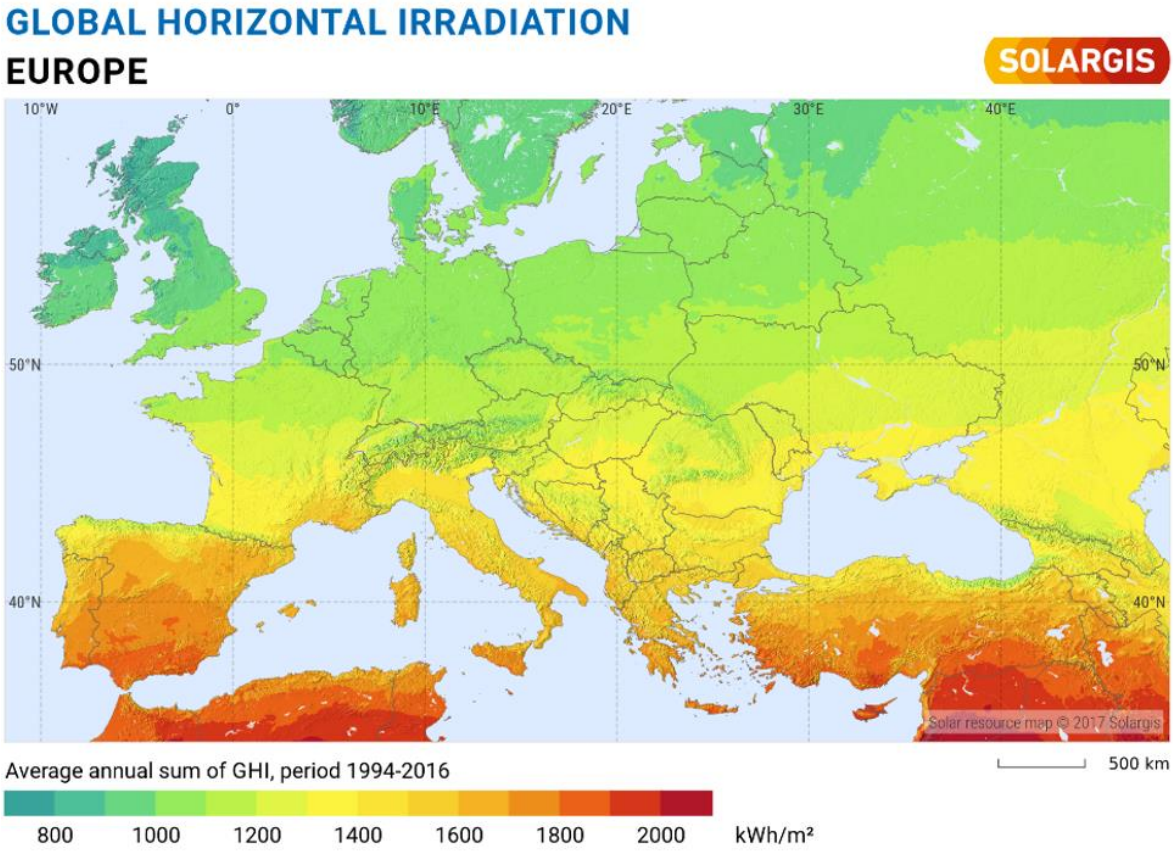

Figure 1.2: European map of global irradiation on a horizontal surface [7].

1.2. The photovoltaic cell

Arguably the most well-known and widespread technology used to harness solar energy to generate electricity is the photovoltaic cell (PV cell), which was first invented over a century ago as an experimental demonstration of the photovoltaic effect by Edmond Becquerel in 1939. It wasn't until the advent of space travel in the 1960s, however, that PV cells were implemented for actual power generation applications, due to their great advantage in generating electricity without moving parts. At the time, the cost of PV cells as a niche and new technology was extremely high. Later breakthroughs in semiconductor electronics, followed by more recent concerns regarding the impacts and usage of fossil fuels, lead to the incentivization of photovoltaic technologies in the energy sector, affirming their role in large-scale, commercially competitive power generation applications. PV plants now account for approximately 586 GW of installed capacity worldwide, with 147 GW in Europe, and 21 GW in Italy [3].

1.2.1. Principle of operation

1.2.1.1. The photovoltaic effect

Most PV devices are composed of crystalline silicon (c-Si)-based materials, which undergo the photoelectric effect when exposed to an energy source, such as sunlight. In pure silicon, the photoelectric effect involves the movement of valence electrons from the covalently bonded silicon atoms following sufficient energization. The threshold energy for this to occur is the bandgap energy, equal to 1.12 eV in the case of silicon. The resulting movement of free electrons inside the semiconductor material determines, by definition, an electric current. Within the semiconductor's atomic structure, each energized electron leaves behind an empty space, referred to as *hole*, that is then filled by another energized electron moving away from a neighboring atom, creating yet another hole. The continual movement of a hole is treated as a positively charged particle moving through the crystal structure [4], occurring in conjunction with the movement of the negatively charged electrons. In this regard, free electrons and holes are referred to as charge carriers. In pure silicon, holes and free electrons are present in equal numbers and rapidly recombine, causing the electrical conduction to cease.

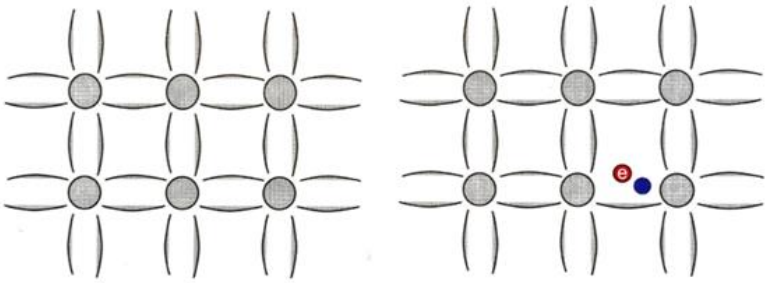

Figure 1.3: Silicon lattice with no free electrons (left) and with a free electron-hole pair (right).

1.2.1.2. The p-n junction

To avoid charge recombination and to sustain the conduction process, semiconductor devices used in actual applications make use of doped semiconductor materials in which positive and negative charge carriers are present in different amounts. Specifically, separate slabs of crystalline silicon are doped[2] with minute quantities (in the order of one part per million [4]) of boron (group III element) and phosphorous (group V), forming, respectively, two types of material: *p-type* material, in which the holes are the majority carriers, and *n-type* material, in which the electrons are the majority carriers. The union of p-type and n-type materials constitutes the well-known p-n junction, which is the constituent element of the vast majority of power electronic devices such as diodes, thyristor, and PV cells (also known as photodiodes). At the p-n junction interface, electrons and holes quickly recombine, creating a depletion layer void of mobile charges which prevents further movement of charge in either direction. In fact, the electrons leaving the phosphorous atoms create immobile, positively charged ions in the n-side, and the holes leaving the boron atoms create immobile, negatively charged ions in the p-side. The presence of these immobile, positively and negatively charged ions in the depletion layer gives rise to an internal electric field that opposes further movement of electrons and holes. It can be observed, however, that small quantities of majority carriers still manage to diffuse through the depletion layer due to sufficient energization, creating a *diffusion current*; additionally, some minority carriers are swept across the junction interface by the internal electric field, creating a *drift current*. At equilibrium, the diffusion current balances out with the drift current, thus the net current flow across the junction interface is zero, and so is the potential difference across the p-n junction terminals [8].

[2] The most common method consists of coating the silicon with a layer of phosphorous and then heating the surface until it diffuses into the crystal; boron is typically introduced into the c-Si during the metallurgical processing part that purifies the Si [4].

1.2.1.3. Exposure to sunlight

The inherent imbalance between charge carriers in doped semiconductor materials is exploited in photovoltaic devices to generate DC current upon exposure to sunlight (or it is used to induce the flow of current in other devices, such as diodes and thyristors, when subjected to an external potential difference). Upon exposure of the PV cell to solar irradiance, the photons with sufficiently high energy generate electron-hole pairs in the depletion layer, where the internal electric field then separates some of the positive and negative charge carriers before they can recombine, accelerating the electrons from p-side to n-side, and holes from n-side to p-side. Consequently, the p-side accumulates holes and the n-side accumulates electrons [4], effectively creating a separation of charge that is in opposition with the electric field at the junction interface, decreasing the net electric field across the cell (favoring the diffusion current). The described movement of charge generated from the exposure to sunlight is defined as *photocurrent*, which is therefore always in opposition to the diffusion current. If the PV cell is not connected to an external load, the generated carriers are confined within the cell, and, at a certain threshold of irradiance, the diffusion current and the photocurrent balance each other out. The voltage across the cell terminals in this equilibrium condition is the open-circuit voltage V_{OC}. When the terminals of a PV cell are connected to an external circuit, as shown in Figure 1.4, the electrons accumulated in the n-side are provided with a conductive path to flow through back to the p-side, where they recombine with the holes. The consequent reduction of negative charge in the n-side and the recombination in the p-side results in a decreased forward bias[3] of the junction compared to the open circuit condition, leading, in turn, to a decreased diffusion current. The current flowing in the external circuit is then the difference between the photocurrent and the diffusion current, and the potential difference across the cell terminals is conventionally positive (forward bias). In the particular case in which the cell is short-circuited, the short-circuit current I_{SC} from the cell coincides with the photocurrent.

[3] A p-n junction is forward biased when the electric field across its terminals favors the flow of the diffusion current, i.e., when the p-side voltage is conventionally positive and the n-side voltage is conventionally negative. The opposite situation occurs when the cell is reversed biased.

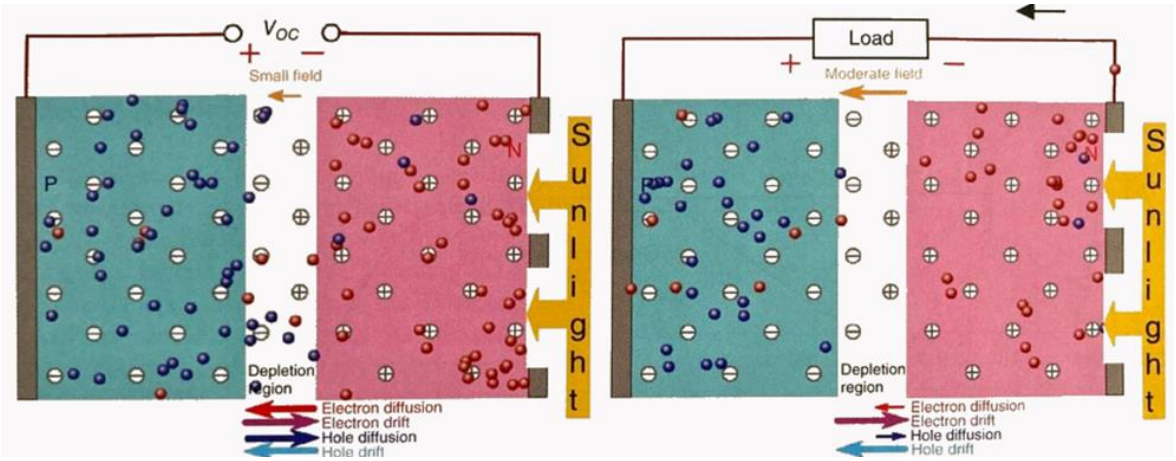

Figure 1.4: p-n junction exposed to sunlight: in open-circuit (left) and connected to a load (right) [4].

1.2.2. Equivalent circuit model and electrical characteristics

The considerations regarding the electric current generated by the cell in the various configurations are based on assumptions allowing for application of the superposition principle[4], whereby the net current in the cell is given by the sum of an ideal p-n diode current and the photocurrent induced in the p-n junction by the incoming irradiance. In other words, the net current is calculated as the resultant of two currents arising in response to two excitations taken separately: the first is the voltage across the cell terminals, that induces the ideal p-n diode current I_D, and the second is exposure of the cell to sunlight, that generates the photocurrent I_P.

The ideal p-n diode current is given by the Shockley equation:

$$I_D = I_o\left(e^{\frac{qV_D}{nkT}} - 1\right) \tag{1.1}$$

where V_D is the voltage across the terminals of the p-n junction, I_o is the reverse saturation current[5], $q = 1.6 \cdot 10^{-19}$ C is the electron charge, $n = 1 \div 2$ is the ideality

[4] The range of validity of these assumptions, and the application of the superposition principle in PV cell analysis are explained extensively in [9].

[5] A diode in the reverse biased state conducts a very small current (in the order μA or pA) [4]: under reverse bias, the diffusion current is significantly reduced, while the drift current is relatively unchanged because it is limited by the number of minority carriers. The analytical expression of the reverse saturation current is $I_o = A_o T^3 e^{\frac{-E_g}{kT}}$ where A_o is a parameter of the material, T is temperature in degrees Kelvin, E_g is the energy gap, and $k = 1.381 \cdot 10^{-23}$ J/K is Boltzmann's constant.

factor[6], $k = 1.381 \cdot 10^{-23}$ J/K is the Boltzmann's constant, and T the junction temperature (in degrees Kelvin) [4].

The photocurrent I_P (of opposite sign to I_D) is evaluated as [4]:

$$I_P = qG_eA_c(L_n + L_p) \tag{1.2}$$

where G_e is the electron generation rate[7], which is directly proportional to the light intensity, A_c is the cell area, and L_n and L_p are the electron and hole diffusion lengths, respectively. With all other cell parameters being equal, the photocurrent is constant for a given light intensity.

The operation of a PV cell as described using the superposition principle is represented by means of the equivalent circuit in Figure 1.5, where the cell is modeled as a parallel combination of the photocurrent source I_P and the diode representing the p-n junction, and the shunt resistance R_{SH} and series resistances R_S are included to account for dissipative phenomena occurring in the metal contacts, at metal-semiconductor interfaces, and in the semiconductor layers [9].

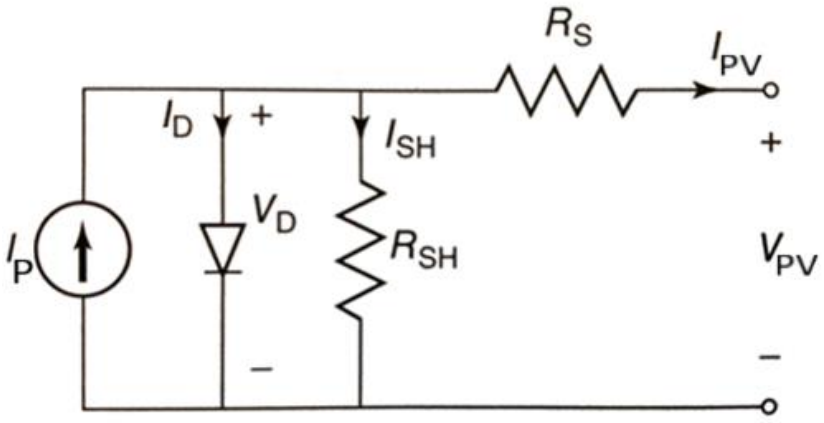

Figure 1.5: Single diode equivalent circuit of a PV cell [4].

With reference to the equivalent circuit in Figure 1.5, Kirchhoff's current law indicates that the output current of the PV cell is:

$$I_{PV} = I_P - I_D - I_{SH} \tag{1.3}$$

---

[6] The ideality factor depends on the generation and recombination phenomena occurring in the depletion region. Typical values of n are 1.5 for Si and 1 for Ga.

[7] The analytical expression of the generation rate is $G_e = \alpha N_o e^{-\alpha s}$ where α, N_o, s are the absorption coefficient [cm^{-1}], the photon flux at the surface [photons/unit area/second], and distance into the material, respectively [10].

where I_{SH} is the current flowing through the shunt resistance, related to the p-n junction terminal voltage by Ohm's law:

$$I_{SH} = \frac{V_D}{R_{SH}} \tag{1.4}$$

Kirchhoff's voltage law applied to the output terminals of the PV cell yields:

$$V_D = I_{PV}R_S + V_{PV} \tag{1.5}$$

And thus

$$I_{SH} = \frac{I_{PV}R_S + V_{PV}}{R_{SH}} \tag{1.6}$$

substituting Equations (1.1) and (1.6) in Equation (1.3) yields the expression for the output current:

$$I_{PV} = I_P - I_o\left(e^{\frac{q(I_{PV}R_S+V_{PV})}{nkT}} - 1\right) - \frac{I_{PV}R_S + V_{PV}}{R_{SH}} \tag{1.7}$$

Equation (1.7) is a transcendental function, meaning it has no general analytical solution [4]; it is solved using numerical methods to obtain the voltage-current characteristic of the PV cell, plotted in Figure 1.6. By multiplying both sides of the equation by the cell's output voltage, the power supplied by the cell P_{PV} is found (also plotted in Figure 1.6):

$$P_{PV} = V_{PV}I_{PV} = V_{PV}\left[I_P - I_o\left(e^{\frac{q(I_{PV}R_S+V_{PV})}{nkT}} - 1\right) - \frac{I_{PV}R_S + V_{PV}}{R_{SH}}\right] \tag{1.8}$$

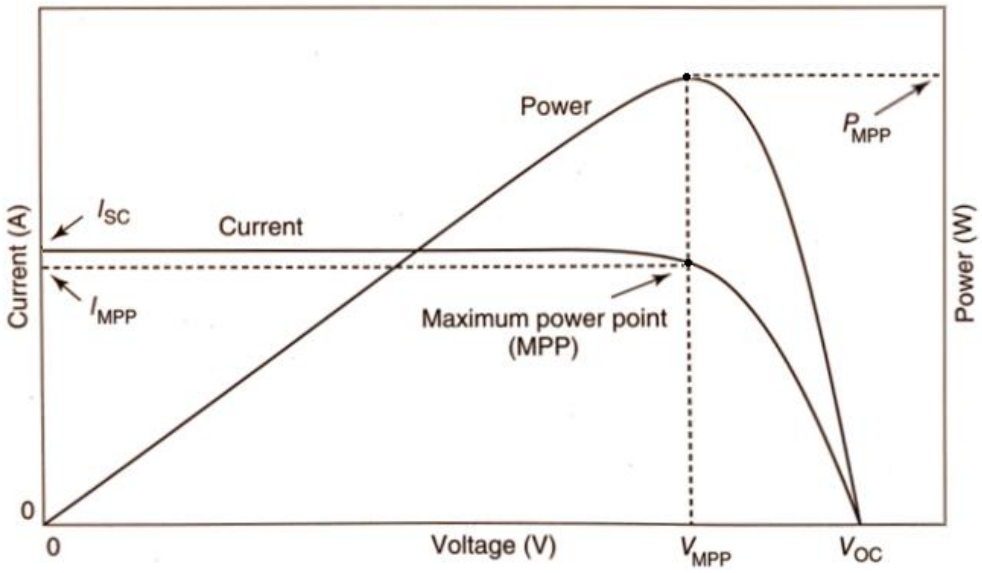

Figure 1.6: Electrical characteristics of the PV cell.

Inspection of the I_{PV}-V_{PV} and P_{PV}-V_{PV} characteristics reveals key information about the operating points of the PV cell: firstly, the highest voltage that can be generated at the output terminals is the open-circuit voltage V_{OC}, occurring when the cell operates at no load and thus when the output current is zero. Considering that modern, high quality PV cells are characterized by low losses, such that the dissipative effects of the resistive components can be considered negligible[8], the following approximation can be used to evaluate the open-circuit voltage:

$$V_{OC} \approx \frac{nkT}{q} \ln\left(\frac{I_P}{I_o} - 1\right) \tag{1.9}$$

The open-circuit voltage of PV devices is specified in reference to standard test conditions (CEI EN 60904-3) of 1000 W/m² of irradiance under AM ratio of 1.5 and at a temperature of 25°C. For the single PV cell, typical values of open-circuit voltage range from 0.6 V in polycrystalline cells, up to 0.764 V in high quality monocrystalline cells, while the output voltage during operation under load at the maximum power point is around 0.5 V [4].

Recalling Equation (1.7) for the output current neglecting the dissipative phenomena, it can be simplified as:

[8] High quality PV cells are typically characterized by low series resistance and reverse saturation current, and high shunt resistance [4].

$$I_{PV} = I_P - I_o\left(e^{\frac{qV_{PV}}{nkT}} - 1\right) \tag{1.10}$$

Considering that[9] $e^{\frac{qV_{PV}}{nkT}} \gg 1$, the generic PV output voltage can be approximated as:

$$V_{PV} \approx \frac{nkT}{q}\ln\left(\frac{I_P - V_{PV}}{I_o}\right) \tag{1.11}$$

When the cell terminals are short-circuited, the output voltage is zero and the short-circuit current can easily be obtained using Equation (1.3) with the usual simplifications:

$$I_{SC} \approx I_P - I_o(e^0 - 1) \tag{1.12}$$

It immediately follows that $I_{SC} \approx I_P$, as is experimentally verified in high quality PV cells [4]. In any case, the range of variability of PV cell current is quite limited between the maximum power point and the short-circuit condition. Typical reference values for the current density of a commercial PV cell are in the range of 30 mA/cm^2 to 36 mA/cm^2. Single crystal PV cells are generally 15.6 × 15.6 cm^2, producing a total current of 9 – 10 A [4].

1.3. The PV module

From a practical standpoint, the PV module is the fundamental building block of PV installations. The PV module is a long-lasting, weather-resistant, protective unit which is encapsulates a number of series-connected PV cells (typically 36, 64, 72, or 96 depending on the application). As such, PV modules are designed and constructed for robustness and durability, and to ensure optimal operating conditions for the cells in terms of exposure to sunlight, electrical functioning, and protection from mechanical and thermal stress. Different layers of special materials are implemented to cover these functions, creating a laminate structure to the PV module. On the front side, modules are typically fitted with tempered, low-iron glass and an antireflection coating to ensure good transmission and low reflection of light. Alternatively, surface texturing of the glass can be implemented to reduce reflection [10], although not as effective due to increased likelihood of lodging of dust and dirt. The front cover is designed to be impervious to atmospheric

[9] The consideration is valid for output voltages greater than 100 mV [10].

conditions and to have good impact resistance. The cells constituting the module are bound in place by a heat-resistant and transparent layer of encapsulant, most commonly EVA (ethyl vinyl acetate) [10], that provides adhesion to the top and rear surface of the module. The rear surface, also referred to as *backskin*, is typically a thin polymer sheet of Tedlar, presenting high mechanical strength and low thermal resistance. The backskin should also be impermeable to water and oxygen entry. Finally, the module is fitted with an anodized aluminum frame that provides rigidity and resistance to bending moments, and further protection against corrosive agents [5]. PV module lifetime generally exceeds 25 years, with warranties typically guaranteeing that PV modules operate at a minimum of 90% of their rated power after the first 10 years, and at a minimum of 80% of the rated power up to 25 years [10].

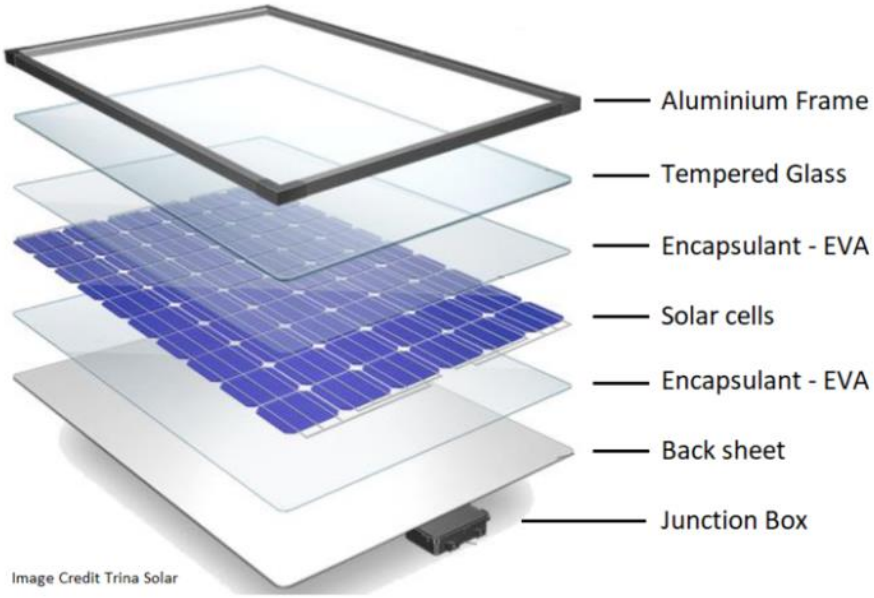

Figure 1.7: Components of a PV module [12].

The current produced by the module is collected from the top contacts of each cell by the interconnecting circuitry terminating with external leads, securely housed in the junction box located on the rear side of the module. In simpler solutions, the back contacts that complete the circuit consist of a sheet of aluminum. The leads can be accessed to interconnect the modules by means of dedicated connectors. To maximize the performance of a module, great engineering efforts are expended to ensure that each cell exhibits identical electrical behavior, that is, to eliminate mismatch between cells. The reason for this is that the current/voltage output in series/parallel connections of cells is limited by the worst performer.

The rated power of a PV module is defined at the maximum power point under the standard test conditions [13] and is expressed in kilowatts-peak [kWp]. The rated power of a complete PV installation is the sum of the rated powers of the constituent modules.

Figure 1.8: PV modules in a 49.7 kWp installation on a rooftop [13].

1.4. Performance parameters of PV devices

A qualitative parameter of PV cells is the fill factor (*FF*), defined as the ratio of the maximum power and the product of short-circuit current and open-circuit voltage [17]:

$$FF = \frac{P_{MPP}}{I_{SC}V_{OC}} = \frac{I_{MPP}V_{MPP}}{I_{SC}V_{OC}} \tag{1.13}$$

Typical monocrystalline silicon cells have fill factor values in the order of 0.75÷0.8 [14]. Higher FF values are usually indicators of better performance.

With regards to the efficiency of a photovoltaic cell, it is intrinsically limited by the fact that only a fraction of the solar spectral irradiance is effectively utilized to generate electricity. For instance, c-Si cells, convert light between 300 nm and 1.11 μm, about 50% of the solar spectral irradiance. Within this range, each wavelength generates the same number of carriers, meaning that shorter wavelengths provide excess energy that is dissipated as heat. Thus, the maximum theoretical efficiency of c-Si cells cannot exceed 50% [4].

In practical applications, the PV cell efficiency η_{PV} is defined as the ratio between the maximum power generated by the cell and the input power P_{irr} that the cell receives in the form of solar irradiance under standard test conditions (STC) [14]:

$$\eta_{PV} = \frac{P_{MPP}}{P_{irr}} = \frac{FFI_{SC}V_{OC}}{P_{irr}} \tag{1.14}$$

Typical values of efficiency under STC are around 25% for monocrystalline Si cells and 20% for polycrystalline Si cells [4]. Efficiencies are generally lower during operation in practical applications due to varying irradiance and temperature and due to power dissipations of various nature, with usual c-Si cells converting approximately 18% of the input power into electrical power. Some laboratory record efficiencies of the main photovoltaic technologies are presented in Table 1.1 [15]:

Table 1.1: Laboratory record efficiencies of PV technologies [15].

Technology	**Efficiency [%]**	**Laboratory**
c-Si	24.7	Panasonic
a-Si	13.4	LG electronics
CIS	19.6	Global Research
CIGS	20.8	Solar Energy and Hydrogen Research
CdTe	20.4	Global Research and First Solar

The efficiency of a PV module comprised of multiple cells is necessarily lower compared to that of the constituent cells, since not all of the module surface is photovoltaic. In general, the modest values of efficiency that characterize PV devices is due to various factors that can be categorized as follows:

- Recombination: not all of the generated electron-hole pairs in the PV cell reach the electric field at the junction due to recombination between oppositely charged carriers, which therefore do not participate in the generation of electric current. The recombination rate depends on carrier lifetime and diffusion length, which are a measure, respectively, of the average time that a carrier remains in an excited state after it has been

generated, and the average distance that the carrier can move from the point of generation [4].

- Light absorption depth: the amount of light that is absorbed and utilized to generate power depends on the absorption depth and thickness of the cell [4]. Higher energy photons are absorbed in a short distance from the cell surface, vice-versa for lower energy photons (for example, red light is absorbed at a few hundred μm [4]). Multijunction cells, a niche technology consisting of different semiconductor materials mechanically stacked to form multiple junctions, have been developed for special applications (mainly in concentration photovoltaics) to utilize a wider spectrum light, achieving efficiencies of 35÷40% [4].
- Light reflection: untreated Si reflects more than 30% of incident light [4]. For this reason, the top surface of the cell is usually textured or coated with a special layer. Still, some photons are reflected, and others are blocked by the metal contacts that collect the current from the cell's top surface.
- Parasitic resistances: electrical resistance at the interface between the metal contacts and the surface of the cell is a source of power losses. In addition, a certain resistance is due to the fine structure of the contacts themselves and to manufacturing defects. Larger contacts can be used to minimize the resistance to current flow, but then more sunlight would be blocked from entering the cell surface.
- Cell Temperature: increasing temperature has detrimental effects on photovoltaic cell performance, both in terms of its electrical characteristics and in terms of the properties of all the materials implemented in PV cell applications [4]. In particular, with reference to Equation (1.7), as temperature increases, the exponential term decreases, but I_o increases exponentially [4]. The net effect is a worsening of the electrical characteristic given by a linear reduction of the open-circuit voltage with increasing temperature [4], and thus a reduction of power output as temperature increases.

1.5. Types of photovoltaic technologies

The majority of photovoltaic cells currently on the market are based on silicon semiconductors. This is mainly due to the fact that silicon, unlike other semiconductor materials, is naturally available in virtually unlimited amounts. Moreover, silicon is widely used in the electronics industry, which has favored the development of current production processes of silicon devices. In addition, silicon waste from the manufacturing processes of electronics can be recycled by the photovoltaics industry, which tolerate lower levels of silicon purity [14]. There are

various technologies to produce PV cells of different configurations: from traditional, flat plate crystalline silicon cells to thin films, single-junction, multijunction, and tandem cells (with these last two types developed to utilize a wider portion of the solar spectrum), etc. Some characteristics (based on information from [16]) of the main types of PV devices are summarized in Table 1.2: Efficiency and PV surface of different PV technologies [16].

Table 1.2: Efficiency and PV surface of different PV technologies [16].

Cell material	**Module efficiency**	**Photovoltaic surface per 1 kWp**
Monocrystalline Si	13÷17%	7÷9 m^2
Polycrystalline Si	10÷14%	8÷9 m^2
Thin film CdTe	8÷12%	9÷10 m^2
Thin Film CIS	8÷12%	9÷10 m^2
Amorphous Si	4÷7%	16÷20 m^2

State of the art PV technologies, both silicon-based and from innovative materials, are presented in the following.

1.5.1. Monocrystalline silicon PV cells

Also known as single-crystal PV cells, their production starts with the melting of silicon crystals of high purity to form single-crystal ingots. The ingots are then sectioned into wafers that are typically 200÷300 μm thick [16] and shaped to optimize surface utilization and to increase the number of cells that can be encapsulated in a module. The wafers are then doped with phosphorous and boron to create n-type and p-type layers. The front metal contacts (usually silver) on c-Si cells are typically screen printed to form a grid-like pattern consisting of several fine conductors (*fingers*) of thickness in the order of tens of μm and typical spacing of 3 mm [10] and thicker busbars that connect to the external leads, which in turn interconnect the cells in a module. Optimal front contact design is a trade-off between minimizing front surface coverage and providing effective current collection and lower electrical resistance associated with a tightly spaced grid. The back contact usually consists of a sheet of aluminum [4]. Typical values of efficiency for monocrystalline Si modules are 13÷17% [16]; best figures are around 23% [4].

Figure 1.9: Monocrystalline silicon PV cell and its metal contacts (busbars and fingers) [10].

1.5.2. Polycrystalline silicon PV cells

Relatively similar in constitution to monocrystalline Si cells (see Figure 1.10), polycrystalline Si cells are made from silicon crystals of different grain orientations that are processed to form polycrystalline ingots, which are then sectioned into wafers typically 230÷350 μm thick [16]. The production process is simpler, and therefore cheaper, than for monocrystalline silicon cells [10], while typical efficiency of polycrystalline Si modules is only slightly lower, at 10÷14% [16]; best figures are approximately 18% [4].

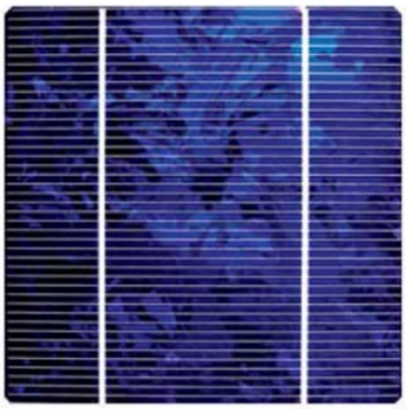

Figure 1.10: Polycrystalline silicon PV cell [10].

1.5.3. Thin film modules

Ultrathin film (in the order of 1-2 μm [16]) of semiconductor material is deposited by means of vaporization, spray, or electrolytic processes on a support surface (typically glass or steel) to create modules that can have a variety of complex shapes and structural flexibility. The most commonly implemented semiconductor materials are amorphous silicon (a-Si), copper indium diselinide (termed CIS),

copper indium gallium selenide (termed CIGS), cadmium telluride (CdTe). Modules of this type, especially those in a-Si, are generally cheaper than c-Si modules and are better able to tolerate the effects of partial shading and temperature fluctuations [16]. However, they are characterized by lower efficiencies, in the range of 4÷7 % for a-Si modules and around 10% for the other thin film modules [16]. Innovative solutions consisting of gallium arsenide (GaAs) and aluminum gallium arsenide (GaAlAs) polycrystalline films characterized by high theoretical efficiencies (around 30%) are being developed, but their application is currently limited to the aerospace sector due to very high production costs [5].

Figure 1.11: Left: CdTe thin film modules in a PV field in south western USA [4]. Right: a-Si thin film production [5].

1.5.4. Multi-junction PV cells

An interesting application of thin film technologies that is entering the market consists of multi-junction cells, constituted by stacked layers of photovoltaic materials that are sensible to different irradiance spectra. The resulting photovoltaic devices utilize a wider portion of the solar spectrum, and are therefore characterized by higher efficiency. In concentrator applications, dual junction GaAs/GaSb cells have been demonstrated to have 35% efficiency [4]; values are even higher, at 41.6%, for the triple junction GaInP/GaInAs/Ge cells [4]. In practice, multijunction cells are predominantly used in high-power concentrator systems (in the 10÷100 MW range [4]), achieving near 40% efficiency [4], [5].

1.6. PV systems for utility-scale power generation

The PV systems considered in utility-scale power generation applications are characterized by power ratings in the order of hundreds of kW to several MW. Unlike small-scale PV systems, which are often integrated with batteries for use in standalone and hybrid applications, large-scale, grid-connected PV systems inject all the generated power into the AC mains. In recent times, the potential to utilize large-scale PV systems for the power supply of high-power DC networks (such as DC electric railway systems), without DC to AC conversion and transformers, has become an area of growing interest.

1.6.1. General structure and characteristics

PV powerplants are essentially structured as series and parallel interconnections of several PV modules in order to achieve considerable voltage and current scale-up. Therefore, the overall nature of the characteristics of a PV system is similar to that of the individual PV cell, albeit at different current and voltage levels. In PV powerplants, the modules are connected in series to form a PV string, which constitutes a complete power-generating unit characterized by the rated voltage. The parallel connection of PV strings forms the PV array, which constitutes the complete PV powerplant (also known as PV farm, PV field, or PV generator). In large powerplants, the PV field is further divided in sub-fields, constituted by parallel interconnections of arrays. A basic overview of the structure of a PV system is shown in the example in Figure 1.12.

Preserving the notation used to describe the model of the single PV cell, which is now extended and applied to the PV system, the total current-voltage characteristic of the PV system is given by:

$$I_{PV} = N_p I_P - N_p I_o \left(e^{\frac{V_{PV}}{N_s nkT}} - 1 \right) \tag{1.15}$$

where N_s and N_p are, respectively, the number of series and parallel connections of cells constituting the PV system. The resulting I_{PV}-V_{PV} and P_{PV}-V_{PV} curves, compared to those of the single PV cell, are scaled accordingly.

As an example, the characteristics in Figure 1.13 and Figure 1.14 are computed for a 1.5 MW PV array interconnected as shown in Figure 1.12: Schematic diagram of a PV array and its components., showing the effects of irradiance and temperature on the PV system's operating conditions. The same PV system is considered for the

power supply of a DC electric railway system. The module and array data are presented Table 1.3: Module data. and

Table 1.4.

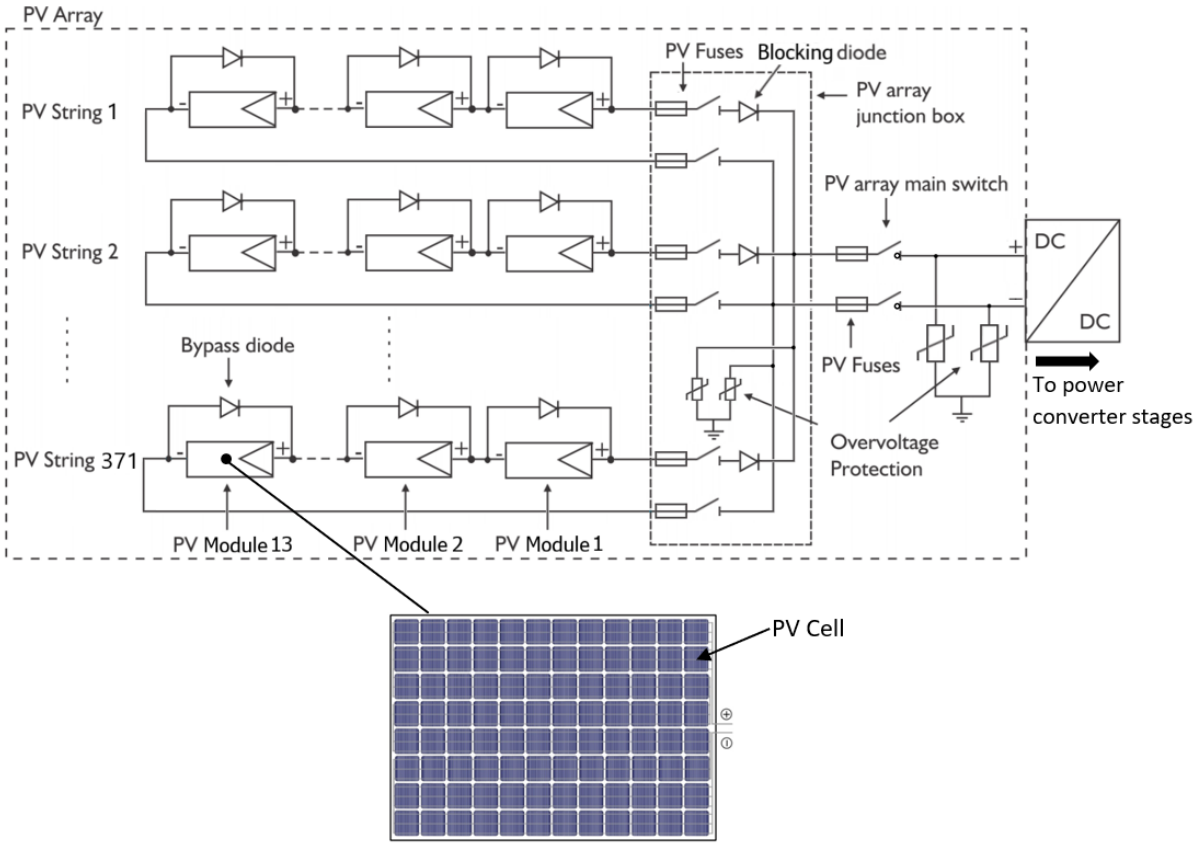

Figure 1.12: Schematic diagram of a PV array and its components.

Table 1.3: Module data.

Module type	SunPower SPR-315NE-WHT-D
Number of series-connected cells	96
Peak power	305.07 Wp
MPP voltage	54.7 V
MPP current	5.76 A
Open-circuit voltage	64.6 V

Short-circuit current	6.14 A

Table 1.4: Array data.

Number of series connected modules per string	13
Number of parallel connected strings in array	371
Peak power	1519.59 kWp
MPP voltage	711.1 V
MPP current	2.15 kA
Open-circuit voltage	839.8 V
Short-circuit current	2.278 kA

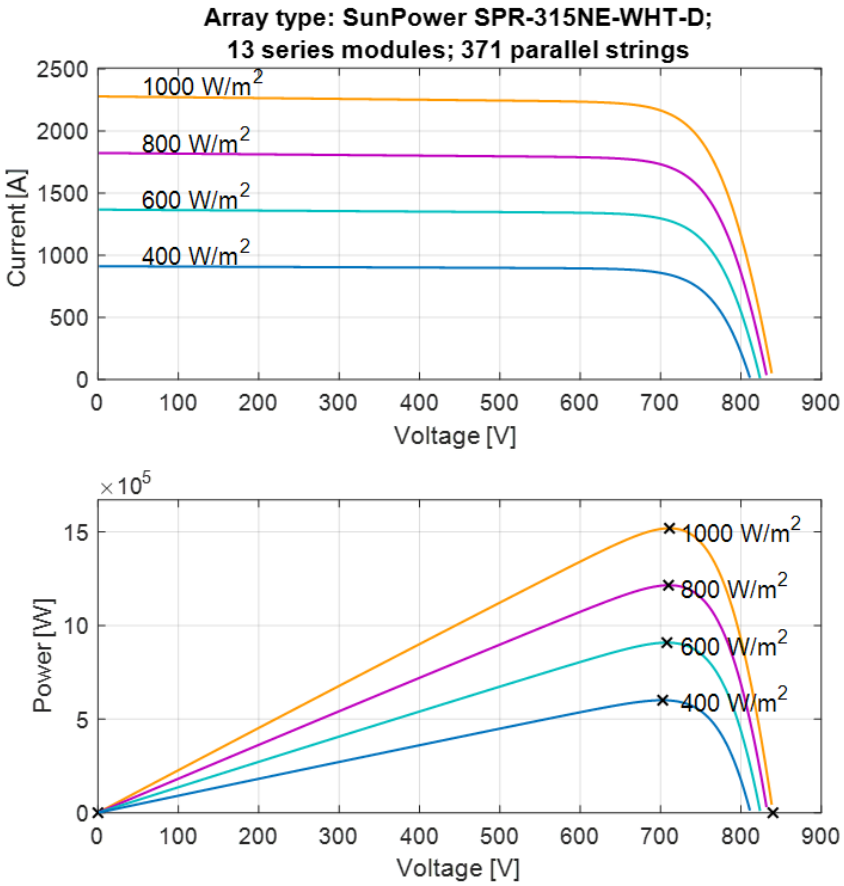

Figure 1.13: Electrical characteristics of a 1.5 MW PV field at 25 °C under different irradiances.

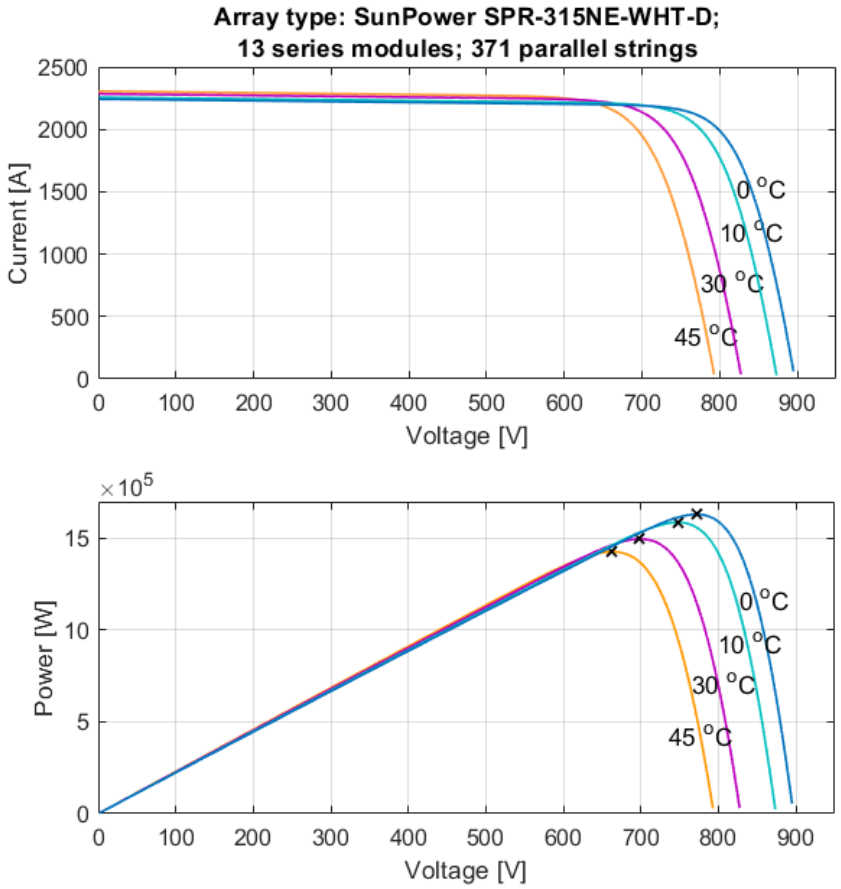

Figure 1.14: Electrical characteristics of a 1.5 MW PV field under 1000 W/m² of irradiance at different temperatures.

The characteristics indicate that solar irradiance has a greater effect on the operating current, while the operating voltage varies within a relatively low range. Conversely, the operating temperature is seen to have a greater effect on voltage.

The daily power output of a generic PV installation can be seen in Figure 1.15, where the effects of cloudy conditions can be noticed.

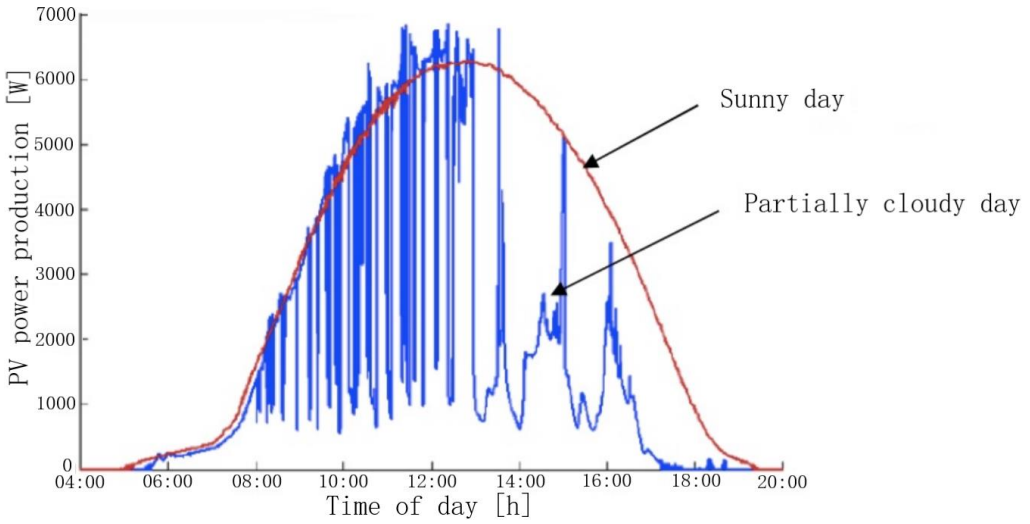

Figure 1.15: Example of daily PV power curve [17].

1.6.2. Protections against partial shading

1.6.2.1. Bypass diodes

Bypass diodes are used to reduce the power losses and to protect the PV module in the event of partial shading. Without bypass diodes, the partial shading of PV cells in the module would result in a significant reduction of the output current (as can be deduced from the characteristics at different irradiance levels). In a string of series-connected cells, the voltage across the shaded cells would then become inverted and roughly equal to the sum of the voltages generated by each non-shaded cell, in accordance with the KVL applied to the system, as represented in Figure 1.16, potentially causing reverse bias breakdown of the shaded cells. In addition, the power generated by the non-shaded cells would be dissipated in the shaded ones, resulting in local overheating (*hot-spots*) that could lead to destruction of the cells, damage to the module's components, and disruption of the continuity of service of the entire unit [10]. As a countermeasure, substrings of 18÷20 cells [5] in the PV module are connected in anti-parallel to bypass diodes that become forward biased in the event of partial shading of any cells in their respective string, protecting the shaded cells from reverse bias breakdown and hot-spots, while simultaneously allowing the flow of current from the non-shaded strings.

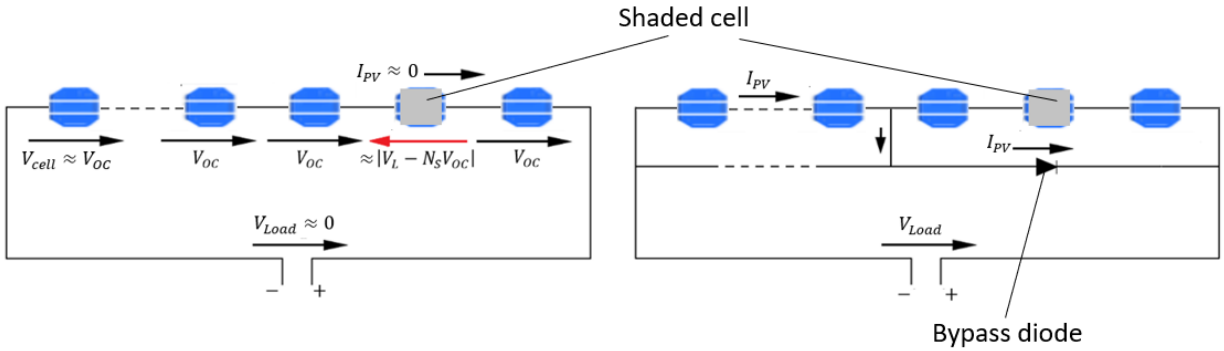

Figure 1.16: Partial shading of a string of cells in a module without bypass diode (left) and with bypass diode (right).

In practical terms, the bypassed substrings do not contribute to the power output while shading occurs, but the continuity of service of the module is preserved, albeit at a lower power. In any case, the effects of bypassing the shaded strings are generally less pronounced in very large PV systems, as the power loss due to shading is small in proportion to the total power output. Regardless, it is of paramount importance that any shading due to the presence of trees, buildings, poles, other modules, etc. be completely avoided, or at least sensibly reduced, by accurately planning the PV field layout and the disposition of the modules. The inclination of the modules is often set to 20° or more, so that objects that deposit on the module surface can slide off ("self-cleaning") [13].

1.6.2.2. Array fuses and blocking diodes

The PV arrays in a PV field are protected by fuses integrated with blocking diodes [13], as an additional precaution against the risk of array current inversion that could occur in the event of module bypass due to shading. The blocking voltage of the diodes must be greater than the open-circuit voltage of complete the array in standard test conditions [5], and the rated current of the fuses must be between 1.25 and 2 times greater than the short circuit current of the array (unless specific indications are given by the manufacturer) [13]. The fuses are usually coupled with disconnectors, as shown in Figure 1.12.

1.6.3. The DC-DC boost converter for maximum power tracking

The operating conditions of a PV system are strongly affected by changes in temperature and solar irradiance, caused, for instance, by changing weather conditions, local shading, and the Earth's rotation. Hence, a continuous regulation of the PV system is required in order to maintain the system in operation at the maximum power point as the environmental conditions change. To this end, power converters are used to adapt the electrical parameters of the PV system via maximum power point tracking (MPPT) algorithms. Considering PV power generation applications in low- to medium-voltage DC infrastructure, the DC-DC converter that is extensively documented in literature for MPP tracking is the boost converter, which also performs a step-up function of the PV-side input voltage (which is typically below 1 kV) to a higher DC voltage to make it more suitable for the next stages of the DC network.

1.6.3.1. Principle of operation

Maximum power tracking is performed by regulating the PV-side voltage through the duty cycle control of the boost converter, as illustrated in Figure 1.17. Depending on the PV system's size and requirements, the converter performing MPPT can be of the decentralized type, installed for every module or set of modules, of the string or multi-string type, installed for each string or at the array-level, or of the centralized type, managing the power of the complete PV system. The decentralized solution offers a more fine-tuned regulation of the power output but is characterized by higher costs due to the higher number of converters, while the centralized solution limits the power regulation to a single converter and is therefore more susceptible to different operating conditions of the individual modules, but less complex.

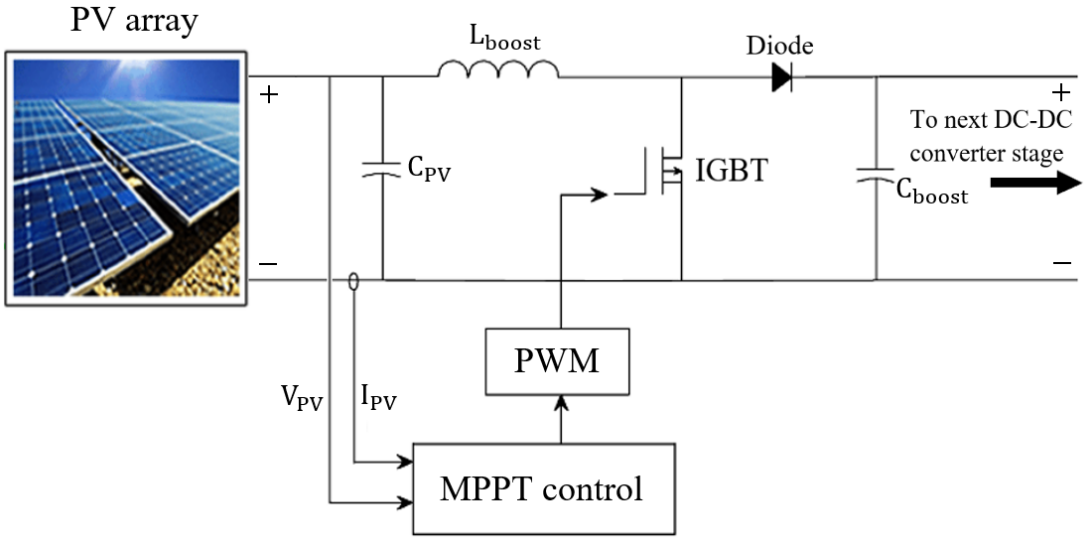

Figure 1.17: Boost converter topology in PV systems.

With reference to the notation used in Figure 1.17, the principle of operation of the boost converter is presented in the following, assuming the converter is ideal and operating at steady state in continuous conduction mode. In addition, it is assumed that, given the high switching frequency at play (typically in the order of 10 kHz), the input voltage is constant over the switching period.

On-state: when the switch is in the on-state, the input inductor is energized by the power supply, and the inductor current increases linearly according to the formula:

$$V_{in} = L_{boost} \frac{di_{L_{boost}}}{dt} \tag{1.16}$$

Ideally, the closed switch decouples the power supply-side circuit and the load-side circuit, hence, in the on-state, the load-side is supplied through the output capacitor.

Off-state: when the switch is in the off-state, the energy stored in the inductor is released through the diode to the output circuit. The inductor current decreases linearly according to the KVL between load-side terminals and power supply-side:

$$V_{in} - V_{out} = L_{boost} \frac{di_{L_{boost}}}{dt} \tag{1.17}$$

with $V_{in} < V_{out}$. Due the conservation of energy, the inductor current has to be the same at the beginning and at the end of each switching cycle, that is, the current rises and falls by the same amount. Defining the duty cycle D as the fraction of the

switching period T_s in which the switch is in the on-state, the current rise and fall are equated:

$$\frac{V_{in}}{L_{boost}} \cdot DT_s = \left|\frac{V_{in} - V_{out}}{L_{boost}} \cdot (1 - D)T_s\right| \tag{1.18}$$

Rearranging, the input/output voltage relationship is found:

$$\frac{V_{out}}{V_{in}} = \frac{1}{1 - D} \tag{1.19}$$

The ideal equation suggests that as the duty cycle tends to 1 (i.e., the switch is always in the on-state), the voltage conversion ratio tends to infinity. Of course, this is not the case in practical applications, where the conversion ratio is limited by the loss mechanisms in the in the circuit including switching losses and conduction losses associated with the semiconductor devices and resistive losses associated with inductors and capacitors [18].

The key waveforms of the boost converter at steady state are shown:

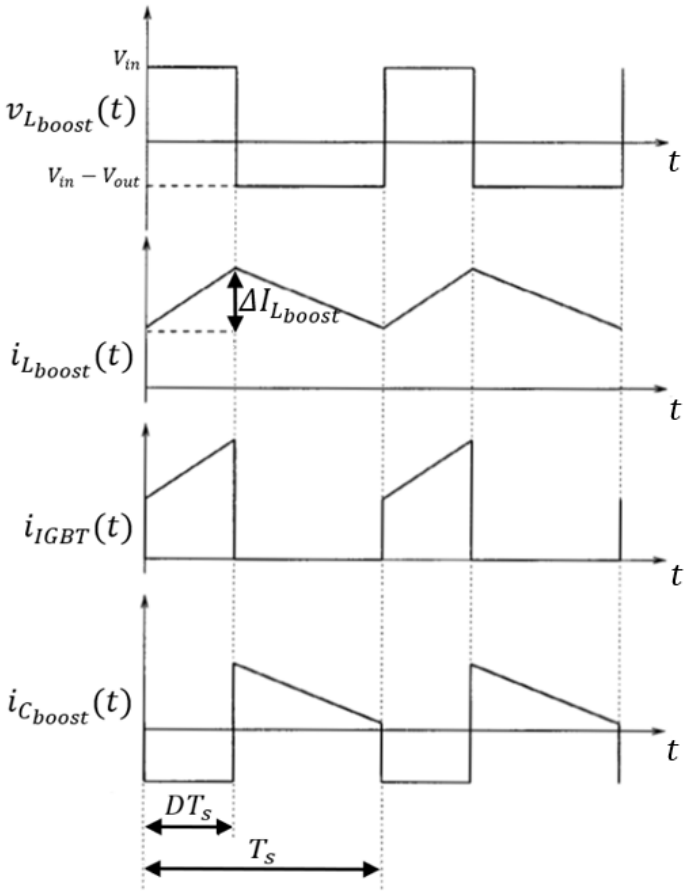

Figure 1.18: Boost converter waveforms.

Given the switching frequency f_s, the input inductor and the output capacitor of the boost converter are designed to limit the current ripple $\Delta I_{L_{boost}}$ and the voltage ripple $\Delta V_{C_{boost}}$ in accordance with the desired tolerances. The values of the required inductance and capacitance are calculated by means of the following sizing equations, derived from the theory of boost converter operation:

$$L_{boost} \geq \frac{V_{in}(V_{out} - V_{in})}{f_s \Delta I_{L_{boost}} V_{out}} \tag{1.20}$$

$$C_{boost} \geq \frac{I_{out}(V_{out} - V_{in})}{f_s \Delta V_{C_{boost}} V_{out}} \tag{1.21}$$

where I_{out} is the average current flowing in the load-side of the circuit.

1.6.3.2. Maximum power point tracking algorithms

Some commonly implemented power point tracking algorithms in practical applications are outlined in the following.

Perturb and Observe (P&O) MPPT: the PV voltage is periodically perturbed by applying small changes to the converter's duty cycle, and the generated PV power, computed as the product of PV voltage and current measurements, is compared to that of the previous perturbation cycle. If the power has increased, the next perturbation is induced in the same direction; if not, in the opposite direction. The algorithm then restarts. In this way, the P_{PV}-V_{PV} curve is progressively "climbed" in discrete steps, eventually leading the system to work around the MPP. The conventional P&O algorithm just described is illustrated in the following flowchart, where D is the duty-cycle of the power converter, and PV voltage and current are denoted as V and I for compactness.

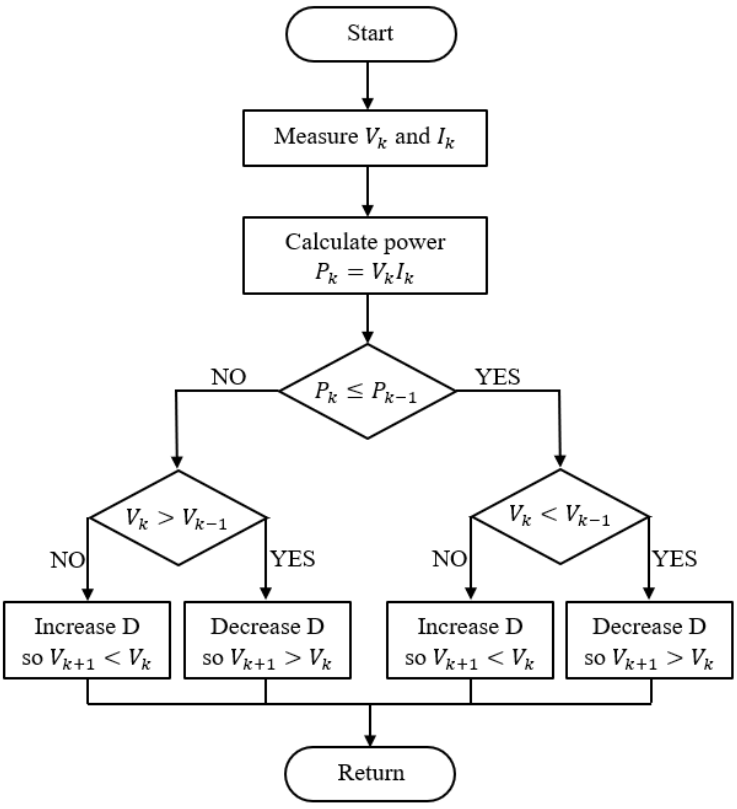

Figure 1.19: P&O algorithm flowchart.

The low complexity of conventional the P&O algorithm makes it easy and economical to implement [19] [20], as such, it is one of the most widely used MPPT methods. The drawbacks however, are that the P&O algorithm is intrinsically characterized by oscillations around the MPP, even at steady state [20]. During

transients (caused, for instance, by rapid variations of irradiance), oscillations become even more pronounced as the system adapts to the new MPP, causing power losses and instability [20] and overall slow response times to transients. Moreover, there is a tradeoff between tracking accuracy and speed [19], as higher accuracy requires smaller perturbations, thus higher discretization and longer computation times. Improved P&O algorithms have been developed to overcome such drawbacks. For instance, one such variant has been proposed in [19], that limits the range of the algorithm to a neighborhood of the MPP rather than to the whole *P-V* curve, successfully mitigating the response time problem and steady state oscillations, even under rapidly varying environmental conditions.

Model-based MPPT: real time temperature and solar irradiance measurements are periodically taken and used to compute the *I-V* and *P-V* characteristics based on the mathematical model (Equations 1.7 and 1.8) of the PV cell, allowing for quick and accurate identification of the maximum power P_{MPP}. In conjunction, the PV system's real time operating voltage V_{PV} and current V_{PV} are measured and used to compute the operating power P_{PV}, which is compared with the maximum power yielded by the mathematical model. If $P_{MPP} = P_{PV}$, the system is left unperturbed. If $P_{MPP} \neq P_{PV}$, a comparison is made between V_{PV} and V_{MPP}: if $V_{MPP} > V_{PV}$, the duty cycle D applied to the power converter is decreased by an amount d proportional to the difference between P_{MPP} and P_{PV}, in order to increase the operating voltage; if not, the duty cycle is increased by the same amount [11]. For compactness, in the following flowchart the MPP power is labelled as P_M, and PV voltage and current as V and I.

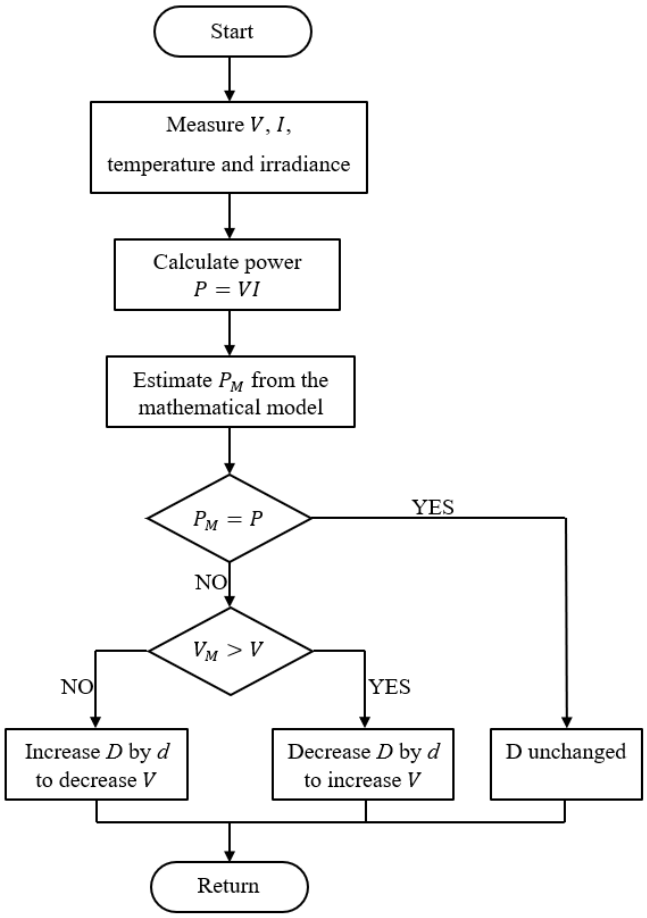

Figure 1.20: Model-based MPPT algorithm flowchart [11].

Model-based MPPT algorithms are distinguished by their enhanced tracking speed and dynamic performance, because the MPP is calculated with real time data, virtually solving all problems related to varying environmental conditions. However, the necessity for irradiance measurements translates into higher costs [21]. Some model-based MPPT variants have been proposed [21] that eliminate the need for irradiance measurements by adopting a simplified model of the PV system that allows direct computation of the modeling equations (i.e., without iterative methods), eliminating their dependence on irradiance, while still allowing to compute the MPP with good accuracy.

Incremental conductance (INC) MPPT: it is based on the following analysis of the *P-V* and *I-V* curves of a PV system (the subscripts $_{PV}$ are omitted for compactness): at the MPP, it is verified that:

$$\frac{dP}{dV} = 0 \tag{1.22}$$

where $P = VI$. Thus,

$$\frac{d(VI)}{dV} = V\frac{dI}{dV} + I\frac{dV}{dV} = V\frac{dI}{dV} + I = 0 \tag{1.23}$$

rearranging,

$$\frac{dI}{dV} + \frac{I}{V} = 0 \tag{1.24}$$

the ratio between current and voltage represents a conductance G. Thus, the notation applies after discretizing:

$$\Delta G + G = 0 \tag{1.25}$$

In the region of the *P-V* and *I-V* curves to the left of the MPP, the voltage varies in a wide range with respect to the current, while the current is almost constant. Thus, the term G prevails over ΔG, yielding $\Delta G + G > 0$, as the conductance G is always positive. Conversely, to the right of the MPP, the range of variability of the current is much larger with respect to that of the voltage, thus ΔG prevails and $\Delta G + G < 0$. The difference between the conductance G and the incremental conductance ΔG is larger towards the extremes of the curve, and tends to zero as the MPP is approached. Thus, a threshold ε is set such that for $|G + \Delta G| < \varepsilon$ the system is considered to operate at the MPP, i.e., at steady-state. The described INC method is implemented in PV systems by periodically measuring voltage and current to compute G and ΔG, checking the sign of $\Delta G + G$ to establish if a perturbation is required in a particular direction, while also verifying if $|G + \Delta G|$ is a the steady-state value so that no perturbation need be induced.

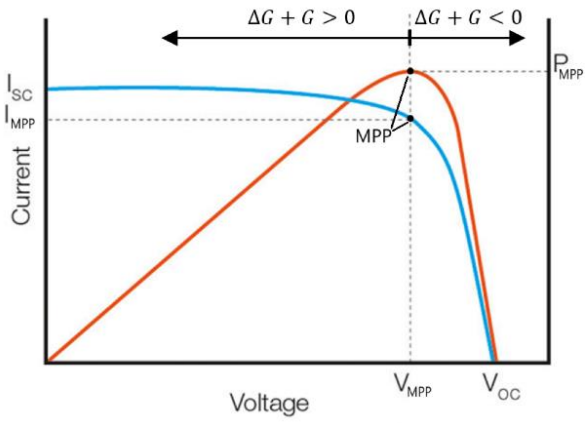

Figure 1.21: PV incremental conductance.

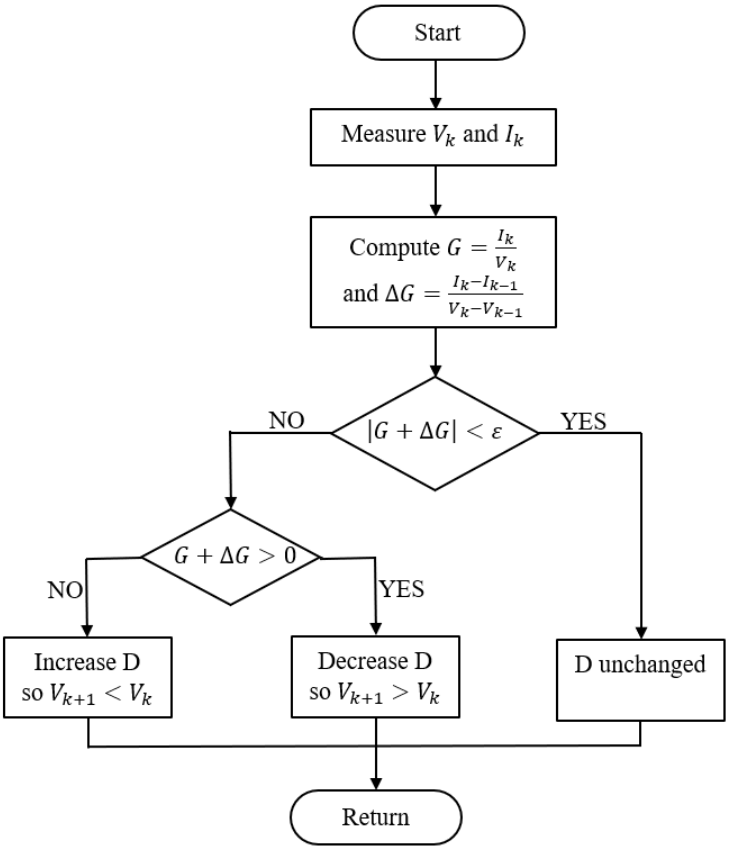

Figure 1.22: Incremental conductance MPPT algorithm flowchart.

Similarly to the conventional P&O algorithm, in traditional INC MPP tracking the voltage perturbations are induced by varying the duty cycle by fixed amounts in either direction until the MPP is reached; the choice of implementing smaller perturbations to improve accuracy will then result in a larger number of iterations and thus slower convergence. Vice-versa, if greater perturbations are used to improve convergence speed, the loss of accuracy is inevitable [22]. An advantage of the INC method is given by the lack of oscillations when steady state is reached (no perturbations are applied if the tolerance is met), however, this condition relies on great accuracy in computing $\frac{dI}{dV}$ [23], which is a numerical derivative susceptible to measurement noise. Comparative studies found in literature suggest that traditional P&O and INC algorithms are essentially the same, with a slight improvement in stability in favor of the latter [12]. Improved INC algorithms have been developed to mitigate the trade-off between convergence speed and accuracy. One such example is Adaptive Step Size INC [23], in which the perturbation is increased as the operating point moves further from the MPP, and is decreased when approaching the MPP.

Constant Voltage (CV) MPPT: perhaps the simplest method of maximum power tracking, it consists of directly estimating the maximum power voltage by periodically measuring the open-circuit voltage and multiplying the measured values by a proportionality constant:

$$V_{MPP} = kV_{OC} \tag{1.26}$$

where $k \approx 0.78$ for PV cells [24]. Once V_{MPP} is estimated, the operating voltage is measured and compared, and the power converter is implemented accordingly as with the other MPPT algorithms. This estimation method is only valid above a certain value of irradiation and for limited temperature variations [24]. The need for open-circuit voltage readings implies that the PV system be temporarily disconnected from the load. This can be done by opportunely controlling the power converter at the output terminals of the PV system. Measurements must then be performed quickly so as to not disrupt continuity of service and to limit the power losses. Alternatively, a pilot cell (identical and under the same conditions to the cells in the PV system, but utilized only for monitoring purposes) can be used to extract measurement information, ensuring continuity of service and eliminating any power losses.

Various other MPPT algorithms have been developed and implemented, often in conjunction (mixed algorithms) to achieve both fast convergence and stability. For example, the CV method can be implemented initially to quickly bring the operating point around the MPP, and then a more refined regulation, such as an adapted P&O, takes over.

1.6.4. The isolated boost full bridge converter for DC grid connection

The integration of photovoltaic systems in the power supply of MVDC grids, such as the 3 kV electric railway system considered in this study, involves multiple DC-DC power converter stages in order to provide the appropriate step-up function of the PV voltage, as well as a number of advantages in terms of reliability and increased regulation capabilities. The converter considered for interfacing the front end of the PV system with the MVDC grid is the isolated boost full bridge (IBFB) DC-DC converter, shown in Figure 1.23.

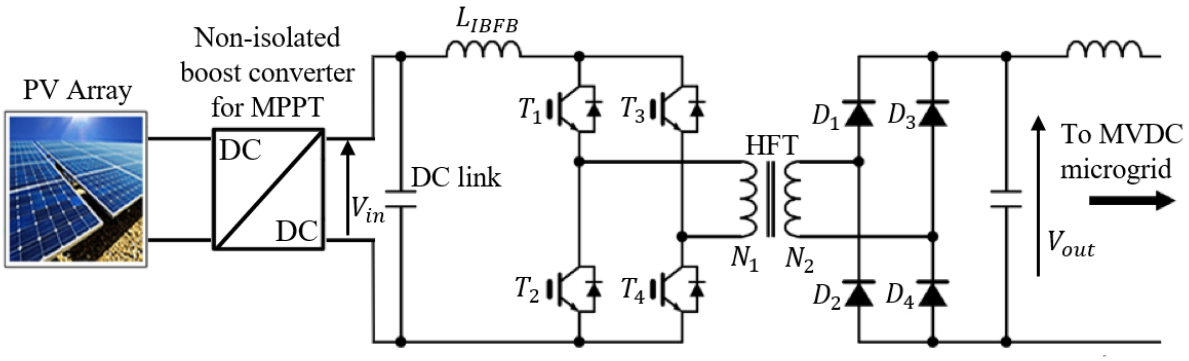

Figure 1.23: The isolated boost full bridge converter.

In essence, the IBFB converter works similarly to the non-isolated boost converter. The input inductor is energized by the power supply and de-energized through the load by opportunely activating the converter switches. Energy is transferred to the load through a high-frequency transformer (HFT) designed to operate at the switching frequency of the converter (typically around 10 kHz or higher). The switching sequence produces an AC waveform on the transformer primary side, which is reflected on the secondary side in proportion to the transformer turns ratio (in this application, a step-up function is considered) and then rectified through the full bridge diode rectifier. The transformer provides galvanic isolation between the load-side and the power supply, increasing the electrical safety of the system. Moreover, the additional voltage gain provided by the transformer allows for the series connection of fewer PV modules to reach a high level of DC voltage [25], increasing the stability of the PV system.

1.6.4.1. Principle of operation

With reference to the notation used in Figure 1.23 and Figure 1.24, a single phase shift switching strategy is used to control the converter: each of the diagonal switch pairs T_1 & T_4 and T_2 & T_3 are controlled by two gate signals that are identical but phase shifted by 180°. In this way, four modes of operation are defined. Assuming that the converter is ideal and operating at steady state in continuous conuduction mode, the four modes of operation are described in the following:

Mode 0: for $t_0 \leq t \leq t_1$, all switches T_1, T_2, T_3, and T_4 are in the on-state, exciting the input inductor L_{IBFB} like a standard boost converter.

Mode 1: for $t_1 \leq t \leq t_2$, T_2 and T_3 are turned off while T_1 and T_4 remain on. The input inductor releases energy through T_1 and T_4 and through the transformer primary. Energy is transferred to the secondary side and to the output side through

the rectifier diodes D_1 and D_4. The input inductor current decreases similarly to a standard boost converter in the output state.

Mode 2: for $t_2 \leq t \leq t_3$, T_2 and T_3 are turned on while T_1 and T_4 remain on. Therefore, all four switches are in the on-state and the input inductor is energized as in Mode 0.

Mode 3: for $t_3 \leq t \leq t_0$, T_1 and T_4 are turned off while T_2 and T_3 remain on, drawing current from the input inductor. In this switching configuration, the flow of current through the transformer is reversed compared to Mode 1. As such, energy is transferred to the output side through the rectifier diodes D_2 and D_3.

The relationship between input and output voltage is given by [26]:

$$\frac{V_{out}}{V_{in}} = \frac{N_2}{N_1} \cdot \frac{1}{1-D} \tag{1.27}$$

where N_1 and N_2 are, respectively, the number of turns of the primary and of the secondary winding, and D is the duty cycle of the converter, defined as the fraction of the switching half-period ($T_s/2$) in which all four switches are turned on simultaneously.

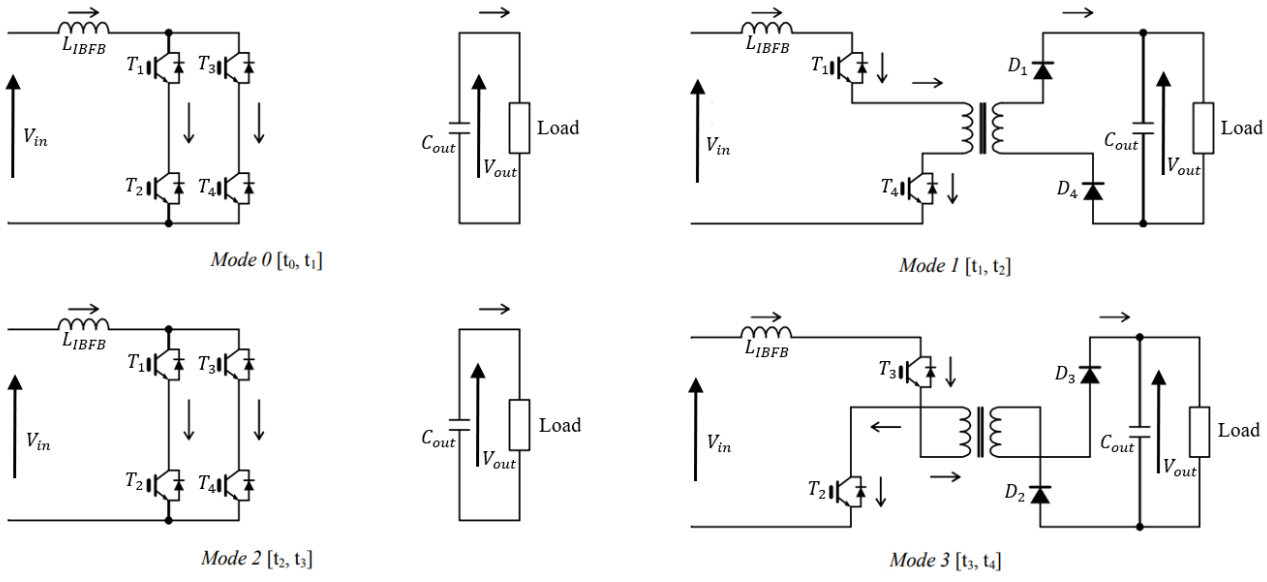

Figure 1.24: Modes of operation of the IBFB converter.

The key waveforms of the IBFB converter at steady state are:

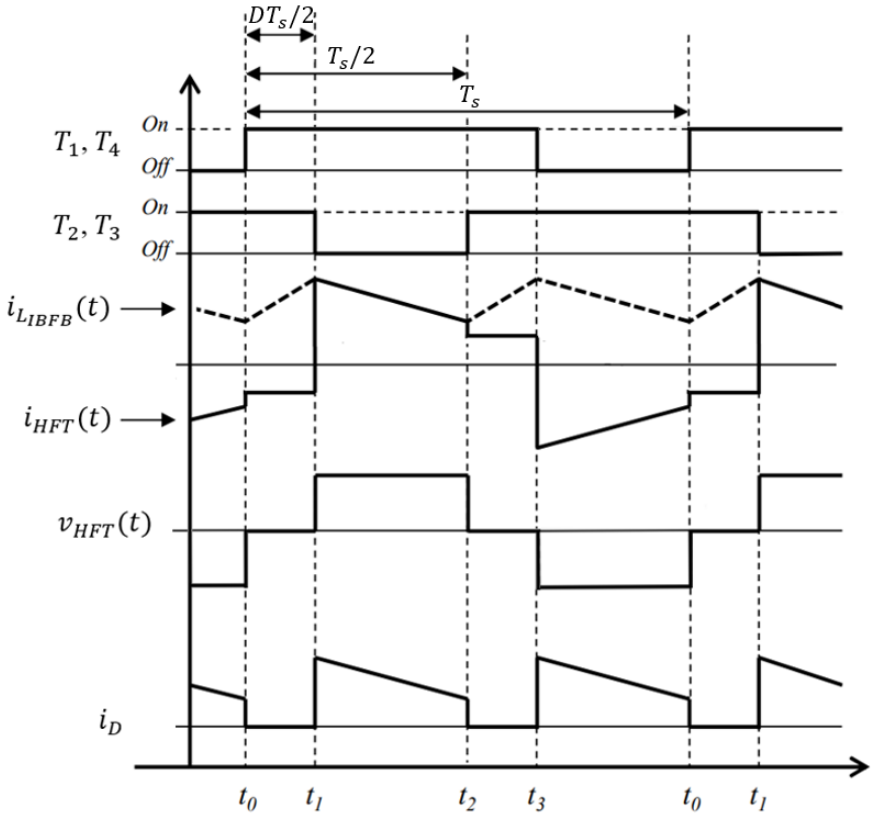

Figure 1.25: IBFB converter waveforms [26].

2 Wind energy

The energy contained in wind ultimately originates from the Sun. Wind energy is, in fact, a form of solar energy, with approximately 2% of the solar irradiance incident on Earth converted to kinetic energy of moving air masses resulting from pressure gradients due to uneven heating of the Earth's surface [5]. Historically, wind power has been used for sailing and for the production of mechanical energy to be used in the first windmills and for the operation of windpumps. The first known wind turbine for the production of electricity dates back to 1888 and belonged to Charles F. Brush, Cleveland, Ohio. With a power rating of 12 kW, it was used to charge batteries. Today, the use of wind turbine generators for the production of electricity has led, as of 2019, to the installment of 622.7 GW of wind energy capacity worldwide and 10.76 GW in Italy [3].

2.1. The formation of global and local winds

The expansion and the convective movement of air masses due to the irregular heating of large geographical areas that receive different amounts of solar irradiance results in the formation of winds that can mainly be distinguished between global winds and local winds.

Global winds arise from the uneven heating between the equator and the Earth's poles. The high insolation at the equator causes the air to heat up, expand, and rise through the atmosphere, creating a region of low pressure near the surface that draws in air from latitudes up to approximately 30°N (north) and 30°S (south) of the equatorial line. The air at the equator rises to an altitude of approximately 17 km and splits into two currents that move towards the poles, progressively losing altitude as the air masses contract due to cooling. Finally, the air masses descend back to the surface about 30°N and 30°S of the equator within a high-pressure region, and move back to the low-pressure equatorial region, reinitiating the convective pattern. This air pattern is known as the Hadley cell, covering two regions extending to 30°N and 30°S of the equator. In the regions extending from 30°N to 60°N, and 30°S to 60°S, a convective air pattern in the opposite direction occurs, known as the Ferrel cell (or mid-latitude cell). Finally, from 60°N and 60°S to the poles, the Polar cell occurs in the same direction as the Hadley cell. The

altitude of the air masses in the three air patterns just described increases from the poles to the equator. Moreover, in each hemisphere, four pressure regions are thus identified: high pressure at the poles (where the air is coldest), low pressure at 60°N and 60°S, high pressure at 30°N and 30°S, and low pressure at the equator (where the air hot). As the air moves from low-pressure regions to high-pressure regions, the Coriolis effect due to the Earth's rotation causes the moving air masses to be deflected to the right in the Northern hemisphere, and to the left in the Southern hemisphere. The rotational effect increases with altitude, as friction with the Earth's surface decreases [5]. The global winds that arise in response to these phenomena are known as the trade winds, the prevailing westerlies, and the polar easterlies.

Local winds have the most interesting effects in power generation applications. Throughout the day, the air masses above oceans, seas, lakes, and large bodies of water absorb less heat than the air masses above continental landmasses, as most of the solar radiation is absorbed by the water [5]. The warmer air above land expands and rises, creating low-pressure regions that are filled by the heavier, colder air from above the water. Examples of this phenomenon are the sea breezes, blowing from the sea to the land during the day. Similarly, in mountainous regions, daytime winds flow upstream along the slopes, as the air in the valleys heats up more and rises in altitude, while the motion reverses during nighttime [5].

2.2. Wind energy resource potential

The most common and reliable method to assess the wind energy resource potential of a particular location consists using anemometers to record wind speed data, as the power associated with wind is proportional to the cube of its velocity. For an air mass m moving smoothly with an average velocity v, the associated power P_{in} (which is effectively the input power provided by the wind to the wind converter) associated with the motion of the air mass is given by [4]:

$$P_{in} = \frac{dE}{dt} = \frac{d}{dt}\left(\frac{1}{2}mv^2\right) = \frac{1}{2}\dot{m}v^2 \tag{2.1}$$

Where E is the kinetic energy of the moving air mass and $\dot{m}$ is the mass flow of air density ρ. Considering the air mass flowing across the rotor of a wind turbine of swept area S, the aerodynamic power P_w associated with the movement of the air mass is:

$$P_w = \frac{1}{2}\rho S v^3 \tag{2.2}$$

which is a reference power (based on known air density, wind speed, and rotor swept area), not to be confused with input power P_{in}. The ratio between the aerodynamic power captured by the wind converter and the input power defines the efficiency of the wind converter, while the ratio between the aerodynamic power and the reference power defines the power coefficient.

The main challenge in estimating the energy potential of a particular location (and of a given wind turbine, once its characteristics are known) is given by the random, intermittent and stochastic nature wind [4], with wind speeds varying substantially on an instantaneous, hourly, daily, and seasonal basis, depending also on elevation and orographic characteristics of the considered site [5]. In practical applications, the mean wind speed is recorded over 10-miute time steps [4], and the collected data is used to calculate hourly, daily, monthly, and yearly average values, as well as peak values within each time interval [5]. To minimize the impact of seasonable variability on the data and to improve measurement reliability, long-duration wind speed measurements are required, possibly in the order of a few years depending on the cost of the measurement campaign and the significance of the final data [5]. In case historical data records are available and the difference between new and old datasets is modest, it may be possible to reduce the duration of the measurement campaign by a few months and improve the uncertainty of newly measured data [5].

In wind measurement campaigns, two anemometers are mounted on a measurement mast at different heights, in order to appreciate the increase of wind intensity at higher altitude [5]. Additionally, wind direction measurement devices and thermometers (needed to calculate air density) are also installed. Wind speed measurements can be adjusted for height by using the Hellman equation, which relates wind speed v_h measured at reference height z_h (usually 10 m) to the generic wind speed v at height z through the friction exponent α:

$$\frac{v}{v_h} = \left(\frac{z}{z_h}\right)^{\alpha} \tag{2.3}$$

The friction exponent is a parameter that depends on the nature of the ground surface and is expected to vary between 0.05 and 0.45 [4], increasing with surface roughness. The friction exponent is taken as 0.4 in urban centers, 0.1 at open sea, and 0.2 according to IEC standards.

2.2.1. The Weibull distribution of wind speed

To estimate the real energy yield of a wind installation, wind speeds at the turbine's hub height are calculated and sorted into classes of 1 m/s, and the frequency (in

terms of number of hours per year) of each wind speed class is recorded. In this way, the frequency distribution of wind speed is obtained. The probability density of wind speed is also presented in terms of the ratio between the number of yearly hours of a particular wind speed and the total number of hours in a year (8760), as shown in the example in Figure 2.1 .

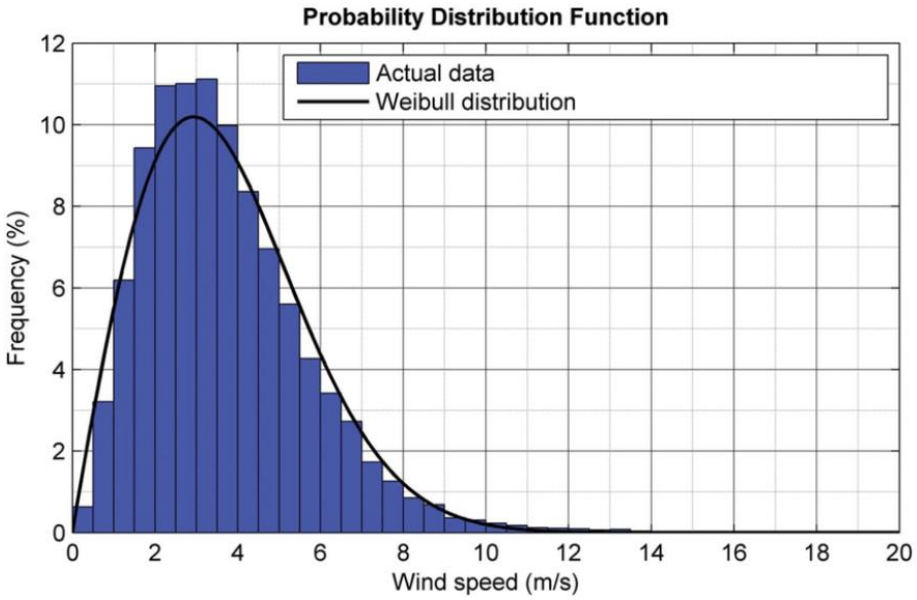

Figure 2.1: Weibull distribution of wind speed data [27].

The frequency and probability density distributions of wind speed can be synthetically represented, with good approximation, by means of mathematical models. To this end, the most widely used function for the description of wind regimes is the Weibull distribution, defined as follows [4]:

$$f(v) = \frac{k}{c} \cdot \left(\frac{v^{k-1}}{v^k} \right)^{-\left(\frac{v}{c}\right)^k} \tag{2.4}$$

Where k is the shape factor, ranging between 1.3 and 2.5, representative of the standard deviation of wind speed measurements (high shape factors are indicative of low standard deviations and high distribution symmetry. Typically, a reference value of $k = 2$ is chosen [5]), and c is the scale factor, related to the average wind speed (which is usually equal to 90% of c [5]).

The Weibull distribution is therefore very useful when estimation of energy production and technical availability is attempted in advance: the probability p of having a wind speed in a given interval ($v_1 \leq v \leq v_2$) is given by the area under the Weibull distribution in that speed interval:

$$p(v_1 \leq v \leq v_2) = \int_{v_1}^{v_2} f(v)dv \tag{2.5}$$

And the number of hours per year for which the speed is expected to be in the given range is found from:

$$h(v_1 \leq v \leq v_2) = 8760 \cdot \int_{v_1}^{v_2} f(v)dv \tag{2.6}$$

2.3. Principles of wind energy conversion

Wind turbine generators (WTGs) are used to convert the primary energy, in the form of kinetic energy of wind, to mechanical energy, and, ultimately, to electrical energy. The mechanical power extracted by the wind converter has been calculated by Albert Betz as the difference in power associated with the air stream before and after the converter, based the following assumptions [4]:

- The fluid flow is homogenous, incompressible and at steady state.
- No frictional drag is present, and the actuator disk has an infinite number of blades and experiences uniform thrust.
- The static pressure both upstream and downstream of the converter is considered as the ambient static pressure ($1.01 \cdot 10^5$ Pa).

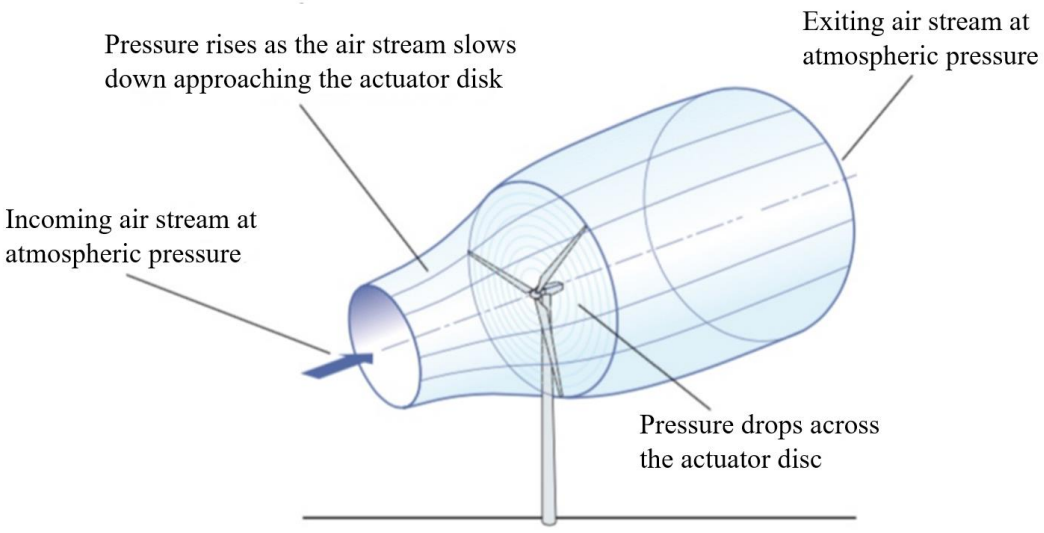

Figure 2.2: Airstream interaction with a wind turbine rotor.

Supposing that v_1 is the undisturbed free-stream velocity before the converter, v_2 the flow velocity after the converter, and S_1 and S_2 the cross-sectional areas of the airflows before and after the converter, the power difference is:

$$P = \frac{1}{2}\rho S_1 v_1^3 - \frac{1}{2}\rho S_2 v_2^3 \tag{2.7}$$

From the continuity equation, the air mass flow of constant density is conserved, thus:

$$\rho S_1 v_1 = \rho S_2 v_2 = \rho S v = \dot{m} \tag{2.8}$$

where v is the air stream velocity through the actuator disk of swept area S. Therefore, Equation (2.7) can be rewritten as:

$$P = \frac{1}{2}\dot{m}(v_1^2 - v_2^2) = \frac{1}{2}\rho S v(v_1^2 - v_2^2) \tag{2.9}$$

The maximum conversion efficiency would be obtained for $v_2 = 0$, which is physically impossible [28]. The maximum power extraction is calculated using the law of conservation of momentum, whereby the force exerted by the air on the wind converter can be expressed as [4]:

$$F = \dot{m}(v_1 - v_2) \tag{2.10}$$

Due to this force, the air mass is thrusted through the plane of the wind converter at an air velocity v, and the corresponding power is:

$$P = Fv = \dot{m}v(v_1 - v_2) = \rho S v^2(v_1 - v_2) \tag{2.11}$$

A relationship of equivalence for the flow velocity through the converter can then be found by equating Equations (2.9) and (2.11), yielding the arithmetic mean value of v_1 and v_2:

$$v = \frac{v_1 + v_2}{2} \tag{2.12}$$

Substituting Equation (2.12) into Equation (2.9):

$$P = \frac{1}{4}\rho S(v_1 + v_2)(v_1^2 - v_2^2) \tag{2.13}$$

It is then possible to find the final velocity v_2 that yields the maximum mechanical power extracted by the converter by optimizing Equation (2.13) as follows:

$$\frac{dP}{dv_2} = \frac{1}{4}\rho S[-3v_2^2 - 2v_1v_2 + v_1^2] = 0 \tag{2.13}$$

this condition is satisfied for $v_2 = -v_1$ and $v_2 = \frac{1}{3}v_1$. The physically valid result is the latter. Substituting the valid result in the power Equation (2.13) yields the maximum mechanical power that can be extracted by the wind turbine:

$$P_M = \frac{8}{27}\rho S v_1^3 \tag{2.14}$$

The mechanical power extracted by the converter and the power of the undisturbed free-air stream that flows through the same cross-sectional area S are related by the power coefficient C_P as follows:

$$P = C_P P_w = \frac{1}{2}C_P \rho S v_1^3 \tag{2.15}$$

In the maximum power condition, the power coefficient is maximum and equal to the Betz Limit:

$$C_P = \frac{P_M}{P_w} = \frac{16}{27} \tag{2.16}$$

Therefore, the maximum power that can be converted is 59.3% of the power of the undisturbed air stream. In practical applications, this value falls to 35÷40% due to the following non-ideal conditions:

- The wind converter has a finite number of blades.
- The air is compressible.
- Presence of aerodynamic friction and vortex formation downstream of the wind converter.
- Air pressure and temperature variation with altitude.
- Blockage effect from front-row wind turbines on downstream turbines.
- Dirt/ice deposits and formation on the blades.

The power output of a WTG is evaluated accounting for the overall efficiency η of the power train, which includes the mechanical efficiency η_m of the mechanical components (turbine shaft, main bearings, gearbox, generator shaft, etc.) and the

electrical efficiency η_{el} of the electrical generator and power converters[10]. The useful power produced by the WTGs is thus [28]:

$$P_{out} = C_P \eta_m \eta_{el} P_w = \frac{1}{2} C_P \eta \rho S v_1^3 \tag{2.17}$$

As the equation for the power output suggests, to maximize the power extraction, the rotor should respond to changes in wind speed to create the aerodynamic conditions that yield the highest power coefficient.

2.4. Principle of operation of horizontal axis wind turbines

Wind turbines operate by the action of the relative wind (the natural wind plus wind caused by rotor motion) which creates aerodynamic forces on the rotor blades due to their airfoil-shaped cross sections. The geometry of the airflow, and the velocity and force triangles on the airfoil section of a rotating wind turbine blade are shown in Figure 2.3.

[10] Technical documents sometimes incorporate the overall efficiency in the power coefficient [28].

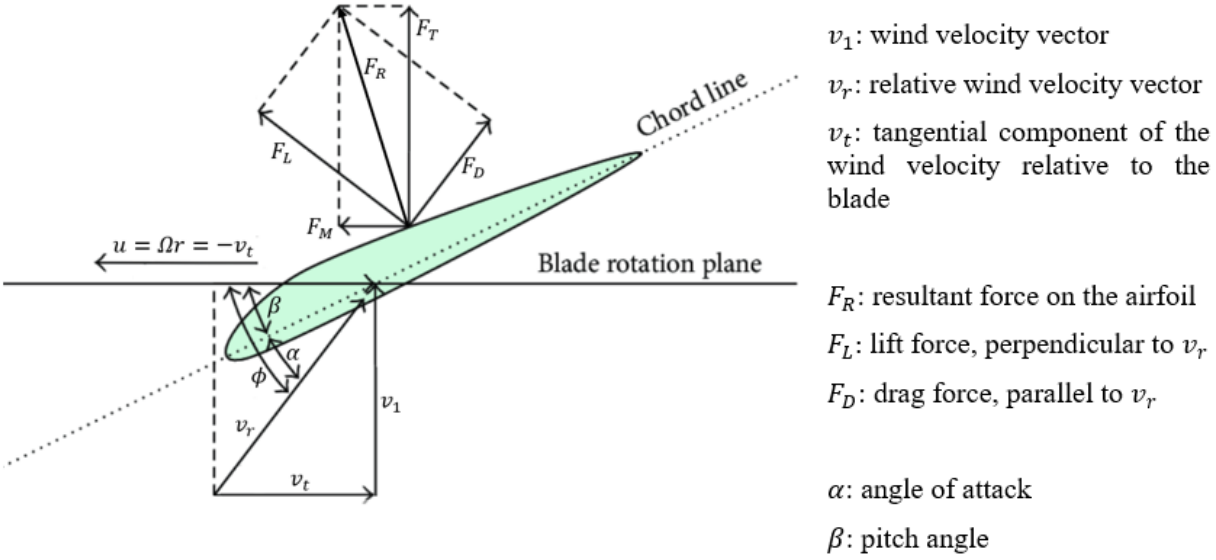

Figure 2.3: Forces acting on a wind turbine blade.

The change in momentum caused by the airfoil on the air stream results in a force that is composed of a lift component and a drag component, respectively acting perpendicular and parallel to the relative wind velocity vector. Aerodynamic similitude allows to express lift and drag forces as follows [28]:

$$F_L = \frac{1}{2} C_L A_p \rho v_r^2 \tag{2.18}$$

$$F_D = \frac{1}{2} C_D A_p \rho v_r^2 \tag{2.19}$$

where A_p is the surface area of the blade as seen from the relative wind, and C_L and C_D are, respectively, the lift and drag coefficients, which depend on the design of the blade and the interaction between the airfoil and the wind. The resultant force component along the direction of rotation, labelled as F_M, is tangential thrust that causes the rotation of the rotor, while the component F_T is axial thrust acting against the wind turbine structure.

The angle α from the relative wind velocity vector to the chord line of the airfoil is the angle of attack, while β is the pitch angle between the direction of rotation and the chord line. The angle of attack is an aerodynamic angle that depends on relative wind direction and intensity, and is optimized for a given blade. The pitch angle is a structural angle that can be changed if the blade can rotate along its longitudinal axis. Because the peripheral speed u increases with the radial extension r along the

blade, the angle $\phi = \alpha + \beta$ decreases from the root to the tip of the blade. Therefore, in order to maintain the angle of attack at the optimized value along the blade, the pitch angle must correspondingly decrease from the root to the tip of the blade: for this reason, the blades of horizontal axis wind turbines always present a twisted geometry, as illustrated in Figure 2.4.

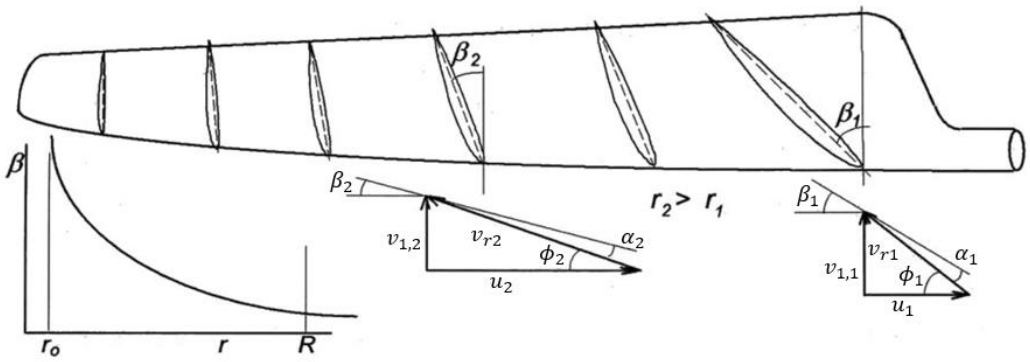

Figure 2.4: Airfoil cross sections and pitch angles along the blade [28].

2.4.1. Tip speed ratio and power characteristics

One of the most important parameters in wind turbine design and performance is the tip speed ratio λ (TSR), defined as the ratio between peripheral speed of the rotor blade tip and the incoming wind speed:

$$\lambda = \frac{\Omega r}{v_1} = \frac{\pi N_r D}{60 v_1} \tag{2.20}$$

Where Ω is the angular speed of the rotor of radius r and diameter D, and N_r the rotor rpm.

The TSR is a key configuration parameter for power extraction: if it is too low, the rotor does not rotate, and thus does not produce power. If it is too high, the high rotational speed makes the rotor appear as a blocked disk that impedes air mass transfer and thus no power is extracted from the moving air mass. In between, the optimal TSR λ_{opt} is found, yielding the maximum power coefficient $C_{P,max}$, and thus the maximum power capture for each wind speed. The relation between the power coefficient C_P and the TSR λ is determined by the shape and design of the rotor blades, and is non-linear [29]. The results are presented in the $C_P(\lambda)$ curve, which can be plotted in advance to simulate the performance of the WT by means of empiric relations found in literature or through computational fluid dynamics software requiring a 3D model of the blades, nacelle, and tower [29]. However, it is often difficult to obtain simulation results that match the WT in practice [29]. A typical example of the $C_P(\lambda)$ curve is shown in Figure 2.5, while Figure 2.6 shows a

typical characteristic of the mechanical power output of a wind turbine as a function of rotational speed, for given wind speeds.

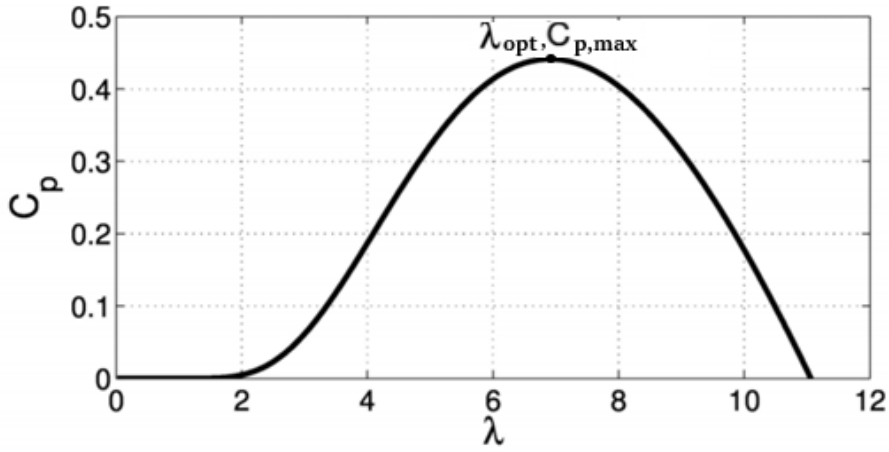

Figure 2.5: Power coefficient-Tip speed ratio curve for HAWTs [30].

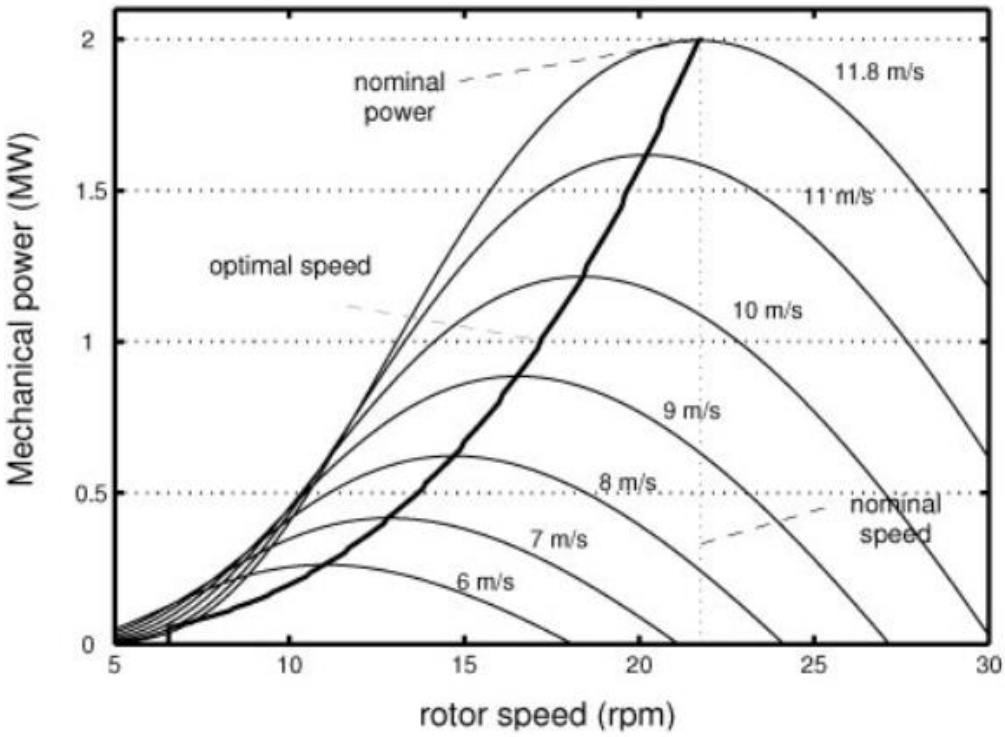

Figure 2.6: WT mechanical power as a function of rotational speed for given wind speeds.

2.5. Power regulation techniques in horizontal axis wind turbines

It can be seen that the mechanical power maxima lie on a curve that is a cubic function of wind speed, represented in region II in Figure 2.7: the blue curve is the power associated with the wind, which is greater than the WT mechanical power output due to the influence of the power coefficient. For maximum energy yield, WTGs are designed to operate along a power curve that closely follows the ideal characteristic shown in Figure 2.7, which is comprised of a cubic function between the cut-in and the rated wind speed (region II), followed by a constant power, equal to the rated power P_r, obtained at the rated wind speed, between the rated wind speed and the cut-out wind speed (region III). In region II, MPPT techniques are implemented for maximum power extraction. In region III, power regulation techniques are implemented to limit the power captured from the wind, maintaining the power output around the rated value and protecting the power train from overcapacity. The cut-in and cut-out speeds are the operating limits of the wind turbine. Below the cut-in speed (typically 2÷5 m/s depending on the wind turbine model [28], region I), the wind does not have enough energy to overcome the aerodynamic, mechanical, and electrical losses of the system (cut-in speed is thus a characteristic of a given connection, and depends on the load as well as on all other components of the system). The cut-out speed is a technological limit that is mainly dictated by mechanical strain on the rotor blades and tower, and is typically in the range of 10÷15 m/s to 20÷25 m/s, depending on the wind turbine used. At the cut-out speed, the braking system brings the rotor to a halt for safety reasons.

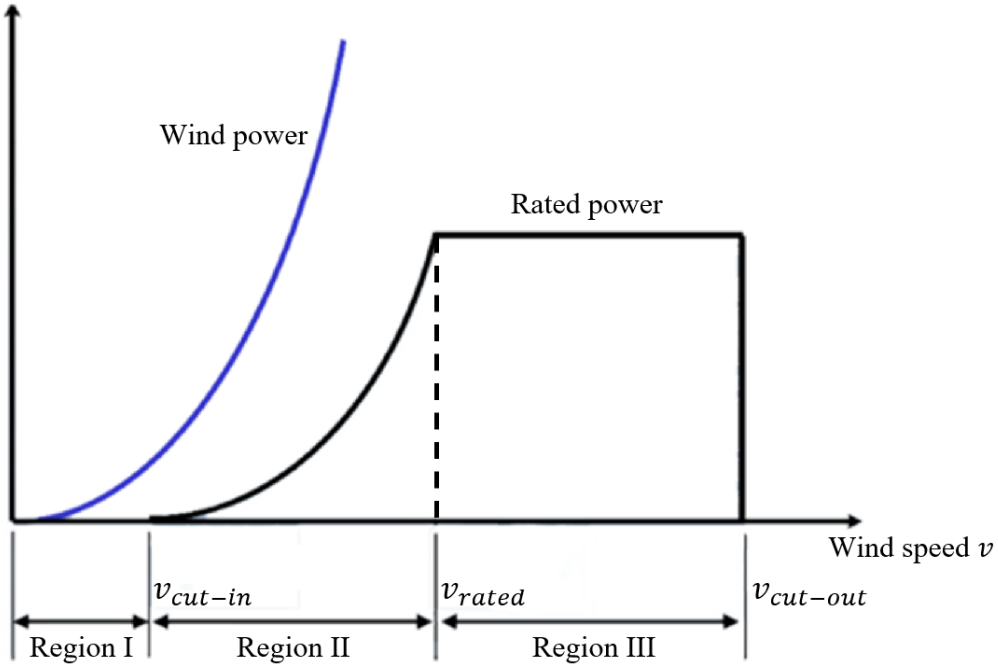

Figure 2.7: Ideal power characteristic of a HAWT [31].

The operation of wind turbines therefore requires the implementation of control techniques which accomplish three main objectives: maximization of the power output and efficiency for wind speeds below the rated value, limitation of the power output and rotor speed for wind speeds above the rated value, and normal startup and shutdown, overspeed protection, and emergency shutdown. Wind turbine control is classified into two main types:

- Passive control: in this type of control, the WTG "self regulates" (without any external intervention) to changes in wind speed by virtue of the aerodynamic design of the rotor blades. An example of this is the passive stall control, whereby the blades spontaneously enter the stall[11] condition above a certain wind speed, effectively limiting the power output.
- Active control: carried out by means of externally powered servomotors that regulate the blade pitch and adapt the aerodynamic characteristics of the blades according to changes in wind speed. Rotor speed regulation is also a form of active control, carried out in variable speed wind turbines by means of electronic control of the generator's electromagnetic torque.

Depending on the control strategy implemented, wind turbines are then classified according to the configurations outlined in the following.

[11] The stall condition occurs when the angle of attack increases to a point where the lift generated by the blades begins to rapidly decrease.

2.5.1. Fixed-speed, fixed-pitch (FS-FP) WTGs

Fixed-speed, fixed-pitch wind turbines are the simplest and oldest type, most commonly adopted in smaller systems [32], characterized by fixed rotor rpm (imposed by the electrical generator) for the entire operational wind speed range, and fixed blade design optimized for power extraction at low wind speeds (operation around $\lambda_{opt}, C_{P,max}$). Because the blades do not change their configuration and the rotor speed is fixed, FS-FP WTGs are characterized by one unique $C_P(\lambda)$ curve, and their efficiency is maximum for one wind speed only (chosen based on comparison among power curves and wind speed probability density models for the location of installation [28]). In the high wind speed region, between the rated and the cut-out wind speed, the blades spontaneously enter the stall condition (passive stall) as the angle of attack widens with increasing wind speed at constant rpm, effectively limiting the aerodynamic power extracted and maintaining the power output around the rated value. Stalling occurs at the blade tips first, where the peripheral speed is highest, and then propagates towards the roots as the wind speed increases. Figure 2.8 illustrates the stall condition occurring spontaneously on a FS-FP wind turbine blade section following an increase in wind speed from v_1 to v_1'.

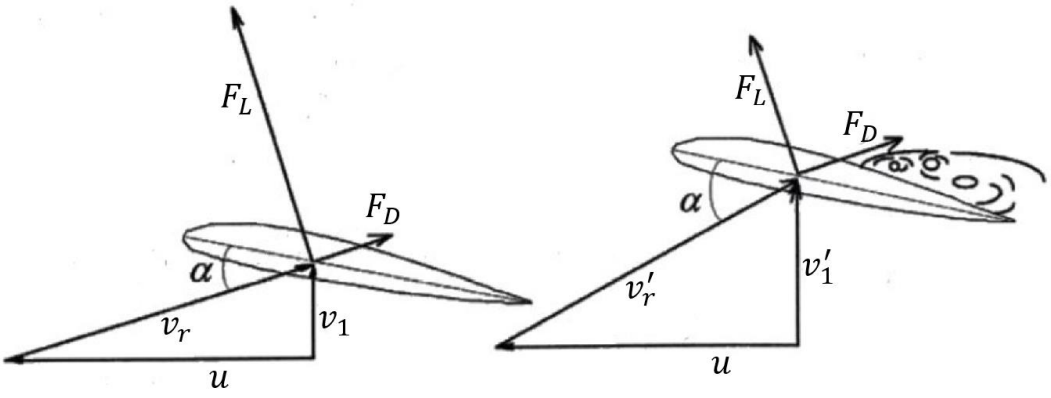

Figure 2.8: Passive stall on a FS-FP WT airfoil section.

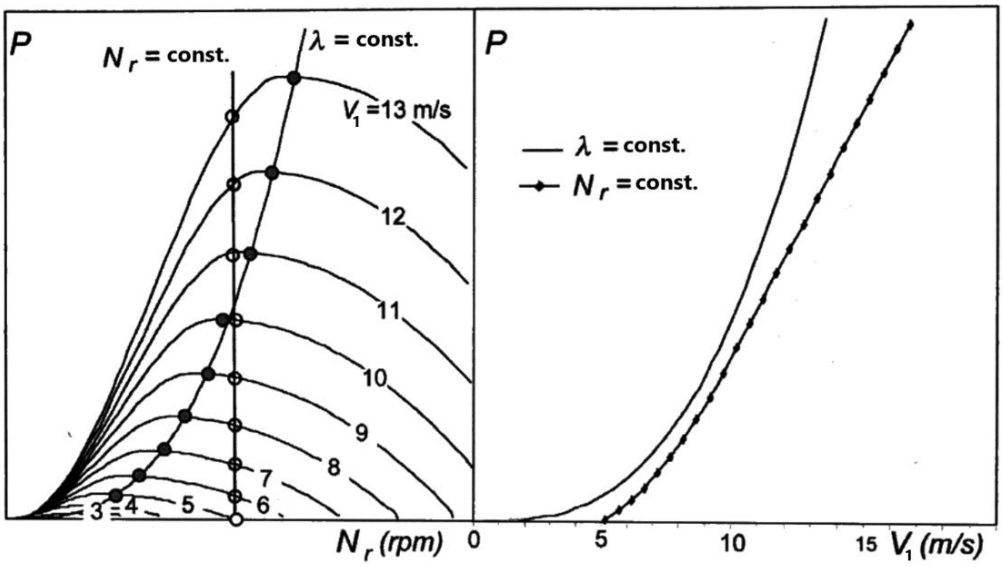

Figure 2.9: Power curve of a FS-FP wind turbine.

Figure 2.9 illustrates a typical power curve (below the rated power) for a FS-FP wind turbine compared to an ideal power curve (i.e., with constant TSR): the two curves tend to converge as the wind speed approaches the value for which the power coefficient is maximum, and diverge for the remaining operational wind speeds, implying losses in energy yield. A solution adopted to reduce the penalty in energy capture makes use of a dual-speed electrical generator with two sets of windings for pole switchover.

2.5.2. Fixed-speed, variable-pitch WTGs

In fixed-speed, variable-pitch (FS-VP) WTGs, the rotor blades can rotate along their longitudinal axis by means of servomotors installed in the hub, thus allowing for blade pitch control. For wind speeds below the rated value, the WTG operates as an FS-FP WTG. Pitch control is activated in the high wind speed region to limit the stress imposed on the mechanical components [33]. In high wind speeds, the power is limited by a blade pitching system either by pitching the blades to feather or to stall, causing in both cases a reduction of the power coefficient. The pitch-to-feather system pitches the blade into the relative wind: as wind speed increases, the pitch angle is increased and the angle of attack is reduced to decrease lift, drag, and thus the power coefficient. The pitch-to-stall system reduces the pitch angle as the wind speed increases, increasing the angle of attack so as to progressively induce the stall condition (active stall), thereby reducing the power coefficient. The two situations are illustrated in Figure 2.10.

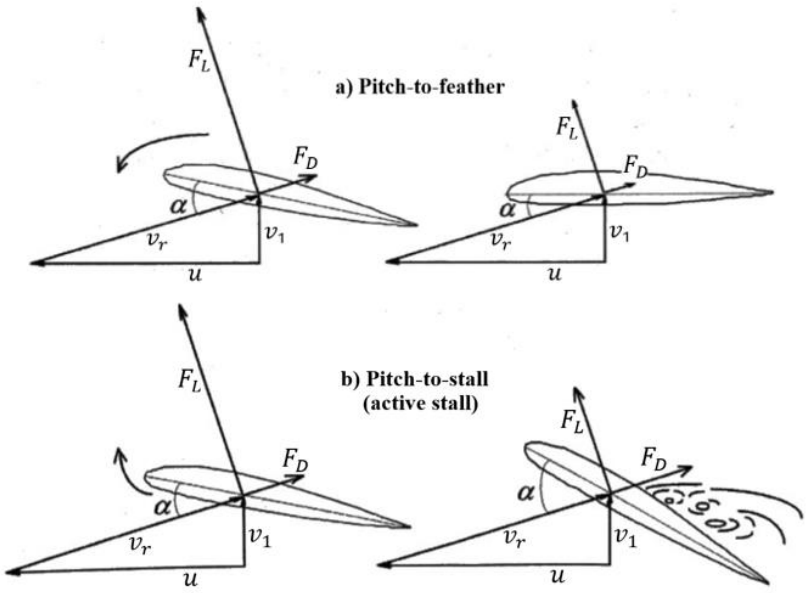

Figure 2.10: Pitch-to-feather (a) and Pitch-to-stall (b) control.

2.5.3. Variable-speed, fixed-pitch WTGs

In variable-speed, fixed-pitch (VS-FP) WTGs, the rotational speed of the rotor is regulated by means of power converter-based electronic control of the electromagnetic torque of the electrical generator (of induction or synchronous type). Below the rated wind speed, the rotational speed is varied proportionally to the wind speed for operation at the optimal aerodynamic configuration, i.e., at the optimal TSR and maximum power coefficient, to maximize the power extraction. Above the rated wind speed, the power is limited around the rated value either by passive stall control, whereby the rotational speed is kept constant and the blades spontaneously and progressively enter the stall conditions as wind speed increases (as described for FS-FP WTGs), or by active stall with rotational speed control, whereby the stall condition is actively induced from a reduction of rotational speed, causing the power coefficient to decrease. In general, the active stall control is more effective [34].

2.5.4. Variable-speed, variable-pitch WTGs

The WTGs belonging to this category are typically of very high power (4÷6 MW [28]), combining the features of rotational speed regulation below the rated wind speed for maximum power extraction (as described for VS-FP WTGs, without the need for pitch control), and pitch control above the rated wind speed for power limitation at the rated value. The control systems in VS-VP WTGs are very

expensive, with complex electronic controllers and actuators allowing for 70÷80° blade rotation, but offer the maximum energy yield and the best response to aerodynamic stress [28].

2.5.5. Comparison between different WTG control strategies

The performances of the abovementioned control strategies are represented in Figure 2.11. The power-wind speed characteristic is specific to the machine being investigated and can only be determined after testing campaigns conducted on the machine prototype[12] [28]. Controlling the blade pitch and the rotational speed are the most effective methods to adjust the power output to best match the ideal power curve. Above the rated wind speed, only pitch/active stall-controlled WTGs allow to maintain constant power at the rated value [33].

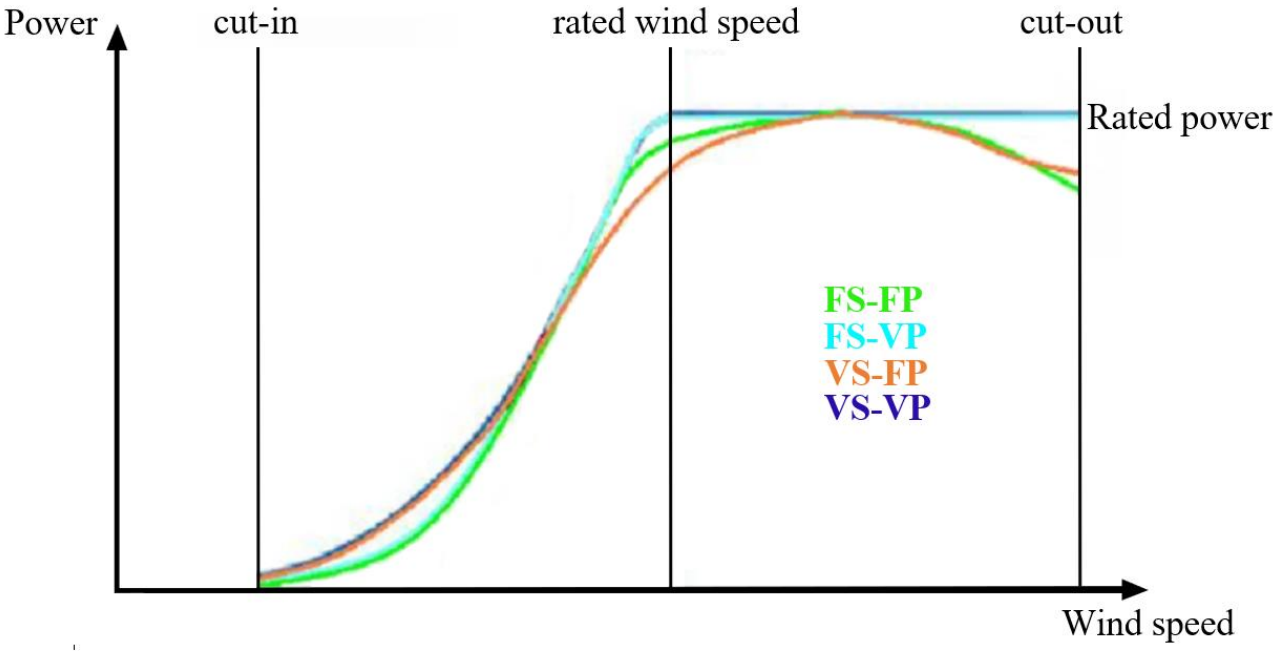

Figure 2.11: Power curves for different WT control strategies [35].

[12] However, the power curve can be plotted with good approximation by means of some mathematical models [28].

State-of-the-art medium and large sized WTGs also include active yaw control mechanisms that orient the rotor towards the wind according to the average wind speed and wind direction measurements taken by sensors placed on the nacelle over 10-minute time intervals. In addition, the tilt angle of the rotor is also optimized.

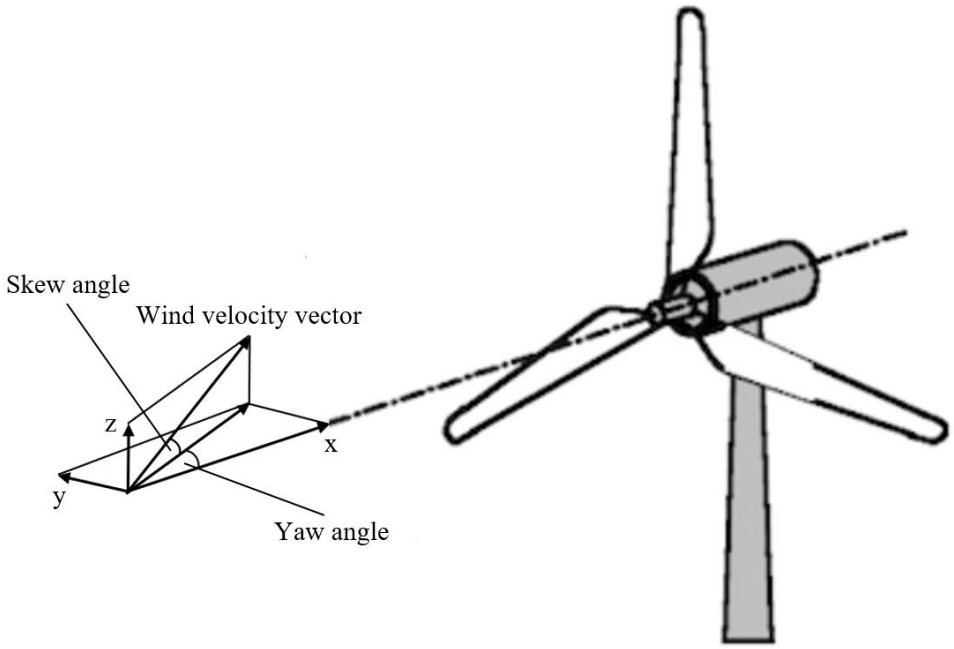

Figure 2.12. Yaw angle and skew angle between wind velocity and WT rotor axis.

2.6. General configuration and components of wind turbines

The main components in the general configuration of state-of-the-art horizontal axis WTGs are illustrated in the following.

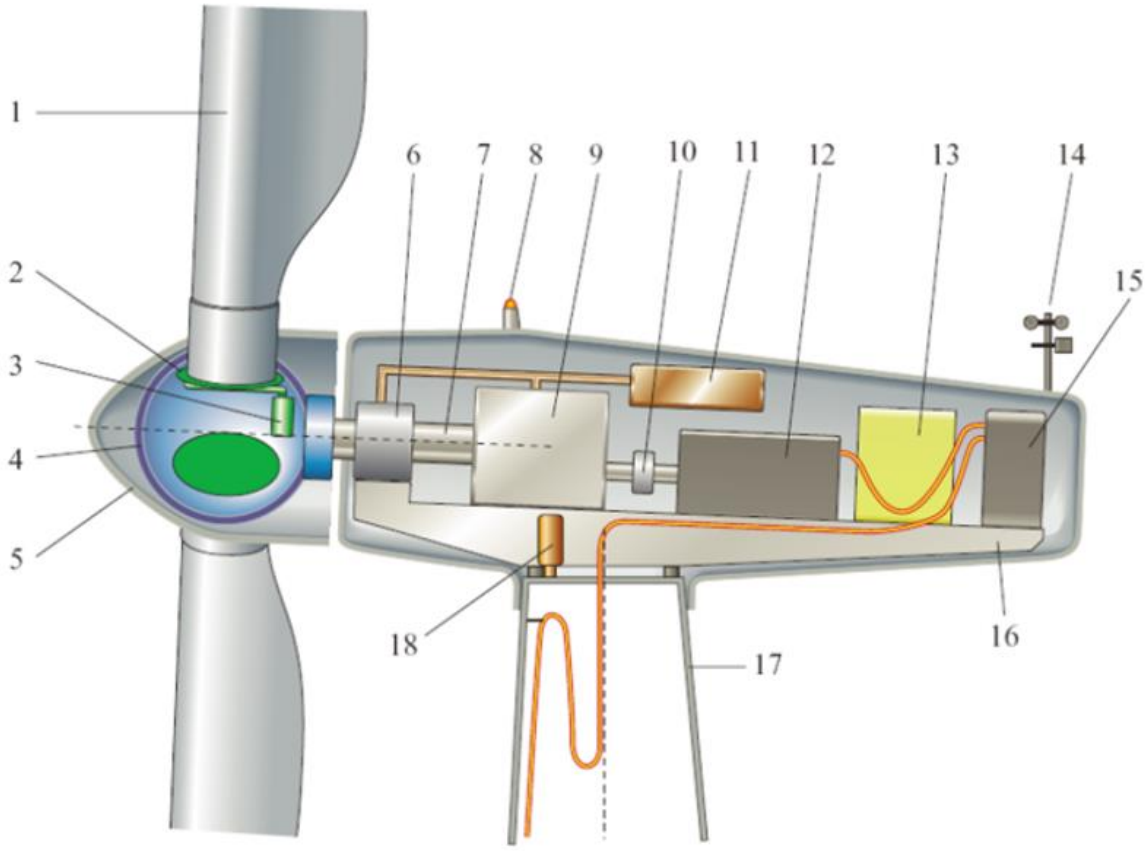

Figure 2.13: Main components of a horizontal axis wind turbine.

1. Blade, 2. Blade support, 3. Blade pitch actuator, 4. Hub, 5. Spinner, 6. Main support, 7. Main shaft, 8. Obstruction lighting, 9. Gearbox, 10. High-speed shaft and brake, 11. Hydraulic unit and cooling, 12. Electrical generator, 13. Electrical instrumentation and controls, 14. Anemometers, 15. Transformer, 16. Nacelle structure, 17. Tower, 18. Yaw control mechanism.

2.6.1. Electrical configuration of wind turbine generators

Depending on the whether the WTGs are used in grid-connected or standalone power generation applications, the electrical generators that are typically used in WTGs to convert the mechanical energy extracted from the wind to electrical energy are of the of the induction (asynchronous) or synchronous type.

2.6.1.1. Asynchronous WT generators

AC induction generators are used in grid-connected WTGs as they require reactive power to produce the rotating magnetic field at the stator. They fall into two types:

- fixed speed induction generator with squirrel cage rotor (SCIG): the generator is coupled to the turbine rotor's main shaft through a gearbox to suitably increase the rpm. Rotational speed should be fixed in order to limit the variations in slip and the associated reactive power fluctuations (compensated by means of capacitor banks). The stator phases are connected to a three-phase transformer to obtain medium voltage output.
- doubly-fed induction generators (DFIGs) with wound rotors: this technology has essentially supplanted the SCIG in wind power generation applications, with over 85% of WTGs utilizing DFIGs [36]. In the DFIG topology, the stator is fed by the grid through a transformer, and the rotor is connected to the grid through bidirectional voltage source converters that can control rotor current, frequency, and phase shift. In this way, DGIGs can operate both in sub-synchronous and super-synchronous conditions (typically ±30% of the synchronous speed [36]). The stator always transfers active power to the grid, while the rotor absorbs active power from the grid in sub-synchronous operation and injects it in super-synchronous operation. The converter that interfaces the rotor with the grid is composed of two AC-DC bidirectional converters (one rotor-side and one grid-side) with a common DC link. In sub-synchronous operation, the grid-side converter acts as a rectifier, while the rotor-side converter acts as an inverter to allow the power flow from the grid to the rotor. Conversely, to transfer the power from the rotor circuit to the grid during super-synchronous operation, the rotor-side converter acts as a rectifier and the grid-side converter as an inverter. DFIGs offer great advantages in terms of increased energy yield, greater controllability of reactive power, and the possibility to operate at variable speed, with consequent lower mechanical stresses on the wind turbine components [36].

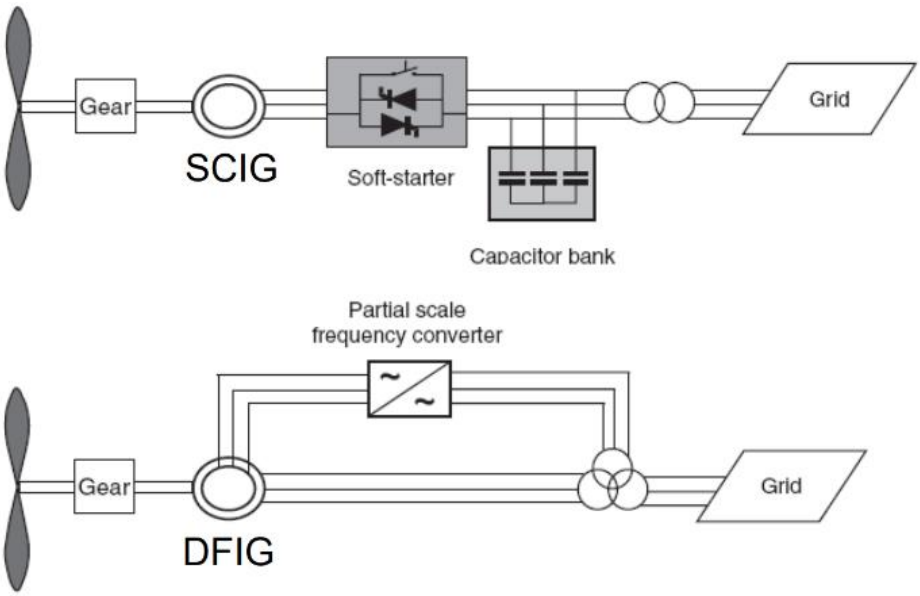

Figure 2.14: Asynchronous wind turbine generator topology.

2.6.1.2. Synchronous WT generators

Synchronous generators are used both for grid-connected and standalone wind power generation and are particularly suitable for variable speed applications. Depending on whether the DC excitation is obtained through permanent magnets or through electromagnets, synchronous generators are termed PM synchronous generators (PMSGs) or electrically excited synchronous generators (EESGs), respectively. The absence of commutators, slip rings, and brushes in PMSGs makes them more rugged, reliable, and simple. However, unlike EESGs, the reactive power characteristics of the WTG cannot be controlled via the field excitation circuit [36]. In variable speed operation, the generated AC power of synchronous WTGs varies in frequency and in magnitude, and must therefore be regulated via AC-DC-AC converters prior to grid connection. Because the rotational speed is essentially decoupled from the load-side, synchronous WTGs can be used for direct drive applications without any gearboxes, reducing the risk of component failure, albeit at the expense of physical size due to the higher number of poles required [36].

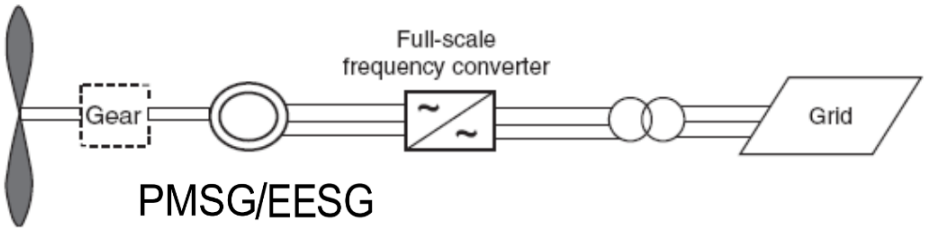

Figure 2.15: Synchronous wind turbine generator topology.

2.6.1.3. Connection topology for DC applications

In DC power supply applications, the generated AC power from synchronous WTGs can be rectified through diode bridges and controlled via DC-DC converters that perform maximum power tracking while supplying the DC system at the required voltage level. An example of this topology, proposed in [25], is shown in Figure 2.16.

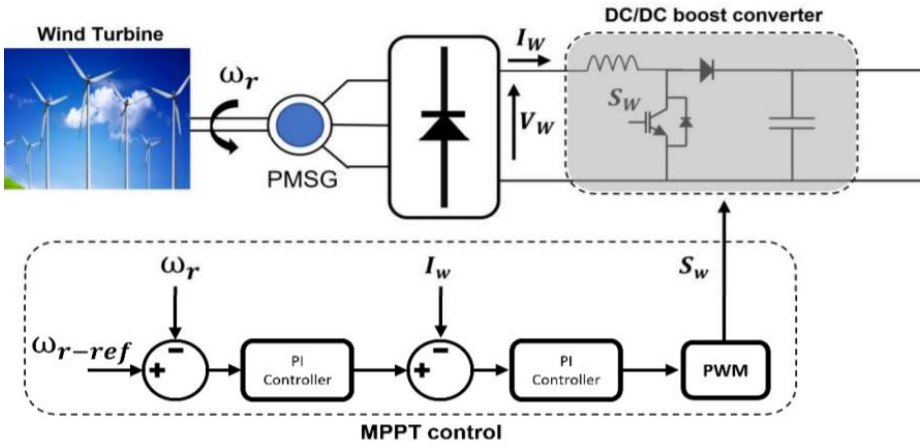

Figure 2.16: Wind turbine DC connection topology and MPPT scheme.

2.7. Wind power production characteristics

2.7.1. Estimation of the annual energy production

Given the wind frequency distribution of the site of installation and the power curve of the selected machine, the WTG's annual energy production E_{WTG} [KWh] can be calculated as the sum of the WTG's yearly energy contributions related to each wind speed:

$$E_{WTG} = 8760 \sum_k f(v_k) P(v_k) \tag{2.21}$$

where the subscript k indicates the wind speed class in the frequency distribution, and $P(v_k)$ the associated power output, which is non-zero between the cut-in and the cut-out speed. The net annual energy production is then estimated accounting for various non-ideal conditions and miscellaneous errors, as summarized in the flowchart in Figure 2.17.

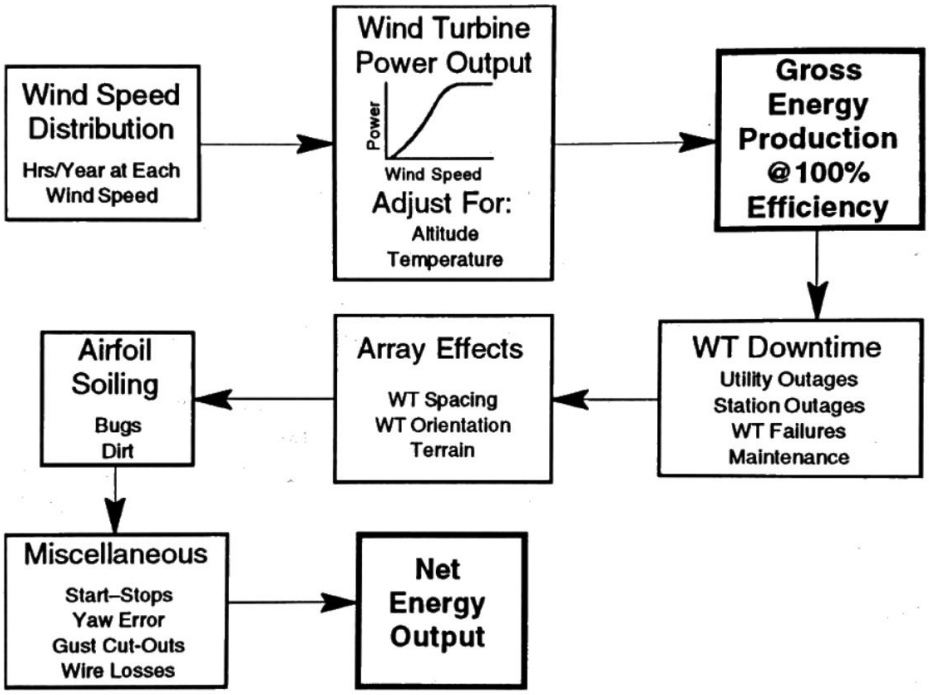

Figure 2.17: Wind farm net annual energy production estimation flowchart [32].

The net energy production of individual WTGs and complete wind power stations is monitored and assessed through various performance parameters, some of the most important being the capacity factor, which relates the actual net energy yield to the maximum theoretical energy yield (corresponding to system operation at the rated power during the entire time interval of interest), and the utilization factor, which relates the actual net energy yield to the maximum energy yield obtainable over the cumulative time the wind speed was in the operating range [35]27. For systems with good energy yield, the utilization factor rarely exceeds 0.25÷0.30 (corresponding to 2000÷2500 yearly hours of operation at rated power), while capacity factors lower than 0.15÷0.20 are considered insufficient for energy production that is competitive on the electricity market[13] [28].

2.7.2. Individual and aggregate wind power production curves

Wind variability translates into power output fluctuations, the entity of which depend on the duration and intensity of the wind variations, and on the wind speed range. Between the cut-in and the rated wind speed, the power fluctuations are amplified due to the near-cubic dependence between power and wind speed. Below the cut-in wind speed or between the rated and the cut-out wind speed, power fluctuations are smoothed considerably [37]. Above the cut-out wind speed, the system is disconnected for safety reasons and the power suddenly drops from the

[13] Low values of CF may be acceptable in certain stand-alone applications.

rated value to zero, leading to significantly higher power fluctuations [37]. Variations in the quasi-instantaneous to one-second time scale, classified as turbulence [28], are largely filtered by the blades' inertia[14], and their impact is mainly considered at the structural level (vibrations) in the design of the system. Power fluctuations generated by wind gusts (defined over time scales in the order of minutes [28]) begin to gain significance. In the context of the power system, the focus is on wind power fluctuations from tens of minutes to several hours [37]. Figure 2.18 shows the power fluctuations (in p.u. of the rated power) of a single WTG compared as compared to the whole wind farm, indicating that the aggregate power fluctuations are proportionately reduced [37]; on a regional level, the power fluctuations are further dampened by geographic separation and greater spatial diversity of wind speeds [32], resulting in a more regular power output, as shown in the example in Figure 2.19 for the aggregate wind power output in the country of Spain.

Figure 2.18: Wind farm vs. single wind turbine power production [37].

[14] Extreme variations can result in power fluctuations in the order of a few percentages of the installed capacity for large wind farms.

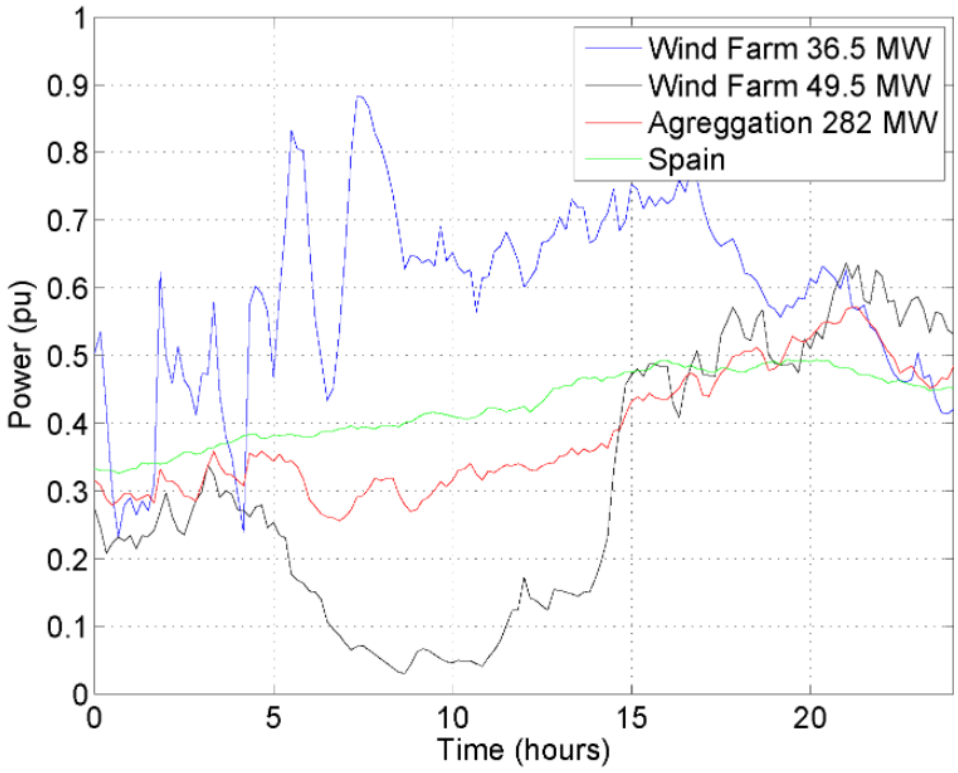

Figure 2.19: Aggregate wind power production in Spain [37].

3 The Italian 3 kV DC railway

3.1. Historical aspects

The first major applications of DC railway electrification date back to the end of the 19th century, when direct current power supply was implemented in tramways, metro lines, and then electric trains, with gradually increasing voltages (750, 1500, and 3000 V) as the technology became more and more established. In Italy, after the Second World War, the DC 3 kV solution was implemented in accordance with the overall electrification policy of the entire network, substituting the three-phase system at railway frequency (historically promoted by the wide availability of hydroelectric resource generating three-phase electricity, but less performant than the 3 kV DC system) following the destruction caused by the war. To date, most of the Italian railway network is conventionally electrified at 3 kV DC (accounting for approximately 11921 km of railway line), and has been recently expanded with the construction of the new 25 kV 50 Hz high-speed rail network (covering 1300 km).

Power supply systems in direct current are widely used to this day in their traditional configuration due to some inherent advantages that stood the test of time. Most notably:

- Power is derived from the utility grid via three-phase unidirectional diode bridge rectifiers, without introducing unbalances and with contained power factors and distortions [37].
- The effects of electromagnetic interference on the contact lines are virtually eliminated, and the voltage drops are limited as they are only due to the resistive components of the line impedance.
- The substations are easily operated in parallel with bilateral power supply of the line segments, further limiting the voltage drops and favoring traction vehicle performance.

The main limitations in DC electric traction systems are due to the maximum applicable voltage, which is dictated by technological limits of the switches. Currently, in fact, it is technically challenging to realize switches capable of withstanding continuous reestablishment of voltages higher than 6 kV [38]. The limited voltage at the contact line implies that in order to supply adequate power to

the traction loads, the current must necessarily be high. However, exceedingly high currents generate uptake problems between the pantograph and the contact line above a certain speed. It thus becomes apparent that in DC power supply systems, the constraints on voltage and current pose limitations on the operating power and speed of the traction vehicles. In this regard, the more complex single-phase AC systems at mains frequency (such as the 25 kV system at 50 Hz) enable high power transmission at sufficiently low current thanks to the higher voltage involved, making them better suited for high-speed and high-power applications.

3.2. Structure and configuration

In conventional 3 kV DC electric railway systems, the power supplied to the traction loads is normally taken from the high-voltage AC primary lines (132÷150 kV at present, 66 kV in the past) and then rectified to DC by means of rectifier bridges at conversion traction power substations (TPSSs) adequately located along the railway line. The TPSSs supply the traction circuit, which is essentially made up of an overhead contact line (constituting the positive conductor) and the rails (constituting the return conductor). The spacing between consecutive TPSSs can vary between 10 and 20 km depending on line traffic intensity and power demand (for instance, the average distance between TPSSs servicing the *Direttissima* 3 kV DC high-speed line between Florence and Rome is roughly 15 km). The general connection scheme for the 3 kV DC ERSs is shown in Figure 3.1

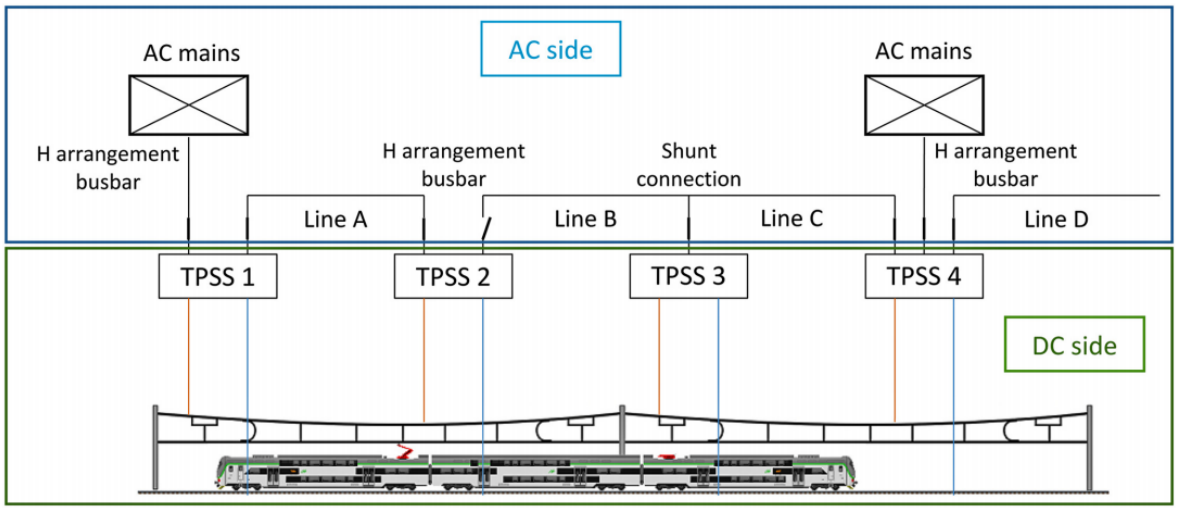

Figure 3.1: General architecture of the 3 kV DC electric railway system [38].

3.2.1. Connection to the AC power grid

Two main modalities of interconnection between the traction substations and the AC mains are implemented, depending on service requirements and local conditions [38]:

- Branch or shunt connection: the conversion substation can be directly supplied from the mains through a grid station, or receives power via branch connection to a dedicated primary line (railway primary), or from two separate primary lines (*dual power supply*) fed by independent grid stations (the dual power supply is implemented whenever possible for increased system redundancy). In any case, an input disconnector is required for isolating the TPSS from the grid for maintenance purposes [38].
- Cascaded or H arrangement busbar connection: the high-voltage primary line is connected to a dual busbar system (favoring redundancy) that provides supplementary output terminals to supply another downstream TPSS (in-out connection). Both ends of the primary line terminating on the substation HV busbars are equipped with a circuit breaker in series with a disconnector, as shown in Figure 3.3. Compared to the branch connection, this solution is more complex, requiring circuit breakers also on the primary line-side, as well as a greater number of disconnectors [38]. The more important power substation nodes may have multiple primary lines that supply two or more busbar systems, further increasing the complexity of the system as additional protection devices (disconnectors, circuit breakers, measurement transformers, and relays) need be installed [38].

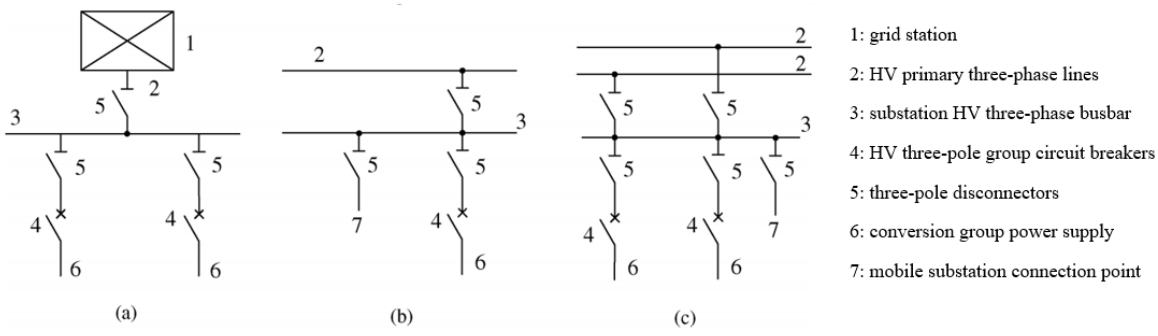

Figure 3.2: Branch connection power supply [38]: (a) from the main grid, (b) from railway primary, (c) from a dual primary.

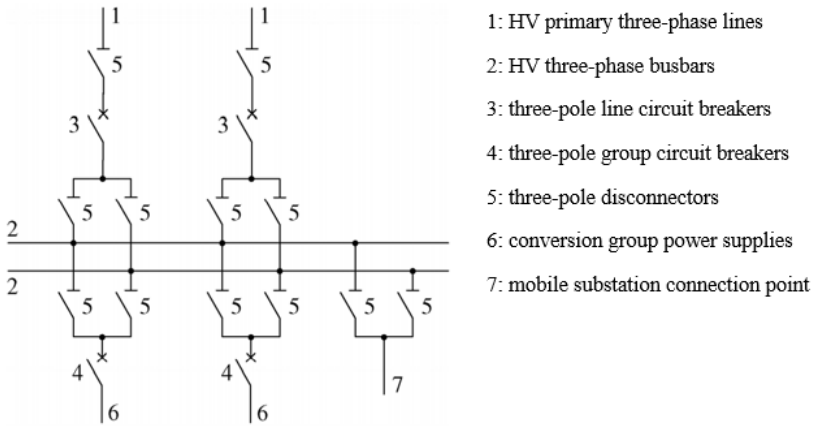

Figure 3.3: H arrangement busbar connection [38].

3.2.2. Structure and components of the traction power substations

The TPSS is at the interface between the AC mains and the DC traction circuit, thus, the typical TPSS power supply architecture can be distinguished into two macro-sections:

1. The AC section, which includes the control gear, protection, and measurement equipment for connection to the grid and for the supply of the transformers and AC-DC converters.
2. The DC section, which includes the AC-DC converters, line filters, and the control gear, protection, and measurement equipment for the traction lines.

In the AC section, the incoming primary lines are connected to a HV bus bar system that constitutes the central node of the substation, acting as a hub for the connection of the group transformers. Each primary line terminal is equipped with the following components:

- input line spark gap anchor points;
- three-pole line disconnector with interlocked earthing blades;
- three-pole line circuit breaker with adequate breaking characteristics determined by the worst-case short circuit conditions;
- three-pole busbar disconnector;
- three dual-secondary voltage transformers (installed upstream of the line disconnector) and three dual-secondary current transformers (downstream of the line disconnector), for separate function of metering and protection circuits.

3.2.2.1. AC-side disconnectors

The disconnectors on each incoming phase are normally of the rotary-type and provide air insulation to the high-voltage sections of the substation, as well as a visible indication of the open and closed positions in accordance with safety standards. Disconnectors can only operate with an open circuit; thus, their activation is interlocked with the circuit breakers. The opening procedure happens with a 90° rotation of the central column that drags the switching blade, which is then grounded via the earthing blade for safety. The fixed contacts are mounted on the lateral columns. Three-phase disconnectors are mounted on sturdy steel tripods, and can be controlled either manually or by means of an electromechanical servomotor.

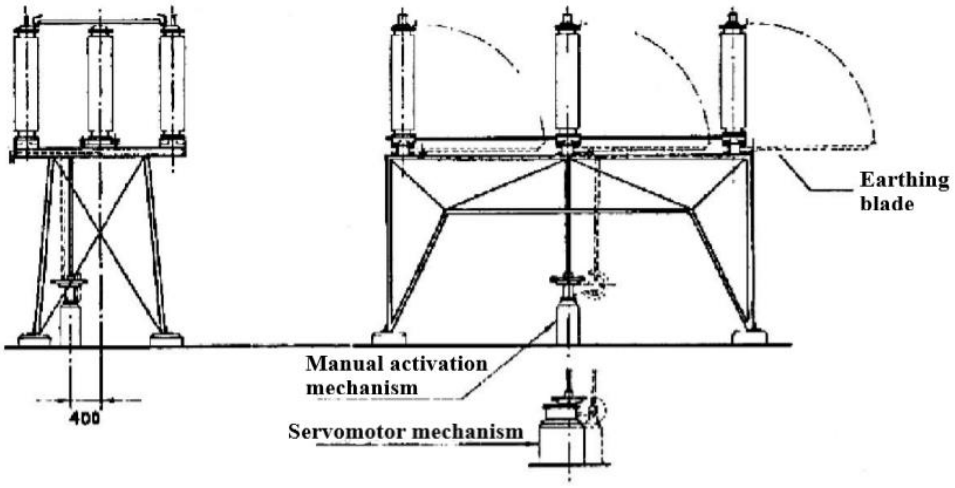

Figure 3.4: Three-phase, three-pole rotary disconnectors.

3.2.2.2. AC-side circuit breakers

The three-pole circuit breakers are able to open and close the circuit under load, and are positioned at a certain height in order to distance the active parts from the ground. Each pole includes two stacked cylindrical insulators, wherein the contacts are immersed in an insulating fluid (special mineral oil or sulphur hexafluoride) for arc extinction upon contact opening, and a current transformer.

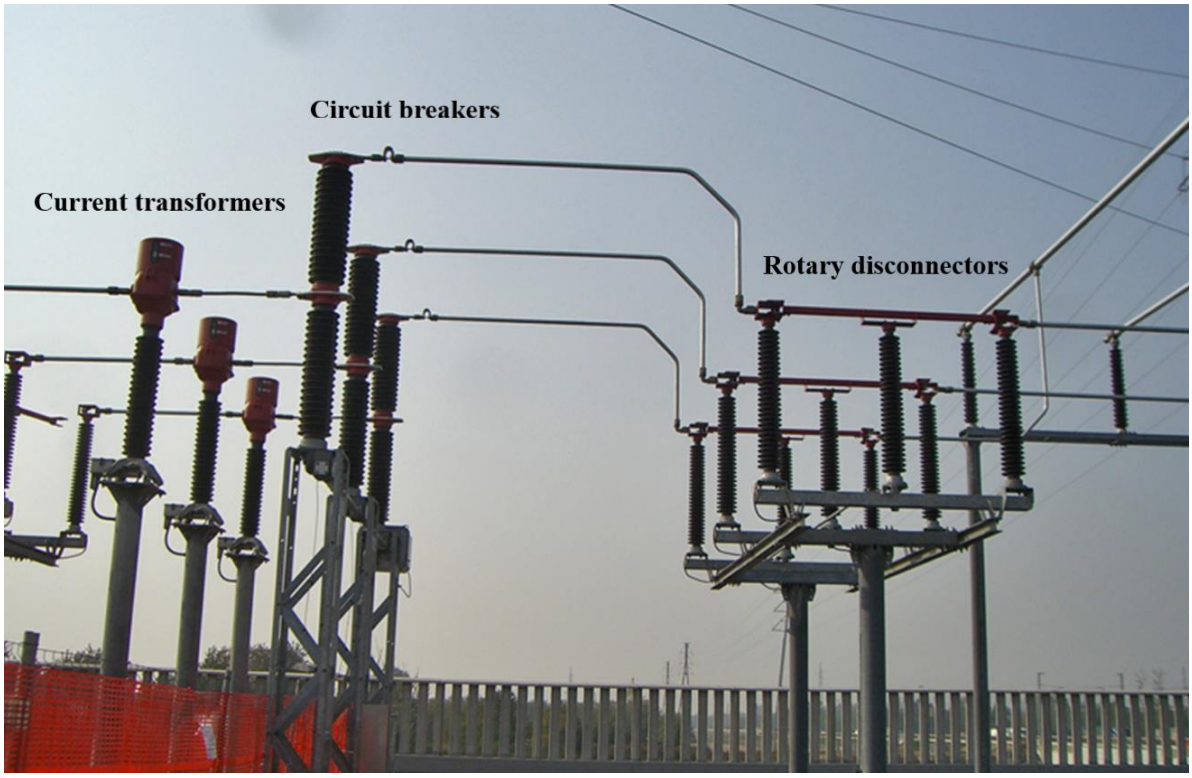

Figure 3.5: Rotary disconnector, circuit breaker, and current transformer unit [38].

3.2.2.3. Surge arresters

Finally, earthed surge arresters protect the substation equipment from primary line overvoltage. They are typically positioned upstream of the traction transformer, at an adequate distance from the devices to be protected. The active part of the arrester is composed of different metal oxide resistors, that present high impedance to the ground under normal operating conditions. In case of voltage surge, air ionization ignites an electrical arc across the electrodes, causing a strong current through the arrester that trips the overcurrent protection.

Figure 3.6: The AC section of a traction power substation [39].

Gravel is laid beneath high-voltage equipment for the drainage of water and any oil spills, and to extinguish fire in the event of ignition. Substation equipment layout can vary based on the number of incoming primary lines and number of conversion groups, as well as on the orography of the site of installation and on the available infrastructure (such as road and rail access points). In any case, the safety distance between the various components must be respected.

3.2.2.4. The transformer group

Downstream of the switching and protection equipment and the measurement devices necessary for their operation, the substation transformer group transforms the HV input voltage to levels that can be used by the various loads. The transformer group is comprised of three different types of transformers according to their function:

Traction power transformers. They are typically three-winding transformers, with a star-connected primary winding and two secondary windings in the star and delta configuration, belonging to the Yyd11 vector group (the neutral terminal may be earthed depending on the management policy of the grid). As such, the secondary

voltages are phase shifted by 30° for feeding groups of 12-pulse rectifiers, which, in turn, feed the DC catenary. The transformer presents a three-legged core, with the secondary windings placed internally to the primary windings (favoring insulation, and, if on-load tap changers are present, accessibility to primary winding connections), and are oil-filled for insulation and internal cooling.

Due to the frequent power peaks of short duration that characterize the traction loads, traction transformers are designed according to different criteria with respect to industrial systems. In particular, they must be able to withstand frequent power overloads according to the following rating cycles:

- Delivery of 200% of the rated power for an interval of 2 hours.
- Delivery of 233% of the rated power for an interval of 5 minutes.
- Combined overload cycles interspersed with intervals of less than 6 h.

In higher power substations connected to the high-voltage grid, on-load tap changers are often implemented to compensate for line voltage variations and to regulate the secondary voltage. In any case, a distinguishing feature of traction power transformers is their relatively high short circuit voltage, usually between 5% and 12% of the rated voltage [40], owing to the high leakage reactance needed in order to effectively limit short-circuit currents. However, the transformer's inductance should not be too high in order to avoid excessive voltage drops and their negative impacts on the DC power supply. Some technical specifications of substation traction transformers are presented in Table 3.1.

Table 3.1: Technical specifications of traction power transformers in TPSSs [40].

Normalized primary line voltage	66 kV	132 kV	150 kV
Denomination	Yy0-Yd11	Yy0-Yyd11	Yy0-Yyd11
Nominal primary voltge	63 kV ± 5.6%	125 kV ± 8%	150 kV ± 8%
Transformation ratio	63000/2710	125000/2710	150000/2710
Rated power	3880 kVA	5750 kVA	5750 kVA
Rectifier group power	2000-3600 kW	5400 kW	5400 kW
Total weight	18760 kg	28000 kg	28000 kg
Weight of oil	5500 kg	8500 kg	8500 kg
Approximate dimensions [mm]	3500x2000x4500	3800x3000x5100	3800x3000x5100
Short circuit voltage [%]	less 13.5% as per IE.TE technical standard, p. 3.1.10		

Auxiliary equipment transformers. Inside the substation building, each transformer group includes an auxiliary equipment transformer that usually receives three-phase power from the star-connected secondary winding of the traction transformer, and supplies power to fundamental services of the substation (such as the control and lighting systems). Their transformation ratio is 2710/380 and the rated power is usually 100 kVA [40]. Finally, dedicated secondary line transformers are sometimes installed to supply secondary railway infrastructure power lines. They are HV-MV transformers with a single secondary [40].

In the DC section of the TPSSs downstream of the transformer group, diode bridge rectifier groups receive power from the AC section and perform AC to DC conversion to feed the DC catenary system, which ultimately powers the traction loads present on the track. The main components of the DC section are the following:

- 12-pulse silicon diode bridge rectifiers;
- positive and negative DC busbars connecting to the contact line and the return conductor through the various protection devices;
- voltage and current measurement unit;
- L-C line filter;
- bipolar disconnector;
- one bidirectional high-speed line circuit breaker for each power supply;
- surge arrester;
- horned disconnector.

3.2.2.5. The rectifier group

It is the "heart" of the DC section of the TPSS. Over the decades, rectifiers have seen considerable progress with the development of electric and electronic components of ever-increasing performance. In the earliest electrification systems, rather complex rotating converter systems were used, followed by static mercury vapor rectifiers, that greatly simplified the substations while delivering excellent performance. A further milestone was the introduction, starting from the 1960s, of silicon diode-based rectifiers, that gradually supplanted all mercury devices. To this day, TPSSs predominantly employ diode bridges for AC to DC conversion due to their excellent performance, reliability, low losses and low energy demands for cooling. The absence of switching controls for the diodes constitutes another advantage in the form of simplicity; however, this excludes the possibility to regulate voltage and control power quality, as well as to reverse the power flow to inject regenerative braking energy from the trains to the AC supply. These high-performance functions have been made possible with the development of controlled semiconductors (thyristors) which have led to the emergence of the first bidirectional traction substations in the mid-1980s. To date, the use of thyristor converters in TPSS applications is still less widespread than that of diode rectifiers (simpler and less costly), and a challenge for the future consists of revamping "traditional" diode-based TPSSs to accommodate for the new generation technology.

The solution adopted for 3 kV DC railway substations in Italy consists of 12-pulse diode rectifiers, consisting of two parallel-connected 6-pulse diode bridges that are fed by the three-winding traction transformer to provide a rectified voltage of 3.6

kV at no-load. To this end, the secondary side voltage of the traction transformer is typically rated at 2710 V [40]. The 30° phase shift between the secondary voltages of the Yyd11 transformer feeding the diode bridges results in a rectified output voltage characterized by 12 pulses in each fundamental period of the sinusoidal input voltages (50 Hz).

Considering that diodes generally have poor overload ratings and high sensitivity to overvoltage, and considering the frequent overloads due to intense railway traffic, the diode bridges in traction substations are adequately sized and protected according to the following measures:

- The diodes are sized to withstand a peak repetitive reverse voltage equal to the nominal value multiplied by a safety factor in the range of 1.5÷2.5. If the overvoltage levels are generally well known, the safety factor may be taken as less than 1.5, while safety factors up to 2.5 are generally used where the diodes are connected to high-power networks and where the overvoltage levels are mostly unknown [38].
- Several diodes are connected in series in each commutator group in order to partition the reverse voltage. To avoid uneven partitioning (due, for instance, to different working temperatures and structural differences between individual diodes), a voltage equalization resistance of high value (in the order of a few thousand Ohms) is fitted across each diode. In addition, each diode is also fitted with a snubber circuit for transient voltage partitioning.
- The number of series-connected diodes in each commutator group is chosen so that, in the event of failure of a single diode, the remaining diodes are still able to withstand the maximum reverse voltage, ensuring continued operation of the rectifier bridge.
- Each rectifier is equipped with an overheating protection system that generates an alarm if a first temperature limit is exceeded, and a second alarm that causes the rectifier output to disconnect [38].

In new-generation substations supplying 3 kV lines there are four series diodes per branch, for a total of 48 diodes for each 12-pulse bridge (24 for each 6-pulse bridge). In older generation substations there are 5 diodes per branch, each with a lower rated reverse voltage, but with greater overall conduction losses and greater cooling requirements. It is clear that the implementation of fewer diodes with better performance characteristics is key to increase the rectifier's efficiency and to reduce the weight and dimensions of the associated heat sinks [38].

The number of series diodes n_s is selected based on the following sizing equation [38]:

$$n_s = \frac{K_V V_{MAX}}{K_S V_{RRM}} \tag{3.1}$$

where K_V is a factor greater than 1 that takes operating voltages into account, V_{MAX} is the maximum permissible continuous DC output voltage (3600 V), K_S is a voltage distribution coefficient, and V_{RRM} is the maximum peak reverse voltage (found on manufacturer datasheet) [38].

Given the frequent overloads associated with normal operation of the traction loads, regulations prescribe the following overload capacity requirements for the TPSS converter groups (at a reference temperature of 40 ˚C) [38]:

Table 3.2: Overload capacity requirements of TPSS converter groups.

Rated power	Max. continuous DC voltage	Rated current	Max. overload current for 2 h	Max. overload current for 5 min
3.6 MW	3600 V	1000 A	2000 A	3000 A
5.4 MW	3600 V	1500 A	3000 A	3500 A

Due to the low thermal inertia of the semiconductor modules, the rectifiers are sized for the maximum load. In case of single diode failure in each branch, the rectifier is able to continue its operation, albeit at a lower power level. If a second diode fails in the same branch, the rectifier is shut down [38].

Principle of operation of the 12-pulse rectifier

Considering the 12-pulse rectifier in the parallel configuration (typical for TPSS applications), the rectified output voltage is obtained through two parallel-connected 6-pulse rectifiers fed by the secondary windings of a three-phase, three-winding transformer typically belonging to the Yyd11 vector group. The first 6-pulse rectifier is fed by the star-connected secondary, while the second 6-pulse rectifier is supplied by the delta-connected secondary. As such, the rectified voltages of each 6-pulse rectifier are phase shifted by 30˚. The schematic of the parallel-connected 12-pulse rectifier is shown in Figure 3.7.

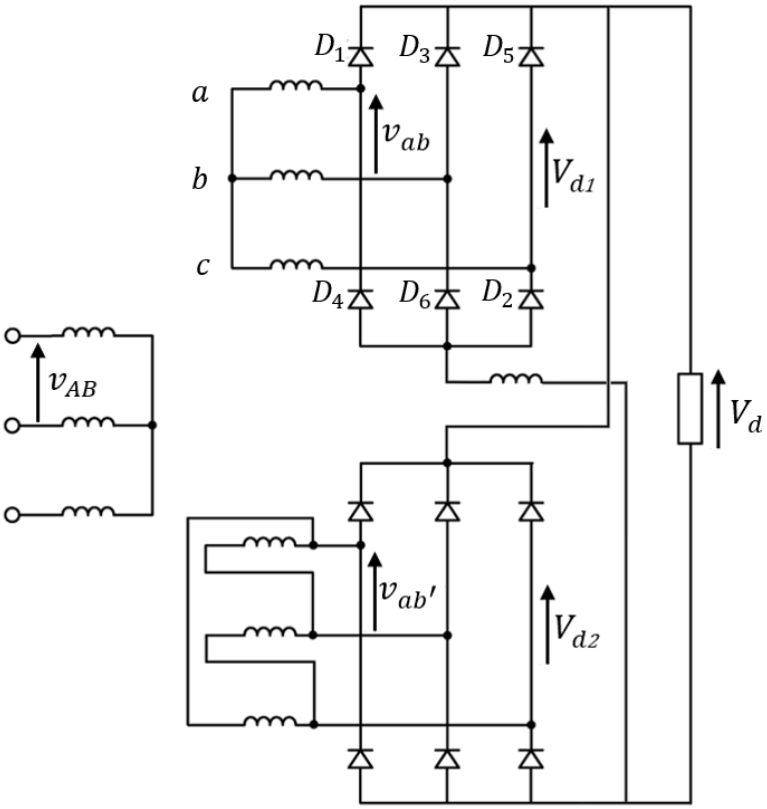

Figure 3.7: Parallel-connected 12-pulse rectifier.

Each 6-pulse bridge is comprised of a set of common cathode-connected group of diodes and a set of common anode-connected group of diodes. In the common cathode-connected group, the diode with the highest anodic potential will conduct. Conversely, in the common anode-connected group, the diode with the lowest cathodic potential will conduct.

With reference to the circuit diagram shown in Figure 3.7 and the phase voltage waveforms shown in Figure 3.8, the first 6-pulse bridge (fed by the star-connected secondary winding) is considered in the following analysis. In the time interval corresponding to $0 \leq \omega t \leq 30^{\circ}$, the highest and lowest phase voltages are, respectively, v_c and v_b, therefore the conducting diodes are D_5 and D_6. Assuming that the voltage drops across the conducting diodes are ideally zero, the rectified output voltage is given by the KVL:

$$V_{d1}(t) = v_c - v_b \tag{3.2}$$

with v_c and v_b having an amplitude of $\sqrt{2}V_s$ (V_s being the RMS value of the phase voltage) and a relative phase shift of 120°. Applying some trigonometric identities, the rectified voltage for $0 \leq \omega t \leq 30°$ can then be expressed as:

$$V_{d1}(t) = \sqrt{2}V_l \cos(\omega t) \tag{3.3}$$

with V_l the RMS line-to-line input voltage.

The same procedure is applied to the remaining intervals, yielding the rectified voltage waveform of $V_d(t)$ presented in fig12412

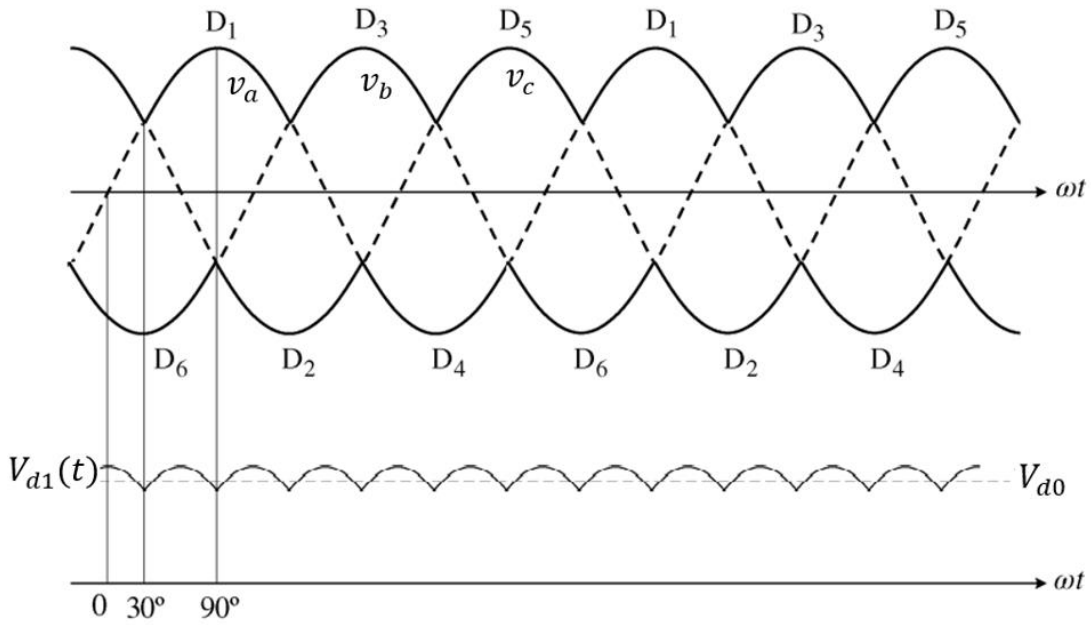

Figure 3.8: Input phase voltages and rectified voltage of the 6-pulse rectifier [38].

The theoretical average value V_{d0} of the rectified voltage is found by applying the mean value theorem for integrals to the function $V_{d1}(t)$, yielding:

$$V_{d0} \approx 1.35V_l \tag{3.4}$$

The exact same analysis is performed on the second 6-pulse diode bridge, with the only difference being that the sinusoidal input voltages of the delta-connected secondary are leading by 30° with respect to those of star-connected secondary (in the Yyd11 connection). As a result, the same 30° phase shift exists between the rectified output voltages of the two bridges, yielding the rectified output voltage waveform $V_d(t)$ shown in Figure 3.9 for the 12-pulse rectifier. In the parallel connection of the two 6-pulse bridges, the difference between the instantaneous

rectified output voltages of the two bridges must be applied to an inductor compensator as shown in Figure 3.7.

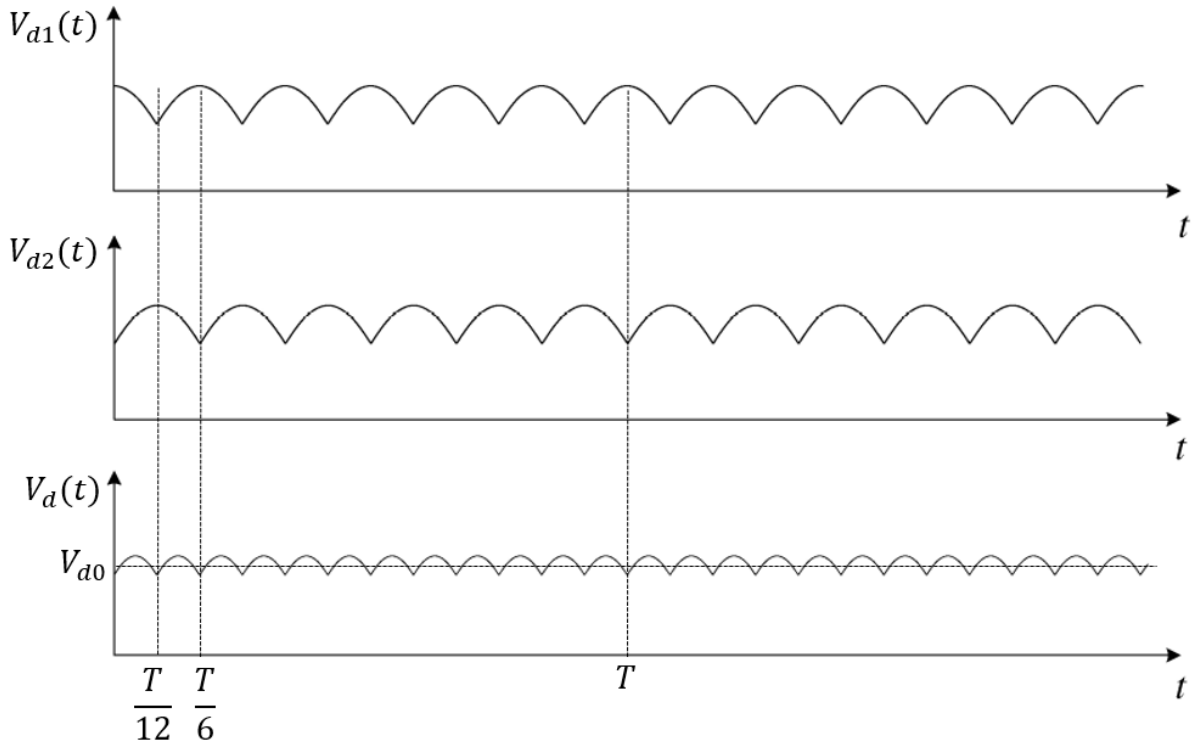

Figure 3.9: Rectified voltage waveform of the 12-pulse rectifier [38].

The use of a 12-pulse rectifier leads to a number of advantages in terms of smoother rectified output voltage characterized by lower ripple, as well as reduced harmonics both in the AC power supply and in the DC output side, reducing the filtering requirements of the system. The harmonics present in the three-phase currents of the transformer primary are of the order $kp + 1$, while the output voltage harmonics are of the order kp, with $k = 0, \pm1, \pm2, \pm3, \ldots$ and p the pulsation index of the rectifier (for the 12-pulse rectifier, $p = 12$) [38].

3.2.2.6. DC-side filter

A filtering system is installed between the rectifier terminals and the bipolar disconnector in order to block the rectified voltage harmonics and avoid disturbances in the telecommunication and signaling systems [40]. The filter is typically a passive L-C filter composed of an inductor connected in series to the positive busbar, and capacitor banks connected in parallel between the positive and the negative busbar. In the 3 kV DC ERS, the filter inductance value is typically 6 mH, while the capacitance is chosen based on the frequency of the dominant voltage harmonic (600 Hz when 12-pulse rectifiers are used to feed the catenary).

3.2.2.7. Bipolar disconnector

It allows the rectifier to be isolated from the rest of the power supply unit and can be activated manually or by means of an electromechanical servomotor.

3.2.2.8. High-speed circuit breaker

The high-speed circuit breaker is a key element for the safety of people and preservation of equipment both on land and on-board vehicles. Its task is to detect faults (on the lines and on the traction loads) due to current overloads and surges and to open the traction circuit in a matter of a few milliseconds. Such short opening times are necessary, given that, in direct current systems operating at multiple kilovolts, fault currents rapidly reach the short-circuit value and must therefore be limited as fast as possible. This problem is not as stringent in AC systems, where the interruption process takes place after the natural zero-crossing of the current. The breaker must also be able to extinguish the arc within two or three hundredths of a second. This action is carried out via electromagnetic blowout, whereby the electric arc is deflected and lengthened due to the Lorentz force created between the arc current and the magnetic field generated by the blowout chokes. In this way, the arc loses energy and eventually extinguishes. Most high-speed circuit breakers are equipped with devices that are able to detect whether the fault has been cleared or whether it persists. After verifying the absence of permanent faults, the device allows for the automatic reclosure of the breaker. The reclosing only allows one attempt, then the switch will remain open until the intervention of personnel.

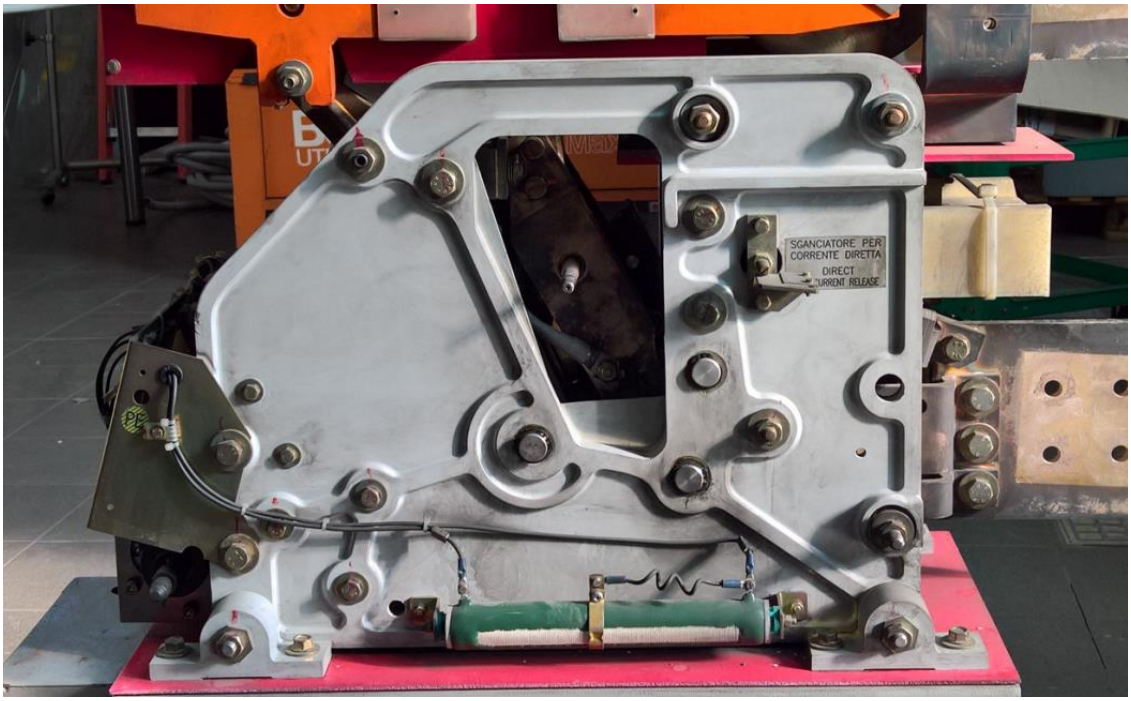

Figure 3.10: High-speed DC circuit breaker [38].

3.2.2.9. Horned disconnectors

Horned disconnectors are connected immediately downstream of the high-speed circuit breaker and the surge arrester and immediately before the contact line. In addition to these switches, known as first-row disconnectors, other devices known as second-row disconnectors are also installed, in order to ensure power supply continuity and to provide safe access for maintenance. In the event of a total substation outage, the second-row disconnectors close and supply the contact line via an adjacent substation. One of the main characteristics of the horned disconnectors is their ability to open the circuit even when current is flowing (albeit with limited intensity) and to extinguish the electric arc as it travels upwards between the dedicated horns.

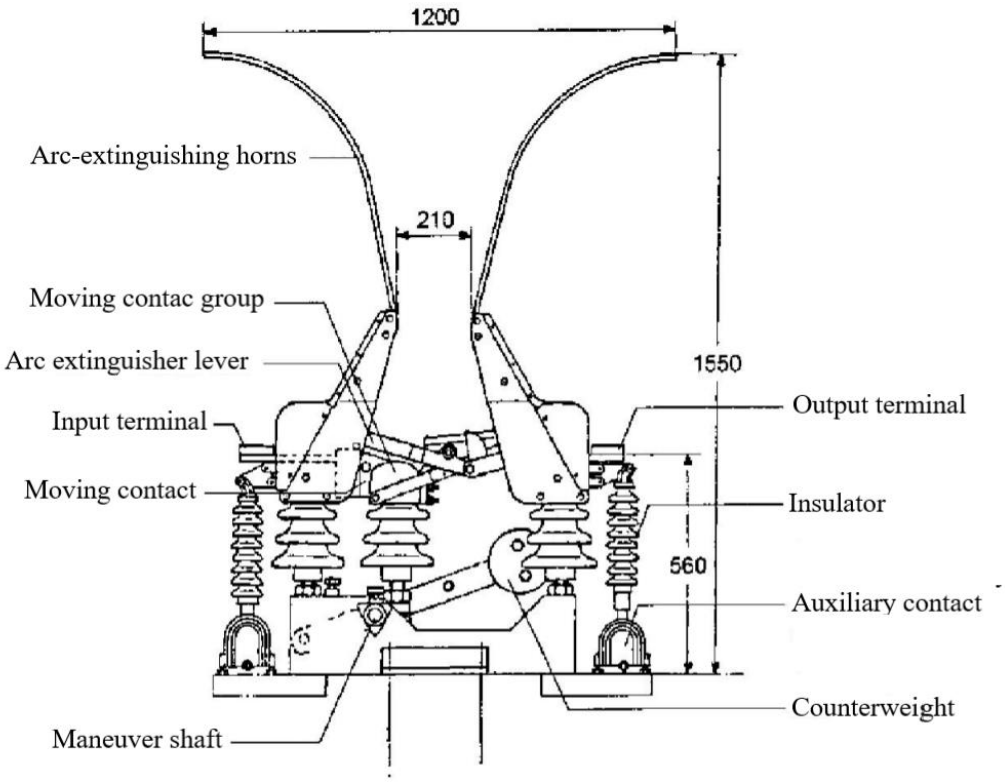

Figure 3.11: Diagram of a horned circuit breaker in the 3 kV DC section [40].

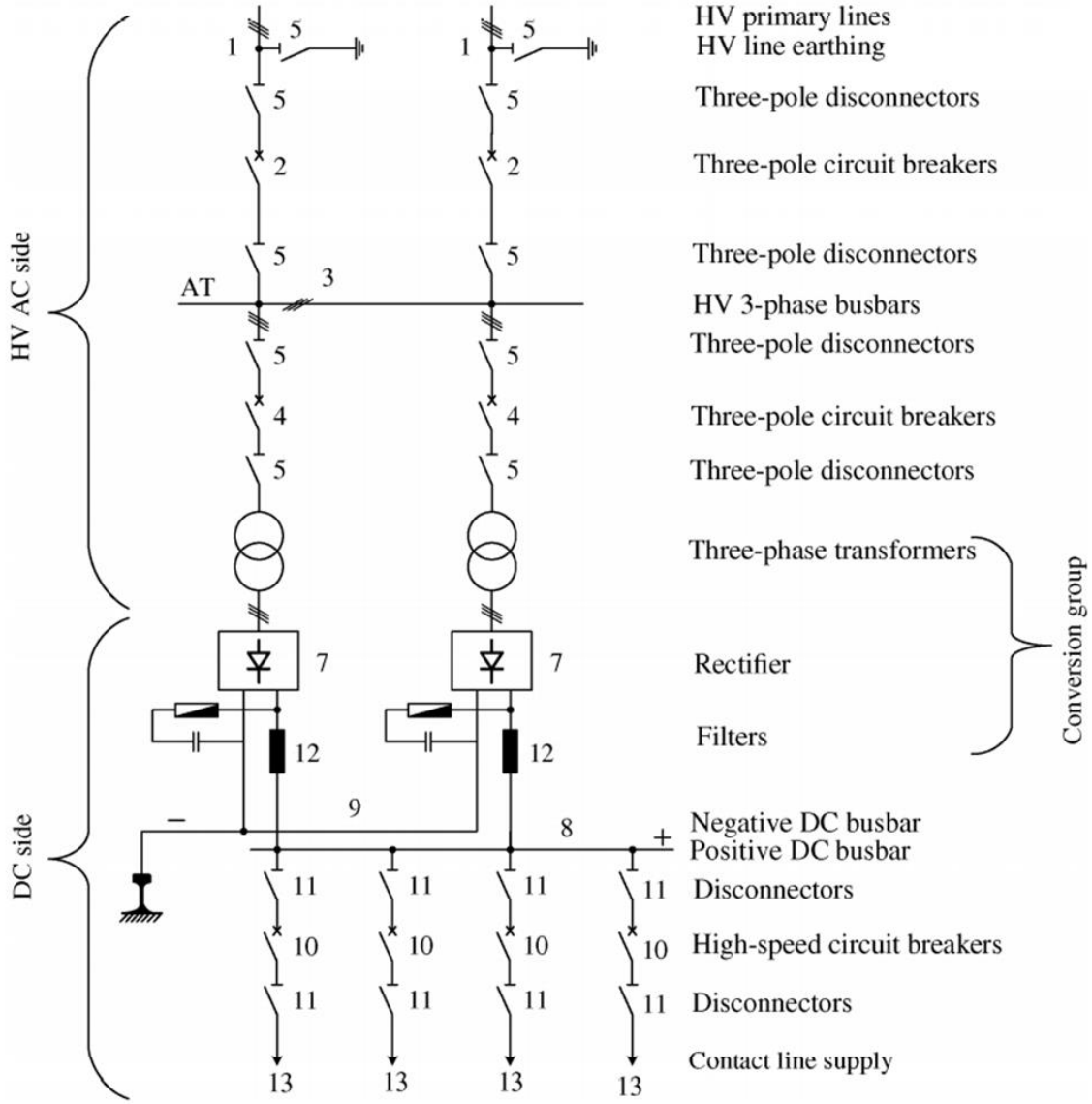

Figure 3.12: Connection diagram of a traction power substation [38].

3.2.3. The contact line

The solution adopted in the 3 kV DC electric railway system for the power supply of the traction loads is the overhead catenary, comprised of a contact wire that is opportunely suspended and fed bilaterally by adjacent substations. In essence, the contact line of each track constitutes an electrically continuous circuit, and, in the double track arrangement, the two contact lines are connected in parallel at the TPSS nodes.

3.2.3.1. Constructional aspects

In order to obtain regular current uptake and to avoid mechanical and electrical damage from the interaction between contact line and pantograph, an ideal contact line should have the following characteristics [38]:

- Maintain constant contact conductor(s) height, also during pantograph transit.
- The contact conductor(s) should run in a symmetrical zigzag path (known as *stagger*) above the track axis to avoid wearing a groove in the pantograph strip.
- Not be appreciably affected by any side wind.

In practice, the solution adopted to respect the abovementioned conditions consists of a top messenger wire that supports one or two contact wires by means of droppers, as illustrated in Figure 3.13 The messenger wire's maximum allowable deflection is in the order of 1 m, which is calculated starting from the suspension equation [38]:

$$y = \frac{mgx^2}{2T} \tag{3.5}$$

with y the deflection [m] at distance x [m] from the closest point of support, m the linear mass [kg/m] of the wire, g the gravitational acceleration [m/s^2], and T the axial tension [N] applied to the wire. The maximum deflection is then found at distance $x = l/2$ between two consecutive support points, yielding:

$$y_{max} = \frac{mgl^2}{8T} \tag{3.6}$$

The span between consecutive support masts for the suspension of the catenary system is typically between 50 and 60 m [38], and the length and spacing of the droppers are calculated so that the contact wire(s) are horizontal with respect to the track level. To counteract the effects of expansion/contraction of the catenary

conductors due to seasonal temperature excursions (on average between -15°C and 45°C), counterweight systems of masses and pulleys are implemented which allow the necessary longitudinal sliding of the conductors without altering their deflection.

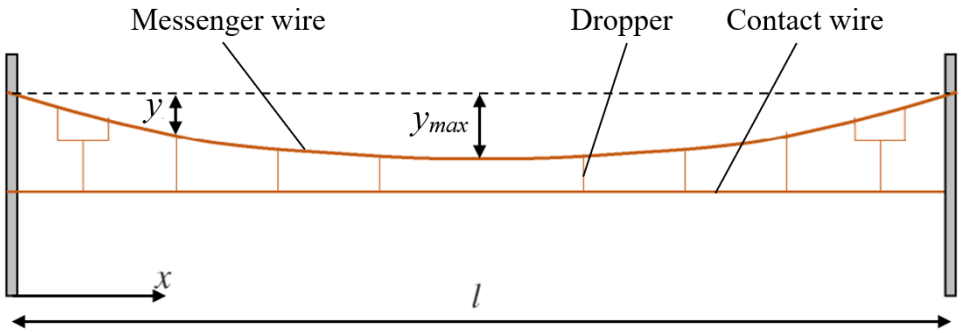

Figure 3.13: Deflection of the messenger wire [37].

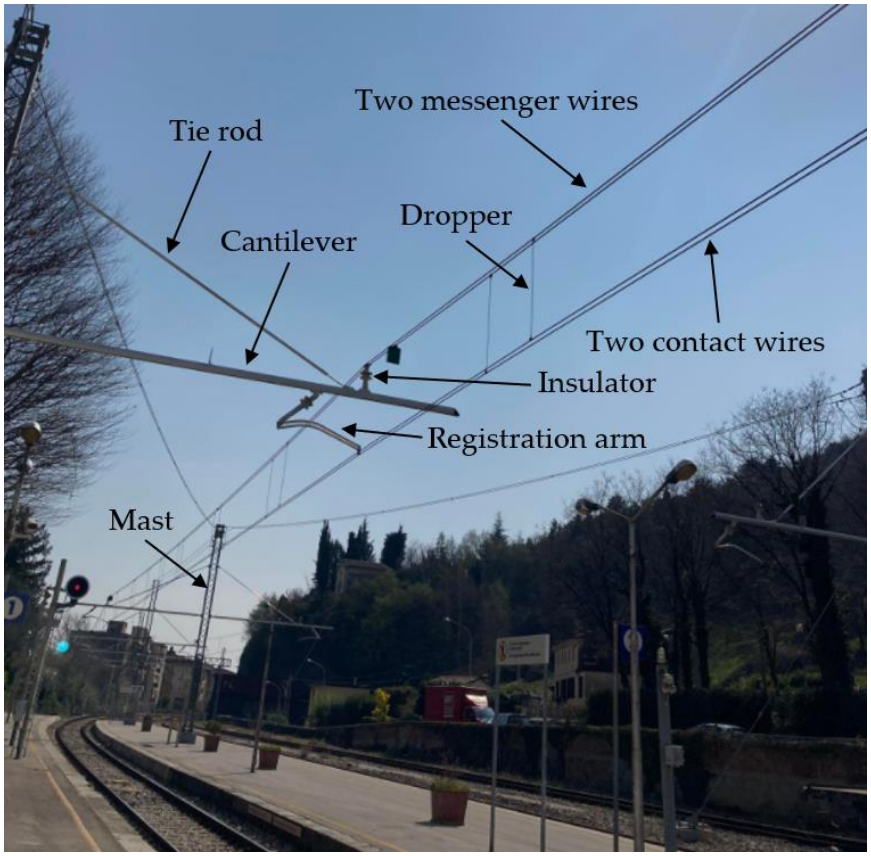

Figure 3.14: 3 kV DC catenary with two messenger wires and two contact wires, Vittorio Veneto railway station.

The staggering of the contact line is obtained by suitable arms and tie-rods that position the wire alternately at ±20 cm with respect to the track's axis [38] (as highlighted in red in Figure 3.15), so that the contact wire spans the pantograph contact strip length (40 cm) to allow even wear of the pantograph's contact strip during transit. The contact wires are grooved to be fixed with the droppers, as shown in Figure 3.15.

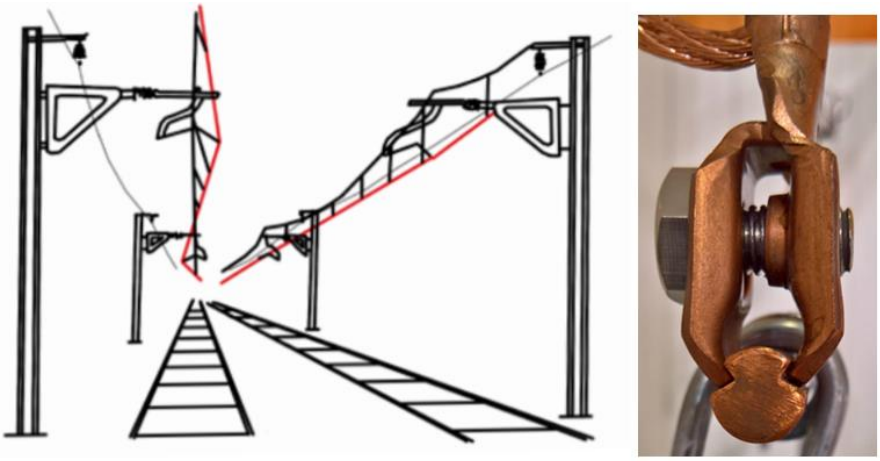

Figure 3.15: Contact wire staggering and grooved contact wire [44], [37].

Continuity bypasses are installed every 120÷180 m [38] to ensure electrical continuity between the messenger wire and the contact wire, which is essential as both conductors participate in transporting the current absorbed by the pantograph from the contact line.

3.2.3.2. Mechanical and electrical specifications

The specific characteristics of the overhead catenary are the result of design considerations regarding the system's structural requirements and power demands, which are dictated by railway traffic intensity, train transit speed, and the altimetric profile of the railway line (for instance, the current absorption of traction loads increases considerably along routes with steep slopes [38]). Different characteristics of standard overhead catenary systems implemented in 3 kV DC railway lines are reported in table 298124 [38]. In this regard, studies are underway to define the characteristics of new contact lines to achieve current uptake quality that is compatible with modern high-speed lines.

Characteristics of railway lines		Contact line	Messenger wires			Contact wires		
Maximum speed (km/h)	Intensity of traffic	Copper wire section (mm^2)	Number	Section (mm^2)	Mechanical tension (N)	Number	Section (mm^2)	Mechanical tension (N)
200	Low	320	1	120	1375	2	100	1000
200	Mean	440	2	120	1125	2	100	1000
200	High	610	2	155	1000	2	150	1125
250	Mean	540	2	120	1500	2	150	1875
250	High	610	2	155	1625	2	150	1875

Figure 3.16: Standard 3 kV DC contact lines [38].

The voltage at the contact line can vary considerably. According to the regulations prescribed by the European Committee for Electrotechnical Standardization (CENELEC) for the 3 kV DC electric railway system, contact line voltage drops must be contained between +20% and -33% of the nominal voltage. If the voltage at the pantograph drops below 2000 V due to line overloads, measures are usually taken to limit railway traffic. Countermeasures to prevent excessive voltage drops include reinforcing the contact line to increase its cross section, or utilizing a feeder, supported by existing infrastructure, in parallel to the contact line. The operational limits as according to EN 50163 for the 3 kV DC electric railway system are listed in Table 3.3: Standards for the 3 kV DC electric railway according to EN 50163.

Table 3.3: Standards for the 3 kV DC electric railway according to EN 50163.

Nominal voltage	3000 V
Lowest permanent voltage	2000 V
Highest permanent voltage	3600 V
Highest non-permanent voltage (max. duration 5 minutes)	3900 V
Highest non-permanent voltage (max. duration 20 ms)	5075 V

4 The DC Railway microgrid concept

The structure of DC electric railway systems makes them highly suitable for the possibility to integrate smart-grid features, in the form of distributed energy resources (most notably photovoltaics, wind generators, and energy storage systems) in the power supply network, as well as high-capacity regenerative braking energy utilization.

The key advantage of integrating distributed energy resources in the power supply of DC railway networks is the fact that most distributed energy resources are based on DC systems (such as photovoltaics and energy storage systems), or have an internal DC section (wind generators), and can therefore be conveniently connected in parallel to a common DC link that collects the electricity produced by the distributed generators and the braking trains, effectively acting as an energy hub for the DC railway microgrid. In this way, in addition to supplying the trains, the DC railway microgrid can be used to supply other loads such as charging infrastructure for electric vehicles (EVs), substation internal loads, or even supply excess power to the grid by means of reversible substations [1]. Thus, DC railway microgrids have clear advantages in terms of [1]:

- energy savings
- optimized power flow
- increased power quality
- efficiency.

Based on the current and developing structures of DC railway systems, two main topologies can be studied, depending on voltage and power levels, namely, the low-voltage and the medium-voltage topologies.

4.1. Low-voltage DC railway microgrids

The traditional low-voltage DC railway microgrids (LV DRMGs) are characterized by voltage levels in the range of 600÷1500 V and are commonly used in low power demand lines including urban rail, trams, light rail, and subways, and over short/medium distances [1]. For medium-power urban railways, the voltage is up to 3000 V in some countries [1]. The key functional advantage of these systems is

their capability to utilize regenerative braking energy, leading to energy savings in the range of 20÷40% [1]. As outlined in Section 3.2.2, most AC-DC substations supplying DC railway systems are currently based on traditional rectifiers and therefore allow unidirectional flow of power, meaning that the power injected from a braking train can only be utilized to supply a nearby train, and cannot be fed back to the main grid. In the absence of a nearby train, the excess energy is dissipated in on-board rheostats to prevent overvoltage in the contact line. In this regard, the DC railway microgrid concept includes the possibility for bidirectional power flow in the AC-DC substations by implementing IGBT-based converters in the substations, maintaining the advantages in terms of balanced current absorption from the AC network [1]. Other advantages of the LVDC microgrid substation configuration are [1]:

- bilateral power supply of trains
- regulation of the DC voltage
- protection of the DC side
- provision of ancillary services to the mains.

DC networks are distinguished by their capability for good power flow and distribution among the various loads, and are thus suited for configurations consisting of a DC busbar acting as an energy hub. The DC busbar acting as an energy hub can be established in two different characteristic positions [1]:

- at the substation level: this is the simplest solution, allowing some protection devices and infrastructure already existing in the substation to be shared and utilized for the installation of distributed energy resources. In addition, the proximity to the mains favors the bidirectional power exchange [1].
- Along the railway line: this solution is more complicated, but allows greater utilization of pre-existing infrastructure in strategic points, such as nearby parking areas or rail freight intermodal terminals, for the installation of distributed energy resources and charging infrastructure [1].

4.1.1. Main components

AC-DC substations. The AC-DC conversion substation is the element that interfaces the AC mains to the DC section. Its main functions are the AC-DC conversion and the bidirectional exchange of power between the AC and DC side (reversible substations). Traditional substations can be conveniently adapted to the reversible configuration by implementing inverter-based converters in parallel with the already installed diode-based rectifiers, thus avoiding additional costs related to redesigning substations [1].

Catenary/Third rail systems. The catenary supplies electrical power to the trains through their pantographs. This solution is mainly implemented in electric railway systems having a voltage level of 1500÷3000 V [1]. For lower voltage levels (600-750 V), the trains are supplied via the third rail system, whereby the current is collected by means of sliding contacts between slippers installed on the trains and a fixed rail alongside the track that is connected to the positive terminal of the substation (the current return path is normally through the running rails [38]). Both catenary and third rail can accommodate other stationary elements lineside, such as renewable generators and charging infrastructure. This would require some modifications to the traditional configurations, especially regarding switching devices and protection relays [1].

Renewable generators. the renewable generators that can be connected to the LVDC hub are in the category of low power generators: these include small-scale PV plants and low-power wind generators integrated with lineside buildings and terrain [1]. Such low power renewable generators are suitable to be directly connected to the LVDC hub without an intermediate voltage level [1]. This solution could also be implemented to supply substations in areas where the grid connection is not available [1].

Energy storage systems. High density energy storage systems (ESSs) based on supercapacitors, flywheels, and batteries can store the excess energy produced by the renewable generators and braking trains, in a very short time (a few seconds [1]). The ESSs in DC railway microgrids can be categorized into three types [1]:

- On-board ESS: implemented inside or on the roof of trains. The proximity to the electric motors favors regenerative braking energy savings, but the high weight of on-board ESSs increases the power consumption, decreases the speed and offsets any gains in efficiency [1].
- Off-board ESS: commonly installed at the substation level, they provide good energy savings (similarly to on-board ESSs), with added functional advantages such as supplying the auxiliary and internal loads of substations (lighting, air conditioning, escalators, etc.).
- Wayside ESS: installed along the railway lines, their main advantages are the capabilities to regulate catenary/third rail voltage and compensating the voltage drops [1]. However, the greater distance from the substation increases the power losses. Other drawbacks are related to higher costs and difficulty of implementation in crowded cities [1].

EV charging infrastructure. An outstanding and ingenious feature of DC railway microgrids is the integration of charging infrastructures for EVs in the DC section [1]. This solution offers the advantages of direct exploitation of the integrated renewable energy sources and regenerative braking energy, minimizing the impact

on the AC power grid, while also promoting sustainable mobility [1]. The power level of LVDC railway microgrids is suitable for mid- and fast-charging systems (respectively: up to 25 kW with charging times of 1-2 hours, and up to 150 kW with charging times of less than half an hour). Higher power solutions known as megachargers and ultrafast charging systems are better suited for medium voltage DC railway microgrids [1]). The charging infrastructures commonly used today in LVDC railway systems are equipped with Combo and/or Chademo plugs that are able to charge most of today's EVs and all of the upcoming ones [1], and must be able to charge vehicles equipped with batteries up to 1 kV [1].

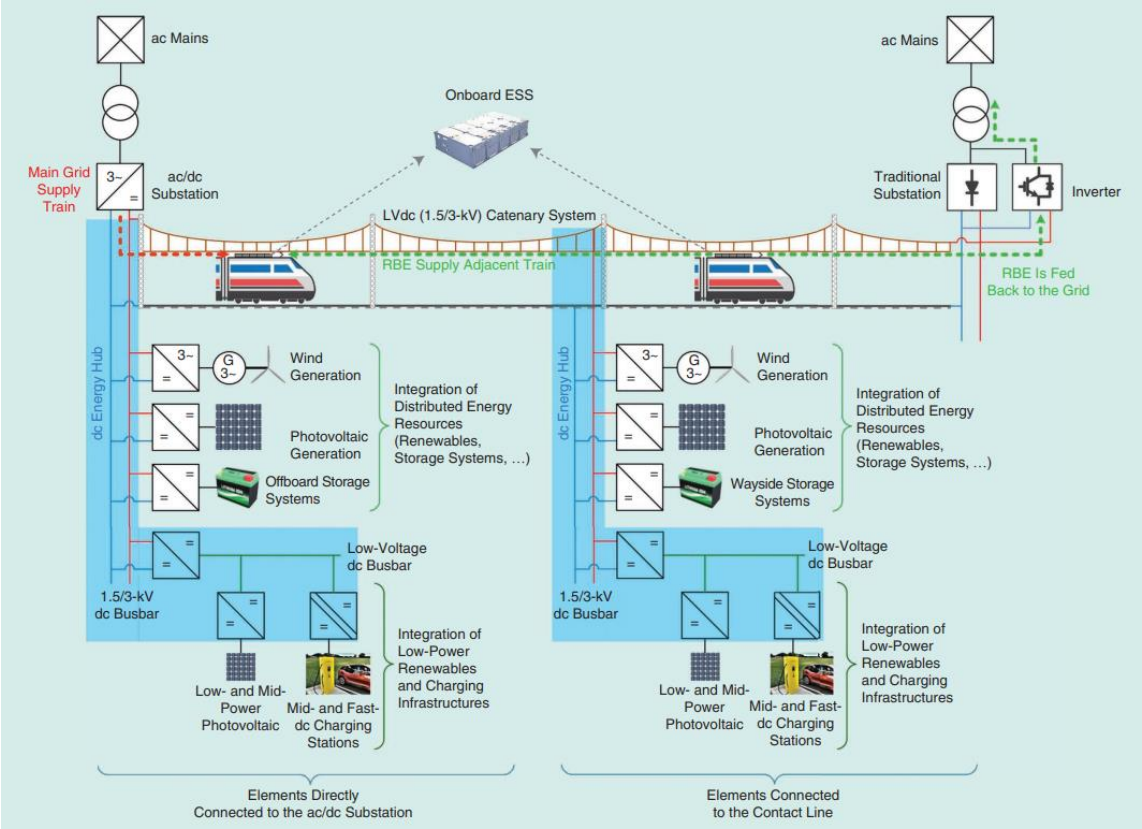

Figure 4.1: The LVDC railway microgrid concept [1].

4.2. Medium-voltage DC railway microgrids

The high currents associated with the low voltage level in LVDC systems pose limits on train power and railway traffic. At present, high-voltage, single-phase AC (HVAC) railway systems are used to service high-power suburban and high-speed trains. However, HVAC systems are particularly susceptible to power quality issues such as inductive voltage drop, low power factor, current/voltage imbalance, and harmonics [1]. Therefore, the substations in HVAC electric railway systems must be

equipped with additional devices to compensate these issues. Moreover, to limit the power unbalance in the AC mains, single-phase AC electric railway systems must be supplied via phase rotation from the AC mains, whereby each of the three phases supply the separate sections of the contact line in an alternate fashion. This makes it necessary to employ a neutral wire between sections of the contact line that are supplied by different phases, introducing problems related to electric arching upon contact with the pantograph, and slowing down of the trains. Finally, additional drawbacks and complexities of AC railway system include the need for expensive power installations, autotransformers, and multi-winding catenary overhead systems [1].

New MVDC electrification systems have been studied and proposed as a solution that would avoid some of the problems related to AC railway networks while still retaining high power capability, leading to dramatic improvements and significant potential for future developments [1]. The high power level of MVDC ERSs makes them suitable for direct connection to distributed energy resources, such as wide-scale wind farms and photovoltaics, without any conversion stage to AC [1]. Furthermore, MVDC systems are suitable for the integration of fast and ultrafast charging stations for EVs, that would otherwise not be supported by the AC mains [1]. The appropriate voltage range for MVDC ERSs has been estimated to be 7.5-24 kV based on comparison criteria with AC ERSs and through evaluation of existing infrastructure and geographic properties [1].

4.2.1. Additional features

Considering the power level and the features of MVDC railway microgrids, the concept of the DC energy hub becomes all the more relevant. The proposed structure of the MVDC railway microgrid is analogous to that of the LV one, albeit at a higher power level, including reversible substations in the power supply of the DC catenary for bidirectional power exchange, as well as distributed renewable generators and ultrafast charging stations for EVs, all rated over 500 kW and fed by the MVDC busbar hub [1]. Alternatively, the MVDC busbar can be connected to a large number of low-power devices such as small PV generators and mid- and fast-charging stations by means of dedicated DC-DC converters that provide the appropriate DC voltage level. The latter solution is cheaper, and the required devices are widely available [1]. In some proposed solutions, the MVDC system could serve as a power supply for LVDC railway subsystems through dedicated DC-DC converters. Compared to the LVDC systems, the MVDC network includes the following additional components:

- **High-power renewable generators.** The voltage level of MVDC systems would be suitable for direct connection of wide-scale PV and wind farms by means of high-power converters.
- **Ultrafast charging systems for EVs.** The high-power capabilities of MVDC systems allows for the direct connection of advanced charging systems, with power ratings up to 350-500 kW and charging time in the order of 10 mins. Moreover, the disturbances caused by charging infrastructure on the AC mains would be reduced thanks to the power supplied by renewable generators and regenerative braking recovery systems. At present, temporary charging systems based on contact bars feeding pantographs are implemented to provide occasional short charge for electric busses and trucks to extend their range during service [1]. These systems are able to handle up to 750 kW of charging power due to the high currents that can be tolerated by the pantograph and contact bars [1], making them promising candidates for power supply from MVDC railway microgrids. The installation of advanced charging systems in proximity to train stations promotes the use of public transport and sustainable, intermodal mobility. Furthermore, the progress made by the main vehicle manufacturers towards the introduction of full-electric trucks and tractor trailers, equipped with [1] MWh on-board batteries, introduces the necessity for ultra-high-power charging infrastructures with power ratings in the order of 1-3 MW [1], which would cause significant perturbations in the AC mains and would therefore have to be integrated into MVDC railway microgrids to smoothen the power consumption.

The MVDC railway microgrid concept combines the superiorities of traditional AC and DC ERSs. The main challenges to be solved before these systems can be developed and implemented in practical applications are related to energy management and control, high cost of power electronics and power modules, and the development of dedicaed DC switching and protection devices [1].

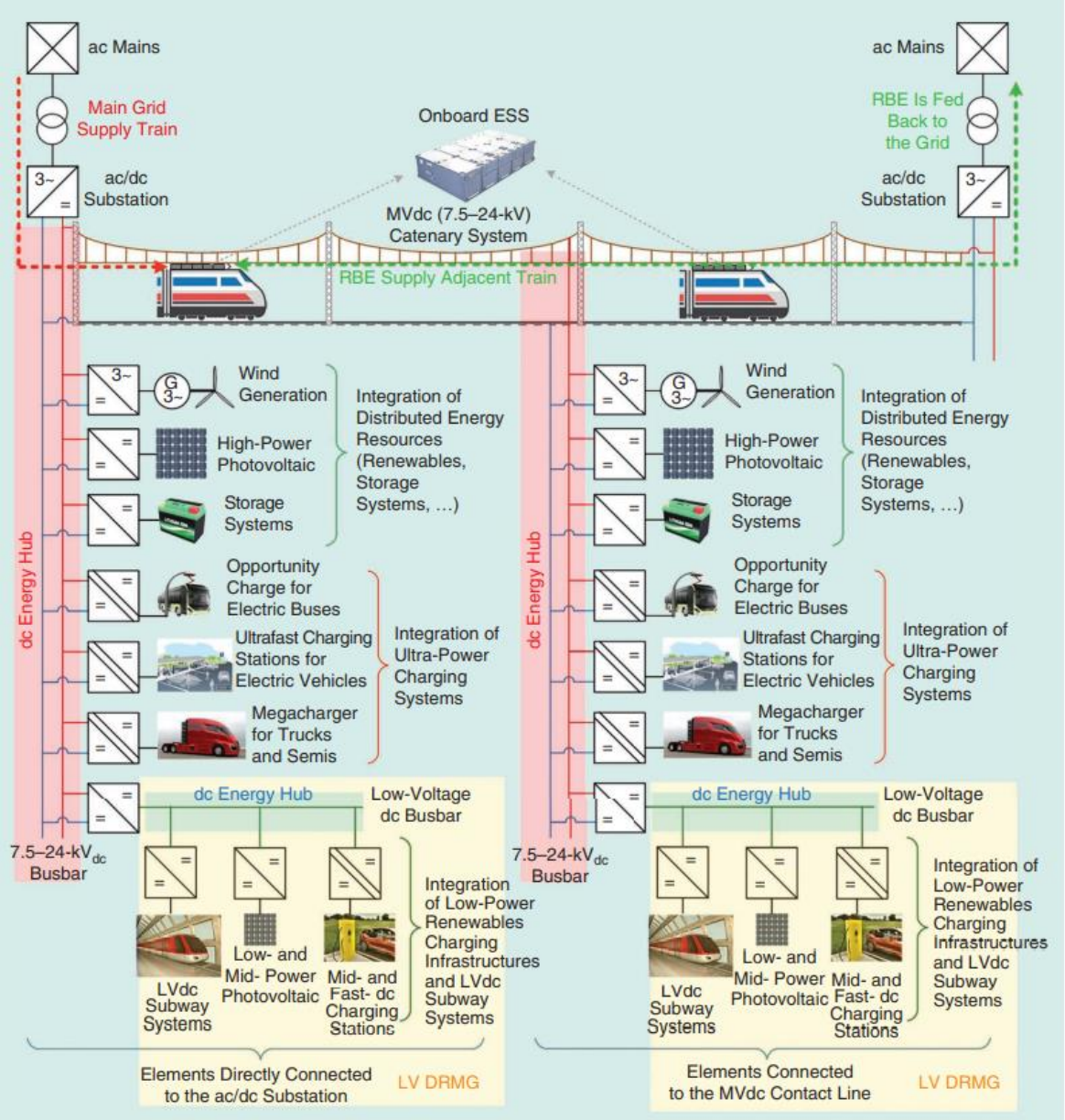

Figure 4.2: The MVDC railway microgrid concept [1].

4.3. Considerations regarding AC railway microgrids

AC electric railway systems are an established technology for the electrification of suburban and high-speed railways. However, unlike for DC ERSs, the "smartization" of AC ERSs through the integration of distributed energy resources, energy storage systems, regenerative braking energy recovery, etc. is significantly more challenging, due to the following limitations:

- Exploitation of regenerative braking energy between trains is impeded by the isolated sections (however, it is still possible to inject RBE into the main grid)
- Power quality issues due to declining system inertia, resulting from power peaks created by renewable generators and trains [1].

The AC ERSs currently implemented for suburban and high-speed rail are supplied by the main grid through traction substations that provide single-phase 25 kV-50 Hz voltage to the AC catenary. The absorption of significant amounts of single-phase power from the AC mains creates power quality issues related to voltage imbalances [1]. To mitigate the perturbations on the AC mains, it is required that the traction substations be connected to points of the high voltage network (>132 kV) with high short-circuit power [1], leading to higher system complexity and costs. Additional problems affecting AC ERSs supply include high levels of reactive power due to inductive elements, and harmonic problems such as harmonic resonances, low-frequency oscillations and harmonic instabilities [1]. The direct connection of smart grid technologies in AC railway microgrids tends to intensify the aforementioned problems [1].

4.3.1. General architecture

The concept of AC railway microgrids (ARMGs) is based on the integration of distributed energy resources and energy storage systems via in a common AC link that collects the electricity produced by generators and braking trains and acts as an energy hub for trains, substation internal loads, charging infrastructures for EVs, or feedback to the AC mains [1]. The distributed renewable generators such as PV installations and other elements are interfaced with the AC link by means of DC-AC converters [1]. The proposed structure of AC railway microgrids includes traction transformer-based substations, capable of RBE feedback to the main grid, that supply each section of the overhead catenary according to phase rotation every 20-40 km (depending on the autotransformer used). The different sections are mutually isolated by means of neutral wire. In addition, the AC busbar in the form of energy hub is used to supply the system in two different characteristic positions:

- At the substation level: this is the preferred solution due to the availability of switching and protection devices and substation infrastructure for the installation of distributed energy resources, as well as greater power transfer due to the proximity of the main grid [1]. This solution has been implemented for the installation of a PV system on the roof of a high-speed traction substation in Japan [1].
- Along the railway line: the installation is more complicated, but offers more space and infrastructure for the installation and connection of distributed

energy resources as well as charging systems for EVs in strategic points, such as parking areas close to railway stations or rail freight intermodal terminals [1].

Due to the aforementioned power quality issues in AC systems and their sensitivity to switching frequencies of DC-AC converters associated with the integration of smart grid features, the power flow capability of AC railway microgrids is inherently limited [1]. Therefore, the appropriate renewable generators for the connection to the AC hub are of the low-power category [1]. As for energy storage systems, AC railway microgrids can be equipped with high density ESSs based on supercapacitors, flywheels, and batteries, that can be installed on-board, off-board, or wayside (this last type can be implemented to regulate catenary voltage drops, but comes with higher power losses in the inductive lines and higher cost of installation in crowded areas [1]).

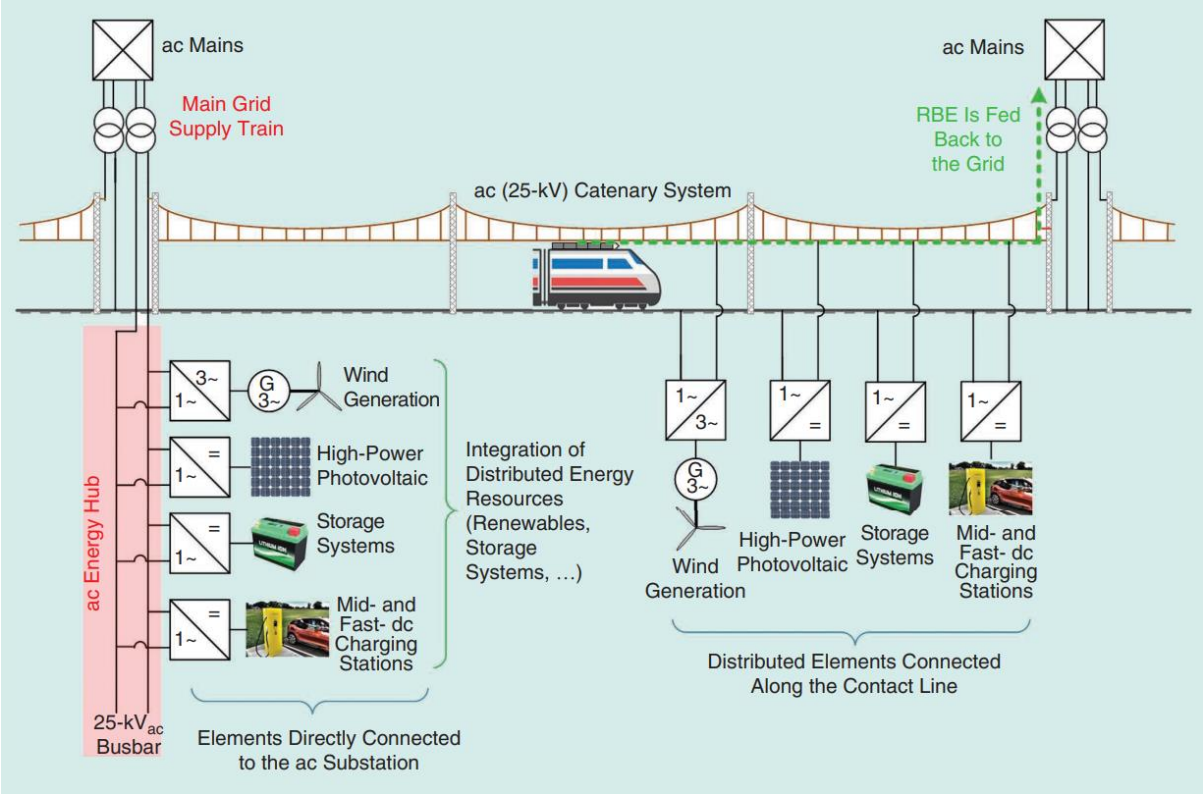

Figure 4.3: The AC railway microgrid concept [1].

4.4. Hybrid railway microgrids

The restrictions on power quality and the limited power flow capabilities of AC railway microgrids have led to the proposition of hybrid solutions consisting of a DC bus at the interface between smart grid elements (distributed generators, energy storage systems, EV charging stations, etc.) and the traction substation that supplies an overhead AC catenary, improving the performance and capabilities of the system. Depending on design priorities, hybrid railway system architecture can be subdivided into three main configurations outlined in the following.

4.4.1. Interfacing converter-based hybrid AC railway microgrid

In this configuration, an MVDC busbar is interfaced with the traction substation and the AC overhead catenary by means of current/voltage controlled smart interfacing converters (IFCs) that perform bidirectional power flow control between AC and DC buses. The MVDC busbar, in the form of an energy hub powered by high-power distributed energy resources, contributes to the power supply of the overhead catenary, or feeds excess power back to the main grid, effectively boosting the power capabilities of the system. Other features, such as high-power EV charging infrastructures, ESSs, and even a LVDC energy hub, can be connected to the MVDC busbar, reducing the impact on the AC mains. However, under heavy load conditions with most elements operating at their full rating, the appropriate control of IFCs to mitigate power quality issues becomes challenging [1].

4.4.2. Railway power flow controller-based hybrid AC railway microgrid

In this solution, the traction substations are equipped with railway power flow controllers (RPFCs) to improve on the power quality mitigation capabilities of hybrid AC railway microgrids. The RPFCs are composed of a back-to-back converter with a shared DC link capacitor and two single-phase step-down transformers connected to the right and left sections of the traction substation [1]. The RPFC also has a third port, at the common DC link, that connects to an LVDC busbar energy hub. In this configuration, the power from the DC energy hub contributes to the supply of the AC catenary, or is fed back to the AC mains, through the RPFC. Moreover, the RPFC allows regenerative braking energy exchange between adjacent sections to supply motoring trains [1]. A drawback of this solution is the lower capacity of the RPFC's common DC link [1]. As a result, the DC bus connected to the RPFC is of the LV category, supplied by low- and mid-power distributed generators and connecting to mid- and fast- DC charging stations and ESSs. The power flow level can be enhanced by adopting high-cost multilevel

RPFCs [1]. Since RPFC technologies are suitable to be installed at the substation level rather than lineside, some of the problems related to neutral sections are still present [1].

4.4.3. Co-phase hybrid AC railway microgrid

The aforementioned IFC-based solution and RPFC-based solution still face the problems of having two adjacent single-phase sections separated by neutral wire, which is detrimental to train speed and power transfer between sections. To alleviate these problems, which are especially inconvenient in high-speed and heavy-load rail, the co-phase traction supply system has been introduced in 2009, and a 10 MVA co-phase power supply device was installed for the first time in 2012 at the Mei Shan substation in China [41]. In the co-phase traction power supply system, a special traction transformer (such as YNvd, Scott, Leblanc, or impedance matching transformer) is used to draw power from all three phases of the AC mains and feed a two-phase system on the secondary side. One of the secondary phases is directly connected to the traction network, while the other phase is connected to an active power quality conditioner (APQC), constituted by a single-phase back-to-back converter, that contributes to supply the traction load whilst performing active power balancing, reactive power compensation, and harmonic filtering [42]. In this way, the need for phase rotation and the associated neutral sections are avoided, improving traction performance. In addition, the capacity utilization of the traction transformer is increased [42].

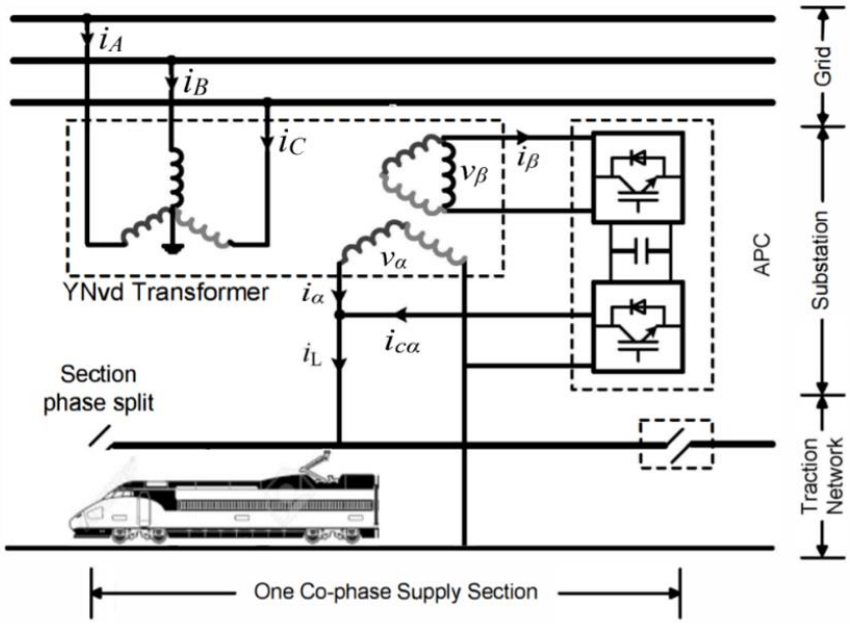

Figure 4.4: Co-phase power supply through YNvd transformer [42].

As an example, the co-phase power supply through YNvd transformer and active power quality conditioner is presented in Figure 4.4. The secondary phases given by the v-connected and the open delta-connected secondaries create a two-phase system of mutually independent voltages having equal magnitude and a relative phase shift of 90° [43], as indicated in the phasor diagram (phasors $\bar{V}_\alpha$ and $\bar{V}_\beta$) in Figure 4.5. One of the two secondary phases is directly connected to the traction circuit, while the other feeds the APQC. More details on this project are presented in [42].

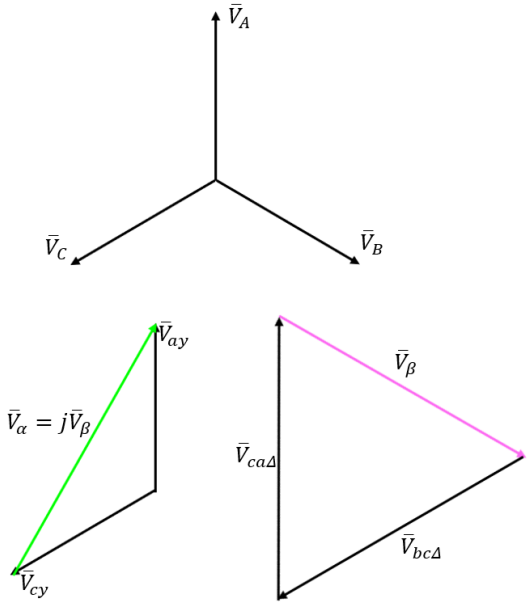

Figure 4.5: Phasor diagram of the YNvd transformer.

5 Modeling of the traction circuit and the traction load

With the ultimate objective to simulate the electrical power exchange within the 3 kV DC railway network due to the presence of traction loads in various modes of operation, the train is initially modeled using theoretical formulas and empirical results in the domain of railway traction mechanics. The electrical model is then implemented, building on the results provided by the mechanical model, to obtain the electrical power and current absorbed by the train (or injected, when regenerative braking is implemented) and the voltage profile at the pantograph, as well as the relevant electrical parameters of the traction circuit. The train considered as the traction load in the simulations is the Italian Frecciarossa 1000, described in the following.

5.1. Introduction of the Frecciarossa 1000

In the 2000s, the Italian state railways (*Ferrovie dello Stato*, *FS*) became increasingly interested in upgrading and expanding their train fleet in order to satisfy the growing demand for mobility, driven by the increasing number of passengers. A further objective was to become more competitive in the Italian and European high-speed markets [45]. To this end, the Frecciarossa 1000 train, also known as the ETR1000 (*ElettroTreno Rapido*) was developed and introduced by the AnsaldoBreda-Bombardier joint venture starting in 2008, on commission by FS. In the early 2010s, the project was first unveiled to the public and prototype testing began. In June 2015, the Frecciarossa 1000 officially entered commercial service in Italy. To date, the ETR1000 fleet is comprised of 50 convoys that are operational along the Turin-Milan-Florence-Rome-Naples corridor [46]. On February 26, 2016, the ETR1000 attained a peak velocity of 393.8 km/h while traversing the Torino-Milano high speed line, establishing the Italian high-speed record [47].

5.2. Technical features of the ETR1000

The new generation, very-high-speed ETR1000 is configured as an electrical multiple unit (EMU) comprised of 8 light aluminum alloy cars, for a total empty weight of 454 tons, and a length of 202 meters. Each car has two bogies, with two wheelsets per bogie, for a total of 16 bogies and 32 wheelsets. Unlike its predecessor, the heavier ETR500, which concentrates the traction power into two E.404 locomotives, the ETR1000 features distributed traction among 16 asynchronous three-phase motors mounted on 8 of the 16 bogies [48], for a total (rated) traction power of 9800 kW under 25 kV AC power supply and 6900 kW under 3 kV DC power supply [49], ensuring passenger comfort and overall enhanced dynamic performance, with an acceleration of 0.7 m/s^2 and a top design speed of 400 km/h. In addition, the ETR1000 is equipped with a multi-voltage system conforming to the European Technical Specifications for Interoperability (TSI), allowing for commercial operation across European borders having different electrification and signaling systems. Other features include the possibility to couple two trainsets to double the payload and improve energy savings [50]. More detailed technical specifications of the ETR1000 are presented in Table 5.1, Figure 5.1, and Table 5.2 [45], [51], [52], [50]:

Table 5.1: Features of the ETR1000 cars.

Wagon type	**Features**
DM	Driver's cab, converter, brake resistors, 4 motors (one per wheelset)
TT	Transformer, 3 kV DC, 1.5 kV DC pantograph
M	Converter, brake resistors, 4 motors (one per wheelset)
T	25 kV 50 Hz AC, 15 kV 16 and 2/3 Hz AC pantograph, batteries

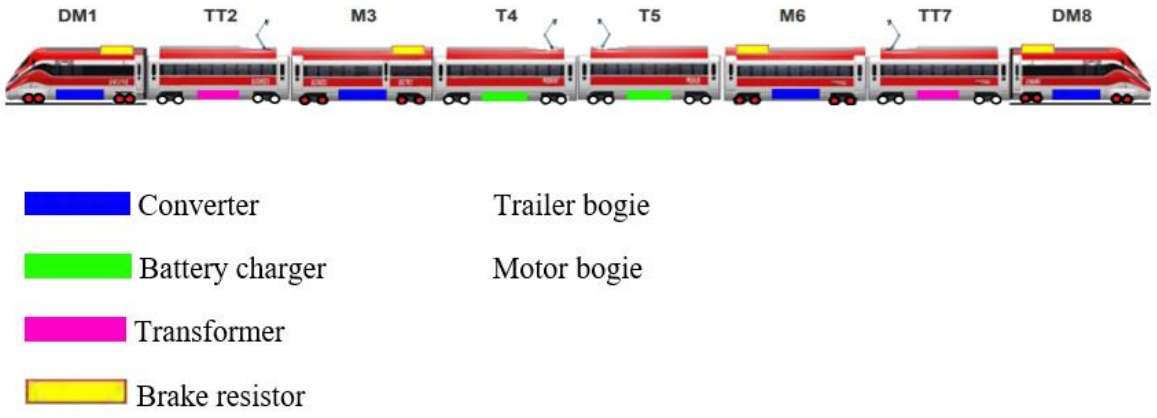

Figure 5.1: Car formation of the ETR1000

Table 5.2: Technical data of the ETR1000.

Nominal power at the wheels	AC: 9.8 MW DC: 6.9 MW
Power supply network	AC: 25 kV 50 Hz, 15 kV 16 and 2/3 Hz DC: 3kV, 1.5 kV
Traction motors	16 three-phase asynchronous motors controlled via water-cooled IGBT converters
Traction chain overall efficiency	25 kV AC: 0.851 3 kV DC: 0.842
Maximum operational speed	3 kV DC: 300 km/h 25 kV AC: 360 km/h
Maximum design speed	400 km/h
Current collection method	4 ATR95 pantographs, from overhead catenary, depending on the network voltage

Acceleration	0.7 m/s
Deceleration	1.2 m/s
Braking system	Regenerative, dynamic, electro-pneumatic
Power at the wheels in electric braking	5.60 MW
Formation	8 cars
UIC classification	$B_0'B_0'+2'2'+B_0'B_0'+2'2'+2'2'+B_0'B_0'+2'2'+B_0'B_0'$
Total number of wheelsets	32
Number of motorized wheelsets	16
Length	202 m
Height, Width	4080 mm, 2924 mm
Wheel diameter	920 mm
Track gauge	1435 mm
Mass, empty	454 t
Mass, loaded	501 t
Passenger capacity	457
Recyclable materials	94%
Noise	<91 dB at 25 m at 300 km/h

Figure 5.2: The Frecciarossa 1000 [50].

5.3. Mechanical model and vehicle dynamics

In this section, the mechanical model of the train is developed through the mechanical characteristics and parameters (provided by manufacturer data or otherwise calculated by means of empirical and theoretical formulas) of the traction vehicle and of the track, in order to represent the longitudinal dynamics of the vehicle (speed, position and acceleration profiles) and the mechanical power at play. During all stages of the train's journey, the mechanical model also accounts for the train's technical constraints on power, speed, tractive and braking efforts, adhesion limits between wheel and track, and acceleration/deceleration chosen for passenger comfort. The mechanical model is developed under the simplifying hypothesis that the train is considered as a material point of equivalent mass m_e undergoing rectilinear and unidirectional motion. The traction, braking, and resistance forces acting on the train cause an acceleration that is considered positive along the same direction as the vehicle's velocity vector, and negative (deceleration) in the opposite direction.

5.3.1. Equivalent mass

To investigate the behavior of the vehicle and to represents its longitudinal dynamics, it is necessary to consider the train's equivalent mass, which accounts not only for the train's static mass, but also for the inertial effects of the train's rotational components (wheels, shafts, axles, etc.), which require an additional accelerating

torque and can be expressed as an additional mass, known as rotating mass, according to the relationship [38]:

$$m_e = m(1 + \beta) \tag{5.1}$$

where m is the vehicle's static mass, and β is a coefficient that accounts for the rotating mass that depends on the type of vehicle. Some experimental values of β are given in Table 5.3.

Table 5.3: Equivalent mass of different vehicles [38].

Vehicle	**Value of β**
Urban bus	0.22
EMU and Trolleybus	0.10÷0.15
Electric Locomotive	0.15÷0.20
Coaches and carriages	0.03÷0.06
Complete trains	0.05÷0.09

According to technical data found in literature [49], the values reported in Table 5.4 apply to the ETR1000.

Table 5.4: Static and equivalent mass of the ETR1000 [49].

Static mass	501000 kg
β	0.04
Rotating mass	20040 kg
Equivalent mass	521040 kg

5.3.2. Resistance to motion

The resistance to motion accounts for all the resistance forces that oppose the train's advancement in the direction of travel. These include:

- Rolling resistance R_0, which is in turn composed of:
  - friction forces between pins and bearings;
  - friction forces at the wheel-rail interface;
  - air resistance.
- Incidental resistance, determined by altimetric and planimetric characteristics of the track, composed of:
  - Gradient resistance R_i;
  - Curvature resistance R_c.

The overall resistance to motion is then expressed as the sum of the above-mentioned components:

$$R_m = R_0 + R_i + R_c \tag{5.2}$$

5.3.2.1. Rolling resistance

The rolling resistance is typically estimated using empirical formulas that yield values of R_0 as a function of velocity, for different types of rolling stock. Some examples taken from data obtained by railway analysts are presented [38]:

- Modern passenger trains:

$$R_0 = [(1.25 \div 2.0) + (0.016 \div 0.025)(0.36v)^2] \cdot \frac{mg}{1000} \tag{5.3}$$

- Normal freight trains:

$$R_0 = [(1.5 \div 2.5) + (0.05 \div 0.06)(0.36v)^2] \cdot \frac{mg}{1000} \tag{5.4}$$

- Lightweight rail (trams, metros, and certain regional commuter trains):

$$R_0 = [(2.5 \div 3.0) + 0.04(0.36v)^2] \cdot \frac{mg}{1000} \tag{5.5}$$

- High-speed trains (not considering the presence of tunnels):

$$R_0 = [1 + 0.0125(0.36v)^2] \cdot \frac{mg}{1000} \tag{5.6}$$

For the ETR1000, Equation (5.6) applies for the calculation of the rolling resistance, yielding results that are compatible with the ones documented in [45].

5.3.2.2. Gradient resistance

The gradient resistance is given by the component of the vehicle's weight that is parallel to the ground [38]. With reference to Figure 5.3, it can be calculated as follows:

$$R_i = G \sin\alpha = G \frac{\tan\alpha}{\sqrt{1 + (\tan\alpha)^2}} \tag{5.7}$$

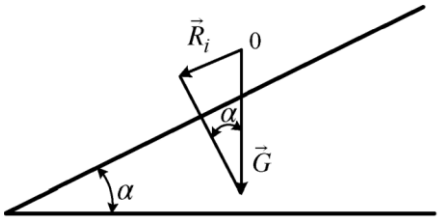

Figure 5.3: Representation of gradient resistance [38].

Considering that the gradient of the track is given by $i = \tan\alpha$, then:

$$R_i = G \frac{i}{\sqrt{1 + i^2}} \tag{5.8}$$

Considering the altimetric profile shown in Figure 5.4 for the *Direttissima* railway line from Florence to Rome [49], it is clear that the grade angle at any position along the line is so small that the gradient resistance can be approximated as:

$$R_i = Gi \tag{5.9}$$

where i is positive or negative according to whether the gradient is respectively uphill or downhill.

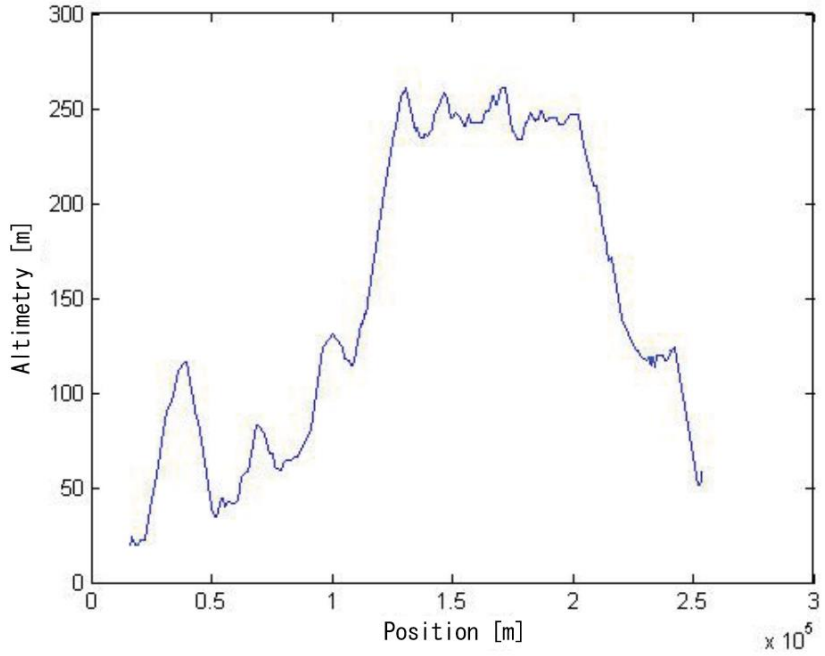

Figure 5.4: Altimetric profile of the *Direttissima* [49].

Finally, the planimetric data about the line [49] reveals that the Direttissima is characterized by a mostly straight path, with several sections having zero curvature, therefore the curvature resistance is set to zero. Based on these observations, the resistance to motion of the ETR1000 on the chosen section of the line is given by the sum of the rolling resistance and gradient resistance, therefore it is expressed as:

$$R_m = [1 + 0.0125(0.36v)^2] \cdot \frac{mg}{1000} + Gi \tag{5.10}$$

5.3.3. Adhesion

Starting and stopping a train relies on the ability of the wheels to grip the rails in order to transfer the traction or braking forces being generated. The amount of grip between the steel wheel and steel rail is known as adhesion, which can be considered as a measure of slipperiness. The adhesion available can vary considerably from extremely low levels, when the rail is severely contaminated and therefore very slippery, to very high levels, when the rail is clean and dry. It is of paramount importance for rolling stock to be operated in a way that is commensurate to the adhesion conditions present, in order to avoid wheelspin (during traction) and wheelslip (during braking) and the consequent destructive friction at the wheel-rail contact footprint [38], as well as to reduce the risk of low adhesion-related incidents, such station overruns and collisions. Low adhesion is often unavoidable, as it depends on naturally occurring weather conditions, such as

precipitation and moisture, or local environmental and industrial factors, such as the settling of leaves, pollution and particulate, sea spray, and other debris on the rails. In technical terms, adhesion is quantified by the maximum traction or braking force that can be applied to the wheels before wheelspin or wheelslip occurs. The force F_{ad} beyond which these occur is referred to as the adhesion limit, and for useful adhesion to exist, the following condition must always be satisfied for each driving wheel or wheelset [38]:

$$|F| \leq F_{ad} \tag{5.11}$$

where F is the active force applied to the wheel or wheelset. The adhesion coefficient is then defined as [38]:

$$f = \frac{F_{ad}}{G_{ad}} \tag{5.12}$$

where G_{ad} is the weight borne by the wheel or wheelset subject to the active force F. Thus, the condition for useful adhesion can be rewritten as:

$$|F| \leq f G_{ad} \tag{5.13}$$

Depending on the wheel arrangement, the driving wheels of a traction vehicle bear a fraction of the total vehicle weight G, that is distributed according to the proportion:

$$G_{ad} = \frac{G N_{w,mot}}{N_{w,tot}} \tag{5.14}$$

where $N_{w,mot}$ is the number of motorized wheels out of the total number of wheels $N_{w,tot}$[15]. Analogous considerations apply for the braking process, where typically all wheels are braked and therefore operate in full adhesion.

5.3.3.1. The adhesion coefficient

The value of the adhesion coefficient f can be estimated using experimental curves and formulas [38], that indicate its dependence on vehicle speed (adhesion decreases as speed increases) as well as on the type of wheel/ground interface:

[15] Modern locomotives always operate in full adhesion, i.e., all their wheelsets are motorized [38].

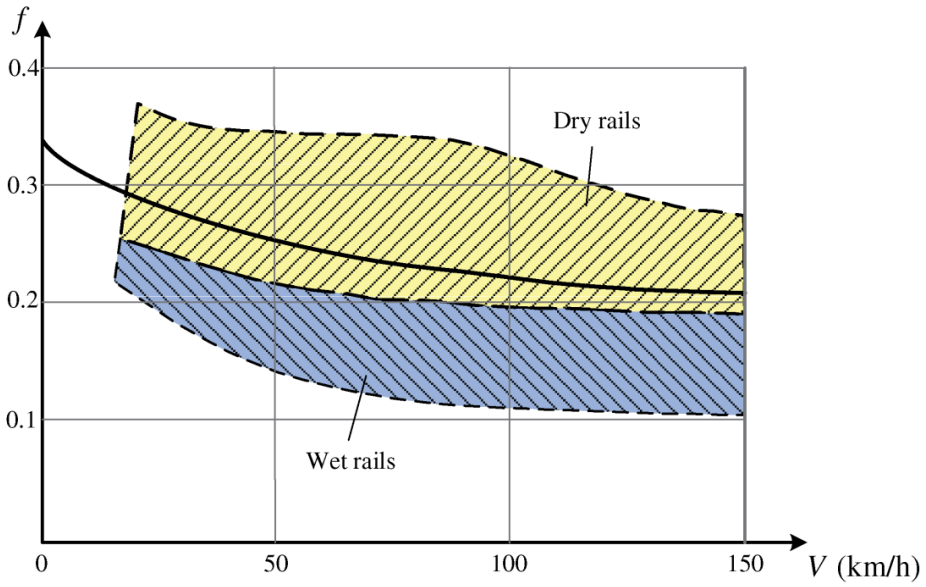

Figure 5.5: The adhesion coefficient [38].

Müller's experimental formula [38] provides the result:

$$f = \frac{f_0}{1 + 0.00396v} \tag{5.15}$$

where $f_0 = 0.25$ for wet rails and $f_0 = 0.33$ for dry rails.

Finally, the adhesion condition for a complete traction vehicle is expressed as:

$$|F| \leq \frac{N_{w,mot}}{N_{w,tot}} \cdot \frac{G f_0}{1 + 0.00396v} \tag{5.16}$$

5.3.4. The traction phase

The traction phase initiates at start-up, when the traction vehicle accelerates from standstill to a steady-state velocity (where the tractive force balances the resistance to motion). The accelerating force is the resultant between the tractive effort F_t, developed by the traction motors, and the resistance to motion, as described by the rectilinear equation of motion:

$$F_t - R_m = m_e a \tag{5.17}$$

The available tractive effort is determined from the mechanical characteristics of the traction motors, illustrated in the experimental curves in Figure 5.6 for the ETR1000 under different power supply networks (3 kV DC shown in red, resistance to motion plotted in grey). The maximum tractive effort is the starting tractive effort $F_{t,max}$, which, for the motor drives of the ETR1000, is approximately 370 kN [49]. The tractive effort is seen to decrease slightly from the starting value as speed increases, until the power limit is reached and the constant power region of the curve begins. The curves terminate where the maximum speed limit v_{max} is reached.

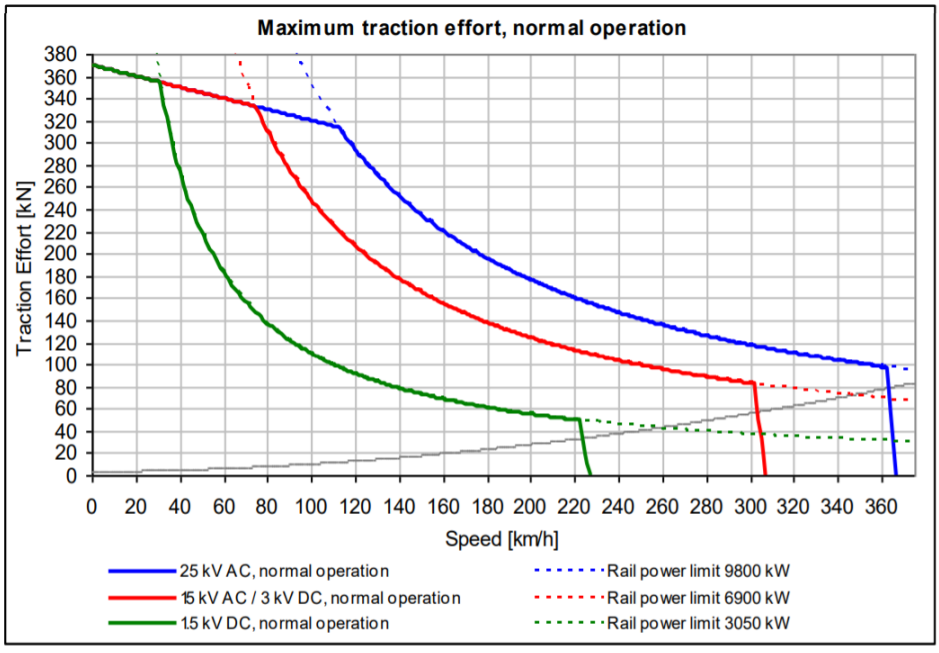

Figure 5.6: Maximum traction effort of the ETR1000 [50].

The tractive effort curve used in the model being investigated is slightly simplified, presenting, for low speeds, a constant tractive effort equal to the starting tractive effort (maximum). This approximation can be justified considering that, at low speeds, the resistance to motion is negligible compared to the tractive effort, and the

acceleration is almost constant [38]. Thus, the starting tractive effort can be calculated as:

$$F_{t,max} = m_e a_{max} \tag{5.18}$$

where $m_e = 521040\ kg$ and $a_{max} = 0.7\ m/s^2$, thus:

$$F_{t,max} = 364.73\ kN \tag{5.19}$$

The instantaneous mechanical power at the wheels P_t is given by the product between the active force acting on the wheels and the vehicle's velocity. It is therefore evident that as tractive effort is constant, the mechanical power increases linearly with velocity. The speed at which the power limit is reached is referred to as base speed v_b, which marks the beginning of the constant power region:

$$v_b = \frac{P_{t,max}}{F_{t,max}} \tag{5.20}$$

where $P_{t,max} = 6900\ kW$, thus:

$$v_b = 18.92\ m/s \tag{5.21}$$

at speeds greater than v_b, the motors are regulated through electronic drives in order to decrease the tractive effort, in compliance with the power limit. Considering also that the resistance to motion depends on the square of the speed, it is clear that, as speed increases, the accelerating force decreases, and so does the acceleration that the train is capable of developing. Figure 5.7 shows the simplified mechanical characteristic of the ETR1000 under normal conditions on a horizontal and straight track. The constant tractive effort and constant power regions of the tractive effort curve are highlighted, and the accelerating force, computed as the difference between the tractive effort and the resistance to motion, is also shown.

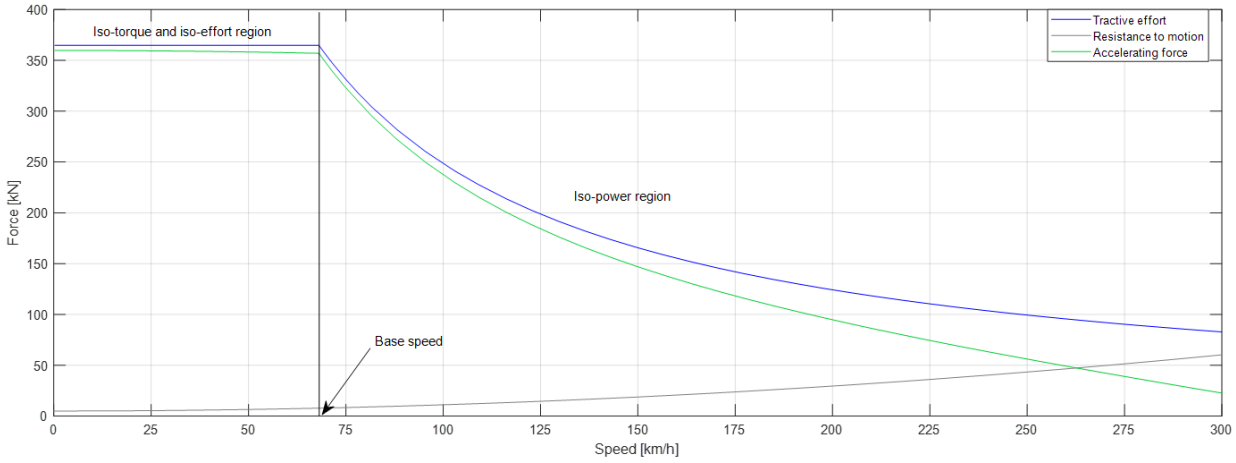

Figure 5.7: Mechanical characteristics of the ETR1000.

5.3.5. The braking phase

In the ETR1000, like in most modern electric rolling stock, braking action is achieved both via mechanical or electric braking, or their conjoined action. The mechanical braking system consists of cast iron or synthetic shoes, activated by compressed air delivered by an on-board pneumatic system, that act on the wheel rims or through gaskets on disks extending from the wheelset axles [38], dissipating the vehicle's kinetic energy through friction. The electric braking system relies on the traction vehicle's own induction motors, which are inherently reversible. Through the electronic control of the stator frequency, the stator flux is made to rotate at lower angular speed than the rotor, while the rotor rotates due to the vehicle's inertia. In this way, the traction motors work in generator mode, operating with negative slip and developing a negative (braking) torque, as well as reversing the flow of power, that can be used for regenerative braking when possible or is otherwise dissipated. In any case, the ultimate safety trip always relies on the mechanical braking system, which is called to integrate the action of the electric brakes (whose effectiveness is lost at low speeds), and to automatically take over at any speed in the event of electric brake failure [38].

5.3.5.1. Considerations regarding braking energy recovery systems

In AC electric railway systems, effective regenerative braking is guaranteed by the intrinsic bidirectionality of the AC power supply. Conversely, under DC power supply, the recovered braking power can be injected in the contact line only in the simultaneous presence of other absorbing traction loads within the same network, otherwise it is dissipated in dedicated on-board brake resistors (dissipative braking) [38]. In any case, regenerated braking power cannot be supplied from the DC contact line to the AC mains unless reversible (thyristor-based) substations are

implemented, which, at present, is not the case in the Italian 3 kV DC ERS. To enhance braking energy recovery capabilities in DC systems, constrained by the presence of other trains and the unidirectionality of traditional substations, several possible alternatives focused on stationary and on-board energy storage systems have been proposed and investigated. For instance, when applied to the ETR1000 operating in the 3 kV DC system, research data [53] suggests that on-board and stationary ESS technologies based on high-power lithium batteries and supercapacitors could lead to the savings, in terms of energy consumption and associated costs, presented in Table 5.5 (assuming the price of electricity in Italy is 100 €/MWh [53], [54]):

Table 5.5: Potential savings due to energy storage systems [53].

ESS location	**Technology**	**Yearly savings**	
On-board	Lithium batteries	1260 kWh	126 k€
	Supercapacitors	150 kWh	15 k€
Stationary	Lithium batteries	1610 kWh	161 k€
	Supercapacitors	1610 kWh	161 k€

5.3.5.2. Electric and mechanical braking action

In the braking phase, active force F_t is applied in the opposite direction (braking force) to that of the velocity vector to decelerate the vehicle. Coherently with the notation and conventions used when describing the traction phase, the equations for vehicular motion yield negative active force and acceleration during braking. The braking force is provided by the combined action of mechanical and electric braking, and the electric braking capability is dictated by the mechanical characteristic of the traction motors in braking mode. For the mathematical modeling of the braking process, the share of the total power at the wheels P_t developed by the electric brakes is denoted as $P_{t,eb}$. According to technical data provided by Trenitalia and Italfer [49] [50], the electric braking characteristic of the ETR1000 is asymmetrical with respect to the tractive effort: the base speed is the same, but the maximum power limit at the wheels in electric braking mode is:

$$P_{t,eb,max} = 5600\ kW \tag{5.22}$$

yielding a maximum electric braking effort of:

$$F_{t,eb,max} = \frac{P_{t,eb,max}}{v_b} = 296.01\ kN \tag{5.23}$$

in addition, it seen that electric braking action ceases at low speeds (around 2 m/s). Based on the data found in literature, the simplified braking effort is plotted in the following (the simplified tractive effort and the resistance to motion are also shown for completeness):

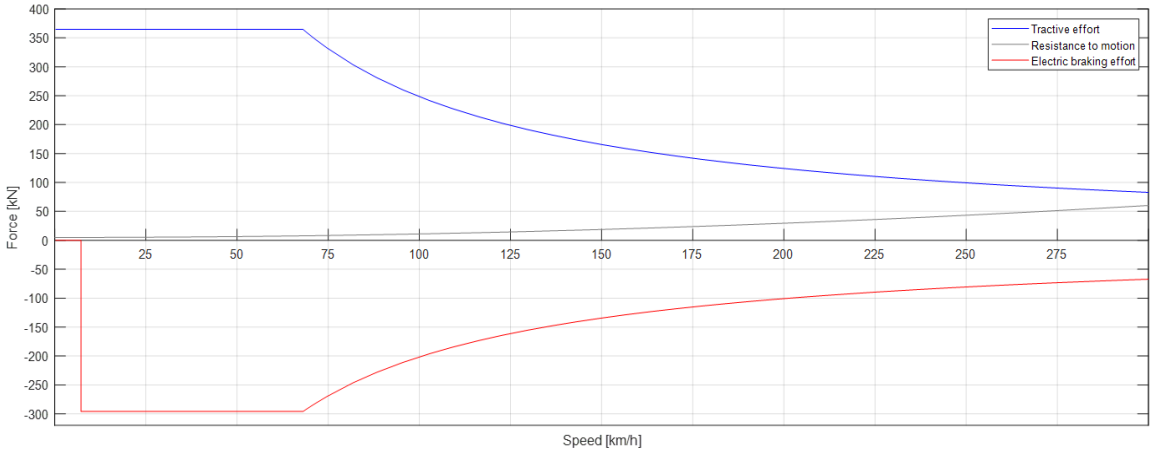

Figure 5.8: Tractive and braking characteristics of the ETR1000.

Any additional braking power required at the wheels to meet the imposed braking profile is integrated by the mechanical brakes.

5.3.6. Computations

Through software, the longitudinal dynamics of the vehicle are simulated using the equations of vehicular motion, solved iteratively in 1-second time steps (time index k). In addition, the conditions for useful adhesion, comfort acceleration, and maximum power limit are checked at every iteration. The results of the mechanical model are then used as a starting point to obtain the electrical power demand and, in turn, the current drawn (or injected, if regenerative braking is possible) and the voltage profile at the pantograph, together with the line impedance parameters, for the development of the electrical model of the system.

5.3.6.1. Start-up:

At start-up, it is known that the initial velocity is zero. All other parameters are iteratively calculated from this initial condition, as illustrated in the following algorithm.

$$v_0 = 0\ m/s$$

$$F_{t,k} = \begin{cases} F_{t,max} & if\ 0 < v_k < v_b \\ \dfrac{P_{t,max}}{v_k} & if\ v_b \leq v_k \leq v_{max} \\ R_{m,k} & if\ v_k = v_{max} \end{cases}$$

$$R_{m,k} = [1 + 0.0125(0.36v_k)^2] \cdot \frac{mg}{1000} + Gi$$

$$a_k = \frac{F_{t,k} - R_{m,k}}{m_e}$$

$$v_{k+1} = v_k + a_k \Delta t$$

$$P_{t,k} = F_{t,k} v_k$$

Where $\Delta t = 1\ s$.

The distance traveled x is simply the discrete integral of the velocity with respect to time, computed as a Riemann sum in sigma notation, providing:

$$x_{k+1} = \frac{v_k + v_{k+1}}{2} \cdot \Delta t + x_k$$

With the initial condition of $x_0 = 0\ m$. The conditions for adhesion, comfort acceleration, maximum power, and speed limit are checked at every iteration, as summarized in Table 5.6.

Table 5.6: Conditions to be verified in the traction phase.

Condition to be verified	**Criterion**	**Limit**
Adhesion	$\lvert F_{t,k} \rvert \leq F_{ad,k}$	$F_{ad,k} = \dfrac{N_{w,mot}}{N_{w,tot}} \cdot \dfrac{Gf_0}{1 + 0.00396v_k}$
Comfort acceleration	$a_k \leq a_{max}$	$a_{max} = 0.7\ m/s^2$
Power limit at the wheels	$P_{t,k} \leq P_{t,max}$	$P_{t,max} = 6900\ kW$
Speed limit	$v_k \leq v_{max}$	$v_{max} = 300\ km/h$

5.3.6.2. Cruising at constant velocity

The constant velocity scenario concerns the maximum admissible velocity (assumed to be 300 km/h under DC power supply, as long as the abovementioned constraints are met) and is an adaptation of the start-up scenario where the tractive force

balances the resistance to motion, and the train travels at steady-state velocity with zero acceleration. It immediately follows that the mechanical model parameters are given by implementing the algorithm:

$$v_0 = v_{max}$$

$$F_{t,k} = R_{m,k} = [1 + 0.0125(0.36v_k)^2] \cdot \frac{mg}{1000} + Gi$$

$$a_k = 0\ m/s^2\ \forall k$$

$$v_k = v_{max}\ \forall k$$

$$P_{t,k} = F_{t,k} v_k$$

And the conditions outlined in Table 5.6 are checked at every iteration.

5.3.6.3. Full-service braking

Considering a full braking maneuver from maximum speed to rest, the vehicle dynamics during the braking phase are computed as follows:

$$v_0 = v_{max}$$

$$a_k = \begin{cases} \dfrac{-F_{ad,k} - R_{m,k}}{m_e} & if\ \dfrac{-F_{ad,k} - R_{m,k}}{m_e} > a_{b,max} \\ a_{b,max} & if\ \dfrac{-F_{ad,k} - R_{m,k}}{m_e} \leq a_{b,max} \end{cases}$$

$$F_{ad,k} = \frac{N_{w,mot}}{N_{w,tot}} \cdot \frac{Gf_0}{1 + 0.00396v_k}$$

$$F_{t,k} = \begin{cases} -F_{ad,k} & if\ a_k > a_{b,max} \\ a_k m_e + R_{m,k} & if\ a_k \leq a_{b,max} \end{cases}$$

$$v_{k+1} = v_k + a_k \Delta t$$

$$P_{t,k} = F_{t,k} v_k$$

When regenerative braking is possible, the relevant power at the wheels is computed as:

$$P_{t,eb,k} = \begin{cases} 0 & if\ v < v_{eb,min} \\ -F_{t,eb,max} \cdot v_k & if\ v_{eb,min} \leq v_k \leq v_b \\ -P_{t,eb,max} & if\ v_b \leq v_k \leq v_{max} \end{cases}$$

Where $v_{eb,min} = 2\ m/s$. The constraints to be verified for the braking phase are:

Table 5.7: Conditions to be verified in the braking phase.

Condition to be verified	Criterion	Limit
Adhesion	$\left\|F_{t,k}\right\| \leq F_{ad,k}$	$F_{ad,k} = \frac{N_{w,mot}}{N_{w,tot}} \cdot \frac{Gf_0}{1 + 0.00396v_k}$
Comfort deceleration	$\left\|a_k\right\| \leq \left\|a_{br,max}\right\|$	$\left\|a_{br,max}\right\| = 1\ m/s^2$
Power limit at the wheels in electric braking mode	$\left\|P_{t,k}\right\| \leq \left\|P_{br,max}\right\|$	$\left\|P_{br,max}\right\| = 5600\ kW$
Speed limit	$v_k \leq v_{max}$	$v_{max} = 300\ km/h$

5.4. Electrical model

The electrical model builds on the results provided by the train's mechanical model in order to determine the electrical power demand of the traction loads. In addition, the electrical model is also used to evaluate the electrical parameters of the traction circuit, with the objective to estimate the voltage and the current profile at the pantograph.

The DC power demand P_e of the traction load is harnessed not only by the traction motors to develop the required power at the wheels, but also for the power supply of on-board auxiliary equipment. It is therefore written as:

$$P_e = \begin{cases} \frac{P_t}{\eta_t} + P_{aux} & for\ normal\ traction \\ P_{t,eb}\eta_{eb} + P_{aux} & for\ regenerative\ braking \end{cases} \tag{5.23}$$

With:

- $\eta_t = 0.842$ is the overall efficiency of the traction chain [50];
- $\eta_{eb} = 0.8$ is assumed to be the overall efficiency of the regenerative braking chain;
- $P_{aux} = 220\ kW$ is the power supplied to the on-board auxiliary services [49].

Once the electrical power demand is calculated, the train current I_t absorbed at the pantograph and the voltage at the pantograph V_t are estimated, linked by the relationship for DC power:

$$P_e = I_t V_t \tag{5.24}$$

5.4.1. Modeling of the bilateral TPSS power supply

The voltage at the pantograph depends on the train's position and on the resistive component of the traction circuit, as well as on the current drawn. In general, the voltage at the pantograph is maximum in correspondence with the position of the connection to the substations, and varies as the train moves, due to the voltage drops that occur in the overhead catenary system and in the rails. The bilateral power supply of the traction load is represented in the following diagram.

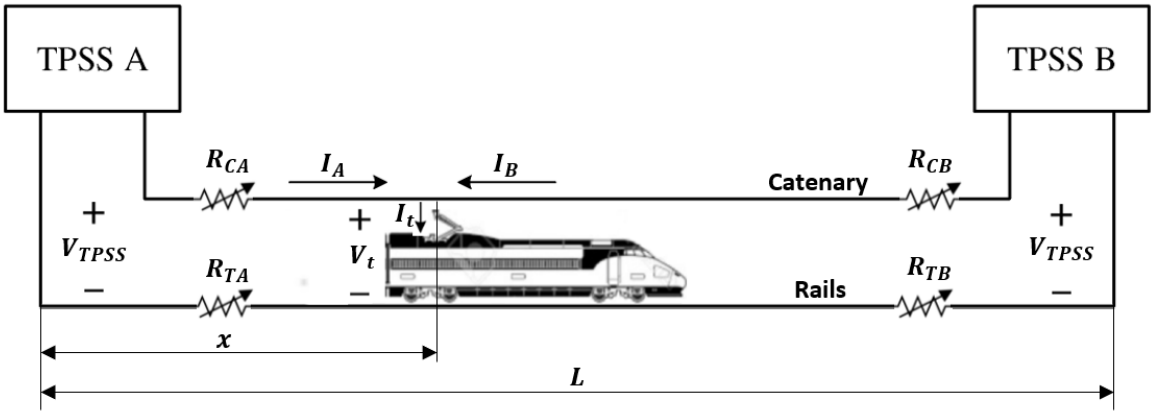

Figure 5.9: Bilateral TPSS power supply.

5.4.1.1. Voltage and current at the pantograph

Following the notation of the diagram in Figure 5.9, in which the substation voltages V_{TPSS} are assumed to be equal, the voltage at the pantograph and the corresponding line voltage drop ΔV are given by:

$$V_t = V_{TPSS} - \Delta V = \begin{cases} V_{TPSS} - I_A(R_{CA} + R_{TA}) = V_{TPSS} - I_A x(r_C + r_R) \\ V_{TPSS} - I_B(R_{CB} + R_{TB}) = V_{TPSS} - I_B(L - x)(r_C + r_R) \end{cases} \tag{5.25}$$

where r_C and r_R are, respectively, the kilometric resistance of the catenary and of the rails. In the following, for compactness, the notation $r_T = r_C + r_R$ is used for the total kilometric resistance of the traction circuit. Applying Kirchhoff's current law at the pantograph node:

$$I_t = I_A + I_B \tag{5.26}$$

The voltage drop ΔV can then be expressed as:

$$\Delta V = r_T x I_t \cdot \frac{L - x}{L} \tag{5.27}$$

5.4.1.2. Kilometric resistance of the catenary and of the rails

The kilometric resistance of the catenary (which includes the contact wire and the messenger wire), composed of copper wires having of overall cross section S_C and resistivity $\rho_{Cu} = 0.018 \left[\frac{\Omega \cdot mm^2}{m}\right]$, is evaluated using the ratio [38]:

$$r_C = \frac{18}{S_C} \tag{5.28}$$

where the chosen cross section of the catenary is chosen based on the data reported in Figure 3.16 as $S_C = 610\ mm^2$, which is the highest standard cross section in 3 kV DC ERS, allowing for greater current and train speed. Thus, the associated catenary kilometric resistance is:

$$r_C = 0.0295\ \Omega/km \tag{5.29}$$

The kilometric resistance of the rails can be found using the ratio [38]:

$$r_R = \frac{1}{2} \cdot \frac{0.75}{m_r} \tag{5.30}$$

where $m_r = 60\ kg/m$ is the linear mass of a standard rail [38], and the coefficient of $\frac{1}{2}$ takes into account the parallel connection between the rails, yielding:

$$r_R = 0.00625\ \Omega/km \tag{5.31}$$

In the simulations conducted, the distance considered between adjacent substations is $L = 20\ km$. Finally, the iterative procedure for the computation of the electrical power, current, and voltage profile at the pantograph, as well as the traction circuit parameters, is illustrated the following.

5.4.2. Computation of the traction load parameters

5.4.2.1. Start-up

In the simulation, the chosen starting position of the trains at start-up is in correspondence with one of the substations. Therefore, the initial condition is that the voltage at the pantograph is equal to the substation voltage (and the initial distance traveled is zero). Therefore, the following algorithm applies:

$$V_{t,0} = V_{TPSS}$$

$$x_0 = 0\ km$$

$$I_{t,0} = \frac{P_{e,k}}{V_{TPSS}}$$

$$\Delta V_k = r_T x_k I_{t,k} \cdot \frac{L - x_k}{L}$$

$$P_{e,k} = \frac{P_{t,k}}{\eta_t} + P_{aux}$$

$$I_{t,k} = \frac{P_{t,k}}{V_{TPSS} - \Delta V_{k-1}}$$

$$V_{t,k} = V_{TPSS} - \Delta V_k$$

The current at the *k-th* iteration is estimated based on the voltage drop at the *(k-1)-th* iteration to avoid circular references between formulas within the computation program.

5.4.2.2. Cruising at constant velocity

The iterative process is identical to that described for the start-up phase.

5.4.2.3. Full-service braking

The braking phase strongly influences electrical quantities at play in the traction circuit, as the power demand by the train for motoring is no longer present, and the only power consumption is related to the auxiliary services. Moreover, in case of regenerative braking, the flow of electrical power is reversed, causing a rise in the voltage at the pantograph. According to the 3 kV DC voltage system specifications outlined in Table 3.3, the catenary voltage may not exceed 3900 V for longer than 5 minutes [55].

The chosen braking scenario includes an initial cruising phase at constant maximum speed, starting at one of the substations, followed by full-service braking, with the train stopping at the next substation. The braking command is given at intermediate position x_b between the substations, as illustrated in Figure 5.10.

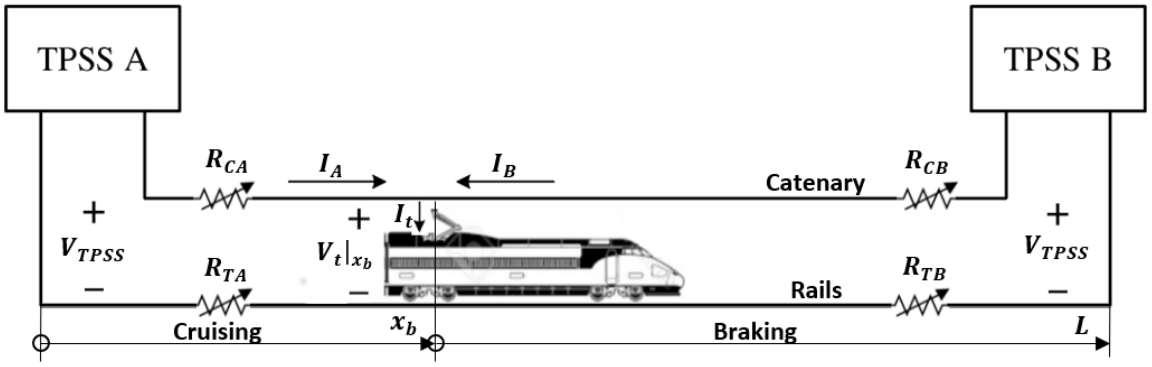

Figure 5.10: Braking position.

In light of these considerations, the initial conditions for the computation of the electrical parameters related to the braking phase are evaluated starting from position x_b. All prior quantities are evaluated as described in the cruising scenario.

$$V_{0,t} = V_t|_{x_b}$$

$$P_{e,k} = \begin{cases} P_{aux} & if\ only\ mechanical\ braking \\ \dfrac{P_{t,eb,k}}{\eta_{eb}} + P_{aux} & if\ renegerative\ braking \end{cases}$$

$$I_{t,0} = \frac{P_{e,k}}{V_t|_{x_b}}$$

$$\Delta V_k = r_T x_k I_{t,k} \cdot \frac{L - (x_k + x_b)}{L}$$

$$I_{t,k} = \frac{P_{t,k}}{V_{TPSS} - \Delta V_{k-1}}$$

$$V_{t,k} = V_{TPSS} - \Delta V_k$$

5.4.3. Computation of the traction circuit parameters

Similarly, for all scenarios, the current and electrical power supplied by the TPSSs in the bilateral configuration, and the resistances of the catenary and of the rails in the segments between the train and the TPSSs are calculated iteratively as follows.

$$I_{TPSSA,k} = I_{t,k} \cdot \frac{L - x_k}{L}$$

$$I_{TPSSB,k} = I_{t,k} \cdot \frac{x_k}{L}$$

$$P_{TPSSA,k} = I_{TPSSA,k} V_{TPSS}$$

$$P_{TPSSB,k} = I_{TPSSB,k} V_{TPSS}$$

$$R_{CA,k} = r_C x_k$$

$$R_{CB,k} = r_C (L - x_k)$$

$$R_{TA,k} = r_T x_k$$

$$R_{TB,k} = r_T (L - x_k)$$

At every iteration, the electrical constraints regarding the overload limits of the TPSSs (as outlined in Table 3.2) and the operational limits of the catenary (Table 3.3) are checked.

Table 5.8: Operational limits of the traction circuit.

Condition to be verified	**Criterion**
Catenary voltage limit	$2000\ V < V_{t,k} < 3900\ V$
TPSS current limit	$I_{TPSS,k} < 3500\ A$

5.5. Results of the model

The 3 kV DC railway system considered in the computations consists of a double line (up-line and down-line) with bilateral power supply, as illustrated in Figure 5.11. Based on the altimetric profile of the *Direttissima*, the up-line gradient is set to +5.7 ‰ and the down-line gradient is set to -5.7 ‰. The electrical model is then applied to each line independently.

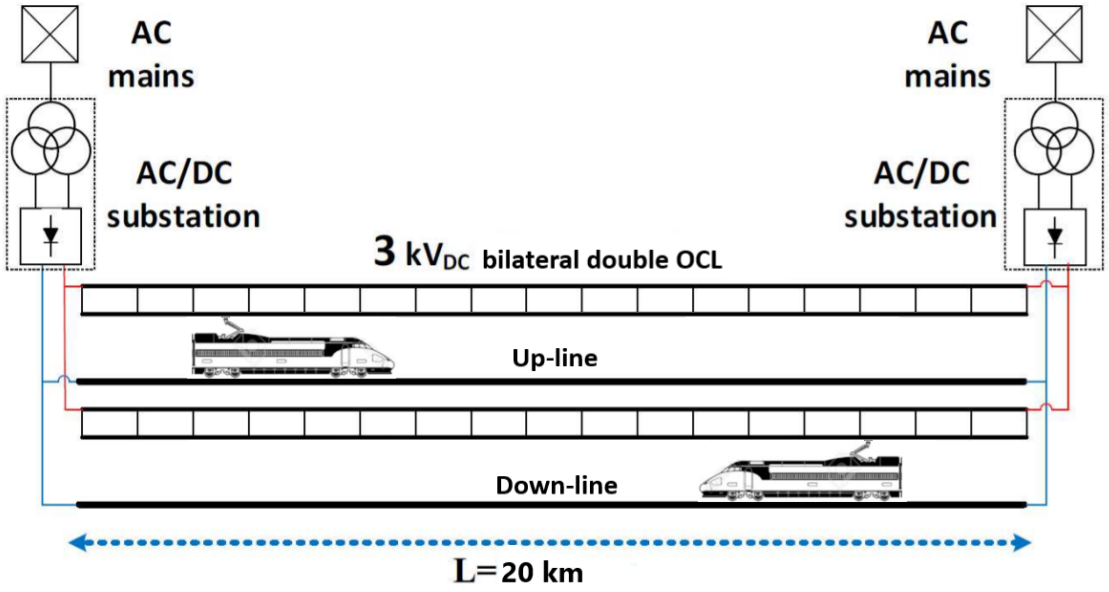

Figure 5.11: Bilateral double line diagram [2].

Some examples of the key results obtained from the aforementioned mechanical and electrical models are illustrated in the following, and used as inputs for the simulation of the traction circuit conducted in MATLAB® and Simulink-SIMSCAPE™. The examples illustrated are relative to the following scenarios:

- Regenerative braking of one train on the down-line (line gradient: -5.7 ‰).
- Start-up of one train on the up-line (line gradient: +5.7 ‰)
- One train cruising at maximum speed on the down-line.

5.5.1. Regenerative braking scenario, down-line

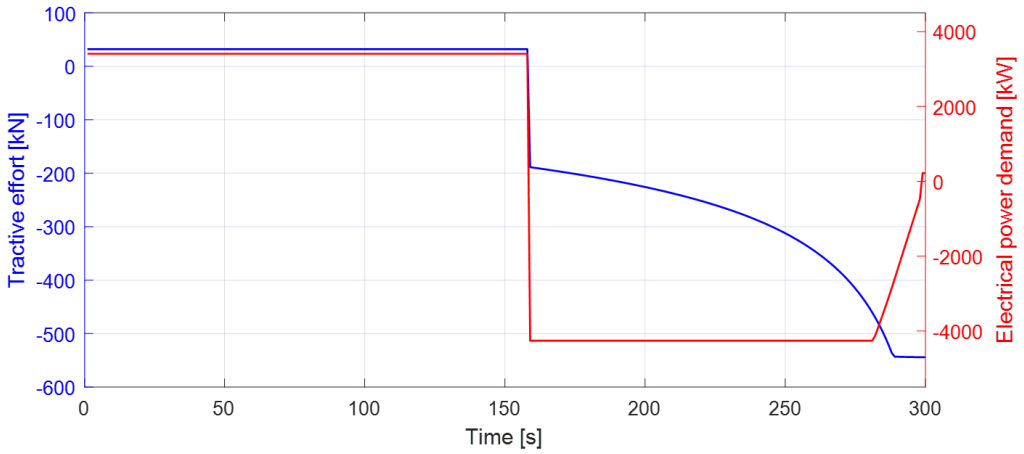

Figure 5.12: Tractive effort and electrical power demand, downhill braking scenario.

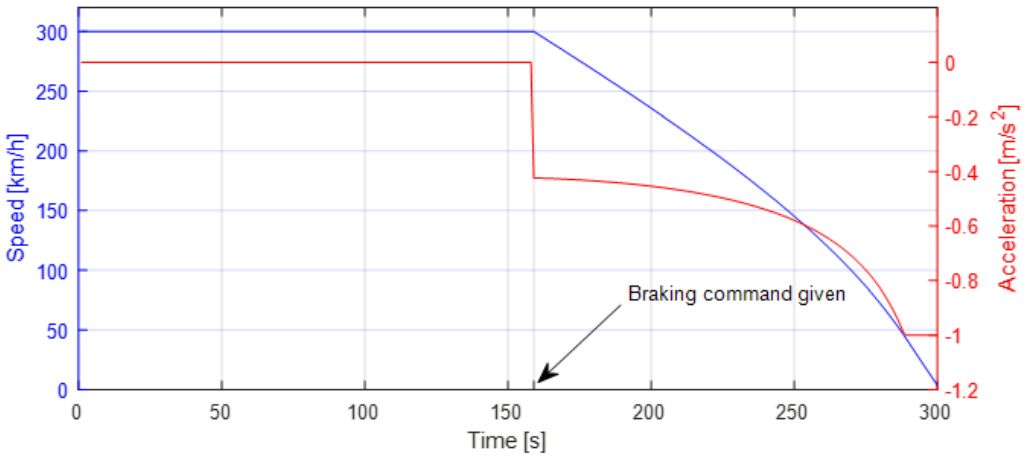

Figure 5.13: Speed and acceleration profiles, downhill braking scenario.

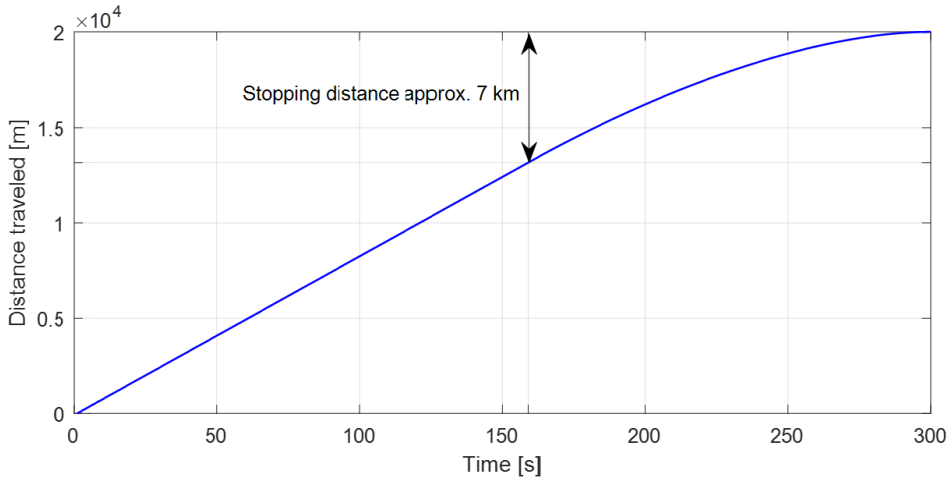

Figure 5.14: Position profile, downhill braking scenario.

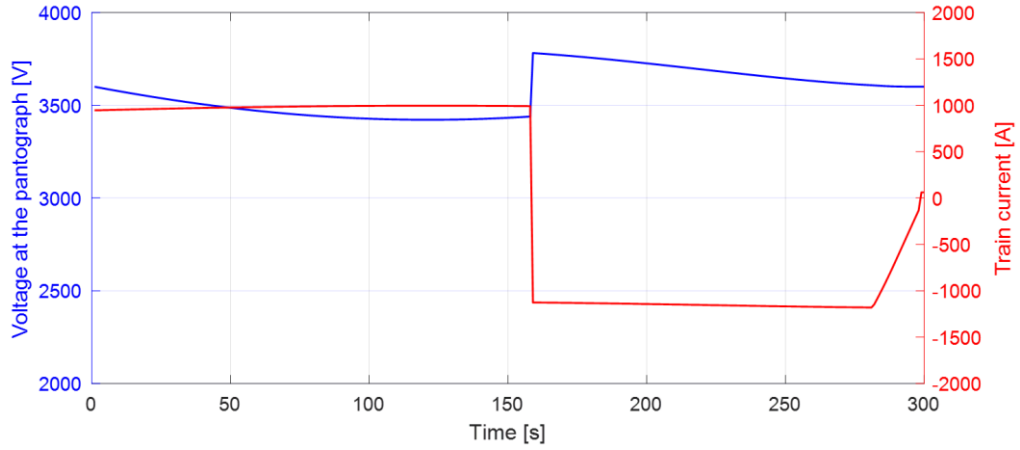

Figure 5.15: Voltage and current at the pantograph, downhill braking scenario.

5.5.2. Start-up scenario, up-line

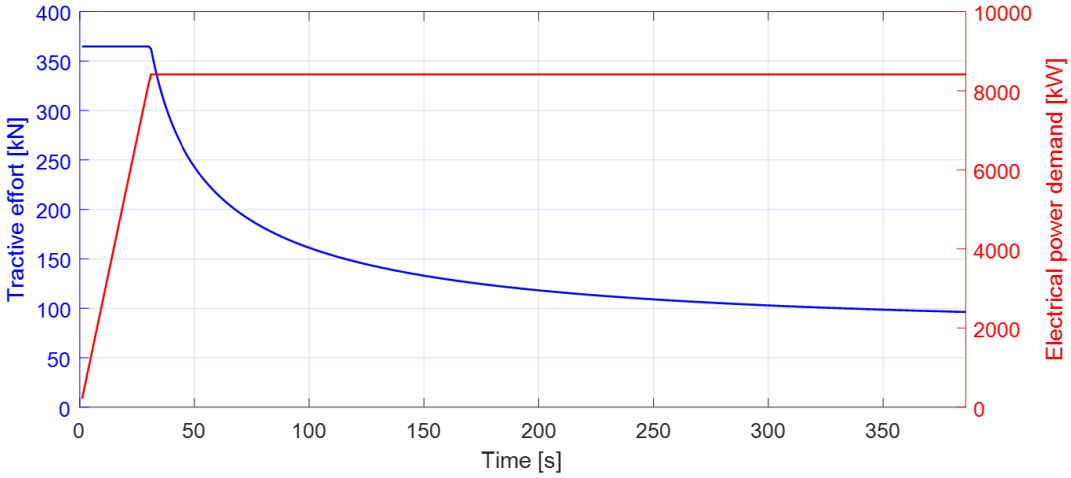

Figure 5.16: Tractive effort and electrical power demand, uphill start-up scenario.

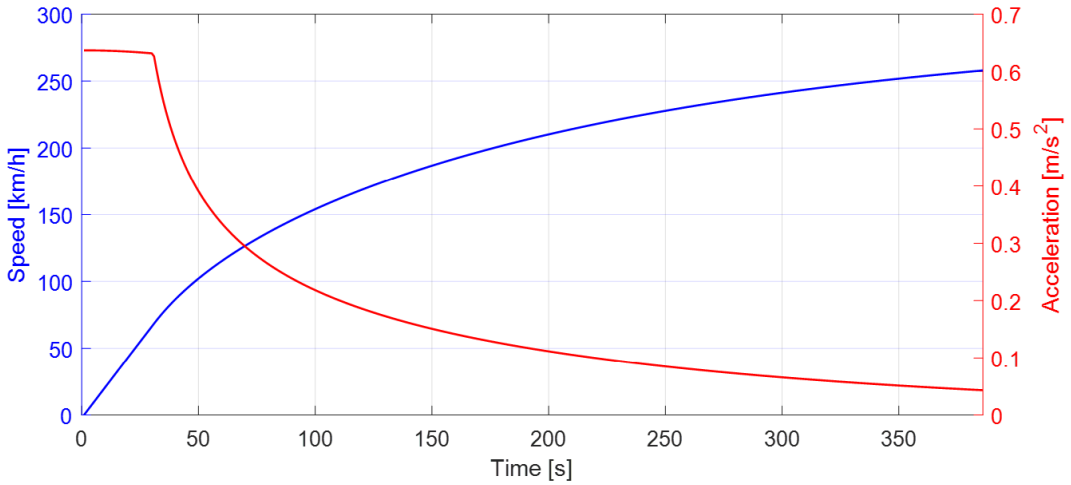

Figure 5.17: Speed and acceleration profiles, uphill start-up scenario.

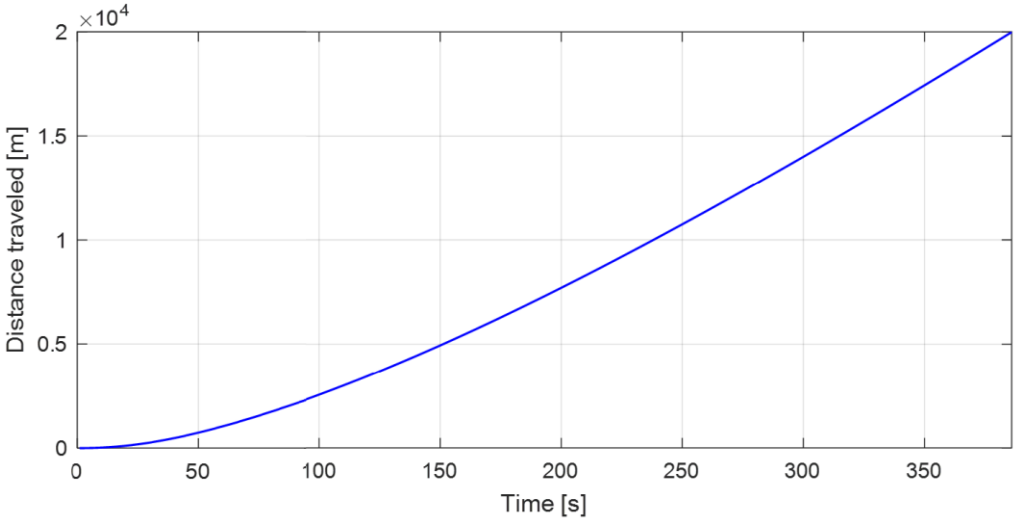

Figure 5.18: Position profile, uphill start-up scenario.

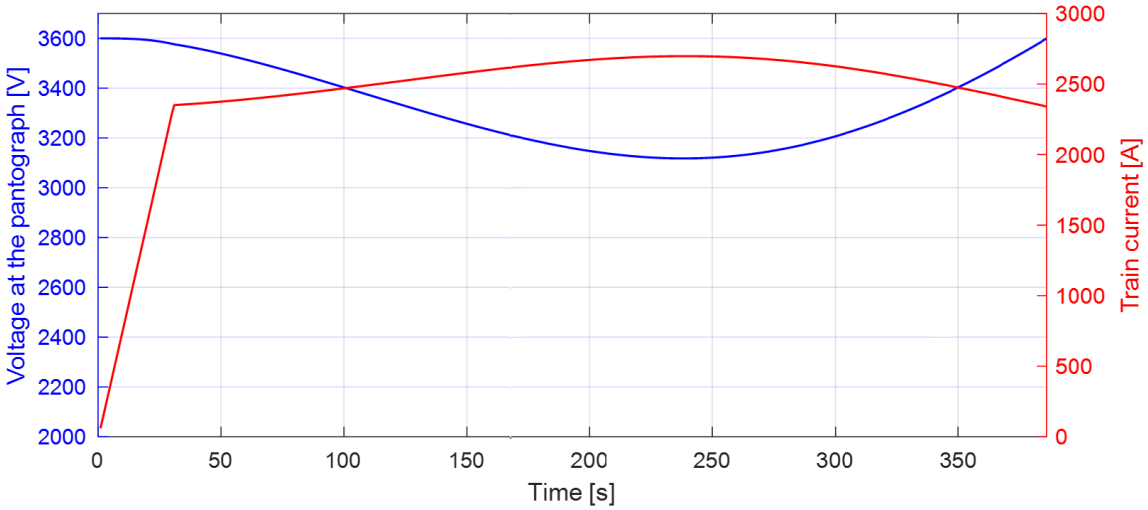

Figure 5.19: Voltage and current at the pantograph, uphill start-up scenario

5.5.3. Maximum speed scenario, down-line

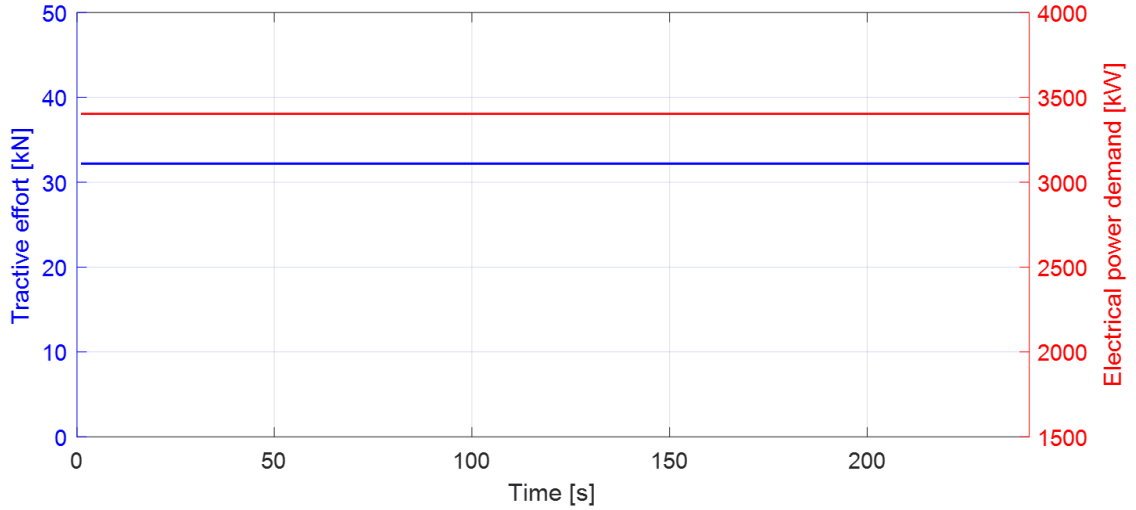

Figure 5.20: Tractive effort and electrical power demand, maximum speed downhill.

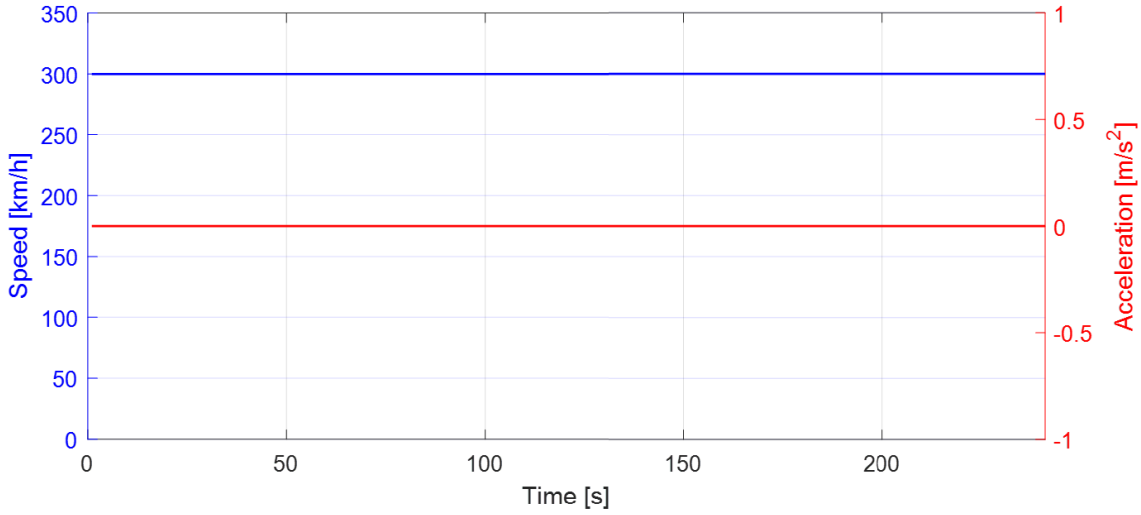

Figure 5.21: Speed and acceleration profiles, maximum speed downhill.

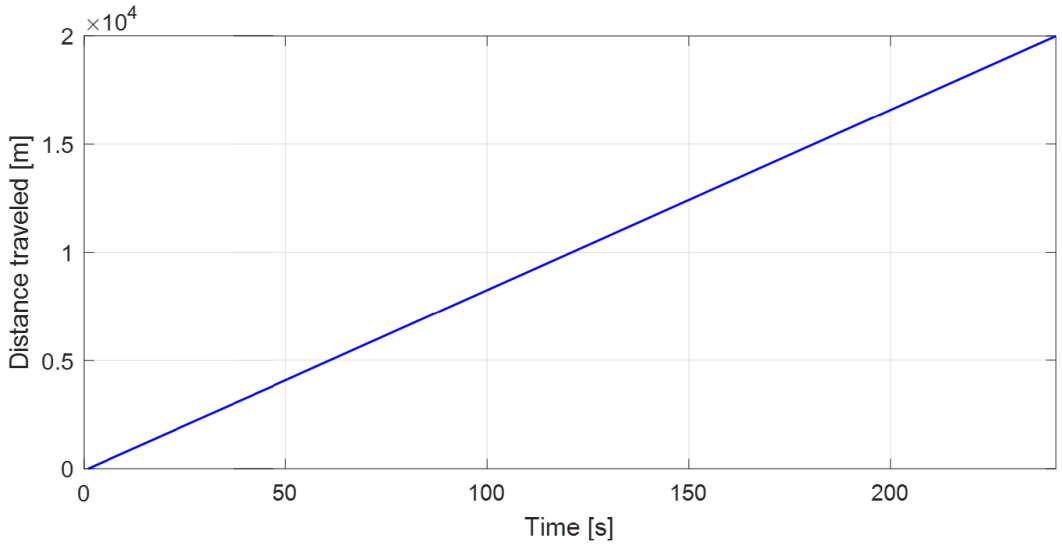

Figure 5.22: Position profile, maximum speed downhill.

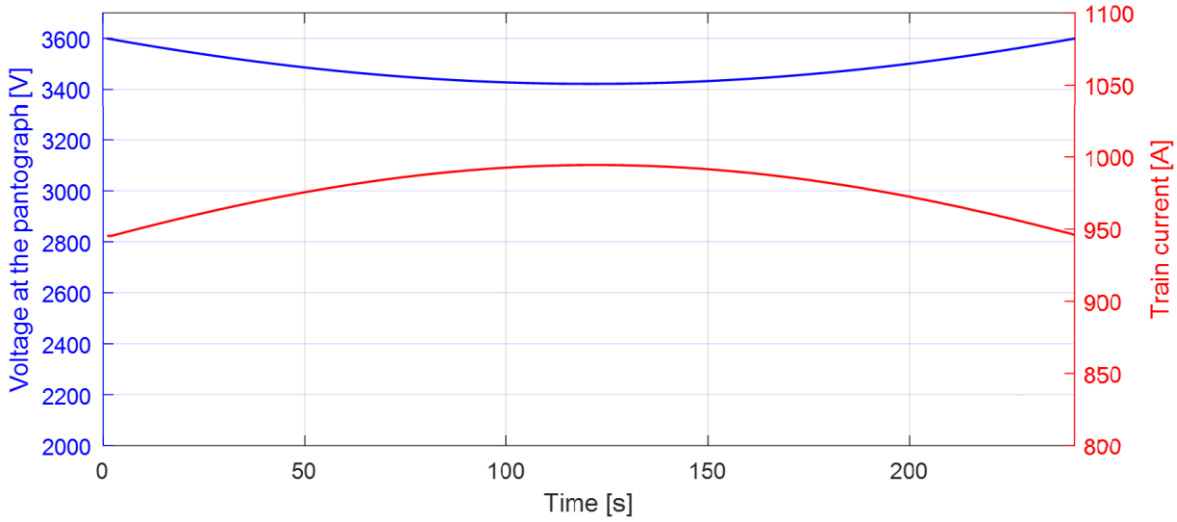

Figure 5.23: Voltage and current at the pantograph, maximum speed downhill.

5.5.4. Traction circuit resistances and TPSS power and currents

Examples of the traction circuit's bilateral resistances and TPSS currents and power supply during the train's crossing between two adjacent substations shown in the following. The curves in magenta apply to one train traveling at full speed on the down-line, completing the crossing in the shortest time, while the curves in blue apply to one train during start-up on the up-line, highlighting the appreciable difference in power demand between the two scenarios.

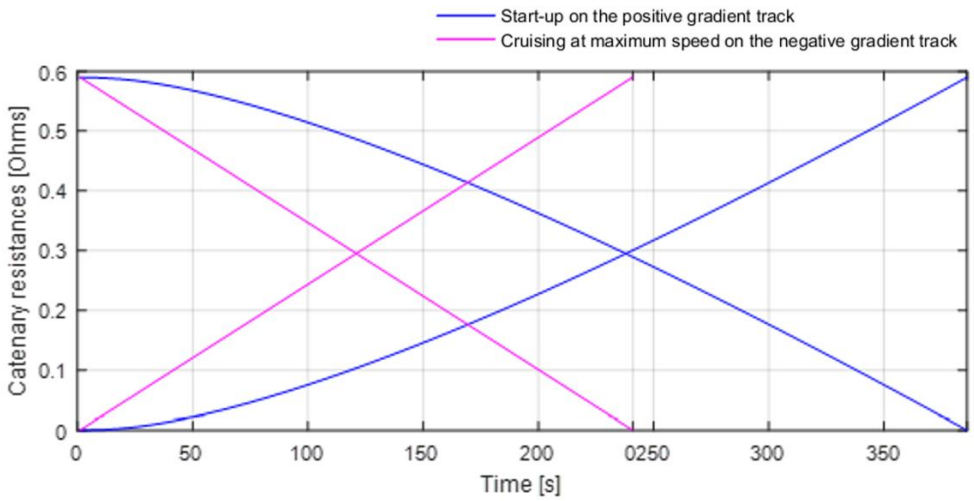

Figure 5.24: Catenary resistances.

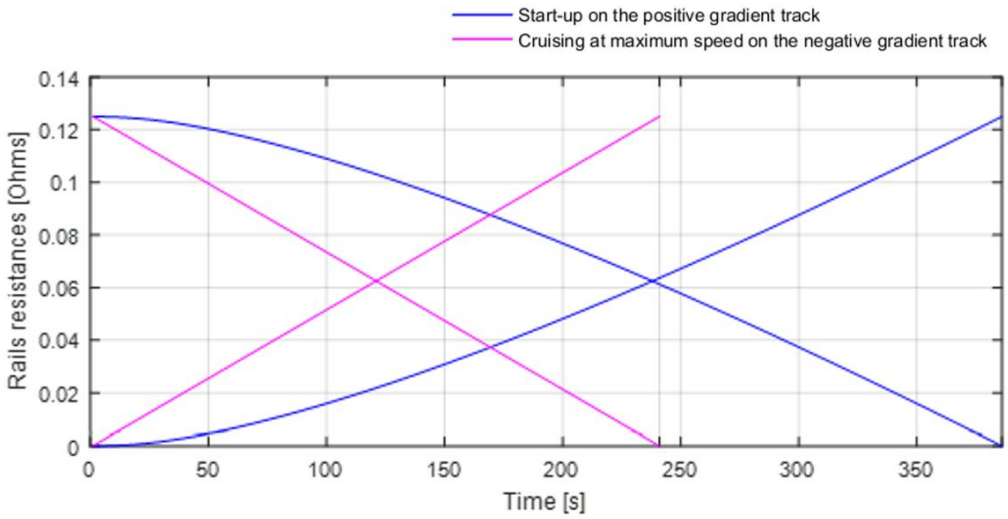

Figure 5.25: Rails resistances.

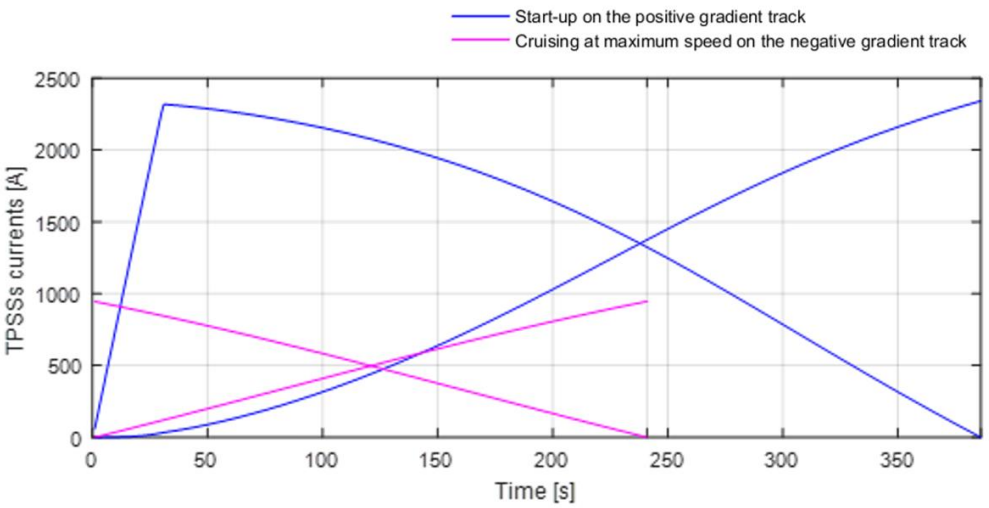

Figure 5.26: TPSS currents.

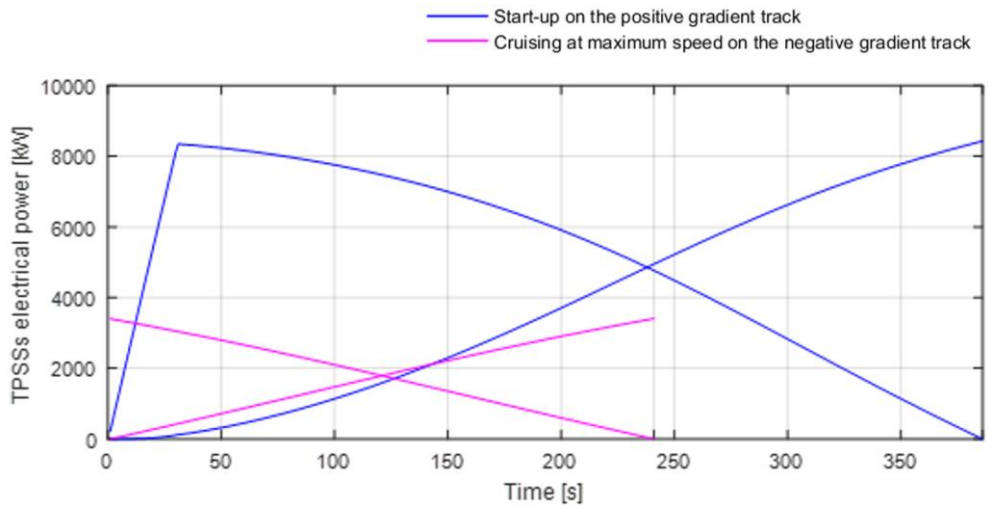

Figure 5.27: TPSS electrical power.

6 Simulation of a 3 kV DC railway system with integrated PV-Wind generators

The complete model developed in MATLAB® and Simulink-SIMSCAPE™ for the 3 kV DC traction circuit includes two traction substations that supply a double track (up-line and down-line), integrated with renewable generators consisting of a 1.5 MW PV system connected in parallel to TPSS 1, and a 1.5 MW wind farm connected in parallel to TPSS2, as shown Figure 6.1.

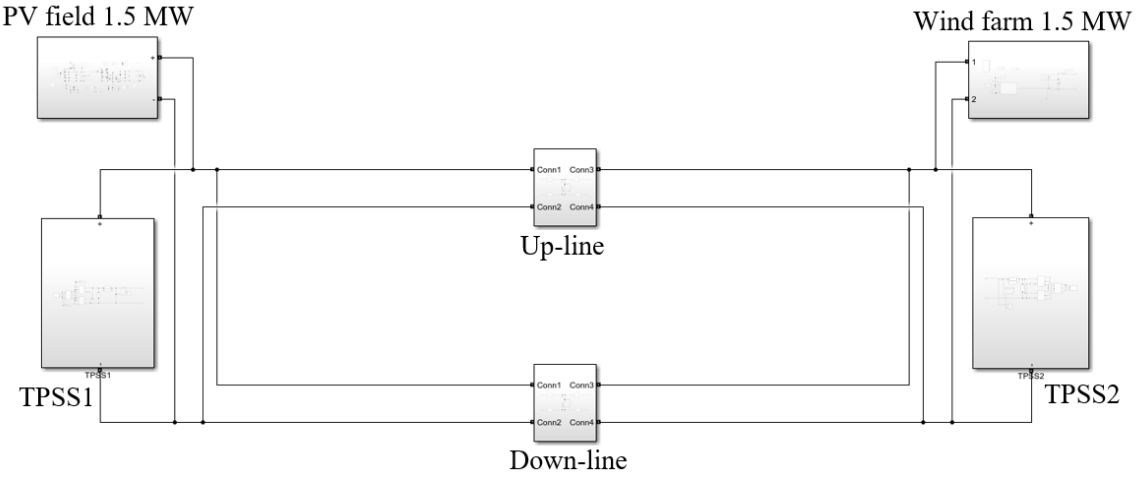

Figure 6.1: Double track with two TPSSs and RES.

The simulations are conducted considering that:

- The two lines are loaded with one train each at most, traveling in opposite directions, with zero temporal offset between train departures.
- The starting position of the train in the up-line (train 1) is in correspondence with TPSS 1, while the starting position of the train in the down-line (train 2) is at TPSS 2.
- Various scenarios regarding different traction modes and availability of RES are considered.

6.1. Construction of the model

The subsystem blocks used in the model are analyzed in the following.

6.1.1. The TPSSs

The TPSS subsystems include the following blocks and elements.

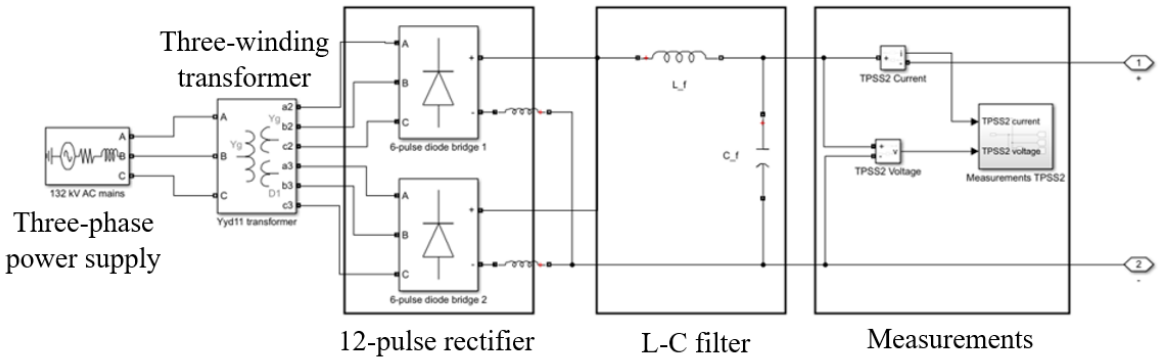

Figure 6.2: The TPSS block.

6.1.1.1. Three-phase power supply

The three-phase power supply block is used to simulate the primary AC mains at 132 kV, 50 Hz. Based on short-circuit power data recorded by Terna for the 132 kV transmission grid [56], a three-phase short-circuit power of 3500 MVA is specified in the block parameters, along with a quality factor (X/R ratio) of 7. The power supply is configured as having grounded neutral, in compliance with grid codes.

6.1.1.2. Three-winding transformer

The traction transformer is configured as a three-winding transformer of vector group Yyd11, nominal power of 10 MVA (given the high power of the traction loads), nominal frequency of 50 Hz, and transformer ratio of 132000/2710 (typical of 3 kV traction substation transformers). The primary winding series resistance and leakage inductance are set to 0.002 pu and 0.05 pu, respectively. For both secondary windings, the values of series resistance and leakage inductance are 0.002 and 0.06, respectively. The magnetizing resistance and inductance are chosen so that the effects of the magnetizing branch can be considered negligible.

6.1.1.3. 12-pulse rectifier

The 12-pulse rectifier is composed of two parallel-connected 6-pulse diode bridges. A small inductance is connected to the negative terminal of each 6-pulse bridge for their parallel connection.

6.1.1.4. The L-C filter

The L-C filter for the attenuation of current and voltage ripples on the DC-side is constructed using the circuit element blocks. The filter is tuned to suppress the dominant harmonic produced by each 6-pulse bridge, i.e., the 6th harmonic (characterized by frequency $f_6 = 300\ Hz$). To this aim, the filter is composed of a series inductance $L_f = 6\ mH$ connected to the positive terminal of the rectifier, followed by a shunt capacitance of $C_f = 47\ mF$, sized for the dominant harmonic in accordance with the tuning formula:

$$2\pi f_6 = \frac{1}{\sqrt{L_f C_f}} \tag{6.1}$$

6.1.1.5. Measurement blocks

A measurement system that includes current and voltage measurements blocks is implemented, along with the "product" operator for the computation of the electrical power supplied by the substations. As an example, the contents of the measurement block of TPSS 2 are shown:

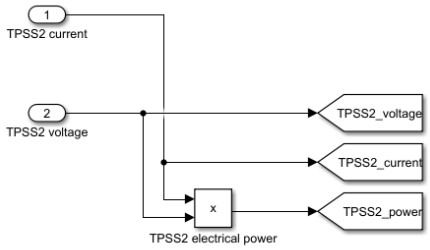

Figure 6.3: Contents of the TPSS measurement block.

The voltage, current, and power measurements are directed through tags to dedicated scopes for the graphical readings of the measured quantities.

6.1.2. The traction line and loads

The blocks related to the traction line loads serve the purpose of simulating the trains' movement along the lines by means of variable parameters. Specifically, they contain the resistances of the catenary and of the rails, modeled as variable resistors,

and the traction load that occupies the line, modeled by means of a controlled current source. The results obtained from electrical model (section 5.4) are given as inputs to the variable resistors and to the controlled current source, based on the selected train traveling scenarios for the simulations. In addition, to limit the voltage fluctuations along the line and to simulate the capacitive elements of the on-board traction system architecture, a capacitor of capacitance 10 mF is connected across the terminals of the traction load. As an example, the traction line and train contained in the up-line subsystem are shown in Figure 1.1

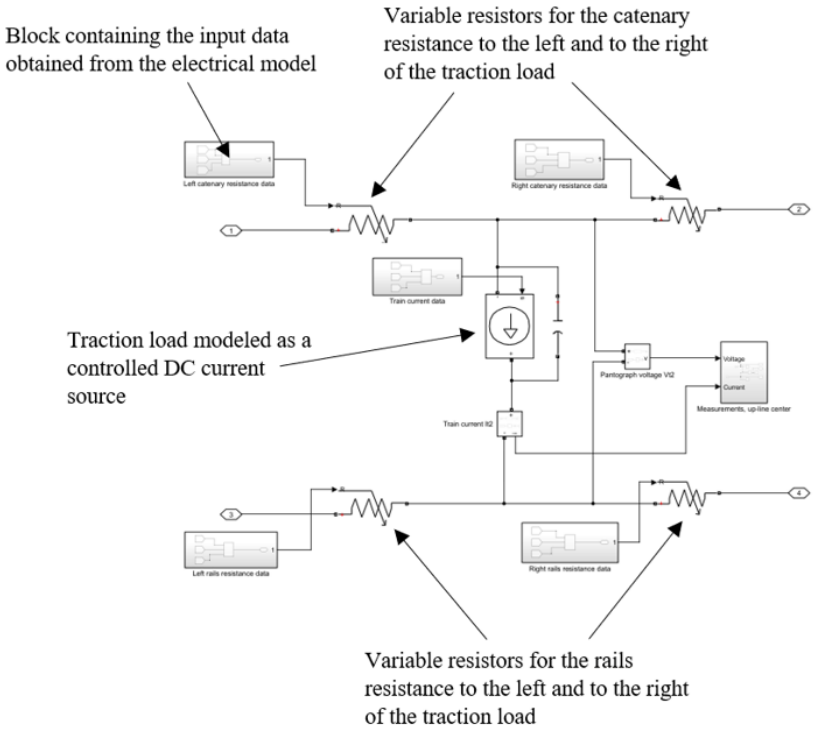

Figure 6.4: Traction line and load blocks.

Measurement blocks are also included for the readings of current, voltage, and electrical power related to the line and to the traction loads. The blocks containing the input data to the variable resistors and to the current source include a "scenario selector" that uses simple logical operators to send the data corresponding to a particular mission profile as an input to the corresponding elements, allowing for the co-simulation of different operating scenarios on the two lines. As an example, the block containing the input data for the current source is shown in Figure 6.5.

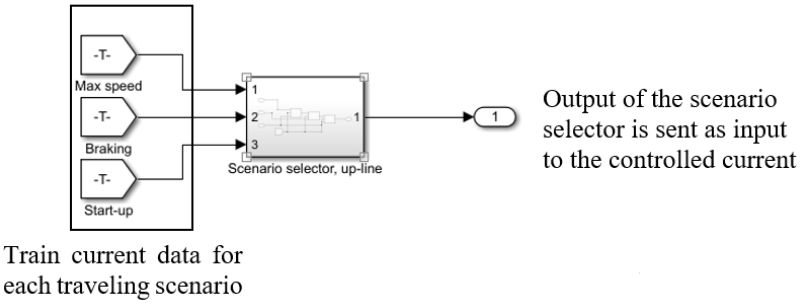

Figure 6.5: "Scenario selector" block.

6.1.3. The PV generator

The PV array considered for the power supply in parallel to TPSS 1 is comprised of PV modules whose characteristics are reported in Table 1.1. To obtain the power rating of 1.5 MW (under STC), the PV system is configured as an array of 371 strings connected in parallel, with 13 series-connected modules per string, producing a rated voltage of 711 V and current of 2.15 kA at MPP under STC. More detailed array data is reported in Table 1.4 The model of the PV system and the associated components are shown in Figure 6.6.

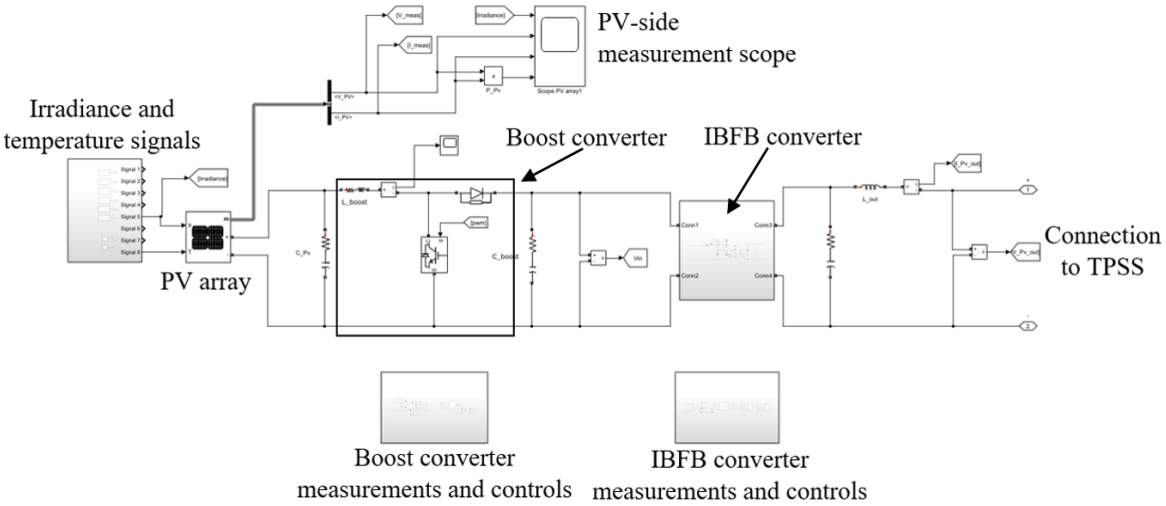

Figure 6.6: Contents of the PV system block.

In practice, PV systems are expected to operate within a range of atmospheric conditions, leading to variable power output. Therefore, a boost converter is implemented to perform maximum power tracking, cascaded with an isolated boost full bridge converter to control the intermediate voltage level at a value of 1 kV and to provide a suitable voltage gain for the connection to the TPSS nodes at 3.6 kV.

6.1.3.1. The boost converter

Based on the power rating of the PV array and based on typical values found in literature regarding boost converter switching frequency and imposed tolerances on high-frequency voltage and current ripple, the specifications of the considered boost converter are presented in Table 6.1.

Table 6.1: boost converter specifications.

Rated power [kW]	1500
Output voltage [V]	1000
Switching frequency [kHz]	10
Maximum output voltage ripple	1%
Maximum input current ripple	5%

The components of the boost converter are sized to ensure its correct operation according to the desired specifications across a range of input parameters. Variations of the PV voltage, current, and power can be seen in Figure 1.13 and Figure 1.14 for different values of temperature and irradiance. A first sizing of the input inductor and output capacitor can then be performed using Equations (1.20) and (1.21) and considering that, based on the array characteristics, the PV operating voltage and current (at the MPP) are expected to vary in the range of 650÷711 V and 2137÷106 A, respectively, for irradiance excursions in the range of 50÷1100 W/m^2. The chosen values of inductance and capacitance for the input inductor and output capacitor are then:

$$L_{boost} = 5\ mH \tag{6.2}$$

$$C_{boost} = 5\ mF \tag{6.3}$$

In the model, maximum power point tracking is performed by implementing the Perturb & Observe MPPT algorithm (described in section 1.6.3). To this end, the PV-side voltage and current measurements are taken periodically with a frequency of 400 Hz by applying the "sample and hold" function to the measurement signals, as shown in Figure 6.7. The sampled measurements are given as inputs to the MPPT P&O function to control the duty cycle of the IGBT switch of the boost converter.

The MATLAB code associated with the MPPT P&O function is included in Appendix A.1.

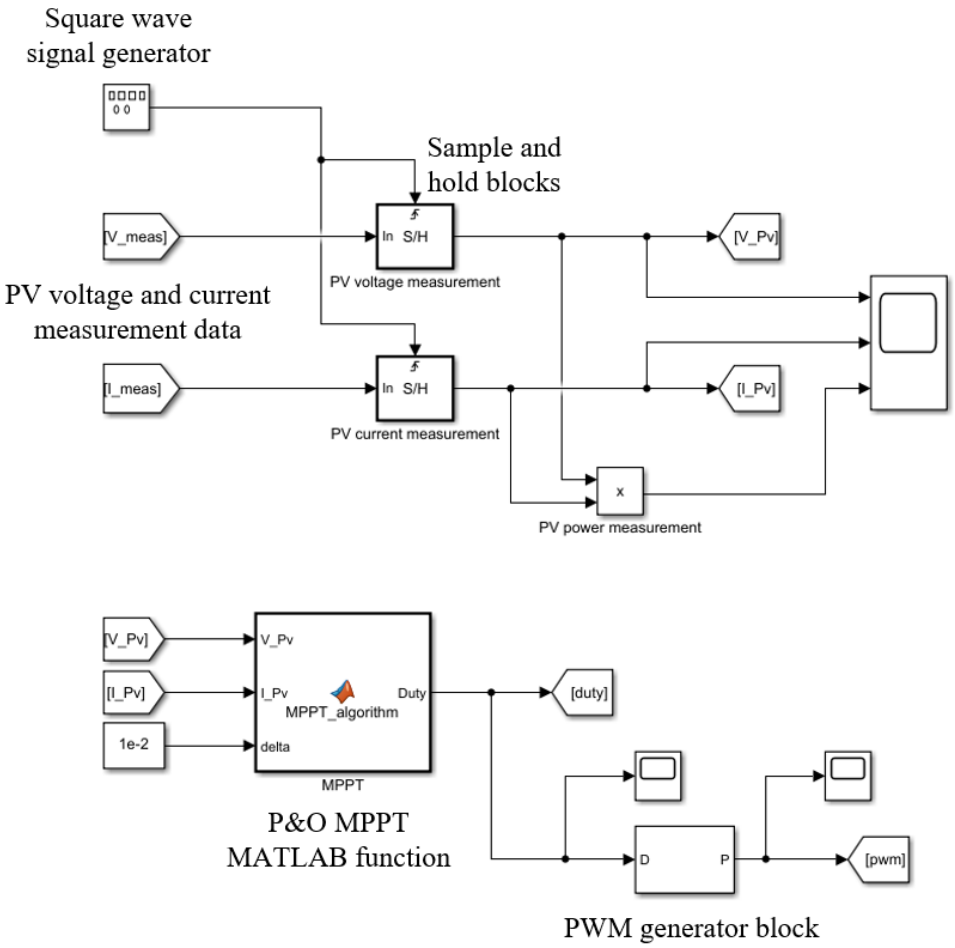

Figure 6.7: MPPT measurements and controls

As shown in the P&O algorithm block, the duty cycle of the IGBT is changed by an amount of 0.01 (denoted as "delta") at every perturbation cycle. The resulting duty cycle is processed through the PWM generator block to produce the gate signal of the IGBT.

6.1.3.2. The isolated boost full bridge converter

The IBFB converter is connected in cascade to the non-isolated boost converter to cover two main functions. Firstly, it is used to stabilize the DC output voltage of the non-isolated boost converter at a value of 1 kV, aiding the MPPT process. Secondly, the IBFB provides the additional voltage gain for the connection to the 3 kV DC railway system by means of the high-frequency transformer. The operation of the IBFB converter is described in section 1.6.4, and the contents of the IBFB converter block and its control scheme are shown in Figure 6.8.

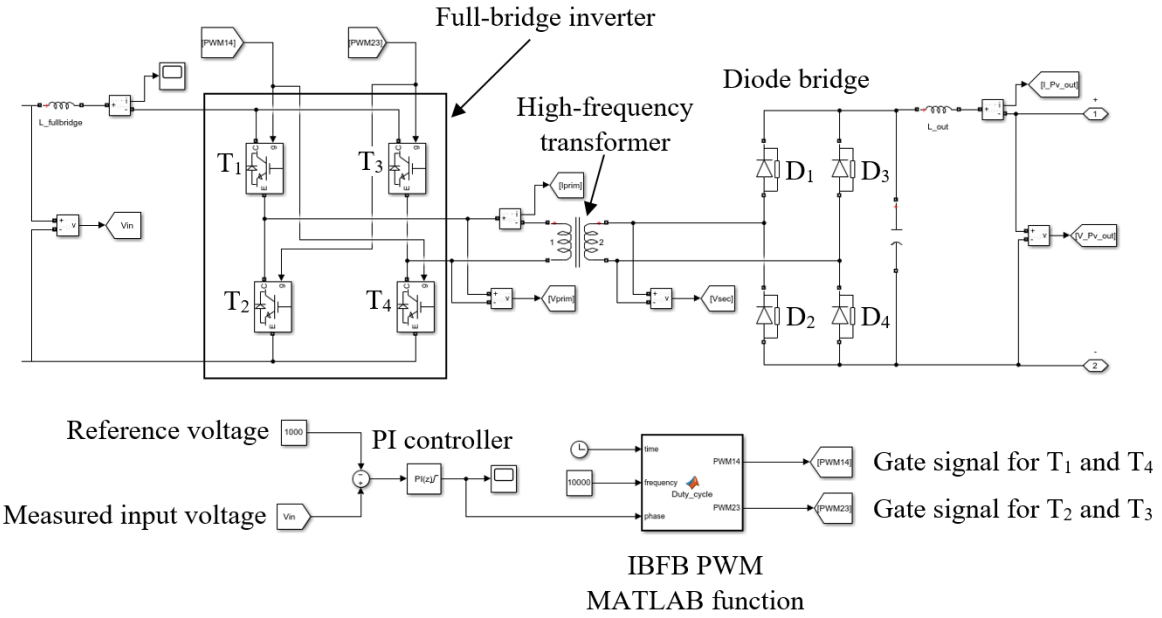

Figure 6.8: Isolated boost full bridge converter model and control scheme.

The values of the circuit parameters of the IBFB converter are chosen to limit the output voltage ripple within reasonable limits and to allow for a smooth regulation of the input voltage while maintaining the converter in the continuous conduction mode of operation. Based on simulation trials, the chosen values of input inductance are set to 0.5 mH and 5 mF, respectively. In addition, a current-smoothing inductor of 5 mH is connected in series to the positive output terminal for the connection to the catenary system. The HFT's transformer ratio is chosen to match the output voltage of the IBFB converter with the TPSS voltage. To this end, the rated voltage of the primary and of the secondary winding are set to 1500 V and 3700 V, respectively. The rated frequency of the HFT is compatible with the switching frequency of the IBFB converter, which is chosen as 10 kHz, in accordance with typical values documented in literature for this application. The input voltage of the IBFB converter is regulated by means of a PI controller which measures the error between the actual value of the input voltage and the preset voltage value of 1 kV, and consequently applies the phase shift between the gate signals of the switch pairs T_1 & T_4 and T_2 & T_3. This single phase shift switching strategy is realized by implementing the MATLAB function described in Appendix A.2, that generates the IGBT gate signals at the desired frequency from the phase shift computed by the PI controller.

6.1.4. The wind farm

The renewable generating unit considered for the connection to TPSS 2 is a 1.5 MW wind farm comprised of 3 individual wind turbines of rated power of 500 kW. The choice to use a small number of large WTGs rather than a higher number of smaller WTGs is in line with recent trends towards the implementation of larger wind turbines that are more efficient, while still preserving reasonable continuity of service in the event of failure of a single WTG, albeit at a lower power level. In addition, due to the relatively scarce wind resource in the considered geographical area (as can be deduced from Figure 6.9), the greater hub height of larger WTGs would allow to extract more power from the available wind.

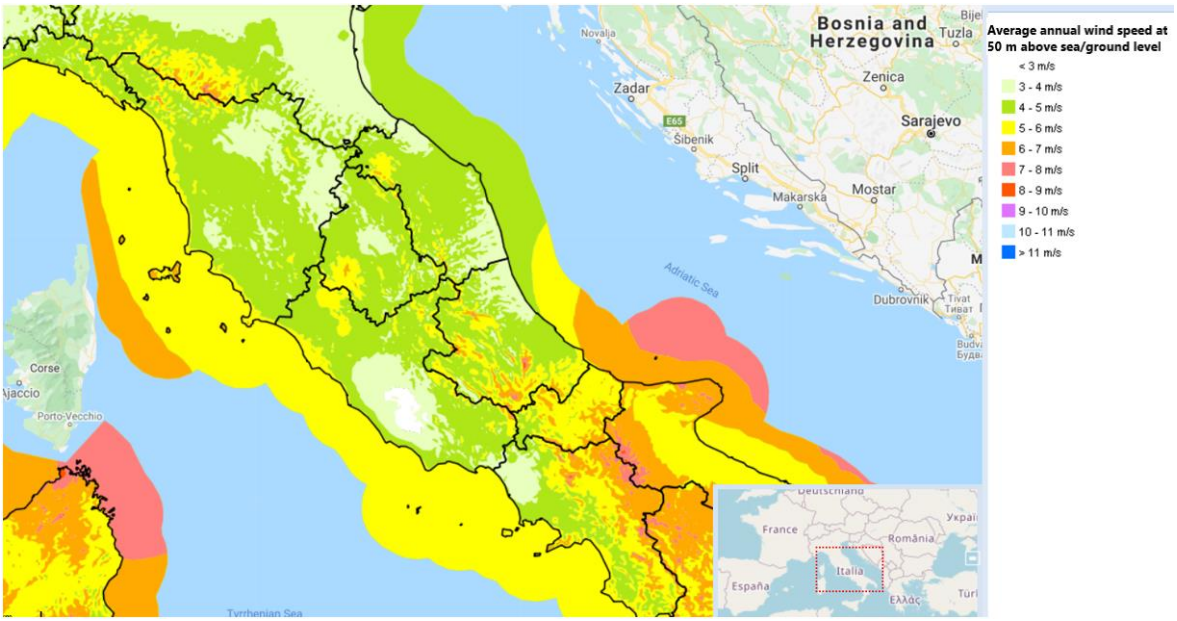

Figure 6.9: Wind resource distribution on the Italian peninsula [57].

The wind farm is modeled as an equivalent current generator connected to the substation terminals, injecting a current that is proportional to the power generated by the wind turbine complex. The model input data are the wind speed and the characteristic quantities of the turbine, that is, the rotor radius rated angular speed, and the blade pitch angle. The input quantities are related by operators based on the theoretical and empirical equations of wind turbine operation to calculate the mechanical power extracted from the wind. The electrical power is then calculated by taking an average efficiency factor and the number of WTGs into account, before computing the equivalent current injected by the system.

The input data regarding wind turbine rotor radius r and rated angular speed are calculated by recalling Equation (2.15), rewritten in the following, in which the rated mechanical power $P_{m,r}$ and the associated rated wind speed v_r are set as design parameters, and the power coefficient is expressed as a function of the tip speed ratio and the blade bitch angle:

$$P_{m,r} = \frac{1}{2} C_P(\lambda, \beta) \rho \pi r^2 v_r^3 \tag{6.4}$$

with air density ρ = 1.225 kg/m^3. An analytical expression for the power coefficient is given [58]:

$$C_P = c_1 \left(\frac{c_2(1 - 0.035\lambda)}{\lambda} - c_3\beta - c_4 \right) e^{-c_5\left(\frac{1}{\lambda + 0.08\beta} - \frac{0.035}{1+\beta^3}\right)} + c_6\lambda \tag{6.5}$$

where $c_1 = 0.5176$, $c_2 = 116$, $c_3 = 0.4$, $c_4 = 5$, $c_5 = 21$, $c_6 = 0.0068$. Selecting a fixed blade pitch angle of 0° for simplicity of design, Equation (6.5) becomes:

$$C_P = 0.5176 \left(\frac{116(1 - 0.035\lambda)}{\lambda} - 5 \right) e^{-\frac{21(1-0.035\lambda)}{\lambda}} + 0.0068\lambda \tag{6.6}$$

This analytical expression of the power coefficient is plotted in Figure 6.10. The graph shows a maximum power coefficient $C_{P,max} = 0.48$ for the optimal tip speed ratio $\lambda_{opt} = 8.1$.

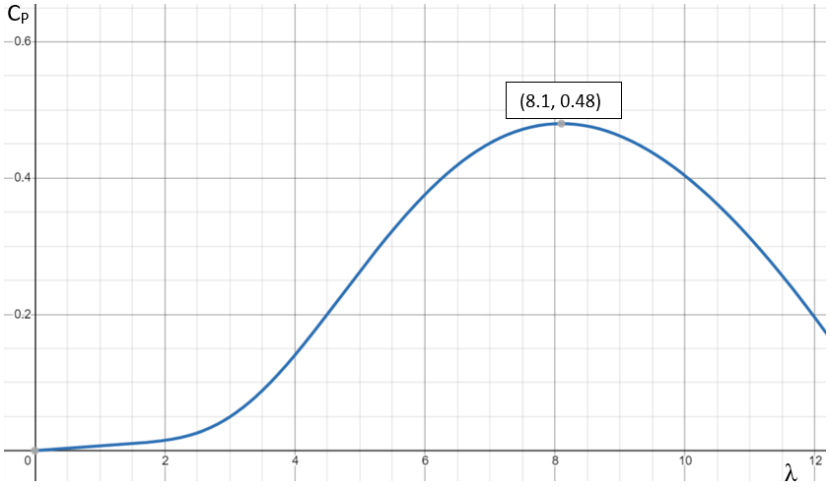

Figure 6.10. Optimum tip speed ratio and power coefficient.

Assuming that the WT operates at the maximum power coefficient for wind speeds between the cut-in and the rated value, and setting the rated electrical power at the desired value of 500 kW for the rated wind speed of 10 m/s, the required rotor radius

can be immediately calculated from Equation (6.4) and considering the overall efficiency reported in Table 6.2:

$$\frac{500000}{0.84} = \frac{1}{2} \cdot 0.48 \cdot 1.225 \cdot \pi \cdot r^2 \cdot 10^3 \tag{6.7}$$

yielding:

$$r = 25.4\, m \tag{6.8}$$

Knowing the optimal tip speed ratio, the rotor radius, and the rated wind speed, the rated angular speed of the rotor can then be calculated from Equation (2.20), yielding:

$$\Omega = 3.19\, rad/s \tag{6.8}$$

Based on values found in wind turbine datasheets [59], the cut-in wind speed is assumed as 2.5 m/s. The main parameters of the wind turbines used in the model are summarized in Table 6.2.

Table 6.2: Wind turbine data.

Rated power output [kW]	500
Rated wind speed [m/s]	10
Cut-in wind speed [m/s]	2.5
Cut-out wind speed [m/s]	20
Hub height [m]	45
Rotor radius [m]	25.4
Blade pitch	0° fixed
Rotational speed	Variable below the rated wind speed
Electrical generator type	PMSG
Overall efficiency	0.84

The model of the wind farm is illustrated in Figure 6.11, in which the individual wind turbines are modeled by means of a mathematical function, included in Appendix A.3, that processes the input data in accordance with Equations (6.4) and (6.6) to obtain the mechanical power extracted from the wind. The function also saturates the power output to zero when the wind speed is lower than the cut-in speed and higher than the cut-out speed. In addition, as a first approximation, the power coefficient computed in the function is maximum for wind speeds between the cut-in value and the rated value, in accordance with the variable speed operation of PMSG wind turbines. The electrical power generated by the wind farm is obtained by applying a gain that accounts for the overall efficiency and the number of WTs, and the current injected into the traction system is finally obtained by dividing the electrical power by the TPSS voltage.

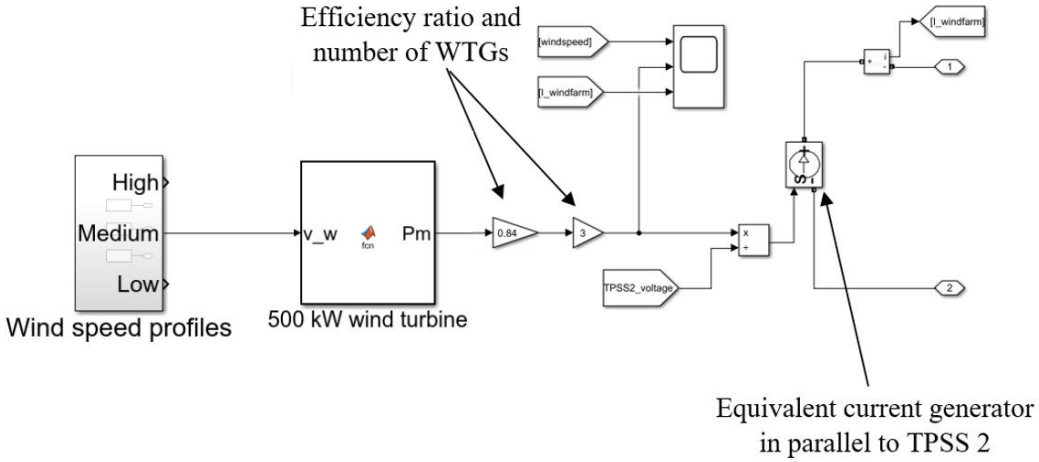

Figure 6.11: Simulink model of the 1.5 MW wind farm.

The wind speed signals fed to the model are constructed from meteorological data from the Viterbo meteorological station [60]. The anemometers are assumed to be at a height of 10 m, and the final wind speed profile is adjusted for the WT's hub height (45 m) using the Hellmann equation as described in section 2.2, assuming a friction coefficient of 0.2 as per IEC standards. An example of a daily wind speed profile on which the wind speed signals are based on is shown in Figure 6.12.

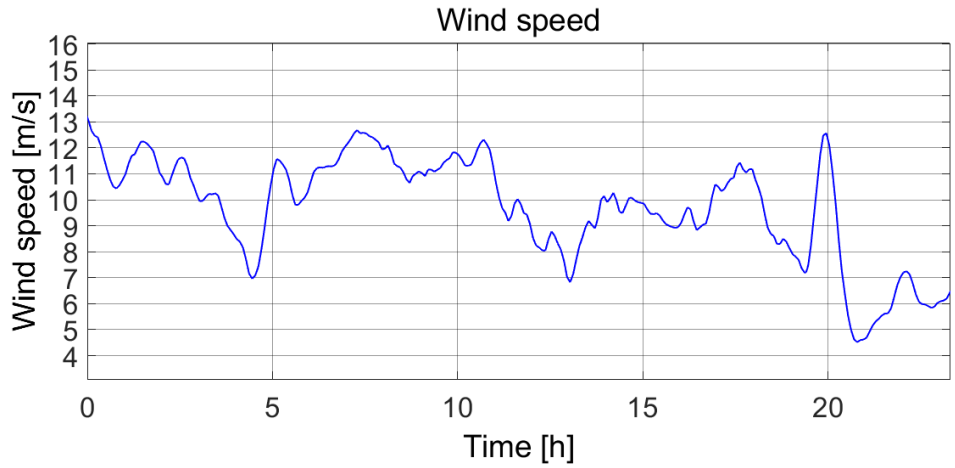

Figure 6.12. Example of daily wind speed profile adjusted for hub height.

6.2. Simulation results

In the following, the dynamic simulation results of the 3 kV DC railway system are presented for different scenarios of traction power demand and availability of the renewable generators. For each scenario, the catenary voltage (i.e., the voltage at the pantograph), the current and the electrical power absorbed by the traction loads are shown, as well as the voltage, current and electrical power delivered by the traction substations and, when available, the PV and wind generators. To run the simulations in a reasonable amount of time, the input signals have been rescaled, resulting in simulation times in the order of one second (whereas the timings associated with the real system are in the order of minutes), therefore the electrical transients related to the measured electrical quantities sometimes appear to be exaggerated and have been smoothed by taking averaging the measurements when possible.

6.2.1. One train traveling at maximum speed on the up-line

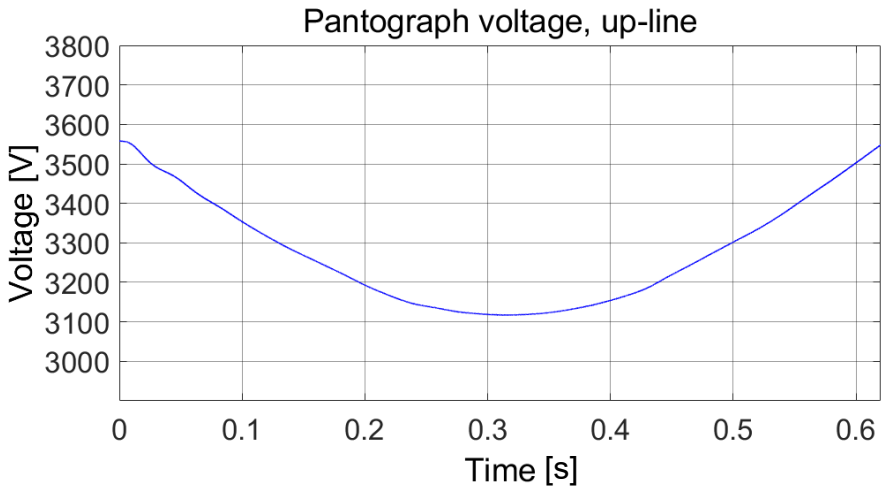

Figure 6.13: Pantograph voltage of Train 1 at maximum speed on the uphill track.

As shown in Figure 6.13, the pantograph voltage is minimum in the middle of the line, and maximum in correspondence with the traction substations, consistently with the parabolic voltage trend that is expected under bilateral power supply. The minimum voltage of 3010 V is within the minimum catenary voltage limit of 2000 V.

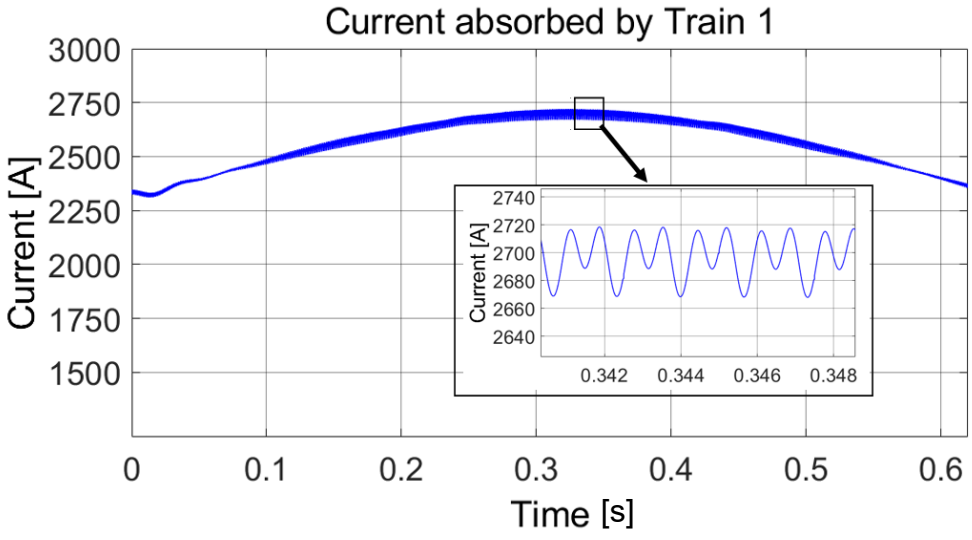

Figure 6.14: Current absorbed by Train 1 at maximum speed on the uphill track.

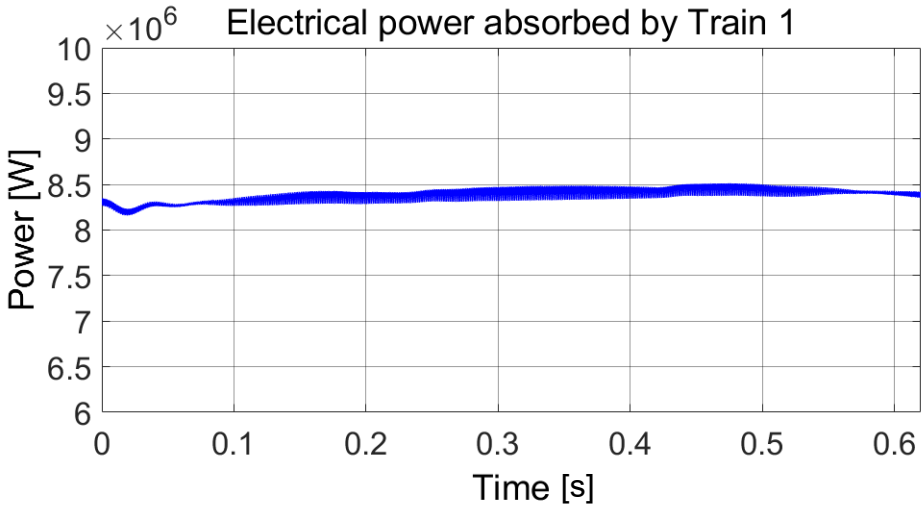

Figure 6.15: Electrical power absorbed by Train 1 at maximum speed on the uphill track.

To maintain the desired mission profile at constant speed, the mechanical power developed by the train and the associated electrical power absorption must also be constant. As shown in Figure 6.15, at maximum constant speed on the uphill track, the absorbed DC power is approximately 8.45 MW, and, as shown in Figure 6.14, the absorbed current increases with the distance from the substations in order to compensate the effects of the voltage drop and ensure constant power delivery, reaching a maximum value of approximately 2700 A in the middle of the line. Traveling at maximum speed on the positive gradient track represents the scenario that is characterized by the highest absorption of electrical power and current for a single train. Figure 16.5 also reveals the presence of harmonics (which affect also voltage and power) at 600 Hz, induced by the 12-pulse rectifiers of the TPSSs, as well as other minor harmonics due to the presence of L-C elements in the system.

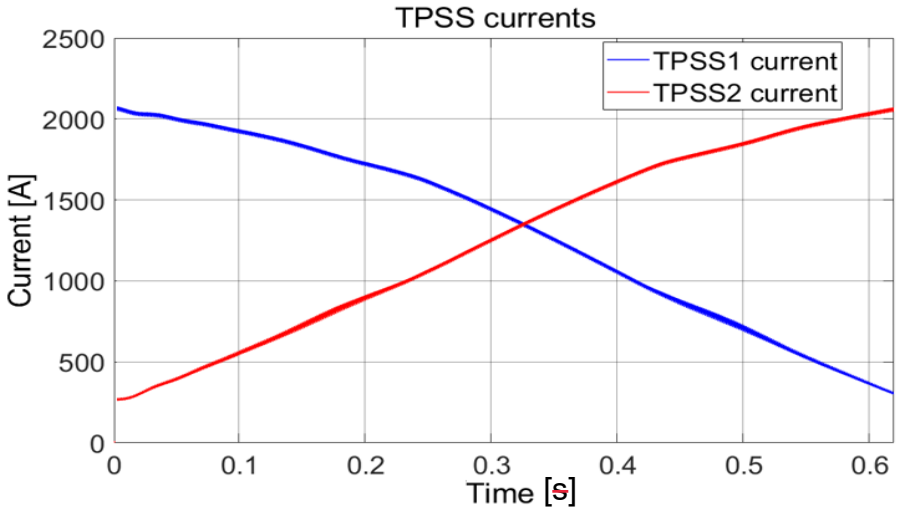

Figure 6.16: TPSS currents for the maximum speed scenario on the up-line.

The currents supplied by the TPSSs show the general, symmetrical trend that is expected under bilateral power supply for a train at constant speed, as can be seen in Figure 6.16. The TPSS closest to the traction load supplies the majority of the current, that decreases as the train moves further. The maximum current of approximately 2010 A is delivered by each TPSS upon the crossover of the train. This value is higher than the rated current of the TPSS, but still well within the maximum 5-minute overload limit of 3500 A. Due to the time compression of the input signals required to allow the simulation to run in a reasonable amount of time, the waveforms are slightly distorted and do not perfectly match the theoretical trend.

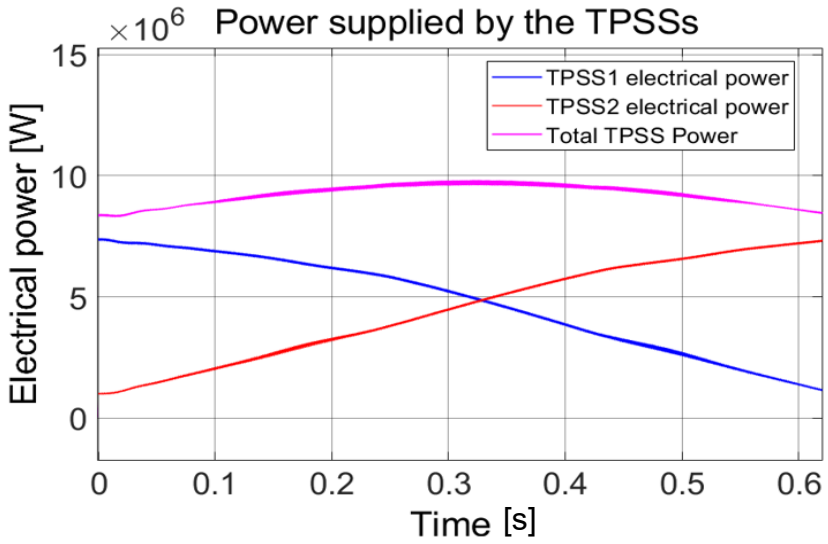

Figure 6.17: Electrical power supplied by the TPSSs.

Similarly to the currents, the electrical power supplied by the each TPSS is commensurate to the distance from the traction load. A shown in Figure 6.17, the total power supplied by the TPSSs has a maximum of 9.88 MW when the train is in the middle of the track, where the transmission losses to be compensated are highest, and a minimum of 8.53 MW in correspondence with the TPSSs.

6.2.2. One train traveling at maximum speed on the down-line

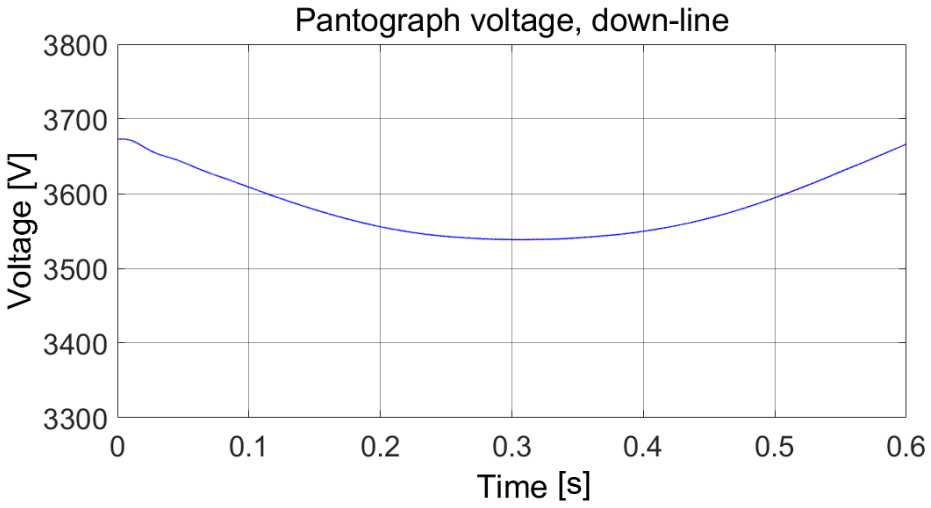

Figure 6.18: Pantograph voltage of Train 2 at maximum speed on the downhill track.

Figure 6.18 reveals that, compared to the uphill cruising scenario, downhill cruising is far less demanding in terms of power and current absorption. This is reflected on the catenary voltage which presents a reduced voltage drop and has a minimum value of 3540 V in the middle of the line, as well as a higher voltage at the TPSS due to lower current drawn from the power supply and the associated voltage drop on the transformer windings.

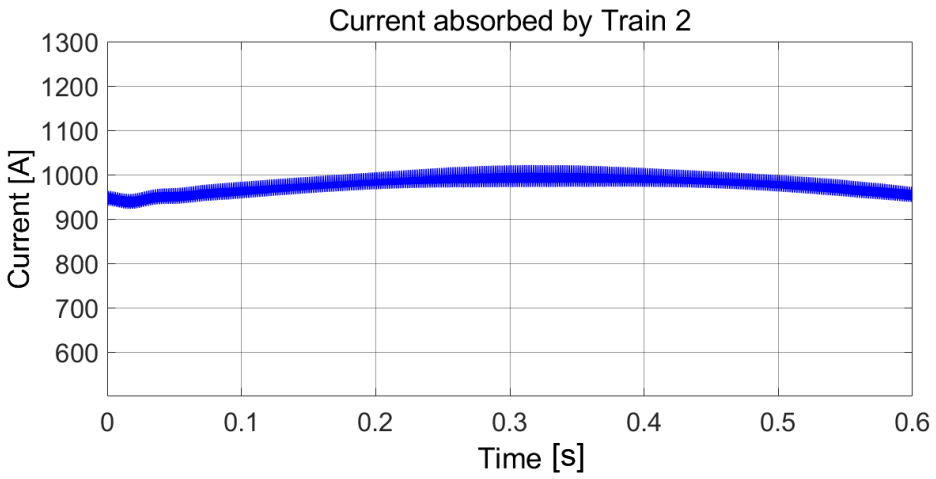

Figure 6.19: Current absorbed by Train 2 at maximum speed on the downhill track.

The train absorbs a maximum current of approximately 997A in the middle of the line, as shown in Figure 6.19, which is just over one-third than that absorbed when cruising on the uphill track.

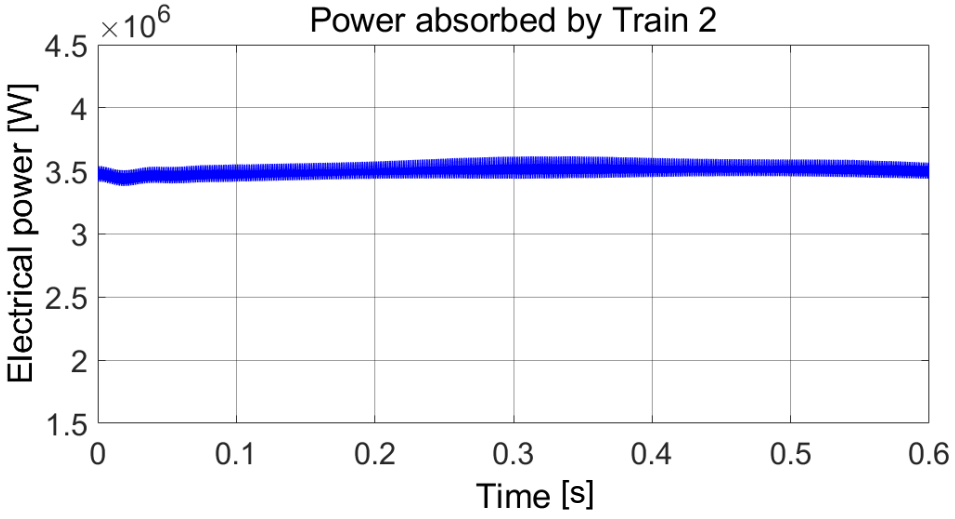

Figure 6.20: Electrical power absorbed by Train 2 at maximum speed on the downhill track.

According to Figure 6.20, the electrical power demand when cruising at maximum speed on the downhill track is approximately 3.5 MW constant, to maintain the desired mission profile at the speed of 300 km/h.

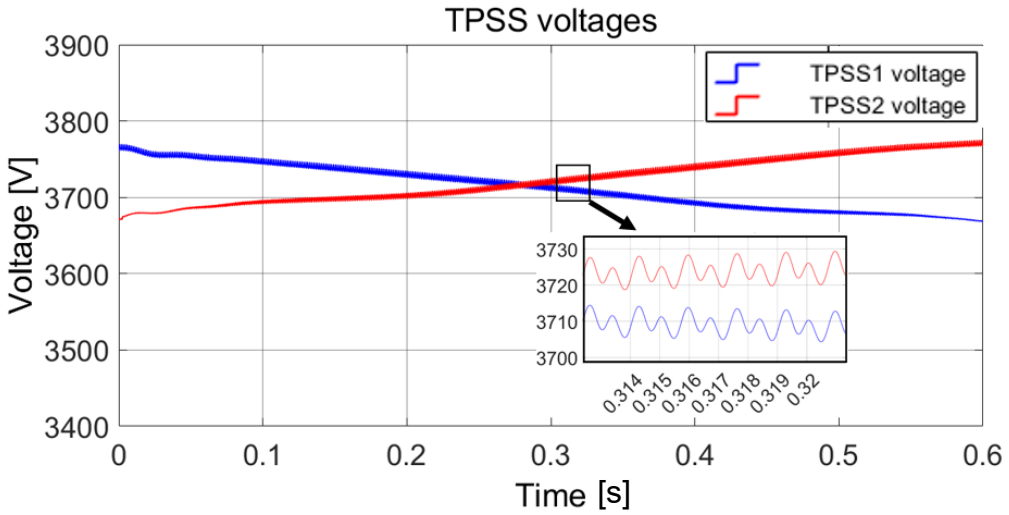

Figure 6.21: TPSS voltages.

For a complete overview of the traction substation operation, the substation voltages are shown in Figure 6.21. As Train 2 moves from TPSS 2 to TPSS 1, the voltage of TPSS 2 decreases (as the electrical load seen from TPSS 2 increases) and the voltage of TPSS 1 increases (as the load seen by TPSS 1 decreases). The trend is inverted on the uphill track, where the direction of travel is opposite. The harmonic component at 600 Hz is once again highlighted.

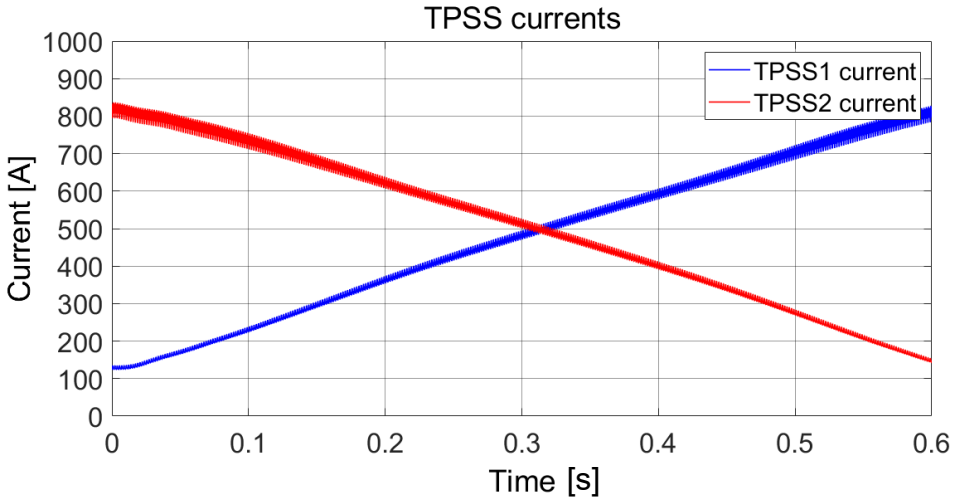

Figure 6.22: TPSS currents for maximum speed scenario on the down-line,

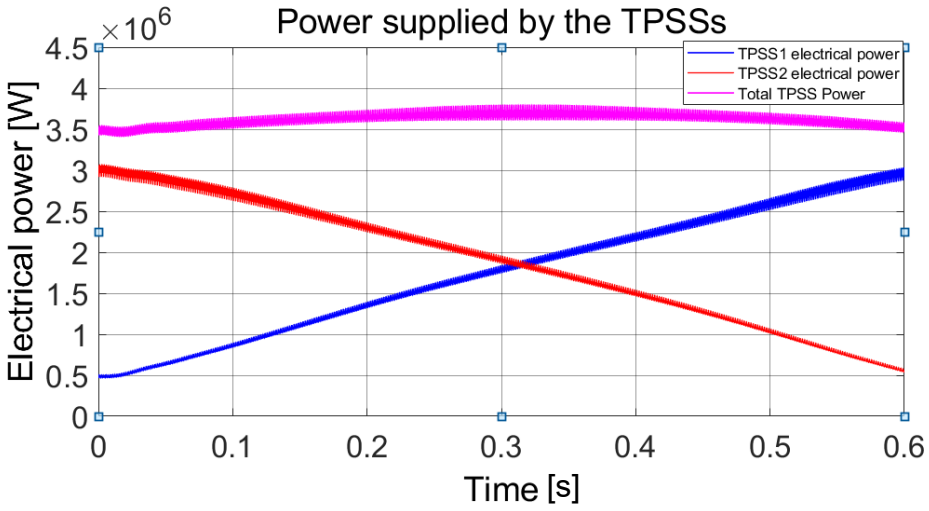

Figure 6.23: Electrical power supplied by the TPSSs.

As can be seen in Figure 6.22 and Figure 6.23, the currents and electrical power supplied by the TPSSs are well within the operational limits of the TPSSs, and follow the trend that is expected under bilateral power supply. The maximum current, when the train crosses the TPSS position, is approximately 800 A and the total power supplied by the TPSSs reaches 3.72 MW, less than half as compared to the maximum speed scenario on the up-line.

6.2.3. Two trains traveling at maximum speed

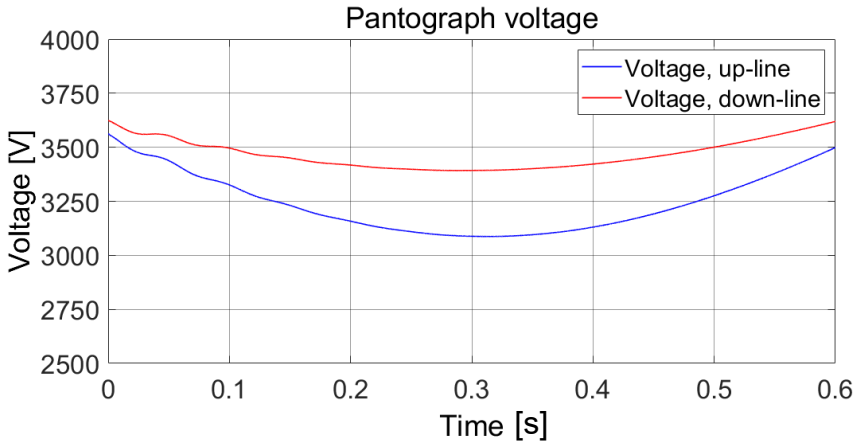

Figure 6.24: Pantograph voltages at maximum speed.

The difference in line voltage drop between the up-line and the down-line can be noticed in Figure 6.24, as anticipated in the previous paragraphs, due to the different power required by the trains to meet the desired mission profile.

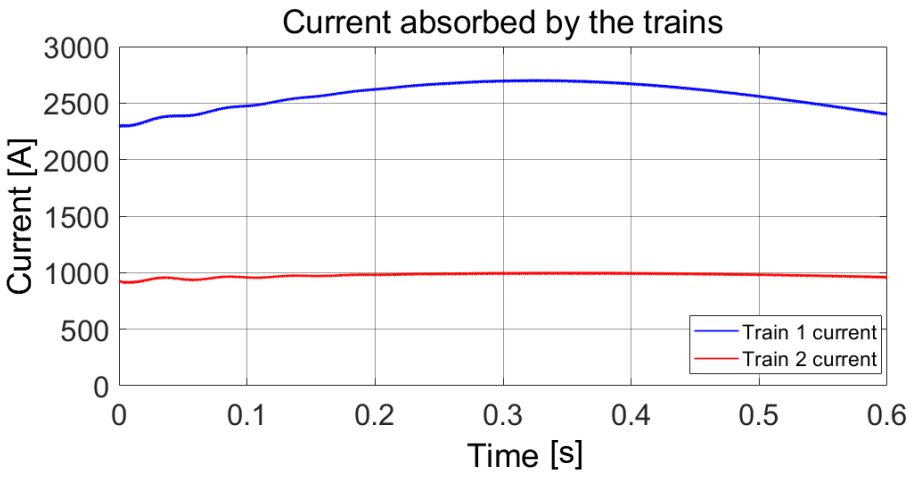

Figure 6.25: Current absorbed by the trains at maximum speed.

The appreciable difference in current uptake between Train 1 on the uphill track and Train 2 on the down hill track can be noticed in Figure 6.25.

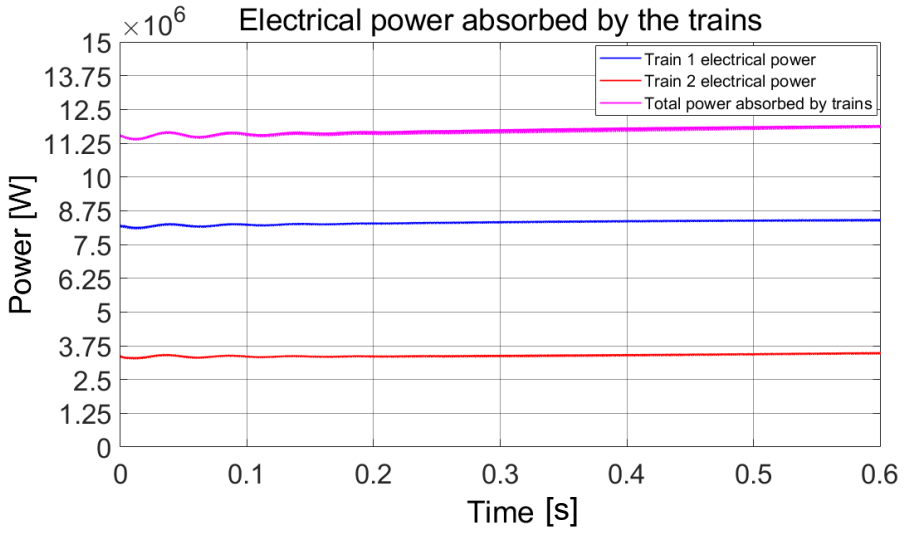

Figure 6.26: Electrical power absorbed by the trains at maximum speed.

The considerable power demand given by the simultaneous presence of the trains traveling at maximum speed in the railway line can be seen in Figure 6.26. The total power absorbed by the traction loads is approximately 11.32 MW.

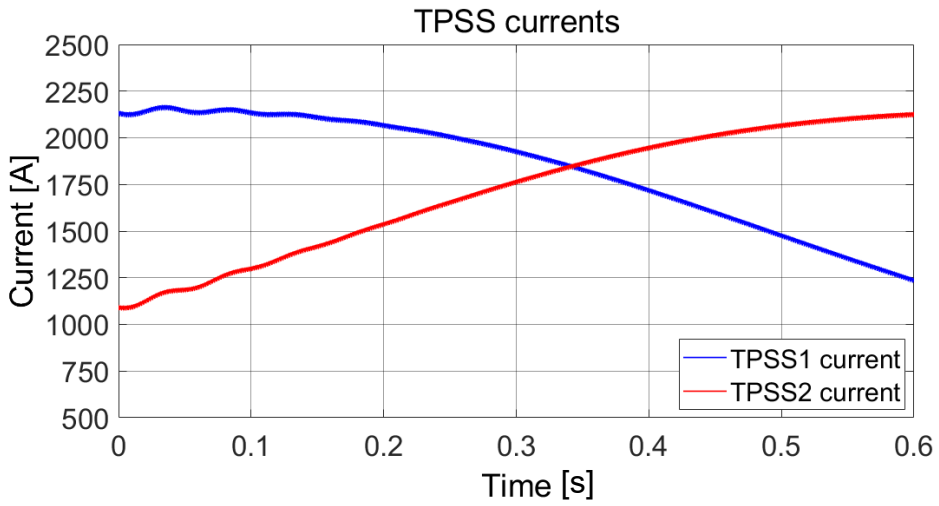

Figure 6.27: TPSS currents supplied to the trains at maximum speed.

In this scenario the TPSSs operate mostly above their current rating of 1500 A, with peak current delivery of 2120 A. Due to the considerable difference between the current absorbed by Train 1 and Train 2, the general trend of the TPSS is mostly dependent on the position of Train 1 (which travels at a slightly lower speed), which explains the slight shift of the intersection of the individual current plots in Figure 6.27.

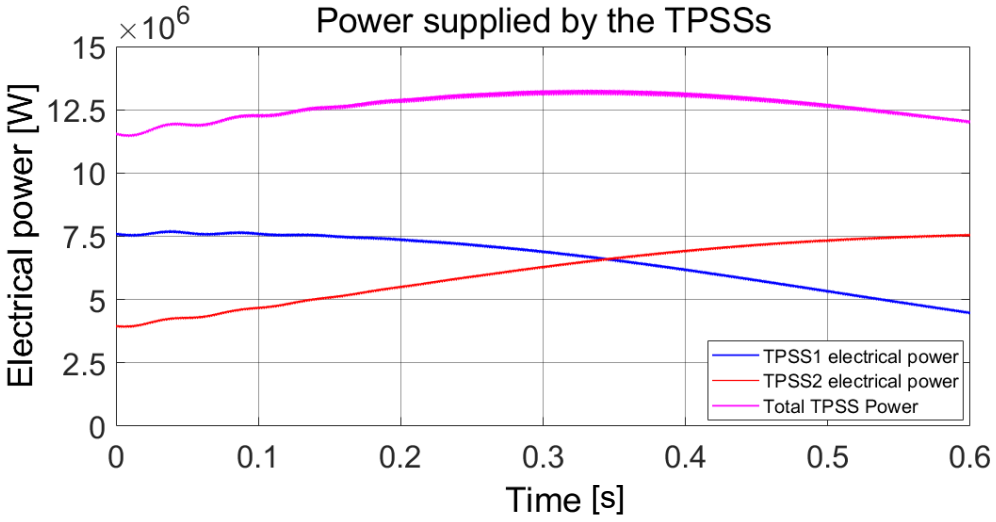

Figure 6.28: Electrical power supplied by the TPSSs.

In accordance with the total power demand of the traction loads in this scenario, the total power supplied by the TPSSs is, on average, 12.5 MW, with a maximum of 13.22 MW as shown in Figure 6.28. For most of the duration of travel the TPSSs work in overload conditions.

6.2.4. Two trains accelerating from rest to maximum speed

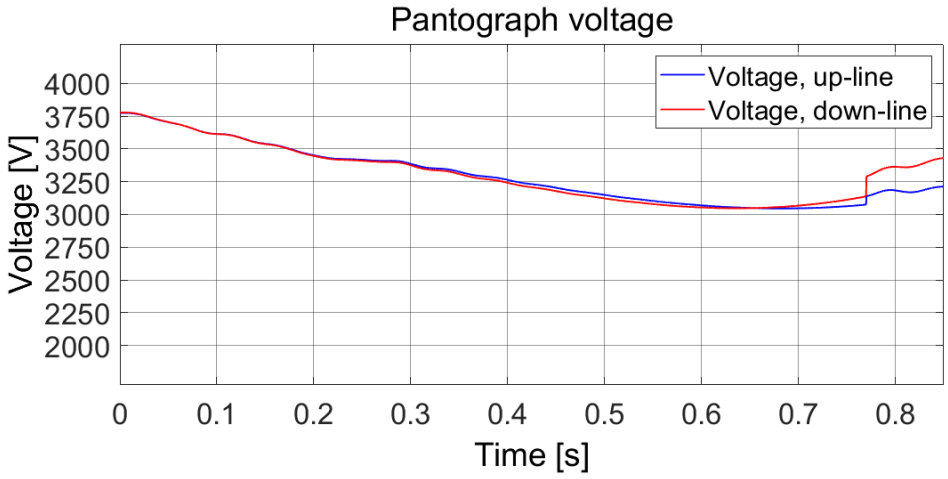

Figure 6.29: Pantograph voltages at start-up

The line voltages vary in time as shown in Figure 6.29, according to the trains' position and speed, which is no longer constant. The maximum voltage drops still occur at the midpoint of the lines, that are reached later due to the initial acceleration stage . The maximum power absorption occurs when both trains have reached the base speed and accelerate to the maximum speed, during which they absorb the same amount of power, equal to the rated power of the ETR 1000. For this reason both lines have the same voltage drop and reach a minimum voltage of approximately 3010 V. Train 2 reaches the top speed of 300 km/h around 0.72 s of simulation time and then cruises at constant maximum speed. This transition between accelerating and cruising at constant speed entails a significant reduction in power and current absorbed by Train 2, causing the line voltage drop to decrease as seen in the final portion of Figure 6.29. The reduction in power consumption given by the transition from acceleration to constant speed cruising of Train 2 also affects, albeit in a minor way, the line voltage of Train 1. Train 1 does not reach the top speed of 300 km/h, but continues the acceleration phase due to the uphill gradient, and continues to absorb the maximum power all throughout the crossing between the TPSSs.

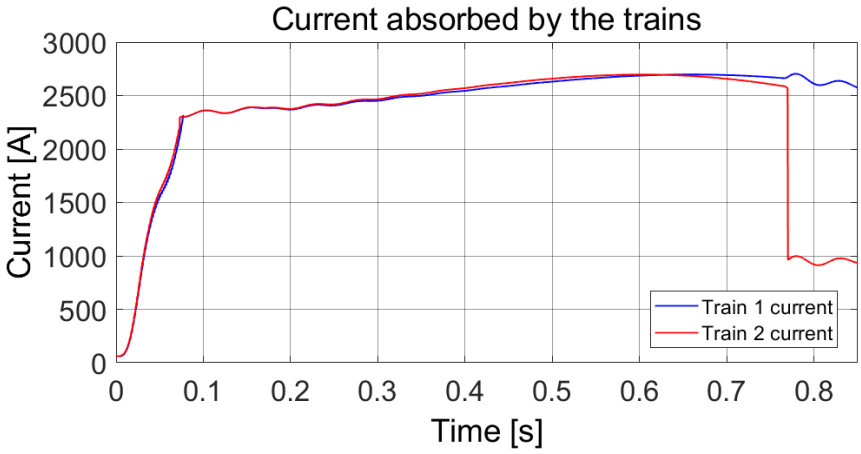

Figure 6.30: Currents absorbed by the trains at start-up

As shown in Figure 6.30, the current absorption profiles are coherent with the fact that, between rest and base speed, the current absorbed by the trains increases approximately linearly, and then takes on the required profile associated with the maximum power consumption throughout the acceleration from base speed to maximum speed. The transition from acceleration to constant maximum speed for Train 2 can be seen in the final portion of the plot, where the current absorbed by Train 2 decreases from 2500 A to approximately 960 A, while the current absorbed by Train 1, on average, maintains remains unchanged (perturbations aside).

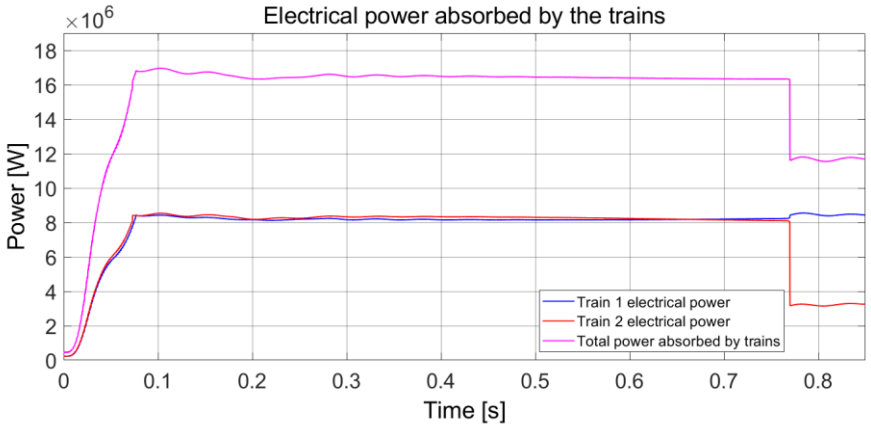

Figure 6.31: Electrical power absorbed by the traction loads at start-up.

During start-up, both trains develop the same power absorption, as shown in Figure 6.31, as they operate within the limits outlined in Section 5.3.4 regardless of the track gradient. When accelerating between the base speed and the maximum speed, both trains absorb the maximum power of 8.45 MW, for a total electrical power absorption of approximately 17 MW, which determines the highest power consumption scenario. As expected, Train 2 reaches the top speed of 300 km/h and

ceases the acceleration phase, causing a significant decrease in power absorption that drops to an average value 3.5 MW as can be seen in the final portion of the plot in Figure 6.31.

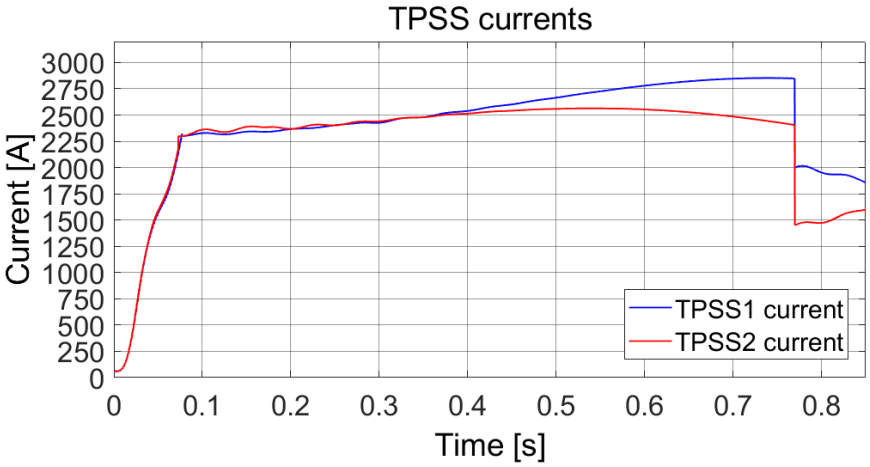

Figure 6.32: TPSS currents supplied to the trains at start-up.

According to Figure 6.32, with Train 1 starting from TPSS 1 and Train 2 starting from TPSS 2, the current delivered by the TPSSs is initially the same, and slightly varies as the distance from the traction loads changes due to the different acceleration profiles according to the track gradient. The overall power reduction as Train 2 switches from the acceleration stage to the cruising stage is again observed at the final portion of the plot. Both TPSSs operate for most of the time in overload conditions but still within the limits outlined in Table 5.8.

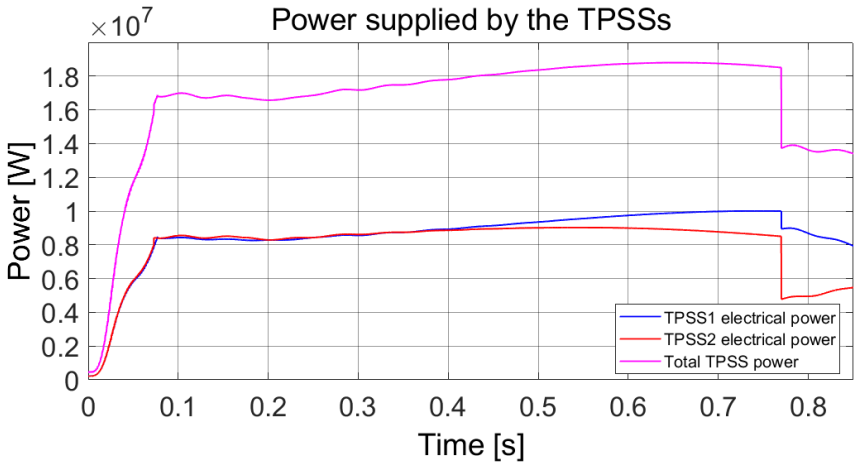

Figure 6.33: Electrical power supplied by the TPSSs

The maximum power consumption scenario given by the simultaneous presence of the accelerating trains along the line can be appreciated from Figure 6.33. The total power provided by the TPSSs reaches a maximum of approximately 19 MW and

drops as Train 2 ceases the acceleration phase and enters the constant cruising speed phase.

6.2.5. Two trains traveling at maximum speed, PV and wind RES available

This scenario considers the simultaneous presence of two trains cursing at maximum speed on their respective tracks and high availability of solar and wind generation.

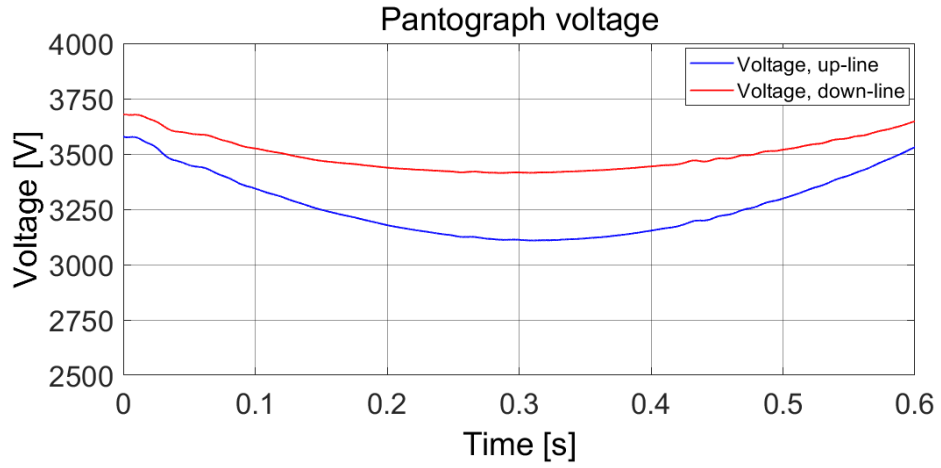

Figure 6.34: Pantograph voltages at maximum speed with RES available.

Comparing Figure 6.34 and Figure 6.24, the voltage profiles along the lines are virtually unchanged if not for some minor perturbations induced by the MPPT process associated with the PV system.

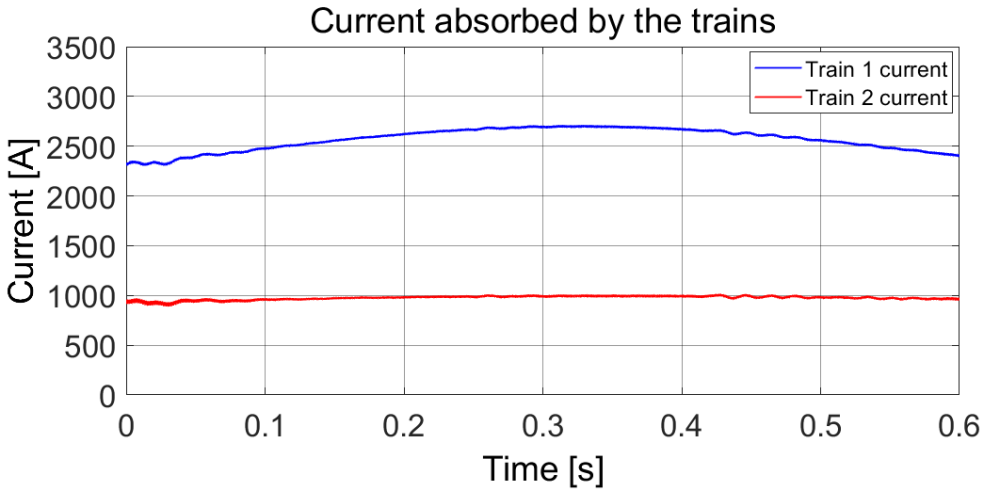

Figure 6.35: Current absorbed by the trains at maximum speed with RES available.

The current absorption profiles shown in Figure 6.35 are practically identical to the case without integrated RES, aside from the minor perturbations induced by the renewable generators.

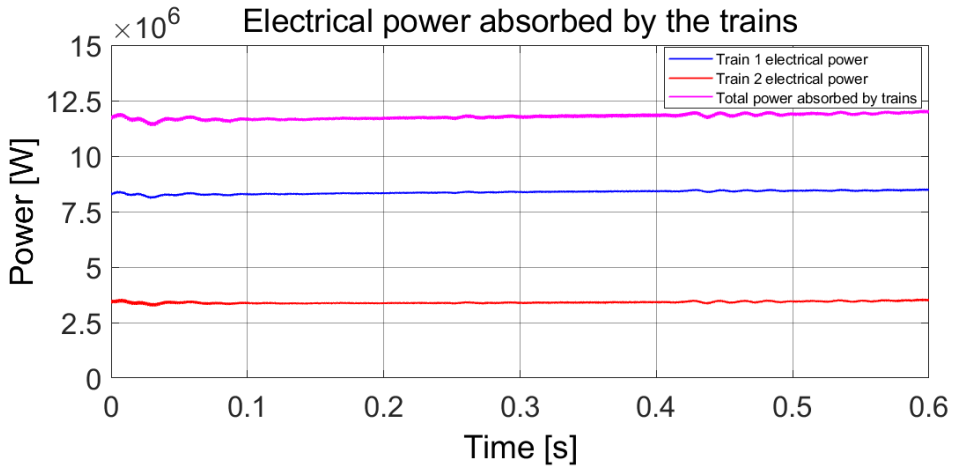

Figure 6.36: Electrical power absorbed by the trains at maximum speed with RES available.

According to Figure 6.36, similarly to the pantograph voltage and current profiles, the electrical power absorbed by the traction loads remains unchanged regardless of RES connection, as the mission profile is the same.

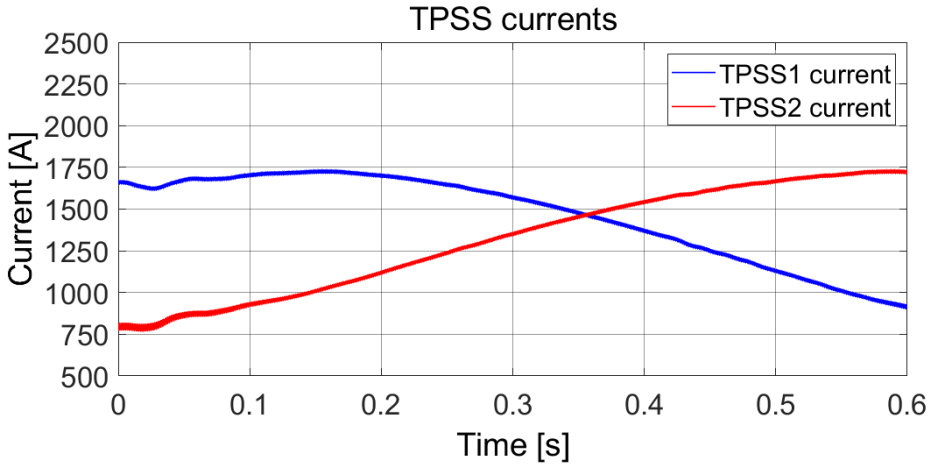

Figure 6.37: TPSS currents supplied to the trains with RES available.

The contribution of the renewable generators can be observed from the current and electrical power profiles associated with the TPSSs, which are significantly reduced. As shown in Figure 6.37, the peak current supplied by each TPSS drops from over

2100 A without RES to just under 1750 A with RES, due to the PV wind generators operating close to full capacity.

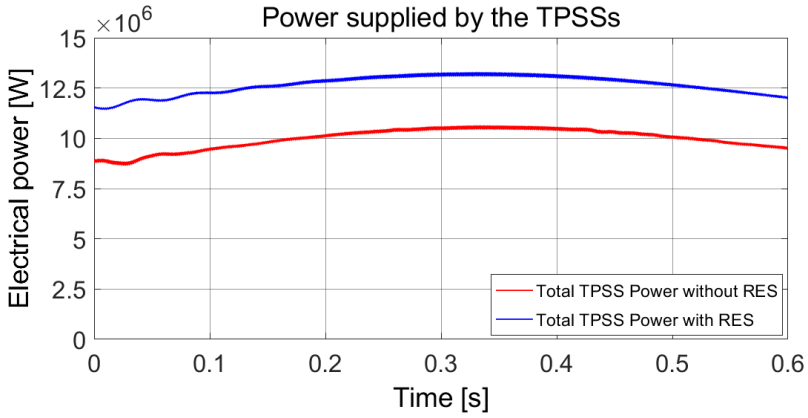

Figure 6.38(a): Total TPSS electrical power with and without RES.

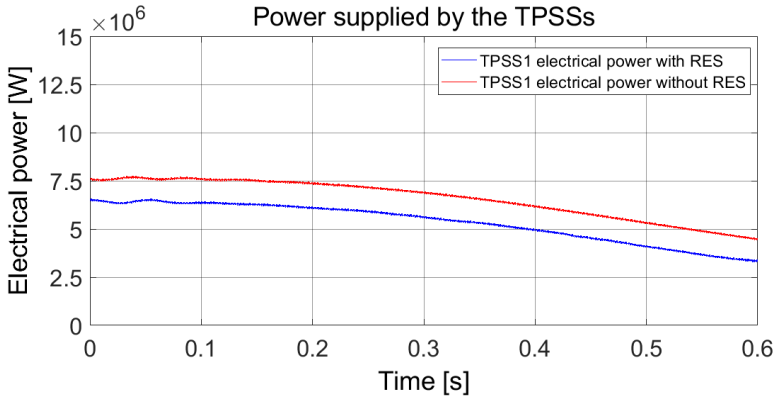

Figure 6.39(b): TPSS 1 electrical power with and without RES.

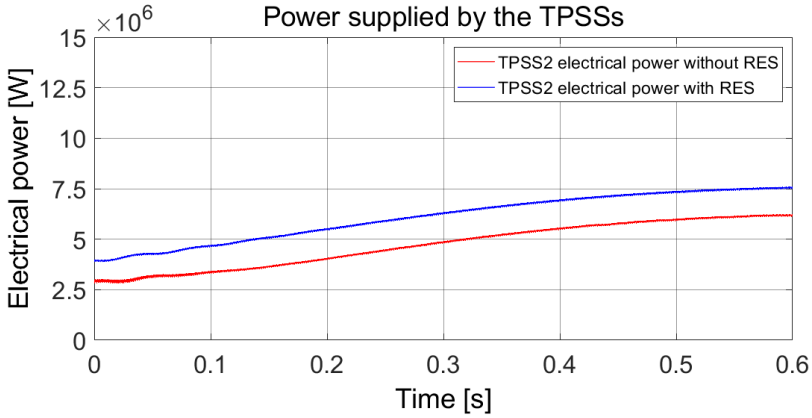

Figure 6.40(c): TPSS 2 electrical power with and without RES.

As shown in Figure 6.38(a), the peak total power supplied by the TPSSs decreases from 13.22 MW without RES to 10.61 MW with RES operating near full capacity, that is, approximately 20% less power is drawn from the mains due to the contribution of the renewable generators. When comparing the individual TPSSs, as shown in Figure 6.38(a) and 6.38(b) with and without RES, the percentage decrease in power demand over the travel time interval is even higher, drastically decreasing the duration of TPSS overloads. Considering the difference in total power demand and that the crossing between TPSSs occurs in 241 seconds, the overall energy savings due to the renewable generators amount to approximately 200 kWh when both trains simultaneously travel at maximum speed.

The following plots show the operation of the PV generator and its components, including the solar irradiance profile, the PV-side and the output-side electrical quantities.

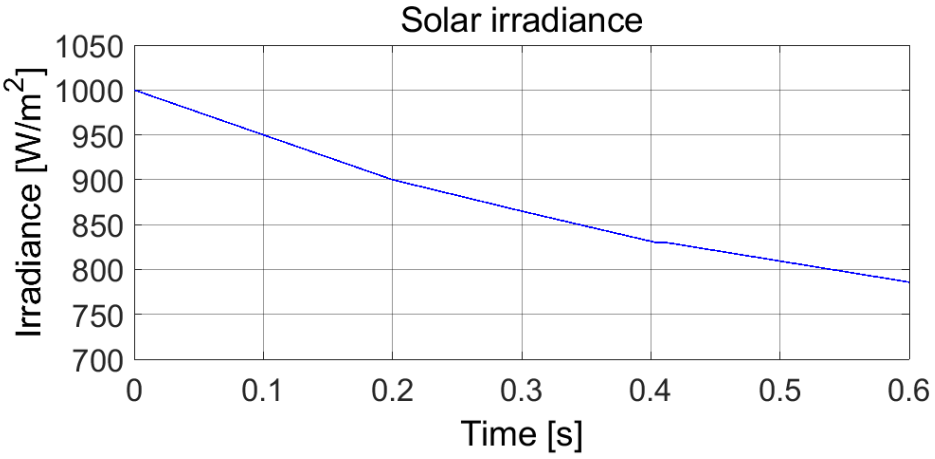

Figure 6.41: Solar irradiance profile.

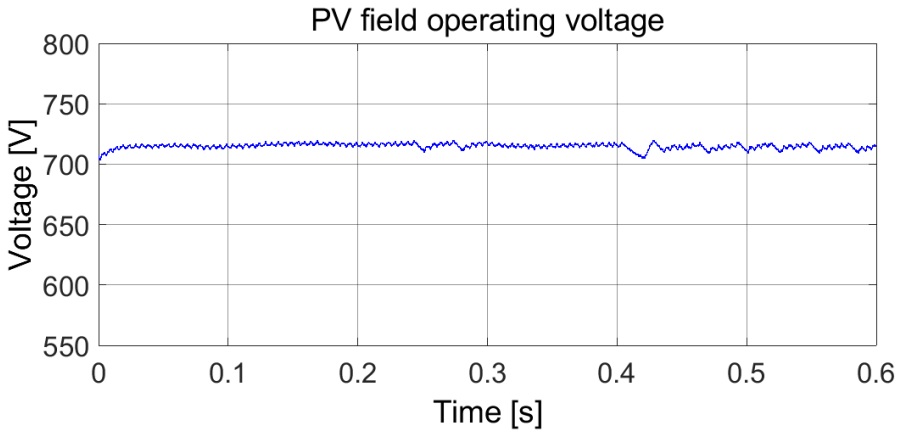

Figure 6.42: PV field operating voltage.

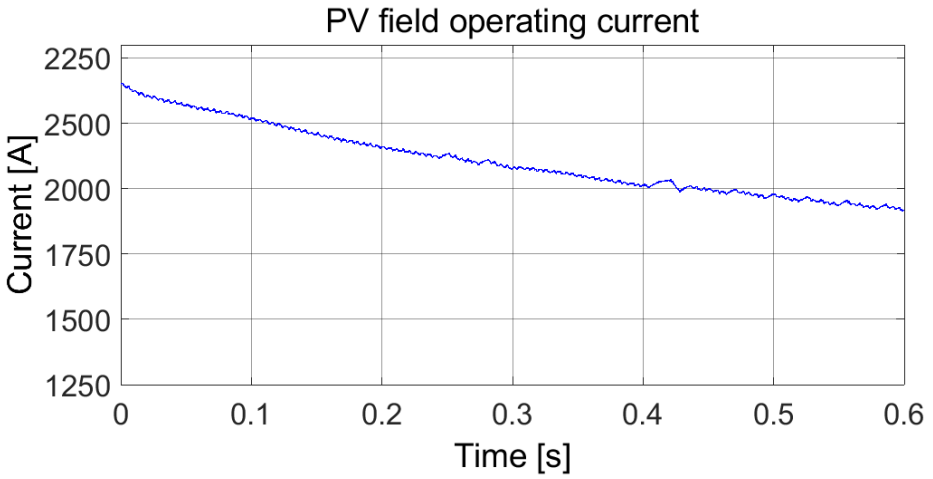

Figure 6.43: PV field operating current.

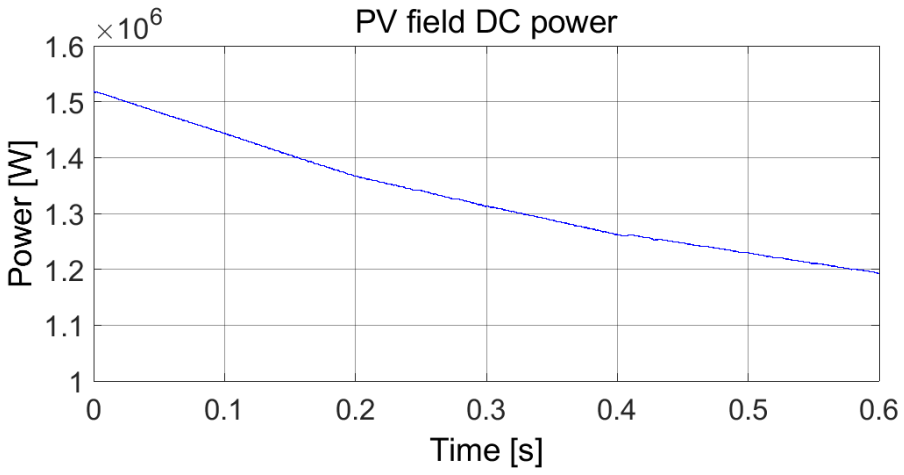

Figure 6.44: PV field DC power.

As shown in Figure 6.42, Figure 6.43, and Figure 6.44, the voltage, current, and DC power associated with the PV field vary under the effects of MPPT according to the incoming solar irradiance. In fact, the DC power closely follows the solar irradiance profile, demonstrating the effectiveness of the implemented MPPT algorithm.

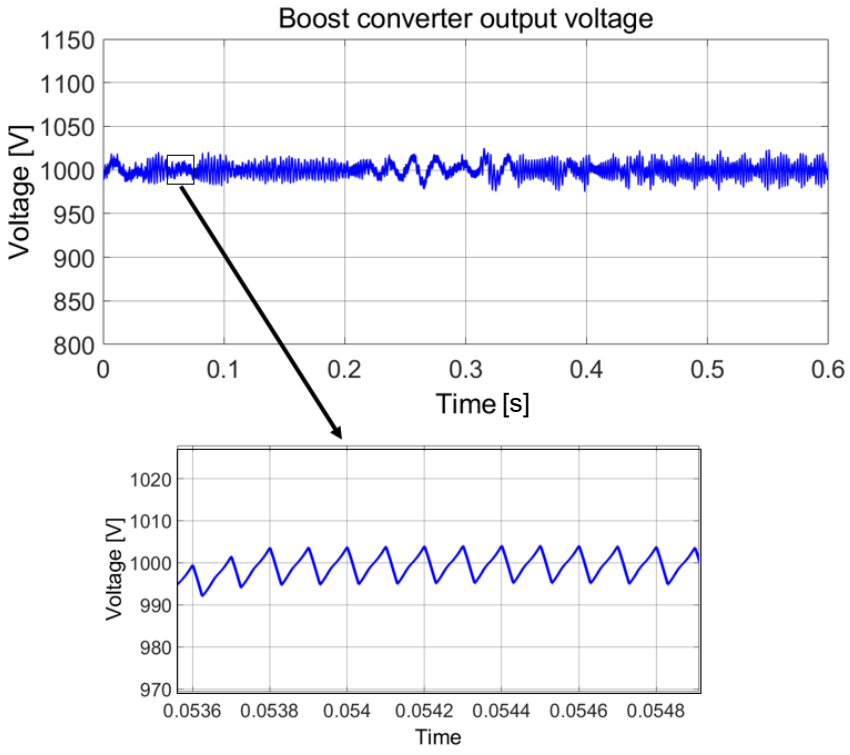

Figure 6.45: Boost converter output voltage.

The DC-DC voltage between the boost converter and the IBFB converter is effectively controlled to be maintained at 1000 V in order to execute the MPPT algorithm. The high frequency voltage ripples are contained to approximately 10 V at the switching frequency of 10 kHz. Lower frequency voltage ripples are also present due to the perturbations induced by the MPPT algorithm.

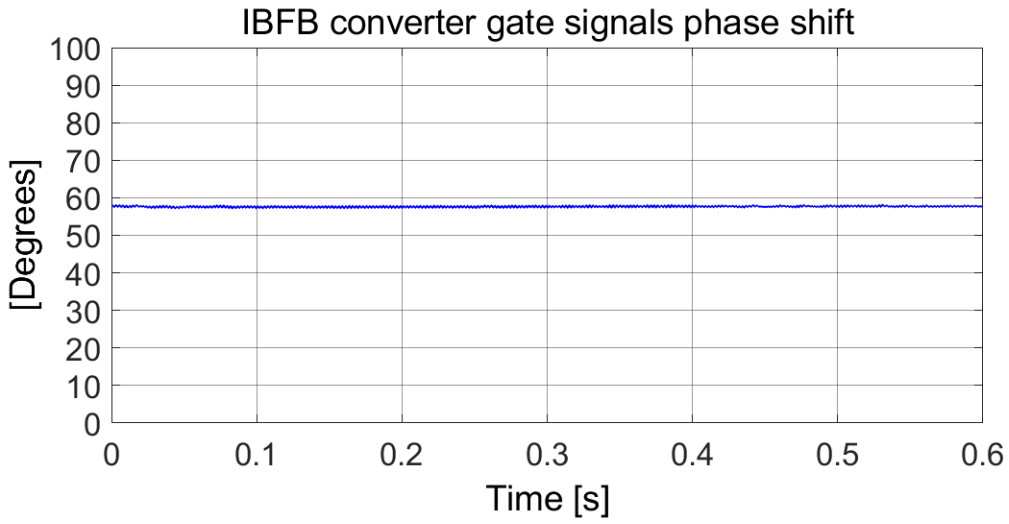

Figure 6.46: IBFB converter gate signals phase shift.

The IBFB switches are controlled to keep the DC-DC voltage shown in Figure 6.43 at 1000 V, to this end the phase shift between the gate signals of the IBFB switch pairs is shown in Figure 6.44.

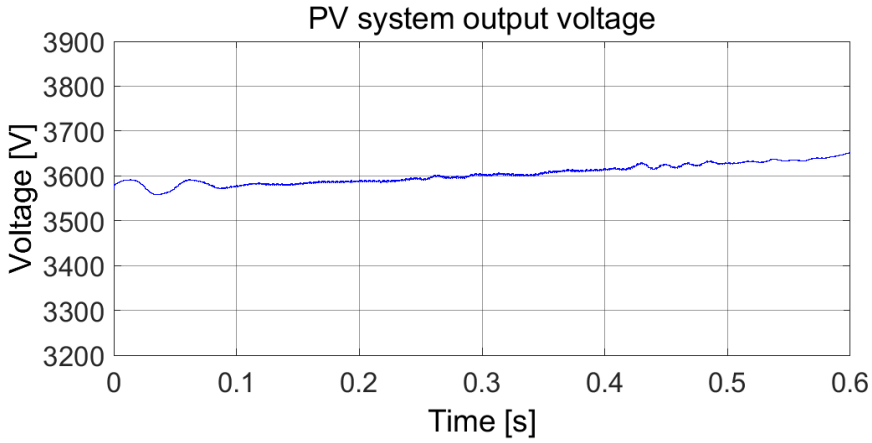

Figure 6.47: PV system output voltage

The PV system output terminals latch onto the voltage of TPSS 1 which acts as the prevailing grid, resulting in the output voltage as shown in Figure 6.45.

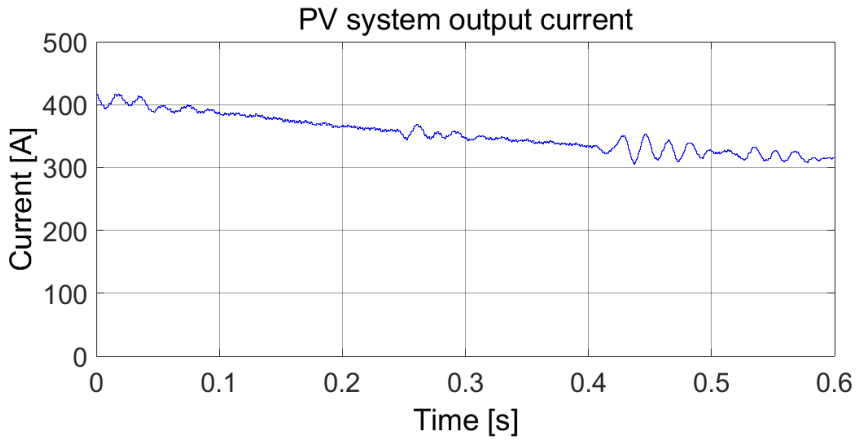

Figure 6.48: PV system output current.

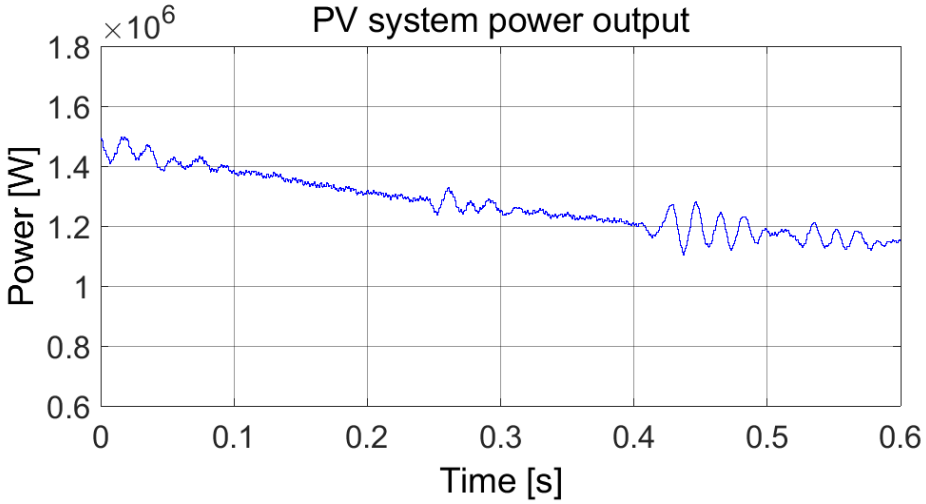

Figure 6.49: PV system power output.

The current and electrical power injected by the PV system into the traction circuit follow the solar irradiance profile, but present some fluctuations induced by the MPPT algorithm, that are further accentuated by the time compression of the simulation input signals, as can be seen in Figure 6.46 and Figure 6.47.

Finally, the wind farm plots for wind speed and electrical power output are shown in Figure 6.48 and Figure 6.49. The wind speed signal fed to the wind system is above the rated wind speed, resulting in a constant power output equal the rated power of 1.5 MW. The simplified model adopted for the wind farm does not produce fluctuations in the electrical power output.

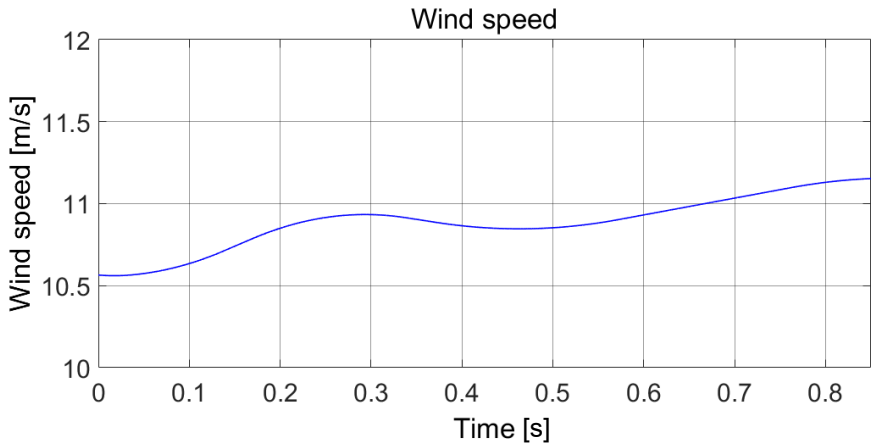

Figure 6.50: Wind speed profile.

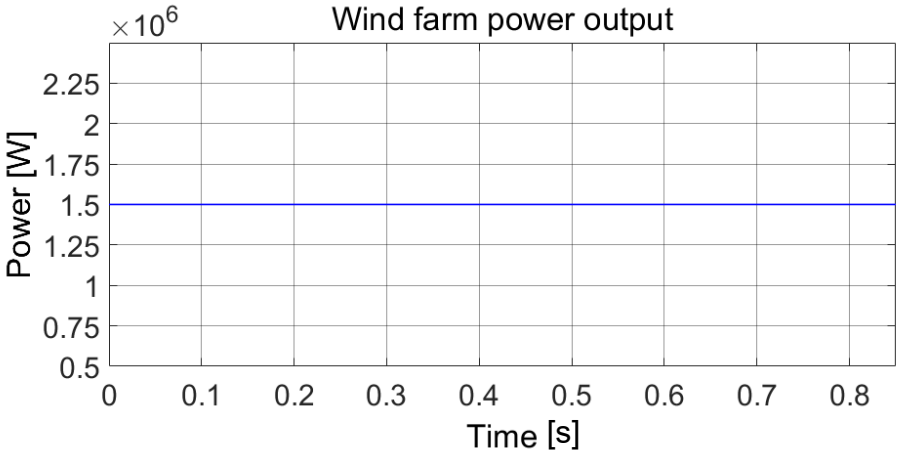

Figure 6.51: Wind farm power output.

6.2.6. One train traveling at maximum speed on the down-line, PV and wind RES available

This scenario considers the presence of Train 2 at maximum speed and high availability of solar and wind resources as in the previous case. The plots shown in Figure 6.50, 6.51, and 6.52 are essentially the same as those for the corresponding scenario without RES, albeit with some fluctuations induced by the PV generator controls.

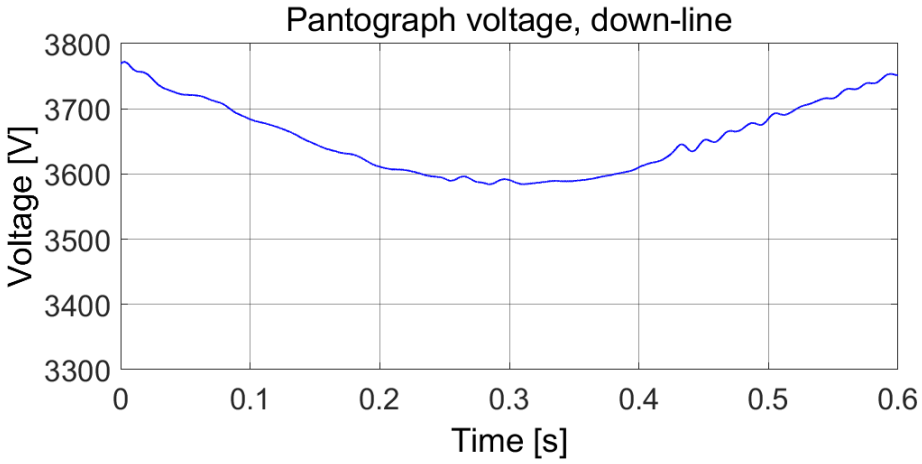

Figure 6.52: Pantograph voltage of Train 2 with RES.

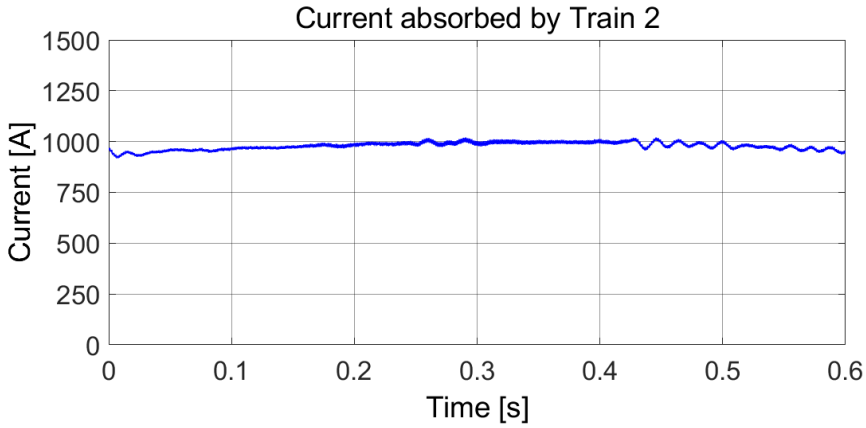

Figure 6.53: Current absorbed by Train 2 with RES.

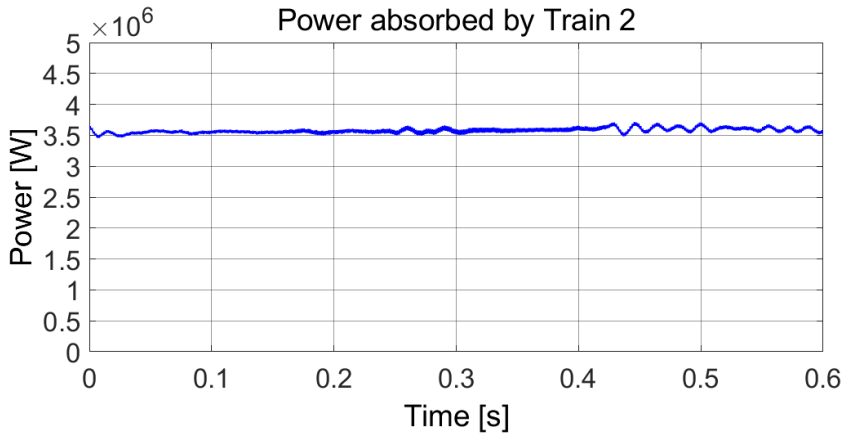

Figure 6.54: Power absorbed by Train 2 with RES:

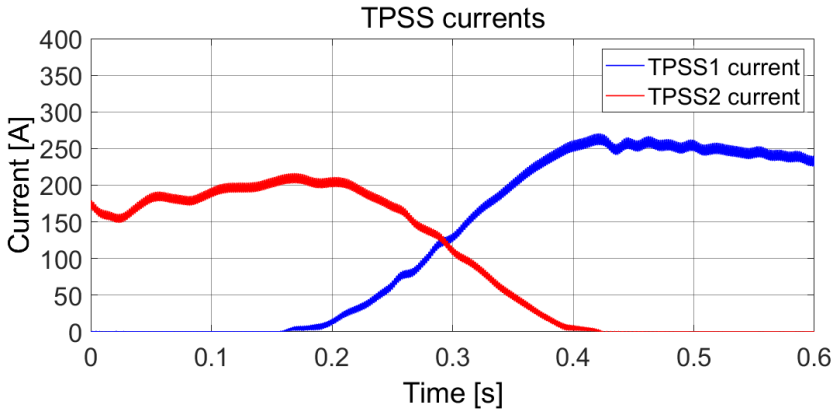

Figure 6.55: TPSS currents supplied Train 2 with RES available.

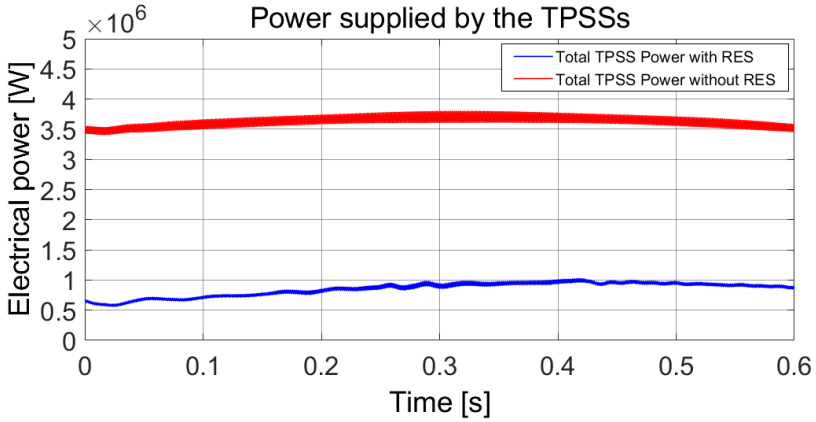

Figure 6.56(a): Total TPSS electrical power with and without RES.

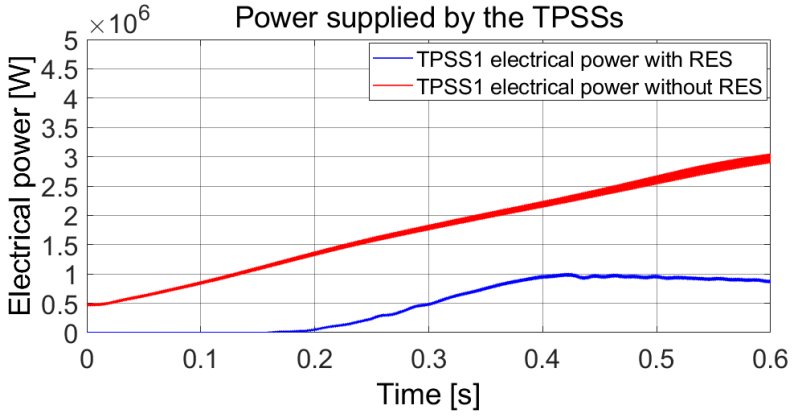

Figure 6.57(b): TPSS 1 electrical power with and without RES.

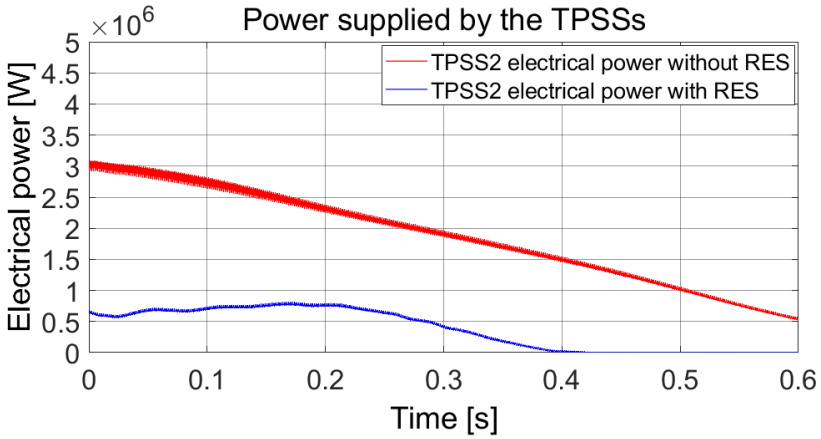

Figure 6.58(c): TPSS 2 electrical power with and without RES.

The significant contribution of the renewable generators to the power supply of Train 2 on the downhill track can be seen from the current and electrical power supply profiles in Figure 6.53 and Figures 6.54(a-c). Each TPPS is not called into action for about one-third of the train crossing time, as the power demand of the traction load is covered by the renewable generators. As shown in Figure 6.54(a), the maximum total power supplied by the TPSSs is 1 MW, compared to 3.72 MW without RES availability, which corresponds to a 73% decrease in peak power demand, highlighting the advantages in terms peak shaving capabilities given by the integration of RES into the power supply of the traction circuit.

The solar irradiance and the main electrical quantities associated with the operation of the PV generator are illustrated for conciseness. The same considerations for the previously considered case apply.

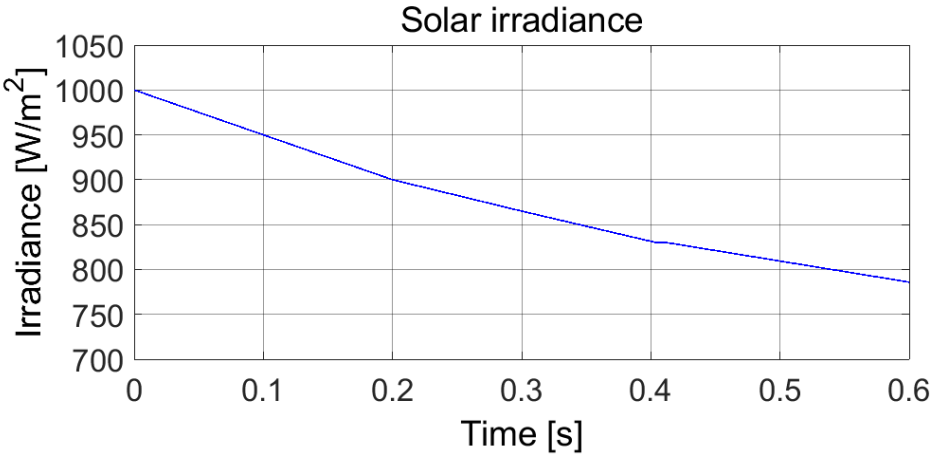

Figure 6.59: Solar irradiance profile.

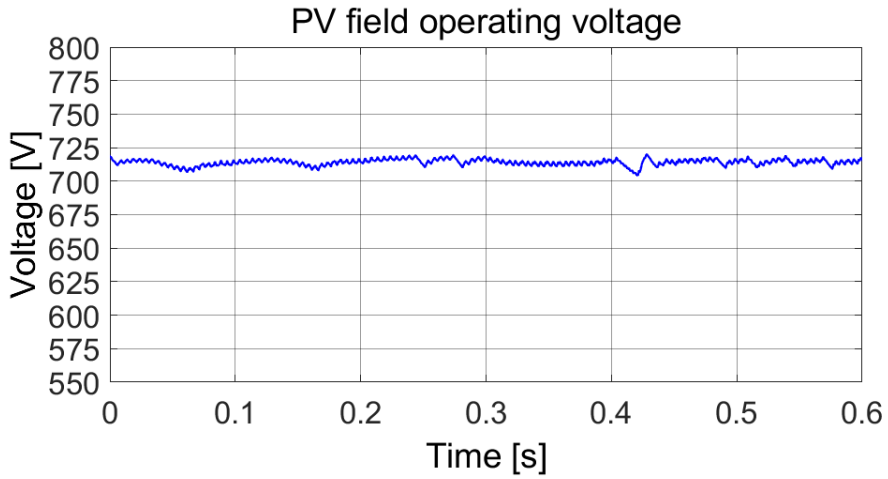

Figure 6.60: PV field operating voltage.

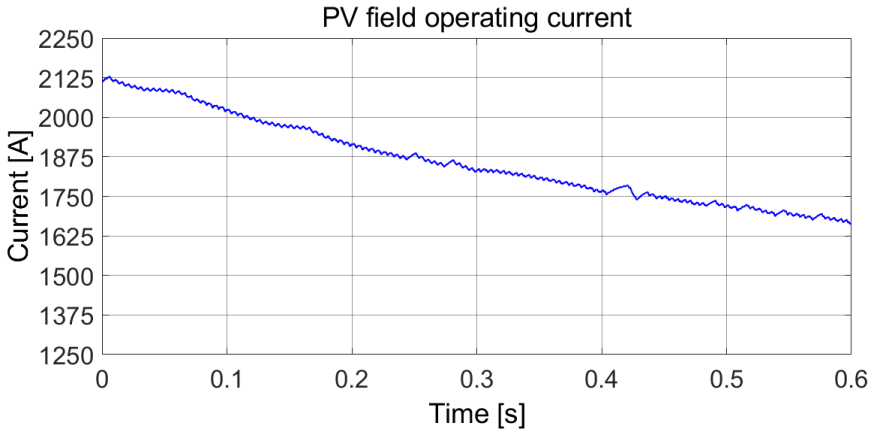

Figure 6.61: PV field operating current.

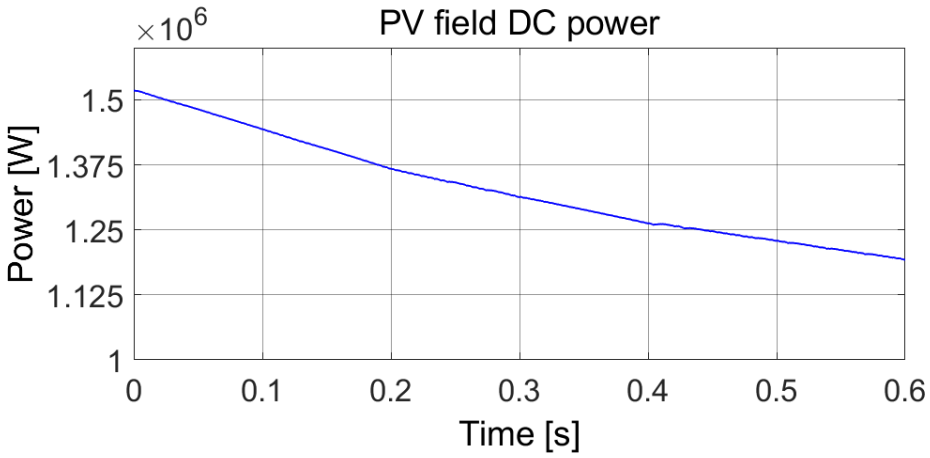

Figure 6.62: PV field DC power.

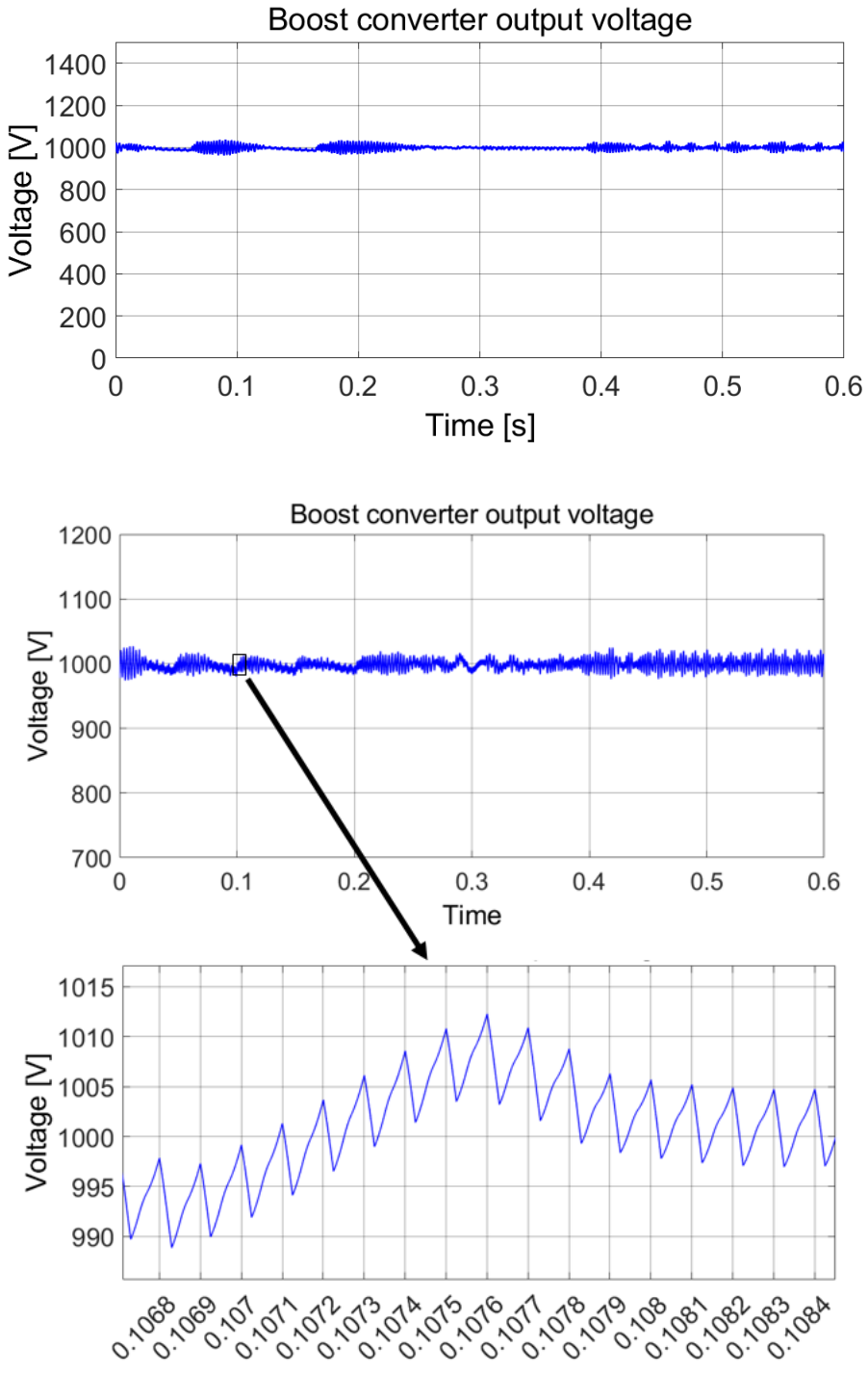

Figure 6.63: Boost converter output voltage.

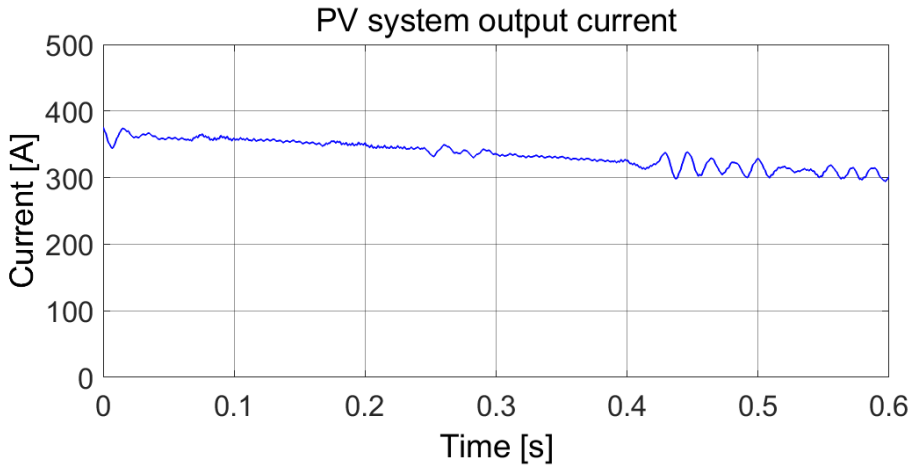

Figure 6.64: PV system output current.

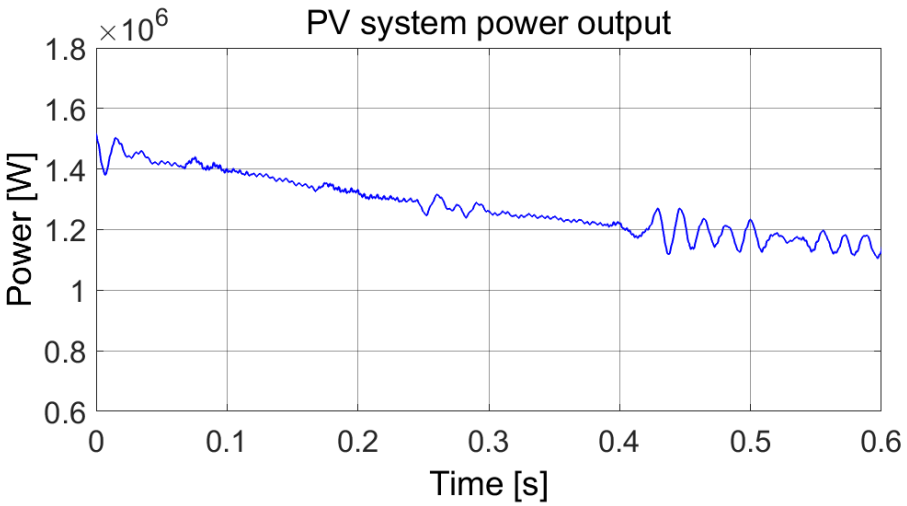

Figure 6.65: PV system power output.

As for the wind generators, the wind speed profile considered is again constantly above the rated wind speed, therefore the electrical power output is constant and equal to the rated power of the wind farm of 1.5 MW, as shown in Figure 6.62 and 6.63.

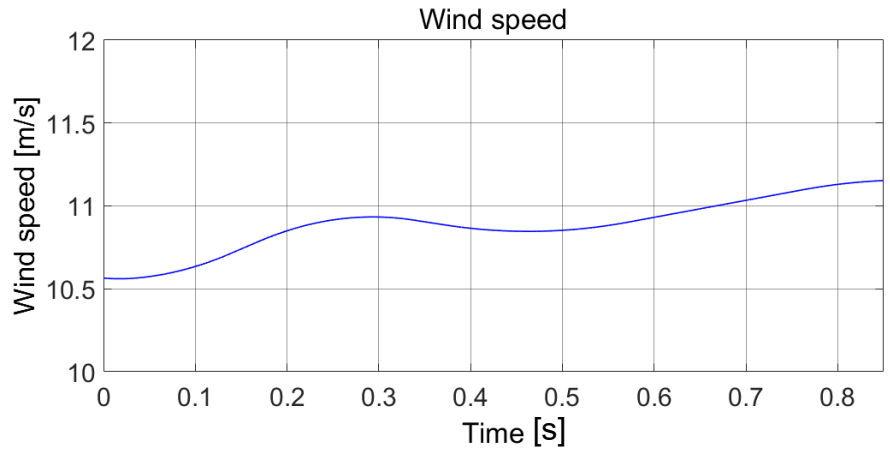

Figure 6.66: Wind speed profile.

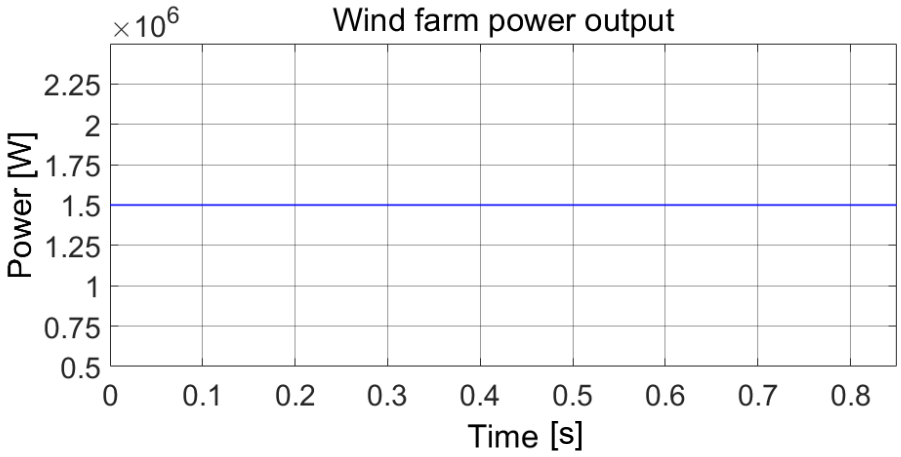

Figure 6.67: Wind farm power output.

6.2.7. Regenerative braking

The final scenario considered for the simulations is the possibility to utilize regenerative braking energy from a braking train on the down-line to power an accelerating train on the up-line.

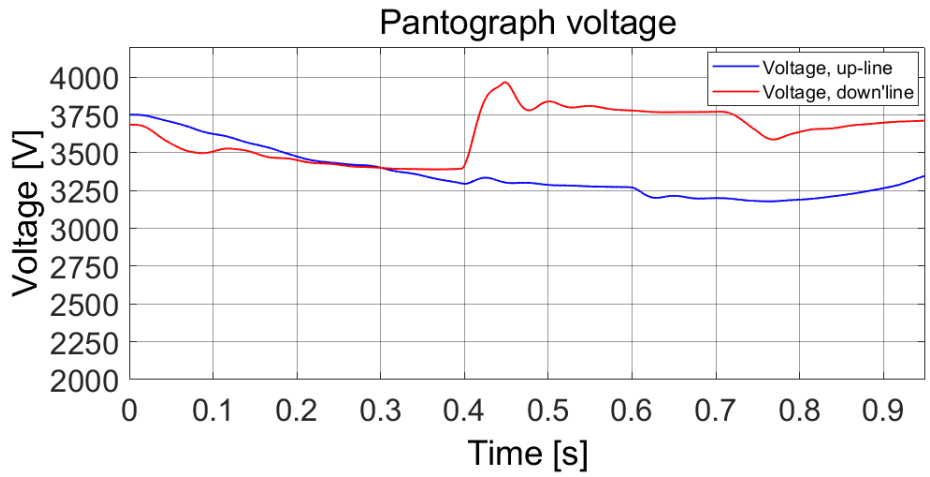

Figure 6.68. Pantograph voltages with regenerative braking of Train 2.

The regenerative braking of Train 2, which initiates around simulation time 0.4 s as shown in Figure 6.64, causes an increase in the voltage of the down-line, which rises from 3400 V to 3750 V after a rapid transient characterized by a voltage surge in the down-line due to the current injected by the braking train. Such voltage surge is still within the maximum voltage limit of 3900 V for a maximum duration of 5 minutes as outlined in Table 3.3 for the 3 kV railway system. The fluctuations visible around 0.7 s are due to the transition between the braking regime between the maximum speed and the base speed, and between the base speed and rest.

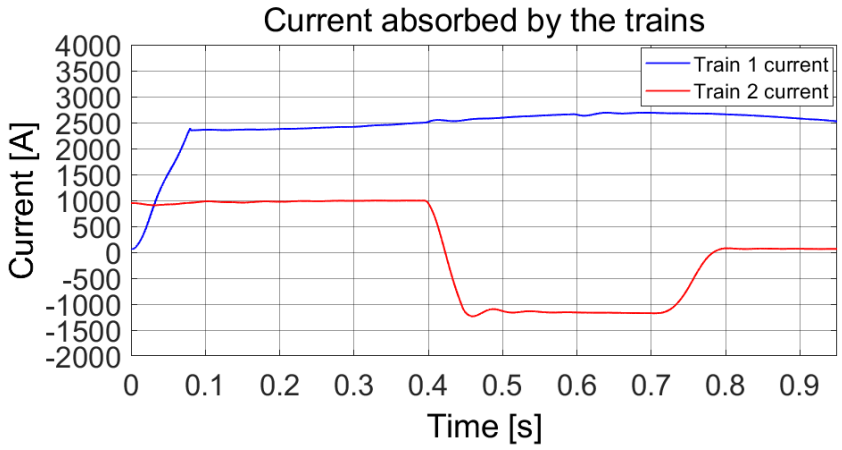

Figure 6.69: Currents absorbed by the trains with Train 2 in regenerative braking.

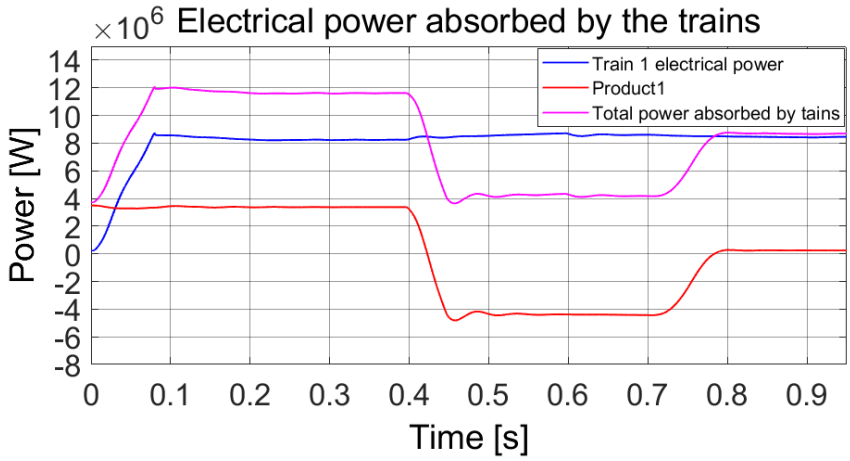

Figure 6.70: Electrical power absorbed with Train 2 in regenerative braking.

The effects of regenerative braking on the current and electrical power associated with the traction load can be understood from Figure 6.65 and 6.66, where, aside from rapid transients due to time compression of the simulation signals, the current and the electrical power associated with Train 2 become inverted and the train effectively acts as a power supply injecting over 1150 A and 4.2 MW into the traction circuit. The total power absorbed by the traction loads drops from 11.32 MW to approximately 4 MW. The current and electrical power injection profile during regenerative braking follow the braking characteristic outlined in Section 5.3.5. Around 0.75 s Train 2 comes to rest and acts as a traction load that only absorbs the electrical power required by the auxiliary services.

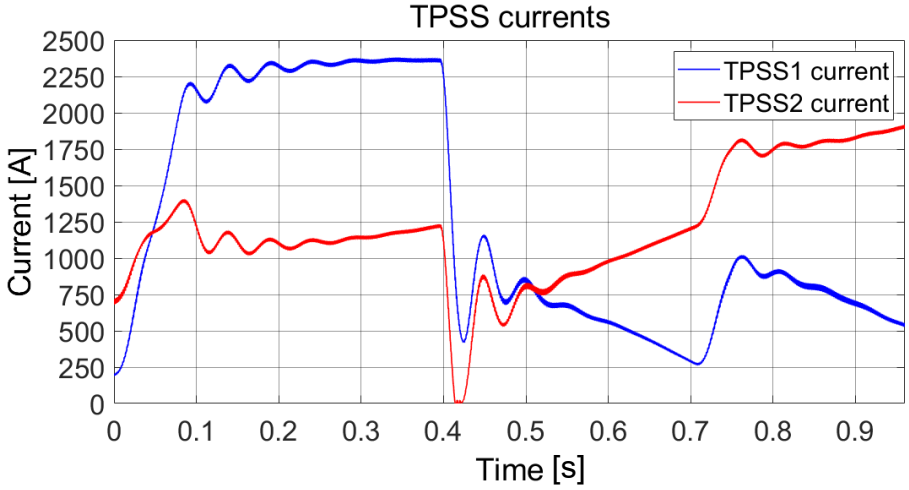

Figure 6.71: TPSS currents with Train 2 regenerative braking.

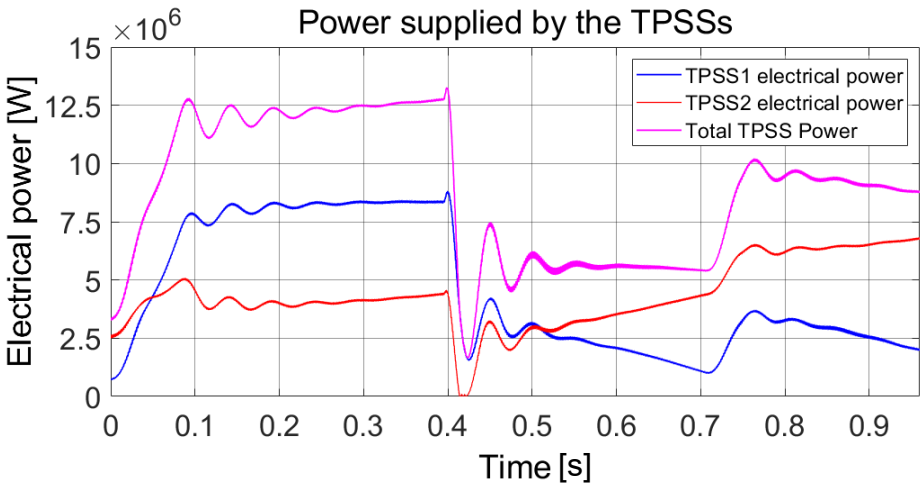

Figure 6.72: Power supplied by the TPSSs with Train 2 regenerative braking.

During regenerative braking of Train 2, the contribution of the TPSSs to the power supply of the traction loads is greatly reduced. As shown in Figure 6.68, the total power supplied by the TPSSs drops from approximately 12.5 MW to 5.5 MW for the duration of the maximum braking effort. Considering that the entire braking process lasts for 130 seconds, the energy savings due to regenerative braking amount to approximately 190 kWh in this case.

7 Conclusions

The simulations conducted on the 3 kV railway system first without, and then with the connection of solar and wind generators at the traction substations have highlighted the contribution of the renewable generators to the power supply of the traction loads in different operating scenarios, and the convenience of their associated DC connection to the 3 kV DC railway system. With the integration of PV and wind generators operating around full capacity, the total power supplied by the TPSSs was seen to decrease from 3.72 MW to 1 MW, i.e., by 73%, in the case of one train traveling at maximum speed on the downhill track, and by 20% (from 13.22 MW to 10.61 MW) in the case of the railway section occupied by two trains traveling at maximum speed, leading to energy savings of approximately 200 kWh for each crossing between adjacent traction substations. Considering the railway traffic associated with high-speed lines and the high number of traction substations, the integration of renewable energy sources in conjunction with energy storage systems into the railway power supply could lead to significant energy savings and reduction in contracted power of railway systems. In addition, although the renewable generators partly cover the power demand of the traction loads, the continuity of service of the traction system albeit at a lower power level, would be favored in the event of TPSS fault or service interruption.

Several other analyses are necessary to evaluate the feasibility of the integration of renewable generators into the 3 kV DC traction system, most notably regarding the implementation of energy storage and energy management systems that are of paramount importance to utilize the energy produced by wind and solar generators in the absence of power demand from the loads and to smoothen the power absorption from the grid-side. Other necessary studies include system reliability and fault analyses that are needed to evaluate short-circuit currents and the necessary protection switchgear, as well as economic feasibility analyses that are beyond the scope of this work.

Bibliogaphy

[1] M. Brenna, F. Foiadelli, and H. J. Kaleybar, "The Evolution of Railway Power Supply Systems towards Smart Microgrids", *IEEE Electrification Magazine*, 2020.

[2] H. J. Kaleybar, M. Brenna and F. Foiadelli, "Compatibility of Present 3 kV DC and 2×25 kV AC High-Speed Railway Power Supply Systems Towards Future MVDC System," *2021 12th Power Electronics, Drive Systems, and Technologies Conference (PEDSTC)*, 2021.

[3] H. Ritchie, M. Roser, and P. Rosado, Energy, Our World in Data, https://ourworldindata.org/renewable-energy, 2020.

[4] R. F. Boehm, H. Yang, and J. Yan, Handbook of Clean Energy Systems, Volume 1, Renewable Energy, West Sussex: John Wiley & Sons Ltd, 2015.

[5] L. Rubini, S. Sangiorgio, Le Energie Rinnovabili: Le Nuove Tecnologie di Produzione Elettrica e Termica, Milano: Ulrico Hoepli Editore S.p.A., 2012.

[6] URL https://www.fondriest.com/environmentalmeasurements/parameters/weather/photosynthetically-active-radiation/.

[7] URL http://www.solargis.com.

[8] T. Buonassisi. Fundamentals of Photovoltaics. Fall 2013. Massachussets Institute of Technology: MIT OpenCourseWare, http://ocw.mit.edu/.

[9] F. A. Lindholm, J. G. Fossum, and E. L. Burgess, "Application of the Superposition Principle to Solar-Cell Analysis", *IEEE Transactions on Electron Devices, vol. ed-26, no. 3*, March 1979.

[10] C. B. Honsberg and S.G. Bowden, Photovoltaics Education Website, www.pveducation.org, 2019.

[11] M. Johnson, S. Shanifa Beevi, and G. Vincent, "Model based MPPT Algorithm for Drift-Free Operation in PV Systems under Rapidly Varying Climatic Conditions", *7th India International Conference on Power Electronics (IICPE)*, 2016.

[12] J. Svarc, "Solar panel construction", https://www.cleanenergyreviews.info/blog/solar-panel-components-construction, 2020.

[13] A. Caffarelli, G. de Simone, M. Stizza, A. D'Amato, Sistemi Solari Fotovoltaici, Santarcangelo di Romagna: Maggioli S.p.A., 2014.

[14] D. Cocco, C. Palomba, P. Puddu, Tecnologie delle Energie Rinnovabili, Padova: Servizi Grafici Editoriali, 2010.

[15] H. Mammar, A. Benmansour and M. Bouzaki, "Improvement of the photovoltaic conversion efficiency using nanostructuring in intermediate-band photovoltaic solar cells," *2014 North African Workshop on Dielectic Materials for Photovoltaic Systems (NAWDMPV)*, 2014.

[16] F. Inzoli, A. Bianchi, Fonti Energetiche Rinnovabili, Milano: Ulrico Hoepli Editore S.p.A., 2014.

[17] M. Van Den Akker, H. Blok, C. Budd, Chris, R. Eggermont, A. Guterman, D. Lahaye, J. Lansink Rotgerink, K. Myerscough, C. Prins, T. Tromper, W. Wadman, "A Case Study in the Future Challenges in Electricity Grid Infrastructure", 2012.

[18] G. F. Reed, L. A. Solomon and B. M. Grainger, "Prototype development of a full-bridge isolated boost converter for solar photovoltaic systems integration," *2010 IEEE PES Innovative Smart Grid Technologies Conference Europe (ISGT Europe)*, 2010.

[19] M. Kamran, M. Mudassar, M. R. Fazal, M. U. Asghar, M. Bilal, and R. Asghar, "Implemenation of improved Perturb & Obeserve MPPT technique with confined search space for standalone photovoltaic system", *Journal of Kind Saud University – Engineering Sciences*, 2018.

[20] J. M. Riquelme-Dominguez and S. Martinez, "Comparison of Different Photovoltaic Perturb and Observe Algorithms for Drift Avoidance in Fluctuating Irradiance Conditions," *2020 IEEE International Conference on Environment and Electrical Engineering and 2020 IEEE Industrial and Commercial Power Systems Europe (EEEIC / I&CPS Europe)*, 2020.

[21] Y. Mahmoud, "A Model-based MPPT with Improved Tracking Accuracy", *IECON 2018 - 44th Annual Conference of the IEEE Industrial Electronics Society*, 2018.

[22] E. Kim, M. Warner and I. Bhattacharya, "Adaptive Step Size Incremental Conductance Based Maximum Power Point Tracking (MPPT)," *2020 47th IEEE Photovoltaic Specialists Conference (PVSC)*, 2020.

[23] S. Khadidja, M. Mountassar and B. M'hamed, "Comparative study of incremental conductance and perturb & observe MPPT methods for photovoltaic system," *2017 International Conference on Green Energy Conversion Systems (GECS)*, 2017.

[24] Yali Liu, Ming Li, Xu Ji, Xi Luo, Meidi Wang, Ying Zhang, "A comparative study of the maximum power point tracking methods for PV systems", *Energy Conversion and Management*, volume 85, 2014.

[25] M. Ahmadi, H. J. Kaleybar, M. Brenna, F. Castelli-Dezza and M. S. Carmeli, "DC Railway Micro Grid Adopting Renewable Energy and EV Fast Charging Station," *2021 IEEE International Conference on Environment and Electrical Engineering and 2021 IEEE Industrial and Commercial Power Systems Europe (EEEIC / I&CPS Europe)*, 2021.

[26] S. Ikeda and F. Kurokawa, "Isolated and wide input ranged boost full bridge DC-DC converter with low loss active snubber," *2017 IEEE Energy Conversion Congress and Exposition (ECCE)*, 2017.

[27] R. Ricci, D. Vitali, S. Montelpare, "An innovative wind-solar hybrid street light: Development and early testing of a prototype", *International Journal of Low-Carbon Technologies*, 2014.

[28] R. Pallabazzer, Sistemi di conversione eolica. La tecnologia delle moderne macchine del vento, Milano: Ulrico Hoepli Editore S.p.A., 2011.

[29] J. D. M. De Kooning, L. Gevaert, J. Van de Vyver, T. L. Vandoorn and L. Vandevelde, "Online estimation of the power coefficient versus tip-speed ratio curve of wind turbines," *IECON 2013 - 39th Annual Conference of the IEEE Industrial Electronics Society*, 2013.

[30] L. F. M. Gevaert, J. D. M. De Kooning, T. L. Vandoorn, J. Van de Vyver and L. Vandevelde, "Evaluation of the MPPT performance in small wind turbines by estimating the tip-speed ratio," *2013 48th International Universities' Power Engineering Conference (UPEC)*, 2013.

[31] S. Schmitz. Wind Turbine Aerodynamics. Penn State University, e-education.psu.edu.

[32] D. A. Spera, Wind Turbine Technology, Fundamental concepts of wind turbine engineering, ASME Press, 2009.

[33] E. Muljadi, M. Singh, and V. Gevorgian, "Fixed-Speed and Variable-Slip Wind Turbines Providing Spinning Reserves to the Grid", *IEEE Power and Energy Society General Meeting Vancouver*, 2013.

[34] B. Neammanee, S. Sirisumrannukul, and S. Chatratana, "Control Strategies for Variable-speed Fixed-pitch Wind Turbines", in Wind Power. London, United Kingdom: IntechOpen, 2010.

[35] “Wind Turbine Control Methods”, https://www.ni.com/it-it/innovations/white-papers/08/wind-turbine-control-methods.html, 2020.

[36] W. Cao, Y. Xie, and Z. Tan, "Wind Turbine Generator Technologies", in Advances in Wind Power. London, United Kingdom: IntechOpen, 2012.

[37] S. Martin-Martínez, A. Vigueras-Rodríguez, E. Gómez-Lázaro, A. Molina-García, E. Muljadi, and M. Milligan, "Wind Power Variability and Singular Events", in Advances in Wind Power. London, United Kingdom: IntechOpen, 2012.

[38] M. Brenna, F. Foiadelli, and D. Zaninelli, Electric Railway Transportation Systems, New Jersey: John Wiley & Sons, Inc., 2018.

[39] “Energia di Trazione”, Rete Ferroviaria Italiana, https://www.rfi.it/it/Sicurezza-e-tecnologie/tecnologie/energia/energia-di-trazione.html.

[40] D. Cattelan, Analisi di un sistema di alimentazione innovativo per treni ad alta velocità con l’utilizzo di convertitori DC/DC, http://hdl.handle.net/20.500.12608/19983, 2015.

[41] L. Wang, Y. Pang, K. -W. Lao, M. -C. Wong, F. Ma and X. Zhou, "Design and Analysis of Adaptive Impedance Structure for Cophase Railway Traction Supply Power Quality Conditioner," in *IEEE Transactions on Transportation Electrification*, vol. 6, no. 3, 2020.

[42] Qunzhan Li, Wei Liu, Zeliang Shu, Shaofeng Xie and Fulin Zhou, "Co-phase power supply system for HSR," *2014 International Power Electronics Conference (IPEC-Hiroshima 2014 - ECCE ASIA)*, 2014.

[43] M. Chen, Q. Li and S. Xie, "Mathematic Model and Operating Performance of YNvd Transformer," *2009 Asia-Pacific Power and Energy Engineering Conference*, 2009.

[44] A. Baxter, “Network Rail: A Guide to Overhead Electrificaton”, London, 2015.

[45] C. Guerriero, P. Della Porta, “Environmental Performance of the ETR1000”.

[46] S. Mungo, “Collaboraring on the Red Arrow”,

https://www.railengineer.co.uk, 2016.

[47] Redazione, “Il Frecciarossa 1000 è ancora da record”, www.ferrovie.it, 2016.

[48] D. Campione, "Il Frecciarossa 1000", www.ferrovie.it, 2015.

[49] Pdf online.

[50] A. Biancucci, "Rotabili di trazione attuale e di moderna concezione", [PowerPoint slides], Trenitalia – direzione tecnica, http://www.cifi.it/UplDocumenti/Firenze16112018/Intervento%20Ing.%20Biancucci.pdf, 2018.

[51] URL https://web.archive.org/web/20150518101507/http://www.ansaldobreda.it/documents/2504363/44816364/SchedaTecnica_ETR1000.pdf.

[52] M. Caposciutti, "ETR1000", [PowerPoint slides], Trenitalia – direzione tecnica, http://www.cifi.it/UplDocumenti/AV_Freccia1000/TRENITALIA%20ETR1000.pdf, 2015.

[53] M. Ceraolo, G. Lutzemberger, E. Meli, L. Pugi, A. Rindi, G. Pancari, "Energy storage systems to exploit regenerative braking in DC railway systems: different approaches to improve efficiency of modern high-speed trains", http://hdl.handle.net/11568/916497, 2018.

[54] M. Ceraolo, G. Lutzemberger, A. Frilli and L. Pugi, "Regenerative braking in high-speed railway applications: Analysis by different simulation tools," *2016 IEEE 16th International Conference on Environment and Electrical Engineering (EEEIC)*, 2016.

[55] F. Perticaroli, Sistemi elettrici per i trasporti, Trazione elettrica, Milano: Casa Editrice Ambrosiana, 2001.

[56] Terna Rete Italia, "Qualità del servizio di trasmissione: valori minimi e massimi convenzionali della corrente di cortocircuito e della potenza di cortocircuito delle rete rilevante con tensione 380-220-150-132 kV", 2020.

[57] URL http://atlanteeolico.rse-web.it/.

[58] A. M. Bouzid, A. Cheriti, P. Sicard, M. Bouhamida and M. Benghanem, "State space modeling and performance analysis of self-excited induction generators for wind simulation," *2015 3rd International Conference on Control, Engineering & Information Technology (CEIT)*, 2015.

[59] URL https://www.wind-turbine-models.com.

[60] URL https://www.wunderground.com/dashboard/pws/IVITER11/graph/2021-08-31/2021-08-31/daily.

A Appendix

A.1. Boost converter P&O MPPT algorithm code

```
function Duty = MPPT_algorithm(V_Pv,I_Pv,delta)

Duty_init = 0.3;
Duty_min = 0.1;
Duty_max = 0.6;

persistent V_old P_old Duty_old

if isempty(V_old)
    V_old = 0;
    P_old = 0;
    Duty_old = Duty_init;
end
P = V_Pv*I_Pv;
dV = V_Pv - V_old;
dP = P - P_old;

if dP ~= 0 && V_Pv>0
    if dP < 0
        if dV < 0
            Duty = Duty_old - delta;
        else
            Duty = Duty_old + delta;
        end
    else
        if dV < 0
            Duty = Duty_old + delta;
        else
            Duty = Duty_old - delta;
        end
    end
else
    Duty = Duty_old;
end
```

```
if Duty >= Duty_max
    Duty = Duty_max;
elseif Duty < Duty_min
    Duty = Duty_min;
end

Duty_old = Duty;
V_old = V_Pv;
P_old = P;
```

A.2. IBFB converter single phase shift switching strategy code

```
function [PWM14, PWM23] =
Duty_cycle(time,frequency,phase)
Ts=1/frequency;
PWM14=0;
PWM23=0;
t_phi=Ts*phase/360;
y1=mod(time,Ts);
if y1<Ts/2+(t_phi)
    PWM14=1
end
y2=mod(time+Ts/2,Ts);
if y2<Ts/2+(t_phi)
    PWM23=1
end
```

A.3. Wind turbine simplified model

```
function Pm = fcn(v_w, r)

p=1.225; %air density [kg/m^3]
P_nom=595200 %WT rated mechanical power [W]
Cp_max=0.48 %maximum power coefficient
v_cut_in=2.5 %cut-in wind speed [m/2]
v_rated=10 %rated wind speed [m/2]
v_cut_out=20 %cut-out wind speed [m/s]
r=25.4 %WT rotor radius [m]
```

```
if v_cut_in<=v_w && v_w<v_rated
    Pm=0.5*Cp_max*p*pi*r^2*v_w^3
elseif v_rated<=v_w && v_w<=v_cut_out
    Pm=P_nom
else
    Pm=0
end
```